Integrated hydrogeological study of San Cristobal Island (Galapagos)

Christian Dominguez

Université Pierre et Marie Curie

École Doctorale Géosciences, Ressources Naturelles et Environnement

UMR.8538-Laboratoire de Géologie de l'Ecole Normale Supérieure

---

Integrated hydrogeological study of San Cristobal Island (Galapagos)

Par Christian G. Domínguez G.

Thèse de doctorat d'Hydrogéologie

Dirigée par Sophie Violette

Présentée et soutenue publiquement le 09 Mai 2016

Devant un jury composé de :

Bruijnzeel Sampurno L.A.	Professeur (King's College London)	Rapporteur
Jourde Hervé	Professeur (Université de Montpellier)	Examinateur
Lemieux Jean-Michel	Professeur (Université Laval)	Rapporteur
Oudin Ludovic	Maître de Conférences (UPMC)	Examinateur
Villacís Marcos	Professeur-Doyen (EPN-Quito)	Examinateur
Violette Sophie	Maître de Conférences (UPMC-ENS)	Directrice de thèse

Abstract

The understanding of the hydrogeological functioning in regions where surface water is limited is fundamental for a suitable management of its resources. San Cristobal is the only island in the Galapagos Archipelago with permanent freshwater resources, in which water is supplied for the inhabitants from water catchments in the streams located in the southern windward side of the island. To date, these water resources are poorly managed as a consequence of the lack of knowledge surrounding its occurrence. In this context, this work is the first study of the hydrogeological functioning of high-level aquifers in the windward side of San Cristobal using a multi-disciplinary approach at watershed scale, based in the implementation of an experimental site, hydro-climatic monitoring, field surveys, indirect methods and numerical modeling. For this purpose a hydrological network was installed in *Cerro Gato* and surrounding watersheds.

Two hydrological years of records from hydro-climatic stations (2013-2014 and 2014-2015), show a median annual rainfall of ca. 1000 mm (300 m a.s.l.) with an orographic rainfall gradient of 270 mm/100 m of elevation. Cloud water interception (CWI) by the endemic vegetation is estimated using a Rutter-type canopy model, which shows that CWI at the windward highlands (600 m a.s.l.) is not negligible. It represents ca. 28% of the water input during the cool seasons, and it reaches 23% of the total water input for a representative year. Deep percolation (DP) is estimated using the joint modeling of a physically based canopy and soil water transfer model. DP rates are markedly different depending of the altitude, land cover and seasonality. It is mainly affected by altitude in mid-elevation watersheds, whereas land cover is the main controlling factor at high-elevation watersheds because of the additional input of fog interception in forests.

A water balance, performed in three gauged watersheds using estimates of recharge and measured streamflow, reveals that recharge is significantly higher than discharge in high-elevation watersheds, while it is lower than discharge in mid-elevation watersheds. Streamflow is simulated in the three watersheds using a lumped hydrological model (GR4J/GR7J) to characterize the hydrodynamic behavior of these watersheds. Results show that losses from the high-elevation basins (above 400 m of elevation) become groundwater inputs in the mid-elevation basins (below 400 m of elevation), while other mid-elevation basins have inputs from basins at the same altitude, such as *Cerro Gato*, where its hydrogeological watershed represents 140% of the catchment surface and its extension is more likely in the same elevation of the catchment.

The detailed geometry of the hydrogeological watershed of *Cerro Gato* is obtained from a 19-layer resistivity model, which was developed from the dataset

of a high resolution AEM SkyTEM survey conducted in San Cristobal. Two types of geometry are defined with a small and a large threshold of resistivity, which is associated with saturated fractured basalt.

The two cases were tested with a hydrogeological approach, using a 2D saturated/unsaturated groundwater flow model, in which the groundwater flow of springs fed by a perched aquifer in fractured basalt suspended by an impervious thin palaeo-soil layer is simulated. Hydrodynamic parameters of the model were assumed either: from the literature, calibrated in the model, estimated from a seismic refraction survey or measured in the field, depending of the concerned lithology. The model is constrained with the spring discharge measurements. Results from the groundwater model confirm the plausibility of the existence of a perched aquifer with an extensive and smaller length and reveals the influence of the sub-surface weathered cover in the hydrodynamic behavior of the aquifer.

Results of this thesis help to improve the general knowledge of the hydrogeology of basaltic islands, especially of high-level perched aquifers. Also, this thesis provides scientific basis for the effective water management, which could be used by the local institutions to offer solutions to the increased water demand and to provide guidelines to the conservation of freshwater ecosystems.

Keywords: Galapagos, fog interception, water balance, geophysics, hydrological modeling, hydrogeological modeling

Résumé étendu

La compréhension du cycle de l'eau d'une région où les ressources en eau sont limitées est fondamentale pour assurer une gestion durable de celles-ci. C'est notamment le cas des îles basaltiques où la complexité de leur structure interne et la difficulté d'acquisition des données en nombre suffisant pour caractériser l'occurrence de l'eau conduit à une certaine méconnaissance de leur fonctionnement hydrologique. Dans la littérature, plusieurs d'approches sont utilisées pour comprendre le comportement hydrologique des iles volcaniques (géologique, géophysique, géochimique, hydrodynamique), mais peu d'études développent une approche pluridisciplinaire.

L'Archipel des îles Galápagos est mondialement connu pour tous ses espèces endémiques rares et son écosystème unique. Ces îles basaltiques relativement jeune (<3 Ma) et aux ressources en eau limitées, subissent depuis quelques décennies un développement accéléré de leur économie sous l'impulsion de l'attrait touristique que revêt ces îles. Ainsi, la pression sur leurs ressources naturelles s'est considérablement accrue, notamment sur leurs ressources en eau. San Cristóbal, est la seule île de l'Archipel qui possède un réseau hydrographique pérenne. Les habitants sont approvisionnés en eau à partir de prises d'eau en rivières situées cote au vent, au Sud de l'île. Faute de connaissances fondées scientifiquement, la gestion de cette ressource, par les autorités locales est défaillante. Les coupures d'eau sont fréquentes et la qualité de l'eau distribuée inégale.

Depuis 2003, le projet de recherche GIIWS (Galápagos Islands Integrated Water Studies), apporte son soutien aux autorités locales en charge de la gestion des eaux, pour acquérir des connaissances fondamentales sur le fonctionnement hydrologique et la quantification des principaux termes du bilan hydrique. Ainsi, une situation contrastée est rencontrée entre : les îles jeunes (<1 Ma), qui sont caractérisées par l'absence d'eau douce à la surface, cas de Santa Cruz, et les îles relativement plus âgées (>2 Ma) qui possèdent des ressources en eau douce pérennes en surface, cas de San Cristóbal. Jusqu'à présent, les recherches se sont concentrées principalement sur l'île de Santa Cruz, alors que les données acquises sur l'île de San Cristóbal restaient en nombre limité. Ce travail de thèse vise à combler ce manque.

La partie sud-est de l'île de San Cristóbal a une forme de bouclier allongé surmonté de cônes volcaniques qui forment un double alignement parallèle de direction SW-NE et encadrent une zone de replat. Cette partie de l'île a émergé ca. 2.35 Ma et coïncide avec la fin de l'activité volcanique, où le bouclier a été recouvert par une épaisse couche de matériel pyroclastique. Compte tenu des conditions humides régnantes sur la côte sud au vent de l'île, the matériel pyroclastique a été fortement altéré. Ainsi une épaisse couverture de sol s'est formée

et a été incisée par un réseau de drainage. Plusieurs ravines sont alimentées par des sources pérennes. Elles sont les exutoires naturels d'aquifères perchés. Pendant six mois de l'année (saison froide de "garua"), une couche de brouillard quasi-permanent se cré dans la partie haute de l'île (ca. 400 m n.m.m.), laquelle peut constituer un apport supplémentaire en eau pour la recharge des eaux souterraines. Sur ce versant au vent, les bassins versants sont relativement petits (0.5-12 km^2) et le débit des rivières est faible, à l'exception d'un bassin versant situé à mi pente (300 m n.m.m.), Cerro Gato. Outre l'intérêt hydrogéologique que revêt ce bassin, la Municipalité de Puerto Baquerizo Moreno assure la gestion d'une prise d'eau en rivière qui fournit plus de 50% de l'eau distribuée aux habitants.

Contrairement aux autres îles des Galápagos, à San Cristóbal, l'existence de rivières pérennes offre la possibilité unique d'une étude intégrée du cycle de l'eau et des trois compartiments qui le composent : atmosphérique, surface et souterrain. De plus, la taille assez réduite des bassins versants est idéale pour assurer une surveillance hydrologique à haute fréquence avec une instrumentation réduite. Dans ce contexte, cette thèse est la première étude intégrée du fonctionnement hydrogéologique des aquifères perchés de la côte au vent de l'île San Cristóbal. Pour ce faire, une approche pluridisciplinaire à l'échelle du bassin versant, fondée sur la mise en place d'un site expérimental sur le bassin versant de Cerro Gato et deux bassins versants voisins : l'un situé à plus haute altitude (El Bayo) et l'autre à moyen-altitude (Chuki Marka), a été conduite. L'approche développée vise à : i) quantifier les variables d'entrées et de sorties du bilan hydrique de l'échelle de la parcelle à celle du bassin versant, ii) caractériser la structure du système avec des méthodes directes d'observation et de mesures sur le terrain et indirectes (géophysique) et, iii) tester la cohérence des données collectées et le modèle conceptuel qui en découle par l'utilisation de modèles hydrologiques et hydrogéologiques et ainsi mieux comprendre l'interaction entre les écoulements superficiels et souterrains, que ces derniers soient en milieu non saturé ou saturé.

Site expérimental

Un nouveau modèle numérique du terrain de 10 m de résolution (IGM, 2014), des images aériennes à haute résolution (IGM, 2014) et un inventaire exhaustif des sources ont permis d'établir la première carte synthétique des ressources hydriques de la zone au vent de l'île de San Cristóbal (Fig. 2.7). Cette carte inclue le réseau de drainage, les rivières pérennes, la localisation des sources et

la définition des bassin versants, y compris ceux de : El Bayo (1,78 km^2), Chuki Marka (0,33 km^2) et Cerro Gato (0,69 km^2).

Ainsi, le long du versant au vent de l'île et à proximité de ces bassins versants, un réseau de surveillance hydro-climatologique a été installé et fonctionne depuis Juin 2013 (Fig. 2.16). Le dispositif de mesures comprend trois stations climatiques automatiques (15 min) situées à différentes altitudes (30, 300 et 600 m n.m.m.). La station située à haute altitude est équipée de façon à mesurer la traversée au travers la canopée et l'écoulement le long des tiges dans un bosquet de *miconias* (espèce endémique des îles Galápagos). Les transferts hydriques dans le sol sont mesurés avec des tensiomètres par mesures automatiques (15 min) et manuelles (1 à 3 fois par semaines pendant une année hydrologique) aux stations situées à moyenne et hautes altitudes. Le réseau est complété par des mesures de débit à trois sections de contrôle à l'exutoire des bassins versants de El Bayo, Chuki Marka et Cerro Gato.

Caractérisation du climat

Les mesures climatologiques acquises au cours de cette thèse ont permis la première caractérisation climatique de la zone au vent de l'île pendant les années hydrologiques 2013-2014 et 2014-2015. Confrontées aux données historiques de la station Charles Darwin sur l'île Santa Cruz (6 m n.m.m.), il ressort que l'année hydrologique 2013-2014 est une année moyenne en termes de pluie et de température, alors que l'année 2014-2015 peut être considérée comme une année chaude et relativement humide. Elle atteint presque le quantile supérieur de pluie annuelle.

Les données observées aux stations mettent en évidence un gradient orographique de la pluie et de l'évapotranspiration de référence (ETo). Pour l'année représentative (2013-2014), la médiane des pluies est de 1000 mm (300 m n.m.m.) et le gradient orographique des pluies est de 270 mm/100 m d'élévation pour une valeur de 200 mm à la côte. L'évapotranspiration de référence est de 680 mm (300 m n.m.m.) et le gradient orographique de l'ETo est de -50 mm/100 m d'élévation et débute avec une valeur de 840 mm à la côte.

Estimation de la recharge vers les aquifères

Pour quantifier les entrées d'eau dans le système hydrologique, les données du réseau de mesure sont utilisées pour quantifier la recharge de l'échelle de la parcelle à celle du bassin versant en utilisant tout d'abord une approche canopée-

transfert hydrique du sol. L'interception de la brume est considérée avec un model d'interception de type *Rutter* dans lequel l'estimation de l'interception du brouillard est validée avec les mesures de la traversée au travers la canopée. Au niveau du sol, un model de transfert hydrique est utilisé pour quantifier de manière plus précise l'évapotranspiration réelle de deux types de couvertures végétales : forêt de *miconias* et herbe. Ce model est validé avec des mesures de pression dans le sol à différentes profondeurs obtenues grâce aux tensiomètres. Les résultats obtenus à l'échelle de la parcelle sont ensuite spatialisés en se fondant sur la distribution spatiale de la couverture végétale, le relief et les gradients orographiques des pluies, du brouillard et de l'évapotranspiration.

L'interception du brouillard dans la forêt avec une végétation endémique dans la partie haute de l'île n'est pas négligeable. Elle représente 28% de l'apport d'eau pendant la saison froide et atteint 23% de l'apport total en eau pour une année représentative.

La percolation profonde (recharge) est différente selon les sites de mesures et dépend de la couverture végétale, de l'altitude et de la saisonnalité. Elle est principalement affectée par l'altitude en raison de l'effet orographique sur les gradients de pluie et d'évapotranspiration. Néanmoins, à haute altitude, la différence est principalement associée à la couverture végétale en raison de leur différent taux de transpiration et de l'apport additionnel fourni par l'interception du brouillard sous la forêt.

A l'échelle du bassin versant, la recharge est principalement affectée par l'altitude. A cette échelle, l'interception du brouillard a un effet réduit dépendant du type de couverture végétal et de l'exposition aux vents dominants (Fig. 3.24). En effet, en comparant une approche simple d'estimation de la recharge (pluie moins évapotranspiration) avec celle que nous avons développée, la recharge peut être surestimée ca. 25%. Cette surestimation n'est pas sans conséquence sur les analyses hydrologique-hydrogéologique des bassins versants. La recharge moyenne estimée pour les trois bassins versants pendant l'année représentative est donc de 1530, 690 et 830 mm à El Bayo, Chuki Marka et Cerro Gato, respectivement.

Analyse hydrologique

Pour mieux comprendre le comportement hydrologique des bassins versants étudiés on a utilisé : i) une analyse des hydrographes mesurés à l'exutoire de chaque bassin et, ii) une modélisation hydrologique avec un modèle conceptuel pluie-débit (GR4J).

Les mesures à l'exutoire des trois bassins versants étudiés montrent que leur débit est diffèrent d'un bassin à l'autre. Le débit médian journalier est ca. 8 l/s pour le bassin versant en haute altitude (El Bayo), alors qu'il est 17 et 29 l/s pour Chuki Marka et Cerro Gato (bassins versants à moyenne-altitude), respectivement. En utilisant une technique de séparation des hydrogrammes de crue (méthode FUKIH) sur nos chroniques de données, le débit de base (contribution de l'aquifère à l'écoulement en rivière) représente 53, 80 et 87% du débit total mesuré à l'exutoire de El Bayo, Chuki Marka et Cerro Gato, respectivement (Fig. 4.4).

A partir de l'analyse de la recharge, du débit à l'exutoire et débit de base pour chaque bassin sur les deux années hydrologiques, il est observé que : i) le débit à l'exutoire de El Bayo est considérablement plus petit que la recharge. Il réagit rapidement au climat et à sa saisonnalité, ii) le débit à l'exutoire de Chuki Marka est plus élevé que la recharge. Il très sensible aux événements de pluie dont il enregistre la saisonnalité de façon retardée, et iii) le débit à l'exutoire de Cerro Gato est plus grand que la recharge. Il est presque constant pendant les deux années hydrologiques. La forte prédominance du débit de base montre qu'il dépend d'un réservoir souterrain de taille importante à mettre en relation avec l'existance d'un aquifère perché.

Le model GR4J et versions modifiées sont utilisés pour simuler le débit des trois bassins versants. La meilleure simulation est obtenue avec la version GR7J (en utilisant 7 paramètres dans le model GR4J), où le critère de Nash-Sutcliffe (NS) pour la racine carré du débit arrive à 0,90 à El Bayo et 0,83 à Cerro Gato (Fig. 4.10). A Chuki Marka, une modification dans la fonction d'échange des eaux souterraines dans le modèle GR7J a été nécessaire pour obtenir une simulation satisfaisante, où NS arrive à 0,79 (Fig. 4.12). Les simulations et les paramètres calibrés du modèle montrent une différence important dans le comportement hydrologique des trois bassins versants. A El Bayo, la plus grande partie de l'eau apportée par la recharge (ca. 60%) est perdue, soit pour un échange avec d'autres bassins adjacents ou pour alimenter en profondeur l'aquifère de base (aquifère côtier en équilibre avec la mer). Dans le cas de Chuki Marka, un très important échange d'eau souterraine se produit qui influence la saisonnalité observée dans le débit mesuré à l'exutoire. Ainsi cet échange se traduit par un gain en eau souterraine représentant 40% de l'apport total d'eau au bassin. Même si Cerro Gato possède le débit à l'exutoire le plus important des trois bassins étudiés, l'apport d'eau souterraine en provenance des autres bassins n'est que de 18%.

De façon générale, il apparait que les pertes des bassins versants situés à haute-altitude (comme El Bayo) deviennent les entrées d'eau souterraine des bassins versants situés à moyenne altitude (comme Chuki Marka). De plus, cer-

tains bassins versants de moyenne altitude reçoivent des entrées d'eau souterraine additionnelles de bassins versants situés à des altitudes similaires (comme Cerro Gato). Ainsi, son bassin hydrogéologique est plus étendu que son bassin hydrologique et cette extension est plus probablement localisée à la même altitude.

Structure Interne

Dans le cadre de cette thèse, deux types de méthodes géophysiques sont utilisées, électromagnétique héliportée et réfraction sismique, la première pour définir l'extension du bassin hydrogéologique de Cerro Gato et, la deuxième pour estimer les propriétés hydrodynamiques de sa structure interne et des autres sites de l'île.

L'acquisition des données par méthode électromagnétique héliportée SkyTEM conduite sur San Cristóbal en mai 2006 et leur inversion permet la visualisation en 3D du model de résistivité et la meilleure compréhension de sa structure interne jusqu'à 400 m de profondeur. Des unités de résistivité contrastée sont présentes à l'intérieur de l'île. Le modèle inversé à l'aide de 19-couches de résistivité permet une meilleure description de la géométrie des unités de faible résistivité (30-70/100 Ωm) liées à la présence d'aquifères perchés, dont les principaux exutoires sont : les sources. En effet, la confrontation entre le modèle de résistivité et les observations de terrain permet d'expliquer le contexte hydrogéologique d'émergence des sources de Cerro Gato. Une unité géologique peu perméable (aquitard) située à ca. 80 m de profondeur sous la surface du sol permet l'existence au-dessus d'un aquifère perché. Le flux d'eau souterraine est redirigé vers la surface car l'unité peu perméable est recoupée par la topographie localement. Ainsi, l'eau souterraine sort à la surface à travers du basalte fracturé situé au-dessus de l'unité peu perméable constituée de paléosols recuit ou de scories altérées. L'extension du bassin hydrogéologique de Cerro Gato est obtenue en effectuant le seuillage du modèle de résistivité avec deux gammes de résistivités (30-70 et 30-100 Ωm). Une surface du bassin versant hydrogéologique de dimension équivalente ou plus grande que le bassin hydrologique sont obtenues (Fig. 5.13). La surface du bassin hydrogéologique se prolonge à l'Est et dans le cas de la surface plus grande, une petit partie se prolonge vers la région située à plus haute altitude.

Les sondages réalisés par réfraction sismique révèlent la structure de la proche surface (ca. 15 m de profondeur) de différents sites de l'île. Les tomographies interprétées montrent trois couches où les vitesses des ondes P sont contrastées (Fig. 5.18). Elles correspondent à : i) un sol ou basalte très altéré en surface (400-

500 m/s), ii) du basalte fracturé non-saturé (1400-1700 m/s) et, iii) du basalte fracturé saturé (2400-2700 m/s). La couverture altérée dans la zone d'étude varie entre 4 m d'épaisseur à moyenne altitude (200 m n.m.m.) à 14 m d'épaisseur à plus haute altitude (600 m n.m.m.). Les propriétés hydrodynamiques sont estimées grâce à un modèle de milieu effectif élastique utilisant les données de vitesses sismiques. Ainsi la porosité totale varie entre 4 et 12% aux sites situés près de la côte alors qu'elle atteint 20% dans la zone de Cerro Gato. La conductivité hydraulique estimée est relativement forte en comparaison avec les autres valeurs de la littérature. Elle varie entre 1×10^{-4} et 1 m/s. Il est à souligner que plusieurs hypothèses et incertitudes conduisent à penser que ces valeurs sont surestimées.

Approche hydrogéologique

Des approches précédemment décrites, découlent un modèle conceptuel hydrogéologique des sources de Cerro Gato. Ainsi, les eaux souterraines de cette sources sont issues d'un aquifère perché de basalte fracturé qui s'est formé à la faveur d'une fine couche peu perméable (Fig. 6.1). Ce modèle conceptuel hydrogéologique est testé par simulations numériques des écoulements couplés en milieux non saturé et saturé le long d'une coupe verticale en 2D conduites avec le logiciel METIS. La géométrie du modèle est conçue à partir d'une section représentative du bassin située dans son axe principale d'élongation. Les conditions aux limites prescrites sont fondées sur la connaissance du système et l'estimation de la recharge. Les paramètres hydrodynamiques utilisés sont soit mesurés, issus de la littérature ou calibrés. La vraisemblance de la géométrie de l'aquifère perchée est évaluée en comparant le débit simulé en régime permanent avec le débit observé aux sources de Cerro Gato. L'utilisation d'une longueur plus ou moins réduite de la couche peu perméable, permet d'évaluer l'influence de la couverture altérée sur la réponse hydrodynamique du système simulé.

Les résultats de plusieurs simulations correspondant à différents jeux de paramètres montrent qu'un aquifère perché se forme et qu'un débit d'eau à l'exutoire comparable au débit observé peut être restitué. Le débit simulé n'est pas sensible à plusieurs paramètres, à l'exception de la conductivité hydraulique de la couche peu perméable, qui doit être inférieure à 1×10^{-8} m/s pour reproduire le débit observé. En utilisant une longueur de la couche peu perméable réduite, la couverture altérée doit avoir au moins 7.5 m d'épaisseur et sa conductivité hydraulique doit être au moins de 3×10^{-5} m/s pour obtenir un flux sub-superficiel suffisant capable d'arriver aux limites de l'aquifère perché et ainsi contribuer à

sa recharge. La simulation optimale, capable de reproduire le débit observé, où le fonctionnement hydrogéologique est cohérent avec les données disponibles et dont la distribution de la saturation simulée est relativement similaire à la distribution de la résistivité, conduit à un âge des eaux aux sources de Cerro Gato de 8 ans. Il s'agit d'un mélange entre une eau de recharge jeune, peu profonde, proche de la source et une eau de recharge plus ancienne et éloignée de la source, ayant eu un parcours souterrain au sein de l'aquifère perché (Fig. 6.11), dont la proportion est plus importante.

Conclusions

Cette approche de modélisation hydrogéologique considère une simplification du système hydrogéologique, via une géométrie simplifiée, des valeurs moyennes de recharge et de débits. L'amélioration de la connaissance du système, pourrait se faire à l'aide d'un modèle plus élaboré prenant en compte une configuration plus complexe, mais l'acquisition de contraintes supplémentaires est impérativement nécessaire. Néanmoins, l'approche développée ici, fournit pour la première fois une compréhension intégrée du système hydrologique du bassin versant de Cerro Gato, dans laquelle chaque partie méthodologique conduit à des résultats importants qui peuvent être utilisés par chacune des différentes disciplines et qui souligne la pertinence d'une étude pluridisciplinaire. L'acquisition de nouvelles données expérimentales au cours de deux années hydrologiques à l'échelle du bassin versant, le développement et l'utilisation d'outil de simulation numérique sont les garants de la réussite de ce travail.

Les résultats de cette thèse aident à améliorer la connaissance générale de l'hydrogéologie des îles basaltiques, notamment celle des aquifères perchés situés en altitude. De plus, cette thèse fournit les fondements scientifiques d'une gestion durable des ressources en eau à partir desquels les institutions locales pourraient offrir des solutions pertinentes pour pallier à la demande croissante en eau tout en veillant à la conservation des écosystèmes d'eau douce.

Mots clé : Galápagos, interception du brouillard, bilan hydrique, géophysique, modélisation hydrologique, modélisation hydrogéologique

Resumen extendido

La comprensión del ciclo del agua en una región donde los recurso hídricos son limitados es fundamental para una gestión durable de dicho recurso. Es de mayor importancia en el caso de islas basálticas, en donde la complejidad de su estructura interna acompañada de la dificultad de conseguir suficientes datos para caracterizar la ocurrencia de agua, conllevan a un cierto nivel de desconocimiento sobre su funcionamiento hidrológico. En la literatura, varias acercamientos han sido utilizados para entender el comportamiento hídrico de islas volcánicas (geológicos, geofísicos, geoquímicos, hidrodinámicos), pero en pocos estudios se ha usado un acercamiento pluri-disciplinario.

El Archipiélago de Galápagos es conocido mundialmente por sus especies endémicas y ecosistemas únicos. Estas islas basálticas relativamente jóvenes (< 3 Ma) y con recursos hídricos limitados, experimentan desde hace varias décadas un desarrollo acelerado de su economía a través de la explotación del atractivo turístico que ofrecen estas islas. De esta forma, la presión sobre los recursos naturales ha aumentado considerablemente, especialmente sobre los recursos hídricos. San Cristóbal es la única isla del Archipiélago que posee un recurso hidrográfico perene. Los habitantes son aprovisionados de agua a partir de tomas de agua en riachuelos situados en el lado barlovento, al sur de la isla. Debido al bajo conocimiento científico, la gestión de este recurso de parte de las autoridades locales ha sido defectuoso. Los cortes en la dotación son frecuentes y la calidad del agua distribuida es regular.

Desde el 2003, el proyecto de investigación GIIWS (Galápagos Islands Integrated Water Studies), ha dado su apoyo a las autoridades locales en cargo de la gestión del agua, para adquirir el conocimiento fundamental sobre el funcionamiento hidrológico y la cuantificación de los términos principales del balance hídrico. De esta forma, una situación discrepante ha sido encontrada entre: islas jóvenes (< 1 Ma), que se caracterizan por la ausencia de agua dulce superficial, el caso de Santa Cruz, e islas relativamente viejas (> 2 Ma) que poseen recursos superficiales de agua dulce permanentes, el caso de San Cristóbal. Hasta el presente, las investigaciones del proyecto han sido concentradas principalmente en la isla Santa Cruz, mientras que los datos obtenidos en la isla San Cristóbal siguen siendo limitados en número. Este trabajo apunto a llenar este vacío.

La parte sur de la isla San Cristóbal tiene una forma de escudo alongado superpuesto por conos volcánicos que forman una doble alineación paralela a la dirección SO-NE. Esta parte de la isla emergió hace aprox. 2.35 Ma y coincide con el fin de la actividad volcánica, donde el escudo fue recubierto de una capa espesa de material piroclástico. Debido a las condiciones húmedas presentes en el lado barlovento de la isla, el material piroclástico ha sido alterado fuertemente.

De esta manera una capa de suelo espeso se ha formado la cual ha sido entallada por una red de drenaje. Varios riachuelos son alimentados por fuentes de agua permanentes, que son las salidas naturales de acuíferos colgados. Durante seis meses del año (temporada fría "garúa"), una capa de neblina casi-permanente se ubica en la parte alta de la isla (aprox. 400 m s.n.m.), la cual puede constituir un aporte suplementario de agua para la recarga del agua subterránea. En el lado barlovento, las cuencas hidrográficas son relativamente pequeñas (0.5-12 km^2) y el caudal de sus riachuelos es pequeño también, a excepción de una cuenca situada a media elevación (300 m s.n.m.), Cerro Gato. Además del interés hidrogeológico de esta cuenca, el Municipio de Puerto Baquerizo Moreno tiene instalado una toma de agua que dota alrededor del 50% del agua distribuida a los habitantes de la isla.

A diferencia de otras islas de Galápagos, en San Cristóbal, la existencia de ríos permanentes ofrece la oportunidad única de estudiar de manera integrada el ciclo del agua en los tres compartimientos en donde se la podría encontrar: atmosférico, superficial y subterráneo. Además, el tamaño reducido de sus cuencas es ideal para asegurar un monitoreo hidrológico de alta frecuencia con una instrumentación reducida. En este contexto, esta tesis es el primer estudio integrado del funcionamiento hidrogeológico de los acuíferos colgados en el lado barlovento de la isla San Cristóbal. Para este fin, un acercamiento pluri-disciplinario a nivel de cuenca hidrográfica ha sido utilizado, cuya base es la instalación de un sitio experimental en la cuenca de Cerro Gato y otras dos cuencas vecinas: la una situada en la parte alta (El Bayo) y la otra a media altitud (Chuki Marka). La metodología propuesta busca: i) cuantificar las variables de entrada y de salida del balance hídrico desde una escala de parcela hasta una de cuenca hidrográfica, ii) caracterizar la estructura del sistemas a partir de métodos directos de observación y mediciones en el terreno combinados con métodos indirectos (geofísica) y, iii) probar la coherencia de los datos colectados y del modelo conceptual propuesto a partir de la utilización de modelos hidrológicos e hidrogeológicos, para entender mejor la interacción entre los flujos de agua superficiales y subterráneos en medios saturados y no saturados.

Sitio experimental

A partir de un nuevo modelo numérico de terreno de 10 m de resolución ((IGM, 2014)), imágenes aerofotogramétricas de alta resolución y un inventario exhaustivo de fuentes de agua, se ha podido realizar el primer mapa de los recursos hídricos de la zona barlovento de la isla San Cristóbal (Fig. 2.7). Este

mapa incluye la red de drenaje, los riachuelos permanentes, la localización de fuentes de agua y la definición del cuencas hidrográficas, incluyendo las cuencas de: El Bayo (1.78 km^2), Chuki Marka (0.33 km^2) y Cerro Gato (0.69 km^2). De esta forma, a lo largo del lado barlovento de la isla y cerca de estas cuencas, una red de monitoreo hydro-climatológica ha sido instalada y funciona desde Junio del 2013 (Fig. 2.16). Los dispositivos de medición comprenden tres estaciones climáticas automáticas (15 minutos) situadas a diferentes elevaciones (30, 300 y 600 m s.n.m.). La estación situada en la parte alta está adicionalmente equipada para medir la neblina, la trascolación y el flujo de agua por los troncos de un bosque de *Miconias* (especie endémica de las Islas Galápagos). La transferencia hídrica en el suelo es medida con tensiometros automáticos (15 minutos) y manuales (1 a 3 veces por semana durante el primer año hidrológico) en las estaciones situadas en la parte alta y a media elevación. La red es complementada con mediciones de caudal en tres secciones de control en la desembocadura de las cuencas hidrográficas de El Bayo, Chuki Marka y Cerro Gato.

Caracterización del clima

Los datos climatológicos adquiridos en esta tesis han permitido hacer la primera caracterización del clima de la zona barlovento de la isla durante los años hidrológicos 2013-2014 y 2014-215. Comparando con los datos históricos de la estación Charles Darwin en la isla Santa Cruz (6 m s.n.m.), el año hidrológico 2013-2014 se puede considerar como un año promedio en términos de precipitación y temperatura, mientras que el año 2014-2015 se podría considerar como un año cálido y relativamente húmedo, donde la precipitación casi alcanza el primer cuartil en la precipitación histórica.

Los datos observados en las estaciones ponen en evidencia la presencia de un gradiente orográfico de lluvia y evapotranspiración referencial (ETo). Para el año representativo (2013-2014), la mediana de precipitación es de aprox. 1000 mm (altitud : 300 m s.n.m.) y el gradiente orográfico de precipitación es de aprox. 270 mm/100 m de elevación con un valor que llega a la costa de 200 mm. La evapotranspiración referencial es de 680 mm (300 m s.n.m.), donde el gradiente es de -50 mm/100 m de elevación y alcanza un valor de 840 mm en la costa.

Estimación de la recarga en los acuíferos

Para cuantificar las entradas de agua en el sistema hidrológico, los datos de la red de monitoreo son utilizados para medir la recarga desde la escala de parcela

hasta la escala de cuenca hidrográfica utilizando un acercamiento del tipo canope-transferencias hídricas en el suelo. La intercepción de la neblina es considerada con un modelo de tipo *Rutter* en donde la estimación de intercepción de la neblina es validada con las mediciones de trascolación en el canope. Al nivel del suelo, un modelo de transferencia hídricas es usado para cuantificar de una manera más precisa la evapotranspiración real de dos tipos de cobertura vegetal: bosque de *miconias* y césped. Este modelo es validado con las mediciones presión del suelo a diferentes profundidades obtenidas gracias a los tensiómetros. Los resultados obtenidos a escala de parcela son especializados en base a la distribución espacial de la cobertura vegetal, el relieve y los gradientes orográficos de lluvia, neblina y evapotranspiración.

La intercepción de neblina por parte del bosque endémico en la parte alta de la isla no es despreciable. Esta representa el 28% del aporte total de agua durante la temporada fría y llega hasta el 23% para un año representativo.

La percolación profunda (recarga) es diferente en cada sitio de medición y depende de la cobertura vegetal, la altitud y la temporada. Esta es principalmente afectada por la altitud debido al efecto orográfico de la lluvia y evapotranspiración. Sin embargo, en la parte alta, la diferencia es asociada principalmente al aporte adicional de la intercepción de la neblina en el bosque.

A la escala de cuenca hidrográfica, la recarga es afectada principalmente por la altitud. A esta escala, la intercepción de la neblina tiene un efecto reducido y depende del tipo de cobertura y su exposición a los vientos dominantes (Fig. 3.24). Comparando un método simple de estimación de la recarga (balance de lluvia menos evapotranspiración) con el método utilizado, la recarga puede ser subestimada aproximadamente en un 25%. Dicha subestimación conlleva consecuencias en el análisis hidrológico-hidrogeológico de las cuencas hidrográficas. La recarga media estimada para las tres cuencas hidrográficas en el año representativo es de 1530, 690 y 830 mm en El Bayo, Chuki Marka y Cerro Gato.

Análisis hidrológico

Para mejorar la comprensión del comportamiento hidrológico de las cuencas estudiadas se ha utilizado : i) un análisis de los hidrogramas obtenidos en la desembocadura de cada cuenca y, ii) un modelo hidrológico conceptual precipitación-caudal (GR4J).

Las mediciones en las desembocaduras de las tres cuencas hidrográficas estudiadas muestran que su caudal es marcadamente diferente. El caudal medio diario es de aprox. 8 l/s en la cuenca de la parte alta (El Bayo), mientras que

éste es de 17 y 29 l/s en Chuki Marka y Cerro Gato (cuencas ubicadas a media elevación), respectivamente. Utilizando una técnica de separación gráfica de hidrogramas de crecida (método FUKIH) en la crónica de datos, el caudal base (contribución del acuífero al caudal del río) representa 53, 80 y 87% del caudal total medido en la desembocadura de El Bayo, Chuki Marka y Cerro Gato, respectivamente (Fig. 4.4).

A partir del análisis de la recarga, del caudal a la desembocadura y del caudal base en cada cuenca durante los dos años hidrológicos, se pudo observar que : i) el caudal en la desembocadura de El Bayo es mucho menor que la recarga y que además, éste reacciona rápidamente al clima y al cambio de temporada, ii) el caudal de Chuki Marka es mucho mayor que la recarga, cuya sensibilidad a los eventos de precipitación es apreciable a lo largo de los dos años y que presenta una reacción retardada al cambio de temporada, y iii) el caudal en Cerro Gato es mucho mayor que la recarga y se caracteriza por ser casi constante durante los dos años hidrológicos. La fuerte predominancia del caudal de base muestra que éste depende de un reservorio subterráneo de tamaño considerable que se podría relacionas con un acuífero colgado.

El modelo GR4J y versiones modificadas de él han sido utilizados para simular el caudal de las tres cuencas. La mejor simulación se obtuvo con la versión GR7J (utilizando 7 parámetros en el modelo GR4J), donde el criterio de Nash-Sutcliff (NS) para la raíz cuadrada del caudal alcanza 0.9 en El Bayo y 0.83 en Cerro Gato (Fig. 4.10). En Chuki Marka, una modificación en la función de intercambio de aguas subterráneas fue necesario para alcanzar una simulación satisfaciente, donde NS alcanzó 0.79 (Fig. 4.12). Las simulaciones y los parámetros calibrados del modelo muestran una diferencia importante en el comportamiento hidrológico de las tres cuencas. En El Bayo, la mayor parte de la entrada de agua se pierde (aprox. 60%), ya sea por un intercambio con otras cuencas adyacentes o por infiltración profunda que alimenta el acuífero de base (acuífero costero en equilibrio con el mar). En el caso de Chuki Marka, un importante intercambio de aguas subterráneas ocurre en esta cuenca, el cual influencia la reacción tardía del cambio de temporada y resulta finalmente en la ganancia de aguas subterráneas representando aproximadamente el 40% de la entrada total. A pesar que Cerro Gato tiene el caudal más alto de las cuencas, el aporte de aguas subterráneas de otras cuencas es de 18%.

De forma general, parece que las pérdidas de las cuencas de la parte alta (como en el caso de El Bayo) se convierten en ganancias en forma de entrada de aguas subterráneas en las cuencas a media altura (como en el caso de Chuki Marka). Además, ciertas cuencas ubicadas a media elevación reciben el aporte de aguas subterráneas de cuencas situadas a una elevación similar (como en el

caso de Cerro Gato). De esta forma, la cuenca hidrogeológica de Cerro Gato es más grande que su cuenca hidrográfica y su parte extendida se localiza probablemente a la misma elevación.

Estructura interna

Dos tipos de métodos geofísicos han sido utilizados, electromagnético heliportado y sísmica de refracción, para definir la extensión de la cuenca hidrogeológica de Cerro Gato y estimar las propiedades hidrodinámicas de su estructura interna y de otros sitios de la isla.

La adquisición de datos por el método electromagnético heliportado SkyTEM conducido en San Cristóbal en Mayo del 2006 y su inversión permiten la visualización en 3D del modelo de resistividad de la isla, que permite una mejor comprensión de su estructura interna. Unidades de resistividad contrastadas son presentes en el interior de la isla. El modelo de inversión con 19 capas de resistividad permite una mejor descripción de la geometría de las unidades de baja resistividad (30-70/100 Ωm) que se relacionan con la presencia de acuíferos colgados, donde su principal salida son las fuentes de agua. En efecto, la confrontación entre el modelo de resistividad y las observaciones de terreno permiten explicar el contexto hidrogeológico de la emergencia de las fuentes de agua en Cerro Gato. Una unidad geológica de baja permeabilidad (acuitardo) situada a aprox. 80 m de profundidad debajo de la superficie del suelo permite la existencia de un acuífero colgado sobre la misma. El flujo de agua subterráneo de dicho acuífero es dirigido hacia la superficie debido a que la unidad de baja permeabilidad corta la topografía localmente. De esta forma, el agua subterránea sale a la superficie a través del basalto fracturado que se encuentra encima de la unidad de baja permeabilidad que está constituida por escoria alterada. La extensión de la cuenca hidrogeológica de Cerro Gato es extraída del modelo de resistividad utilizando dos umbrales de resistividad (30-70 y 30-100 Ωm). La superficie de la cuenca hidrogeológica es equivalente o más grande que la cuenca hidrográfica dependiendo del umbral (Fig. 5.13). Dicha superficie se prolonga hacia el Este en los dos casos, y en el caso del mayor umbral también una pequeña parte se extiende hacia la parte alta.

Los sondeos realizados durante la campaña de refracción sísmica muestran la estructura cerca de la superficie (aprox. 15 m de profundidad) de diferentes sitios de la isla. La interpretación de la tomografía muestra tres capas principales donde la velocidad de la onda P es bastante contrastada (Fig. 5.18). Estas corresponden a: i) suelo o basalto muy alterado en la superficie (400-500 m/s), debajo,

ii) basalto fracturado no saturado (1400-1700 m/s) y finalmente, iii) basalto fracturado saturado (2400-2700 m/s). La cobertura alterada en la zona estudiada varía entre alrededor de 4 m de profundidad a media altura (200 m s.n.m.) a 14 m de espesor en la parte alta (600 m s.n.m.). Las propiedades hidrodinámicas fueron estimadas gracias a un modelo de medio efectivo elástico utilizando los datos de velocidad sísmica. De esta manera, la porosidad total varía entre 4 y 12% en los sitios cercanos a la costa mientras que alcanza 20% cerca de la zona de Cerro Gato. La conductividad hidráulica estimada es relativamente alta en comparación a otros valores encontrados en la literatura. Esta varía entre 1×10^{-4} y 1 m/s. Cabe recalcar que varias hipótesis e incertidumbres durante la estimación conducen a pensar que estos valores pueden estar sobreestimados.

Acercamiento hidrogeológico

Los acercamientos precedentemente descritos, conllevan a un modelo hidrogeológico conceptual para las fuentes de Cerro Gato. Este modelo describe que el origen del agua en las fuentes es el resultado de un acuífero colgado de basalto fracturado que se forma gracias a la existencia de una fina capa poco permeable (Fig. 6.1). Este modelo conceptual hidrogeológico es probado con una simulación numérica de flujos en medio saturado y no saturado a lo largo de un perfil vertical en 2D que se realiza con el programa METIS. La geometría del modelo es obtenida a partir de una sección representativa de la cuenca estudiada situada en el eje principal de elongación. Las condiciones en los límites prescritas son basadas en el conocimiento del sistema y de la estimación de la recarga. Los parámetros hidrodinámicos utilizados son medidos, sacados de la literatura o calibrados. La plausibilidad de la geometría del acuífero colgado utilizado es evaluada comparando el caudal simulado en régimen permanente con el caudal observado en las fuentes de Cerro Gato. El uso de una longitud más o menos reducida de la capa poco permeable, permite evaluar la influencia de la cobertura alterada sobre la respuesta hidrodinámica del sistema simulado.

Los resultados de varias simulaciones que corresponden a diferentes juegos de parámetros muestran que se puede formar un acuífero colgado cuyo caudal a la salida es comparable con el caudal observado en las fuentes. El caudal simulado no es sensible a la mayoría de parámetros, a excepción de la conductividad hidráulica de la capa poco permeable, que debe ser inferior a 1×10^{-8} m/s para reproducir al menos el caudal observado. Utilizando una longitud reducida de la capa poco permeable, la cobertura alterado debe de ser de al menos 7.5 m de espesor y su conductividad hidráulica debe ser menor a 3×10^{-5} m/s para

lograr obtener un flujo sub-superficial suficiente que sea capaz de llegar a los límites del acuífero colgado y así contribuir a su recarga. La mejor simulación, la que es capaz de reproducir el caudal observado, cuyo funcionamiento hidrológico es coherente con los datos disponibles y donde su distribución de saturación es relativamente parecido a la distribución de resistividad, tiene una edad del agua de las fuentes de Cerro Gato de alrededor de 8 años. Esta, es formado de una mezcla entre la recarga joven, poco profunda, de la superficie cerca de la fuente y de una recarga más antigua y alejada de la fuente, que se encuentra en camino a la fuente por el acuífero colgado (Fig. 6.11), en donde la última es más influyente.

Conclusiones

Este acercamiento de modelación hidrogeológica considera una simplificación del sistema hidrogeológico, usando una geometría simplificada y con valores promedio de recarga y caudal. Un mejor entendimiento del sistema se podría hacer con la ayuda de un modelo más elaborado tomando en cuenta una configuración más compleja, pero la adquisición de más datos es imperativamente necesario. Sin embargo, el acercamiento de esta tesis, provee por primera vez una comprensión integrada del sistema hidrológico de la cuenca hidrográfica de Cerro Gato, en la que cada parte metodológica ha conducido a resultados importantes que pueden ser utilizados en diferentes disciplinas y que subrayan la pertinencia de un estudio pluri-disciplinario. La adquisición de nuevos datos experimentales a lo largo de dos años hidrológicos a la escala de cuenca hidrográfica, el desarrollo y utilización de instrumentos de simulación numérica son los garantes del éxito de este trabajo.

Los resultados de esta tesis ayudan a mejorar el entendimiento general de la hidrogeología de islas basálticas, especialmente en el tema de acuíferos colgados situados en el altitud. Además, este tesis brinda los fundamentos científicos de una gestión durable de los recursos hídricos, con las que las instituciones locales podrían ofrecer soluciones pertinentes para mitigar la demanda creciente del agua tomando en cuenta la conservación de los ecosistemas de agua dulce.

Palabras clave: Galápagos, intercepción de neblina, balance hídrico, geofísica, modelación hidrológica, modelación hidrogeológica

Forewords

This PhD thesis was conducted in a first instance in the laboratory *Sisyphe* (then *METIS* since 2014) of the *Université Pierre et Marie Curie* (2012-2014) and in a second instance in the *Laboratoire de Géologie* of the *École Normale Supérieure* (2014-2016) under the supervision of Sophie Violette. This work takes part of the project *"Galapagos Islands Integrated Water Studies"* (GIIWS) started by Sophie Violette and Noémi d'Ozouville in 2003. This thesis was funded by the *Agence Nationale de la Recherche* (ANR-blanc 2010 GIIWS Ref. 601-01), *Galapagos Conservancy* and the Ecuadorian Government through the *Secretaría Nacional de Educación Superior, Ciencia y Tecnología* (SENESCYT) with a scholarship.

This research was conducted thanks to the collaboration of several specialists which have supported a specific thematic and/or field surveys: Patrick Goblet (MINES ParisTech, Centre de Géoscience, Fontainebleau), Jérôme Fortin (Laboratoire de Géologie, ENS, Paris), Mathilde Adelinet (IFD, Paris), Julien Tournebize, Cedric Chaumont, Bernard Vincent (IRSTEA, Paris), Alexandre Pryet (ENSEGID, Bordeaux), Tatiana Izquierdo (Universidad de Atacama, Chile), Marcos Villacis, Andres Gonzalez, Miguel García Vera (Escuela Politécnica Nacional, Quito-Ecuador), Patricio Urbina, Gustavo Moreira (SENAGUA, Galapagos-Ecuador) and Noémi d'Ozouville (Charles Darwin Foundation, Galapagos-Ecuador).

Contents

List of Figures

List of Tables

Chapter 1

Introduction

A suitable understanding of the hydrogeology of a region is fundamental for the management of their water resources. The interest is particular in locations where surface water is limited and the water supply is based in the exploitation of groundwater such as the case of volcanic islands. Nevertheless, the hydrogeological functioning of basaltic islands remains to some extend unknown. This is a consequence of the intrinsic complexity of its internal structure which exhibits the alternation of constructing and dismantling stages, and the difficulty to obtain enough data to properly characterize groundwater occurrence.

Several methodologies have been used to define a hydrogeological conceptual model for basaltic islands. Each of these studies, with its own limitations and achievements, have founded the current understanding of the hydrogeology of volcanic islands, which is summarized in two conceptual models: i) the Hawaiian model (Peterson, 1972; Macdonald et al., 1983), valid for young islands, and ii) the Canarian model (Custodio et al., 1983, 1988), commonly applied for older islands. Such models explain groundwater occurrence in a regional scale. However, few attention has been paid to particular hydrological processes in a local scale, which might have an impact at a larger scale.

The Galapagos Islands are worldwide known for their endemic species and near-pristine ecosystems. 97% of the terrestrial area is protected national park land. These young basaltic formations (younger than 2.3 Ma (Geist et al., 1986; White et al., 1993)), characterized by limited freshwater resources, have experimented an accelerated economic development consequence of the marked growth of the tourism industry. As a result, the pressure on their natural resources, most notably water resources, has increased considerably. Santa Cruz, the most inhabitant island (ca. 15000 inhabitants), do not have permanent surface freshwater, therefore, the brackish basal aquifer is used for domestic water supply and drinking water thanks to desalination plants. Whereas in San Cristobal, the only island with permanent freshwater resources, water is supplied for the

inhabitants from water catchments in the streams located in the southern windward side of the island. To date, these water resources are poorly managed and there is not guidelines for the protection of these freshwater ecosystems. This is a consequence of the lack of knowledge surrounding the occurrence of freshwater.

After several years of an interdisciplinary study on the Galapagos Islands conducted in the frame of the *Galapagos Islands Integrated Water Studies* project, we are starting to have a better understanding of the hydrogeological functioning of these islands. After the investigation, which features interpretation from field work combined with remote sensing imagery and airborne geophysical surveys; a contrasting configuration has been found between: i) young islands (< 1 Ma) lacking of perennial surface freshwater, such as Santa Cruz; and ii) relative old islands (> 2 Ma) characterized by perennial springs, such as the case of San Cristobal. Most of the *GIIWS* research has been concentrated in Santa Cruz, whereas data collected in San Cristobal was limited.

The southern windward side of San Cristobal is a relatively small region of the island characterized by the presence of a drainage network, in which several streams are fed by perennial springs. The occurrence of springs is explained by the existence of high-level perched aquifers. Rainfall has a seasonal distribution and follows an orographic gradient with altitude. During six months of the year, a semi-permanent fog layer is present in the highlands that might be an additional input to the groundwater recharge as observed on the neighbored island of Santa Cruz (Pryet et al., 2012a). Watersheds are relatively small (0.5 - 12 km^2) and the discharge of their streams is low, except for one of them located in *Cerro Gato* watershed. Besides the hydrogeological interest of this watershed because it has a discharge considerably larger than its neighbors, a water catchment is installed in its streams, which supplies more than 50% of the water to the inhabitants. Thus, any attempt to study this watershed is relevant for the water management of the entire island.

Contrary to Santa Cruz and any others islands in Galapagos, in San Cristobal, the existence of streams, offers the unique possibility of an integrated study from a hydrological and a hydrogeological point of view. Moreover, stream measurements can increase the number of constraints in a numerical model. Another feature asset is the small sizes of its watersheds, which allows an adequate hydrological monitoring with relative reduced efforts and materials.

In this context, this work aims to undertake the first study of the hydrogeological functioning of high-level aquifers in the windward side of San Cristobal to seeks to answer questions like: *What is the recharge rate and which are its controling factors? Why the stream of Cerro Gato has such a large discharge? What is the influence of groundwater on this stream?* The research is focused at

the watershed scale, which allows the quantification and understanding of many hydrological processes needed for an adequate management of the resource. The objective of this thesis is to understand the hydrodynamic functioning of watersheds on the southern windward side of the island that have permanent streams. A multi-disciplinary approach has been used for this, which is based on the combination of experimental and modeling methods throughout the implementation of an experimental site. The approach includes the characterization of its structure from field and indirect methods, the quantification of the inputs and outputs of the water balance, including the quantification of cloud water interception by an innovative design device and deep percolation combining the modeling of canopy and soil water transfers, and the use of hydrological and hydrogeological models to understand the surface and groundwater dynamics.

The results of this thesis will help to improve the general knowledge of the hydrogeology of basaltic islands, especially of high-level perched aquifers. Also, this thesis will provide scientific basis for the effective water management, which could be used by the local institutions to offer solutions to the increased water demand and to provide guidelines to the conservation of freshwater ecosystems. This thesis, as part of the *GIIWS* project, have improved and expanded the scientific collaboration between French and Ecuadorian institutions.

1.1 Background knowledge of the hydrogeology of volcanic islands

1.1.1 Influence of the geological structure and formation

The hydrogeology of volcanic islands is still narrowly known partly because of the complexity of its internal structure. This is a consequence of a multi-phase volcanic activity (a succession of constructive and destructive events) under the influence of climatic conditions. Different geological materials with different weathering processes and periods result in complex and heterogeneous systems due to their contrasting permeability. These geological units with contrasting permeabilities can be summarize in:

- Dykes and silts: are massive sheets of intrusive rock (Marshak and Repcheck, 2004). Basically, this magma is injected into fractures that cools very quickly and forms a hard and low permeability rock. Depending of their number, density and distribution they can act as vertical barrier (dykes) to the horizontal groundwater flow forming local reservoirs (Macdonald et al., 1983; Izquierdo, 2014; Pryet et al., 2012b) or as horizontal barriers (silts) limiting infiltration.

- Pyroclast deposits: are the product of a relative violent eruption in which fragmented magma (pyroclast) is spitted into the air and transported to the surface. Pyroclasts varies on size and can be from coarse blocks to ashes. Pyroclast deposits may be deposited as cooled fragments remaining loose, which is very permeable, or as hot fragments that could be cemented (Fowler, 1990), specially if they are fine, such as ashes, and that can act as impermeable layers depending of their thickness. Pyroclast deposed at the end of the formation of an island, could reduce infiltration and favor runoff, reducing the recharge of groundwater bodies.

- Paleosols: are formed when lava flows from an active eruption spread over a consolidated soil, product of the chemical weathering of the basaltic rock. These soils are thin or thick zones of clay-rich material formed during periods of calm of the edifice formation. Because the overlying lava heats the soil, it acquires a characteristic reddish color and are highly impermeable (similar to a cooked clay). Similar to ash deposits, paleosol can decrease vertical infiltration through the unsaturated zone and sustain aquifers.

- Landslides: are triggered in steep slopes due to several factors such as : erosion, earthquakes or uplifting (Pryet, 2011). They change the internal

structure of the volcanic formation because the sliding surface can form an impermeable layer product of the friction and pressure. Moreover, it is also accompanied by an avalanche of deposits that contribute to the formation of the impermeable layer.

Faults and fractures also play an important role in the regional hydrogeology. The hydraulic properties of a medium varies depending of the aperture, spacing, orientation and connectivity of the fractures (Manda et al., 2013). Contrary to the above units, faults and fractures can act as a preferential drainage for surface and groundwater flow (Caine et al., 1996). At the regional scale, if fractures are orientated towards a same direction, it can cause marked isotropic effect in the regional permeability.

1.1.2 Recharge processes

Groundwater recharge is the quantity of water that moves downwards the surface to the groundwater (Rushton et al., 2006). It is a critical hydrogeological parameter which is essential to water resources assessment and management, especially in location where groundwater is exploited. Its estimation is important for managing where aquifers are depleted. It is also important in terms of contamination transport, as a proper delimitation of the recharge areas is necessary (Scanlon and Cook, 2002). Estimating potential recharge is challenging because it depends of several factors, such as climate conditions, land cover and soil characteristics (recharge can also occur from irrigation).

Rainfall characteristics, such as spatial and seasonal variability, are difficult to assess. Indeed, tropical islands with relative high temperatures and exposed to trade winds, show seasonal patterns in rainfall. Trade winds provoke an orographic gradient of rainfall and temperature in the windward side that have been observed in Hawaii (Giambelluca and Nullet, 1991; Nullet et al., 1995), Canary Islands (Fernandopullé, 1976; García-Santos and Bruijnzeel, 2011), Madeira (Prada, 2000) and Cape Vert (Mannaerts and Gabriels, 2000).

During a rainfall event, vegetation intercepts precipitation, storing water in the canopy where a proportion is evaporated and the rest drips into the ground as net precipitation. Net precipitation shows a considerable spatial variability which depends of the rainfall intensity and canopy structure (Staelens et al., 2006; Ziegler et al., 2009; Zimmermann et al., 2009). Estimates have been reported in a wide range of values (typically 51 - 91% of the incident rainfall), but in locations under fog occurrence net precipitation can increase due to the interception of cloud water interception. The effect of the fog presence have been studied in other volcanic islands such as Hawaii (Brauman et al., 2012; Giambelluca et al.,

2011), Canary Islands (Ritter et al., 2008; García-Santos and Bruijnzeel, 2011), Madeira (Prada et al., 2009) and Santa Cruz in Galapagos (Pryet et al., 2012a). These studies highlight the effect of fog interception in the hydrological process.

Once water yields the soil, water either infiltrates into the soil or is retain in the surface to re-infiltrate or become runoff. Finally, recharge depends of the difference between the infiltrated water into the soil and water uptake by roots as actual evapotranspiration. Soil hydraulic properties, slope and thickness control the groundwater recharge.

Different methodologies have been used to estimate groundwater recharge such as field studies (water table fluctuation (Healy and Cook, 2002; Moon et al., 2004; Crosbie et al., 2005), lysimeters (Kitching et al., 1977; Young et al., 1996; Xu and Chen, 2005) and tracer experiments (Cook and Solomon, 1995; Forrer et al., 1999; Edmunds et al., 2002)), remote sensing (Saraf and Choudhury, 1998; Jackson, 2002; Brunner et al., 2004), conceptual models (e.g. Arnold et al. (2000); Panigrahi and Panda (2003); Eilers et al. (2007)), physically-based models (e.g. Fayer et al. (1996); Gandolfi et al. (2006); Herrada et al. (2014)) and empirical approaches (Liu et al., 2006; Izuka et al., 2010). For an exhaustive list and comprehensive description of these methodologies, the author encourages to see Scanlon et al. (2002). An approach that considers the whole soil-plant-atmosphere system and that have enough field observations is more likely to reduce uncertainties and increase confidence in the estimates.

1.1.3 Groundwater occurrence

1.1.3.1 Aquifers

An aquifer is a groundwater mass in a porous substrate. It can be found in several configurations. In volcanic islands, a basal aquifer is typical observed. It is the freshwater lens that lies above the denser seawater and extends around all the island. Given that salt and freshwater are supposed to be immiscible, the freshwater/seawater interface can be obtained with Ghyben-Herzberg equation (depth is 40 times the head of the water table). However, in reality, a transition zone of mixed fresh and salt water delineates the interface, as a consequence of the heterogenety and anisotropy of the aquifer, tidal effects and recharge fluctuations (Pryet, 2011). This transition zone can have hundred of meters thick (e.g. 110 m in Oahu, Hawaii reported by Gingerich and Voss (2005)).

High level aquifers can also be observed in volcanic islands. Dyke-impounded aquifers are formed when vertical dykes acts like impermebale walls producing compartments of relative low permeability in which freshwater is impounded. These aquifers can increase the water level several hundred of meters (e.g. until

1500 m a.s.l. in the Canary islands as reported by Santamarta et al. (2014)). Another type of aquifer at high elevations is a perched aquifer. Perched aquifers are formed when an impermeable substratum retained the vertical infiltration saturating the media. Groundwater can either be stored or flow sub-horizontally in the relative permeable media. The impermeable substratum can consist of paleosols, ash deposits, landslide sliding surface. Perched aquifers can remain buried (generally in young islands) or outcrop when conditions are favorable (Pryet, 2011; Violette et al., 2014).

1.1.3.2 Hydrogeological models

In the literature, two hydrogeological conceptual models have been proposed that explain the occurrence of groundwater in basaltic volcanic islands (Fig. 1.1):

The *Hawaiian* model, developed by Peterson (1972) and improved by Macdonald et al. (1983), consist in the existence of a basal aquifer with a weak hydraulic gradient (notably seen by the gently slope of the water table) consequence of the high hydraulic conductivity of the basalt medium. The existance of perched groundwater bodies at higher elevation is conditioned to the presence of dykes-compartements or low permeability layers. Under this configuration, the basal aquifer is vulnearable to sea water intrusion as a conseuqeucne of the high permeability that produce a thin freshwater lens as it is rapidly drained to the ocean. Current exemples of this configuration are the islands of Hawaii (Gingerich and Voss, 2005), the young Piton de la Fournaise (La Réunion) (Violette et al., 1997), Madeira (Prada et al., 2005) and Cape Vert (Heilweil et al., 2009).

The Canarian model, proposed and developed by Custodio et al. (1983, 1988), considers a high-elevation basal aquifer in which the water table follows the surface topography and remains at a shallow depth. In this case, the low permeability allows the water table to reach higher altitudes. The decreasing of low permeability of the volcanic formations is related to long periods of weathering processes (Cruz, 2003). Thus, older volcanic formations are more likely to have this type of configuration (Pryet, 2011; Vittecoq et al., 2014; Violette et al., 2014). High-elevation aquifers have been identified in the islands of Tenerife (Canary) (Custodio et al., 1988), Kauai (Hawaii) (Izuka and Gingerich, 2003), old Piton des Neiges (La Reunion) (Join et al., 1997) and Eastern Island (Chile) (Herrera and Custodio, 2008).

1.1.3.3 Methodologies

Several methodological approaches have been used to define the hydrogeological model of basaltic islands. The most feature approach is geological and hydrogeological reconnaissance (in fact it is a necessary feature in any other approach).

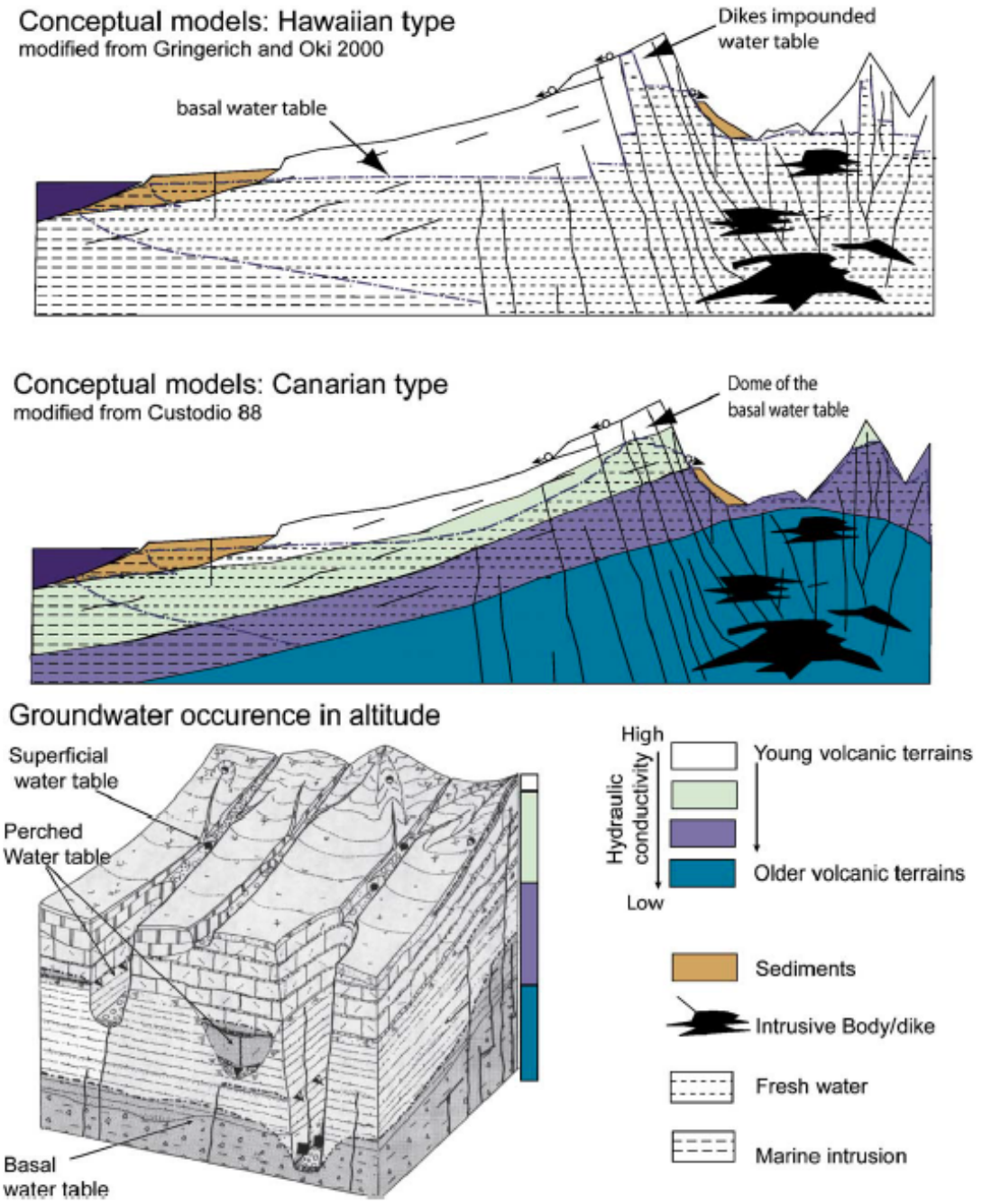

Figure 1.1: Conceptual models of groundwater in volcaninc islands (Join et al., 2005).

This includes the observation of outcrops, inventory of dykes and springs, description of volcaniclastic deposits and its weathering and identification of impermeable geological units. The existence of boreholes allows the identification of the water table and if pumping tests are available, the transmissivity values of the aquifers. An exemple of this approach is the conceptual model of La Gomera (Canary Islands) proposed by Izquierdo (2014). Based on the reconaissance of several geological features and hydrogeological data, Izquierdo (2014) classified the island into four aquifer systems due to its geological complexity and heterogeneity.

A common approach is the use of numerical models. Given the limited availability of data, which is common in this type of systems, conceptual models are tested with numerical models making assumptions where data is limited. If properly constrained, these model offer several advantages because they can describe in detail groundwater occurrence. In young Piton de la Fournise (La Reunion), without direct information about the internal structure of this island until that moment, Violette et al. (1997) used limited hydrological data and based on the geological context of the island and tested several assumptions about its groundwater flow. Thus, Violette et al. (1997) proposed a conceptual hydrological and thermal model that was confirmed with a numerical code, in which the island has a thick shell that protects the magma chamber, a low-elevation basal aquifer and successive perched aquifers. Another advantage of numerical models is that they can be used to simulate different scenarios useful for groundwater management. For example, Gingerich and Voss (2005) used a three-dimensional model of the basal aquifer of Oahu (Hawaii) to simulate the freshwater-saltwater transition zone, testing the effect of pumping in the size and position of the freshwater lens and the salinity of several wells.

Geophysics provides indirect observations about the internal structure of a medium, which can allow the differentiation of geological units. For this reason, geophysics has successfully contributed to the characterization of the internal structure of volcanic islands. Depending of the technique, different lengths and depths can be covered. Land-based surveys, such as electrical and electromagnetic methods, have been successfully used in Hawaii (Lienert, 1991), Canary (Gómez-Ortiz et al., 2007) and La Reunion (Descloitres et al., 1997; Courteaud et al., 1997; Lénat et al., 2000). The drawback of these methods is that surveys at large scale are complicated due to time, cost, equipment and accessibility. In this mattern, Airbone Electromagnetics (AEM) surveys can cover large extensions in relative small time. Vittecoq et al. (2014) used geological and hydrogeological observations with 3000 km of inverted resistivity data from an helicopter-borne TDEM geophysical survey to propose an adapted conceptual model of the island

of Mayotte.

Another tool used for hydrogeological models is hydrochemistry, in which the movement and distribution of several elements in the island are analyzed to assess the underlying path of groundwater. The geochemical analysis is based from the composition of freshwater or groundwater at different geological units. This type of analysis have been succesfully performed in La Reunion (Join et al., 1997), Azores (Cruz, 2003; Cruz and França, 2006), Madeira (Prada et al., 2005), Eastern Island (Herrera and Custodio, 2008) and Cape Vert (Heilweil et al., 2009).

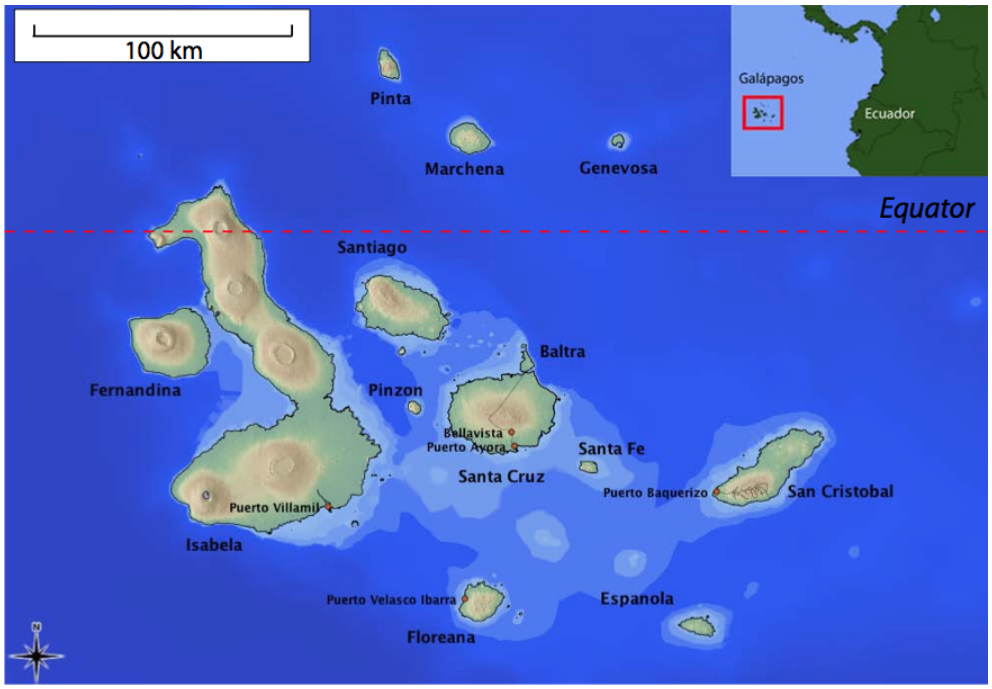

Figure 1.2: The Galapagos Islands located 1000 km west of Ecuador. (Pryet, 2011)

1.2 Galapagos in the insular volcanic context

1.2.1 Geographical and geological context

The Galapagos Archipelago is located in the Eastern Pacific, 972 km west of the Ecuadorian mainland (Fig. 1.2). The total surface is 7880 km^2 of land over 45000 km^2 of ocean. It is composed of 18 main islands (surface greater than 10 km^2) and 215 rocks and islets (DGNP, 2013). Galapagos is a province of Ecuador, where only 3% of its territory is inhabited. The remaining 97% of the land area of Galapagos is part of the *Galapagos National Park* (GNP), which is an UNESCO World Heritage Site. The total population is ca. 25000 inhabitants according to the 2010 national census (INEC, 2010). Only four islands are inhabited: Santa Cruz (15400 inhabitants), the economical and tourism center; San Cristobal (7480 inhabitants), the administrative capital; Isabela (2260 inhabitants), the larger island (4640 km^2); and Floreana, the first inhabited island (160 inhabitants).

The Archipelago emerges from a shallow submarine platform at the Nazca Plate, which was built from continuous eruptions as a consequence of the interaction between a hot-spot and a segmented mid-ocean ridge (*Galapagos Spreading Center*) (Geist et al., 1986; White et al., 1993). The Nazca plate moves toward the east at a speed of 71 mm/year (Hey et al., 1977), therefore commonly the western islands (Isabela and Fernandina) close to the hot-spot are the youngest

and the eastern islands (San Cristobal and Española) are the oldest. Islands on the western side (e.g. Isabela and Fernandina) have high elevation volcanoes with overturned-soup-plate profile and dominant calderas (Geist et al., 1998). Islands on the central part of the Archipelago (e.g. Santa Cruz and San Cristobal) are built by alkaline-olivine basalt deposits and characterized by subdued shield volcanoes without a caldera. Age of the lava flows of San Cristobal is 2.35 Ma for the southern shield to 0.6 Ma for the northeastern region (Geist et al., 1986; White et al., 1993). In the case of Santa Cruz, most of the island is covered by younger lava flows, from 0.56 to 0.05 Ma (White et al., 1993).

Eruptions that formed that islands were mostly of effusive type with occasional explosive events that produced the deposit of pyroclastic material such as ashes and scoria. Aligned systems of scattered parasitic cones can be seen on the flanks of shield volcanoes, yet pyroclastic formations constitute only a small portion of the total volume of the islands (d'Ozouville, 2007; Pryet, 2011). The large and thick flows of pahoehoe and clinker scoriaceous aa' formed gently sloping profiles. The current substrates are the consequences of the weathering of basaltic and pyroclastic material mixed with organic material.

1.2.2 Climatic conditions

The climatic conditions are atypical to its equatorial position (cool and dry). Essentially, there are two distinctive seasons (Fig. 1.3 and Fig. 1.4): 1) The cool "garúa" season from June to December, where the sea surface and air temperature are low due to the upwelling of the cold Humboldt Ocean current from the south-east (Palmer and Pyle, 1966; Grant and Boag, 1980; Dunbar et al., 1994; Trueman and d'Ozouville, 2010). During this season, orographic precipitations are common over the windward slopes, where a semi-permanent fog layer covers the highlands of the main islands due to an inversion layer formed above 400 m a.s.l (Trueman and d'Ozouville, 2010; Pryet et al., 2012a). This provokes a marked spatial contrast between the wet highlands, commonly covered by fog, and the dry coast, lacking of precipitation. 2) The hot "invierno" season from January to May, characterized by high sea and air temperatures, and convective precipitations since the InterTropical Convergence Zone, with warmer water, moves southward as the intensity of the southest trade winds and the cold currents decrease (Grant and Boag, 1980; Dunbar et al., 1994; Trueman and d'Ozouville, 2010). The presence of el Niño Southern Oscillation (ENSO) in the Galapagos, induces extremely high inter-annual variability, especially during the invierno season when intense rainfall or droughts are observed (Snell and Rea, 1999). The relief of the main islands induces an orographic effect on temperature and rainfall, producing contrasting conditions between the windward

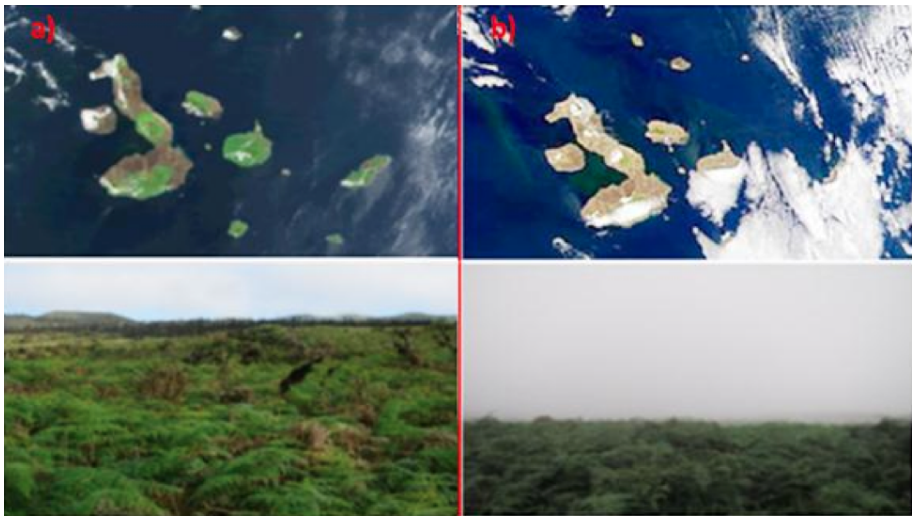

Figure 1.3: Google Earth images of the Galapagos Islands and photographies taken on the windward side of Santa Cruz Island (González, A., 2013). (a) the hot *Invierno* season and (b) the cool *Garua* season.

side which is exposed to the trade winds and the leeward side (d'Ozouville, 2007; Pryet et al., 2012b; Violette et al., 2014).

1.2.3 Vegetation and land use

As a consequence of the contrasting climatic conditions and the substrate between the coast and the summit, different vegetation stages are observed along the windward side of the main islands (Hamann, 1984; Itow, 2003). The vegetation staging can somehow differ in altitude and species between islands, but four stages can be identified in the main islands (Itow, 2003):

i) The lowlands, below 50 m a.s.l., is the dry zone composed mainly by white-barked trees, spiny shrubs and cactuses growing in thin soil layer spots over unweathered basalts. Some species are drought-deciduous. This zone is characterized by the absence of ferns and a white to gray coloration of the landscape.

ii) The transition zone, between 50 and 200 m of altitude, presents weathered and deeper soils, and host deciduous and evergreen trees. Undergrowth of the forests begins to appear with the presence of ferns.

iii) The humid zone, between 200 and 600 m of altitude, presents shrubs, herbs and terrestrial ferns in the forests, which have abundant epiphytes on the tree's trunks and branches. This zone has suffered dramatic anthropogenic disturbance. It was originally covered by endemic species such as *Scalesia* tree and *Miconias* shrubs (Hamann, 1984; Trueman et al., 2013), but the development of agriculture provoked the clearing land of the native vegetation for introduced trees, pasture,

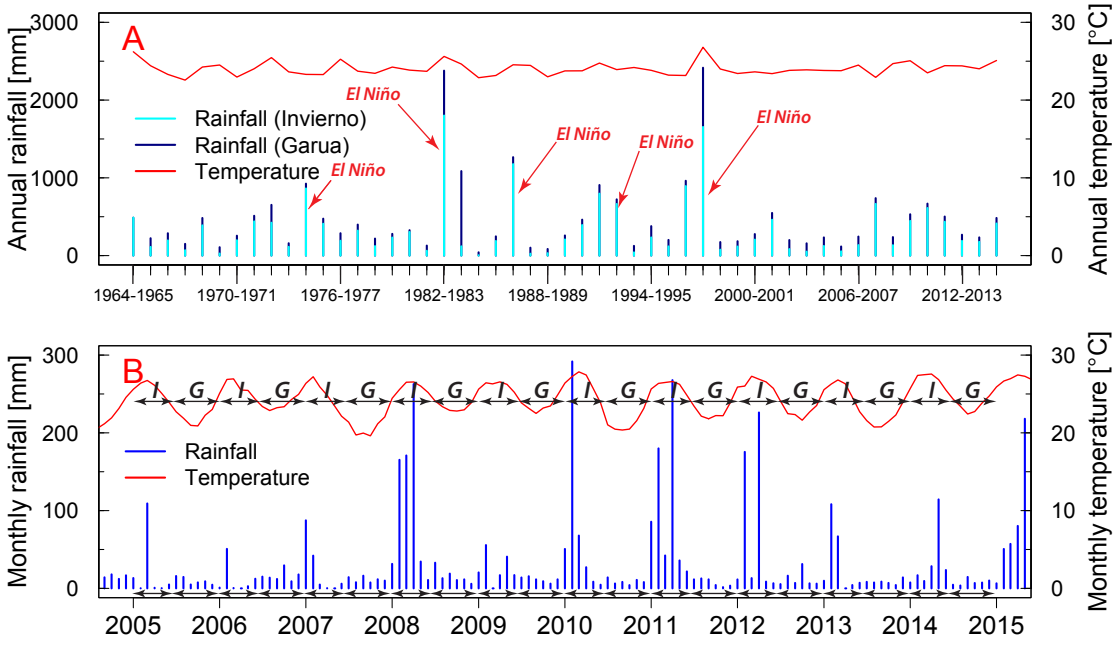

Figure 1.4: Historical rainfall and temperature records from the weather station (4 m a.s.l.) operated by the Charles Darwin Foundation at Puerto Ayora, Santa Cruz Island from 1965 to 2015. (A) Inter-annual and (B) monthly total rainfall and average temperature. Years are considered as hydrological years (June-May).

and crop cultivation. On the islands of Santa Cruz and San Cristobal, this zone can be subdivided into two sub-zones: the humid zone below 400 m of altitude, that host secondary forests and pastures, and the very humid zone above 400 m of altitude that host mostly *Miconias* shrubs and endemic ferns. On Santa Cruz, above 450 m of altitude, the territory is a conservation area that belongs to the Galapagos National Park (GNP). This area was invaded by *C. pubescens* (Jäger et al., 2009), but it has been almost eradicated thanks to successful control programs conduced by the GNP. On San Cristobal, the agricultural zone extends until the summit. Most of the farms are located at the windward and leeward sides of the highlands. San Cristobal has a critical issue with the *Blackberry*, which is a badly invasive specie that extends from the transition zone to the highlands. It is usually grouped along streams and sources, therefore the access to them is extraordinarily challenging. The control programs from the GNP for the eradication of this species had been ineffective.

iv) The summital zone, above 600 m of elevation, is characterized by treeless vegetation. The plant species observed on this zone are ferns, herbs and grasses, only some shrubs are presented on leeward slopes and depressions. On San Cristobal, this zone is very limited and only a small part belongs to the GNP.

1.2.4 The Human impact over the environment

A significant risk that the Galapagos Islands face, is the loose of conservation in its environment. An increase in the number of tourists, migrants, along with human development, threaten the pristine ecosystem of the islands. The conservation and preservation of the habitat is a matter of serious concern for governmental authorities. Specially considering that an environment with this particularity is extremely vulnerable to changes in flora and fauna (De Groot, 1983).

The human activity in the Galapagos could be traced almost 500 years ago. During this period, the impact on the environment has been a serious concern as a result of the long history of flows regarding visitors and inhabitants. One important effect, product of the human activity, is the alteration of the island's food chain, which is a consequence of the whaling activity that harms the sea turtle population and which could unleash a ripple effect across the species (Jackson, 1993). Another serious issue is the invasion of introduced animals and plants. The number of introduced animals by 1960, reached 11 species, including dogs, cats and pigs. Several plant species were introduced adding 250 species to a native flora of 750 species (De Groot, 1983). In the highlands of Santa Cruz, 86% of the territory is degraded by the effects of agriculture and plant invasion (Watson et al., 2010). Moreover, several invasive species that require management have been associated with the presence of freshwater (e.g. black fly, rats, Tilapia).

The tourism is another fact that has severe implications over the environment. Tourist attractiveness such as the so called eco-tourism is one of the principal hazards as a result of the human activity (Jackson, 1993). In fact, the number of tourists has exponentially increased during the last years. Studies from DGNP (2013) shows that the number of tourist has changed from 41.000 in 1990, to over 135.000 in 2014; furthermore, the number of residents went from 10.000 to 28.000. This quantity of visitors and inhabitants that is increasing every year, damages the islands by causing pollution, wastes and water contamination. Moreover, it causes stress over the natural resources, specially water.

1.2.5 Water resources and management

The Galapagos Islands are characterized by a scarcity of freshwater resources. Except for San Cristobal, permanent surface water is absent on the islands. In Santa Cruz and Isabela, the only perennial large resource identified is the brackish and contaminated basal aquifer (d'Ozouville, 2007; Pryet, 2011). The lack of surface water on these islands is related to the thin soil layer and the high permeability of the rocks that rapidly infiltrates the water income from precipitation. The Municipalities distribute the brackish water from the basal aquifer

without treating to the population of Puerto Ayora (the main city of Santa Cruz and the Galapagos). Moreover, there is no sewage system, wastewater is kept in private septic tanks or discharge directly to the underground, therefore to the aquifer from which the water is extracted. Indeed, the level of contamination of the aquifer is high (Liu, 2011). Despite of the scarcity and bad quality of the water, the specific demand supplied reaches 370 liters per capita per day (Reyes et al., 2015).

In Floreana, on the leeward side of the island, only one small spring highly mineralized has been identified and it is used to supply with freshwater to the inhabitants. On the windward side of San Cristobal, surface water can be observed in form of a permanent freshwater lake and streams. Water catchments on the streams are used to supply of water the population of San Cristobal and for irrigation purposes. 4 sites are used for this purpose Fig. 1.5:

- Encañada Cerro Gato: is used for the supply of water to the population of Puerto Baquerizo Moreno. A water catchment (175 m a.s.l), that consist of a simple intake connected to a settling tank, draw off water from the stream to a new improved 12 km pipe (150 mm diameter).

- Embalse La Toma: it is located at 520 m of elevation and consist in a small dam (12 m x 60 m) that collects water from the highlands. The water from this dam is supplied to Puerto Baquerizo Moreno, El Progreso and other small sectors.

- Encañada La Policia: is used by tankers that distribute water in small sectors of the island. The small caption is located at 320 m of elevation, near the road.

- Encañada del Platano: it is used eventually for irrigation purposes. The small tank is located at the outlet of *El Bayo* watershed at 500 m of elevation.

Water from Cerro Gato and La Toma reach a water treatment plant (ca. 10 l/s). Despite the plant is equipped for several treatments, since its inauguration (2014), the only treatment performed is water chlorination until the date. Water is distributed in Puerto Baquerizo Moreno by a piping network with several leaks. Despite, the service covers 85% of the population, it is restricted to two hours a day per district.

Several sectors of the island are favorable for agriculture. Indeed, a large part of the windward side (except for the coastal zone) and the highlands are dedicated to the agriculture and ranching at several levels. Nowadays, the local

government is supporting the improvement of the local agricultural production, where the effects of land use change to the local hydrology have not been assessed. Given that streams are located in this sector, the use of pesticides, bad practices in ranching and others can be causes of contamination of the streams. This is a serious issue because the potential zones of recharge of the streams of the water catchments are not defined.

1.2.6 Hydrogeology of Galapagos

1.2.6.1 Hydrological and hydrogeological studies performed in the Galapagos Islands

Despite numerous scientific studies about biology and geology are available in the literature, there is only few studies regarding water resources of the Galapagos Islands. This is a peculiar situation considering the scarcity of water resources in this region. Studies on climate (Palmer and Pyle, 1966), oceanography (Dunbar et al., 1994) and biology (Grant and Boag, 1980; Hamann, 1984) provide the first description of the characteristics of rainfall and fog ocurrence in the region. Then, (Snell and Rea, 1999) published rainfall estimates from climatic stations installed by the Charles Darwin Foundation (CDF) in Santa Cruz island in an attempt to assess the pattern of el Niño.

By the end of the eighties, the local authorities, under the name of "Instituto Nacional Galapagos" (INGALA), in collaboration with the French "Institut de recherche pour le développement" (IRD, ex ORSTOM), performed an extensive mapping project on the inhabited islands (Ingala, 1989). Maps included the cartography of vegetation, geomorphology and water resources.

The first academic investigation about the hydrogeology of Galapagos started in 2003, with the launching of the Galapagos Islands Integrated Water Studies (GIIWS) project by the University Pierre et Marie Curie (UPMC-Sorbonne Paris VI) in collaborations with local partners and leaded by Sophie Violette. The purpose of the GIIWS project is to understand the hydrogeological functioning of the Galapagos islands and provide recommendations to their water management.

The project started in 2002, with a PhD thesis (d'Ozouville, 2007). This study provided a first characterisation and quantification of the hydrological functioning of the Galapagos, notably in the islands of Santa Cruz and San Cristobal. Between the main results, a digital elevation model (DEM) of 20 m resolution was built for Santa Cruz from the combined data of the Shuttle Radar Topographic Mission (SRTM) (Rabus et al., 2003) and ENVISAT radar acquisitions (d'Ozouville et al., 2008b). In 2005, Adelinet (2005) measured the discharge of several streams and springs during a 5-month period. In 2006, an

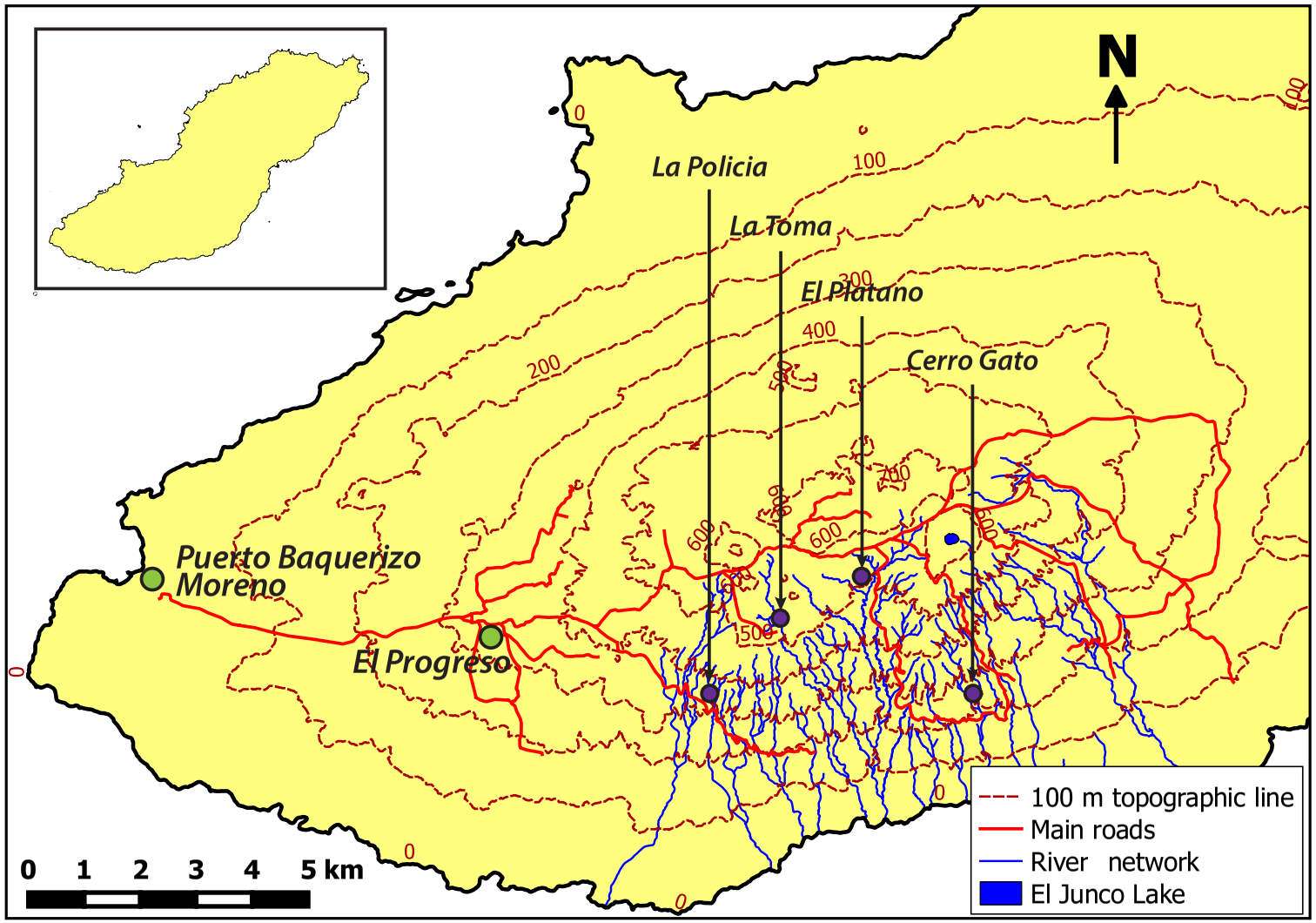

Figure 1.5: Localization of the water catchment systems in San Cristobal. Four main water catchment systems (Cerro Gato, El Platano, La Toma, La Policia) supplies the populations of Puerto Baquerizo Moreno, El Progreso and other small sectors of the island.

extensive air-borne electromagnetics survey (helicopter-borne transient electromagnetics - SkyTEM) was conducted in Santa Cruz and San Cristobal testing the innovating system for the first time on volcanic islands (d'Ozouville et al., 2008a; Auken et al., 2009). This thesis was complemented by a study of the physical and hydrodynamic properties of the soil along the windward slopes of both islands (Adelinet et al., 2007), which provided insights about the weathering mechanism at different altitudes.

The project continued with a second PhD thesis (Pryet, 2011). This study provides a deeper understanding of the contrasting hydrogeological configurations of Santa Cruz and San Cristobal Islands, which is explained by an evolution pattern (Violette et al., 2014). However, efforts were more focused in Santa Cruz. The first main result reported in this thesis, is a technique for the three-dimensional visualisation of large sets of 1D resistivity datasets (Pryet et al., 2011). In mid-2010, two weather stations were installed on the windward side of Santa Cruz, which completed the two long-term weather stations at lower altitudes operated by the CDF, in order to estimate the recharge orographic gradient. These stations allowed the estimation of cloud water interception generated by the semi-permanent presence of fog in the highlands, which resulted to be an additional input in the water budget increasing groundwater recharge (Pryet et al., 2012a). In San Cristobal, the dataset analysis of the SkyTEM survey combined with geomorphological observations, allowed the proposition of the first hydrogeological conceptual model for the island (Pryet et al., 2012b).

Others studies published outside the GIIWS project have also contribute to the understanding of the hydrogeology of these islands, such as the characterisation of the Galapagos climate reported by (Trueman and d'Ozouville, 2010) and the noble gases and stable isotopes campaign reported by Warrier et al. (2012) (even though the latter was made witht the *GIIWS* support). The most comprehensive study of the hydrogeology of the Galapagos Islands, can be seen in Violette et al. (2014), which is an original synthesis of the recent studies in Santa Cruz and San Cristobal where the controlling factors that explain their difference are identified (it is highly recommended by the author). Finally, there are new studies about the weathering of soils (Stoops, 2014; Taboada et al., 2016) and most notably the first scientific publication about the water demand in Santa Cruz (Reyes et al., 2015).

1.2.6.2 Current knowledge of the hydrogeology of the Galapagos Islands

As mentioned in the above section, hydrogeological studies are recently in Galapagos. Very few drill holes were executed in Floreana and Santa Cruz which

do not provide reliable information. There are few observations of geological units due to different aspects such as accessibility, degree of alteration of lava flows and dense vegetation cover. Moreover, climatic conditions in the expected recharge areas are scarce. For these reasons, any attempt proposed to describe groundwater occurrence is still subject to many uncertainties.

Most of the studies have been focused in the two main islands: Santa Cruz and San Cristobal. Interpretations from field data, remote sensing imagery and comprehensive helicopter-borne geophysical survey, allow the definition of groundwater occurrence in these islands. The hydrogeological configuration of both islands is more consistent with the Hawaiian conceptual model (Peterson, 1972; Macdonald et al., 1983):

- *Santa Cruz* has a low-lying basal aquifer subject to seawater intrusion, which extends up to at least 9 km inland (d'Ozouville et al., 2008a; Auken et al., 2009; Pryet, 2011; Violette et al., 2014). The weak hydraulic gradient is expected several kms inland due to the relative young and permeable basaltic formations. The high hydraulic conductivity and transmissivity of the basaltic media is attributed to cooling joints, interflow voids and fractures (Violette et al., 2014). In the highlands, a hidden perched aquifer, which is buried and is not exposed to outcrops, may exist at the windward side of the island (d'Ozouville et al., 2008a; Auken et al., 2009; Pryet, 2011; Violette et al., 2014). The buried perched aquifer, indirectly recharge the basal aquifer. As a consequence, preferential areas of the basal aquifer are recharged, which exhibits depressions in the seawater-freshwater interface (Auken et al., 2009; Pryet, 2011; Violette et al., 2014).

- *San Cristobal* probably also has a low-lying basal aquifer subject to seawater intrusion (d'Ozouville, 2007; Pryet et al., 2012b; Violette et al., 2014). However, the freshwater lens is thicker in the windward side (Pryet et al., 2012b), where a concentration of ravines is observed. The presence of springs, which fed streams in this side of the island, is associated to perched aquifers formed over an impervious unit of ash deposits or paleosols (Pryet et al., 2012b; Violette et al., 2014). In the summit zone of the island, a dyke-impounded aquifer might exist along two volcanic cone line ups (Pryet et al., 2012b; Violette et al., 2014). A wider description of the hydrogeology of San Cristobal can be seen in section 2.1.

Comparing both islands, Violette et al. (2014) declares that, Santa Cruz is in a younger evolutionary phase than San Cristobal, which is evidenced by their hydrological development. In this context, Violette et al. (2014) reports that Santa Cruz is well-located within the Hawaiian model, whereas San Cristobal is

in an age-advanced stage of the Hawaiian model towards the Canarian model. Following the evolution pattern of these two islands in the Galapagos, Floreana should be in a intermediate stage, with several highlands springs (most of them no-perennial) and a developed drainage network in the windward side, and Isabela, should be in a earlier stage, similar to Santa Cruz.

1.3 Approach

The lack of water resources on the islands is a relevant issue, because of the increasing demand related to the rapid growth in human population, agriculture production and pressure from the tourism industry. Quantitative knowledge about the water resources is fundamental for the efficient management and the application of conservation politics. The new management plan of the GNP ("Plan de Manejo de las Areas Protegidas de Galápagos para el Buen Vivir") has as one of the main objectives, the management of protected and non-protected areas, where ecosystem units have been defined as the focus to the research and management policies. An integrated study of the parameters involved in this media will allow the baseline knowledge to the conservation and management.

In contrast to other basaltic islands (e.g. Hawaii, La Réunion, Canarias), the hydrogeological settings of the Galapagos are still poorly known. After several years of an interdisciplinary study on the Galapagos Islands conducted by the *GIIWS* team, we are starting to have a better understanding of its hydrological functioning. Most of the research has been concentrated in Santa Cruz, essentially because it is the most inhabited island, and its lack of freshwater has been considered a primary concern. On the opposite, studies in San Cristobal are limited. The focus is now directed to the hydrology and hydrogeology of San Cristobal, the unique island with permanent surface freshwater. Even though the water is used to supply the growing populations and to the agriculture, and its presence have been also associated with numerous invasive species, there are not appropriate guidelines on water management, basically because of the limited information regarding the quantification of the resource and its behavior.

This thesis aims to undertake the first study of the hydrological functioning of San Cristobal at the watershed level. The objective is to understand the hydrodynamic functioning of watersheds on the southern windward side of the island that have permanent streams in order to improve the knowledge of high-level perched aquifers in basaltic islands and to provide the scientific basis for a suitable water management.

A multi-disciplinary approach was used in this thesis, in which the proposed methodology is built on: i) the existing general knowledge of San Cristobal hydrology and hydrogeology and, ii) in function of the funding and unavailable data. Despite the investigation is focused at a watershed scale, the methods conducted in the frame of this thesis can be useful to characterize the regional groundwater occurrence in Galapagos.

Before proposing the methodology, from the broad exploratory phase of research already carried out on San Cristobal and Santa Cruz by the *GIIWS* project, it was identified the following aspects:

- The hydrogeological conceptual model proposed by (Pryet et al., 2012b), where the springs on the windward side are supposed to be fed by high-level aquifers perched over an impervious unit and not connected to the basal aquifer, deserves further examinations.

- The airborne electromagnetic (AEM) SkyTEM dataset collected by d'Ozouville (2007), and the 3D resistivity gridding technique of this dataset developed by Pryet et al. (2011), could reveal insights about the geometry of these perched aquifers.

- The existing DEM data (SRTM - 30 m resolution) is too coarse for accurately define the surface watershed and hydrological modeling.

- The predominant recharge occurs above 300 m of elevation (Pryet, 2011; Warrier et al., 2012) and the additional input of fog interception on the highlands may not be negligible in correspondence to the situation of Santa Cruz (Pryet et al., 2012a; Violette et al., 2014).

- Continuous climatic and hydrological monitoring on the windward side are necessary for further groundwater studies.

- The presence of ravines fed by springs is an unique opportunity in Galapagos to validate groundwater recharge estimations with measurements of the discharge of these streams.

- The flow measurements of the ravines and the inventory of springs conducted by Adelinet (2005) revealed a contrasting hydrological functioning between different watersheds, such as the *Cerro Gato* watershed, which has a larger flow than its neighbors watersheds. Nevertheless, the inventory and measurements were incomplete and part of the data set collected was still unused.

After the recognition of these observations, the focus is placed on the processes at the watershed scale, in order to have a close monitoring and quantification. The watershed of *Cerro Gato* is chosen for this study because: i) it is the main watershed that supplies water to the population of the island and, ii) its outflow appears to be larger than the drainage surface, which implies that its hydrogeological watershed may be larger than the surface watershed. Additionally, two others basins are monitored for comparison purposes: *Chuki Marka*, located at west side of *Cerro Gato* and *El Bayo*, located at the highlands. The research questions we are seeking to answer are:

- What is the influence of the soil on physical surface and sub-surface processes?

- What is the influence of the weathered basaltic cover in the hydrodynamic functioning of the perched aquifer?
- How much is the recharge rate, and which are theirs controlling factors?
- How much is the discharge of streams?
- What is the dynamic fluctuation of surface and groundwater discharges and, the influence of groundwater on the discharge of streams?
- What could be the extension and geometry of the hydrogeological watershed of *Cerro Gato*?

In order to address an answer to these questions, an integrated approach, focused in an experimental site (Fig. 1.6), is proposed based on three fundamental axes:

- **Recharge and discharge processes:** Quantify the inputs from precipitation and fog interception, the outputs of evapotranspiration, deep percolation and flow discharge, and characterize their influence by water balance estimations using climatic, vegetation, soil and hydrological monitoring from plot to watershed scale.
- **Structure:** Investigate the geomorphology, geology and the structural properties of the volcanic formations using geophysics, remote sensing and field work.
- **Hydrological and hydrogeological modeling:** Characterize the dynamics of surface and groundwater flows using conceptual and numerical models at watershed scale.

Despite the methodology is planned following the features described above, the organization of this thesis is not done in such a way. Instead, it follows a result oriented order, so that the readers will find a direct and linear progression throughout the text. This thesis is organized by chapters as follows:

- chapter 2, **Methods**, describes the background knowledge of the hydrogeology of San Cristobal and the proposed methodology for this study, which includes the experimental sites and field work necessary for data acquisition.
- in chapter 3, **Climatic monitoring and recharge processes**, inputs of rainfall and fog interception are quantified, then groundwater recharge is estimated from plot to watershed scale.

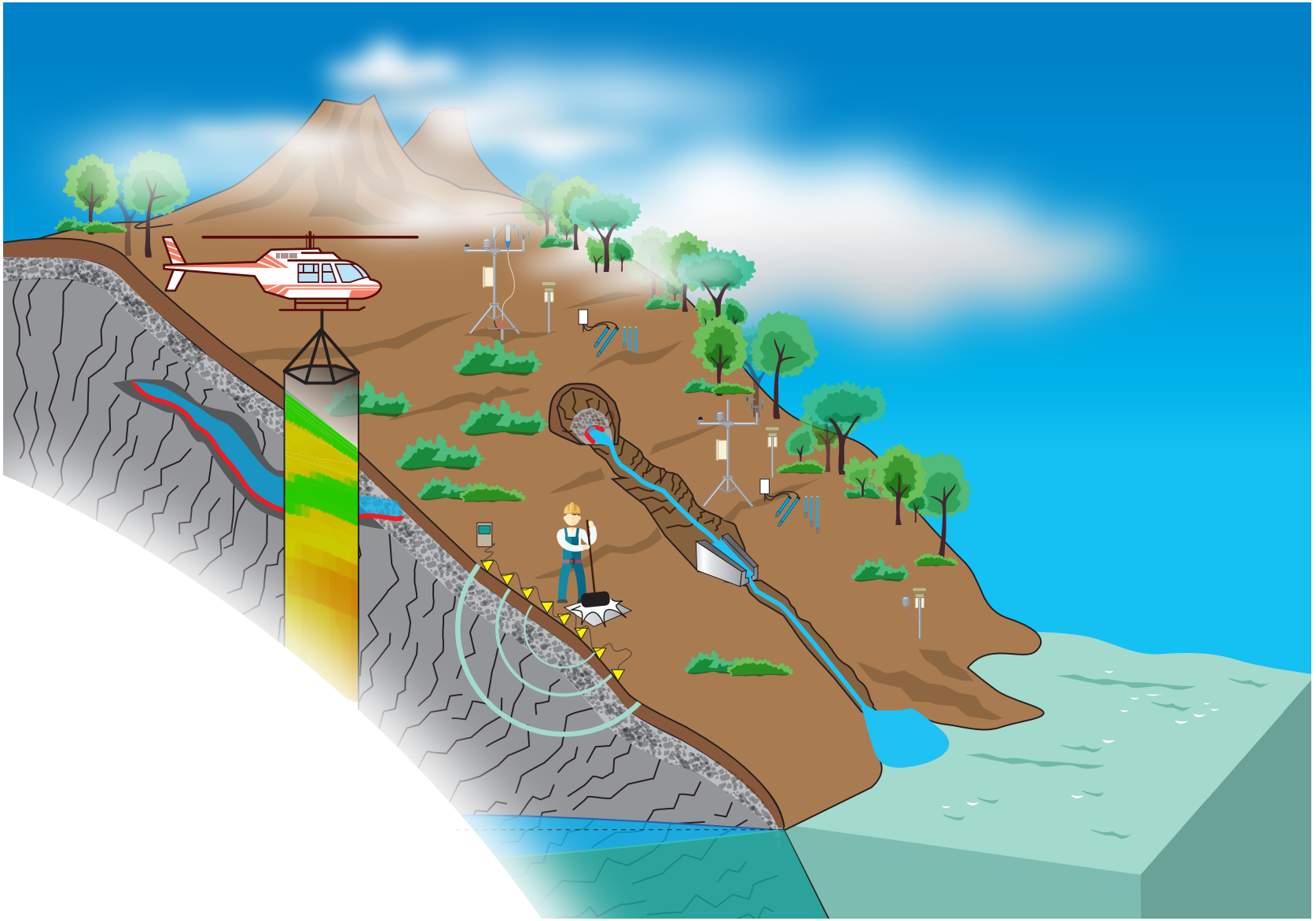

Figure 1.6: Schematic view of the experimental site in thw windward side of San Cristobal Island.

- in chapter 4, **Hydrological analysis**, outputs are quantified, the discharge of streams. Then, a lumped conceptual hydrological model is used as a first approach to explain streamflow in *Cerro Gato* and the others two watersheds.

- chapter 5, **Hydrodynamical properties of the internal structure**, is about the extraction of the geometry of the perched aquifer of *Cerro Gato* and the estimation of the main hydrodynamic properties of the internal structure.

- chapter 6, **Hydrogeological modeling of Cerro Gato watershed**, gathers all elements from the previous chapters to propose a conceptual model for *Cerro Gato*, which is tested with a numerical model.

- finally, **conclusions** and **perspectives** are presented.

Chapter 2

Methods

Introduction

This chapter, **Methods**, presents the direct and indirect methodologies proposed to the acquisition of the complementary datasets necessary in this work.

An helicopter-borne transient electromagnetic (SkyTEM) mission carried out over San Cristobal Islands, limited streamflow measurements on some ravines and measurements of the hydrodynamic properties of soils are useful data to have insights about the hydrodynamic functioning of the island. However, this information is insufficient to properly describe the hydrological processes and it needs to be complemented.

This chapter is organized as follows:

- In section *Background knowledge of San Cristobal*, a description of the current knowledge and available datasets in San Cristobal, especially on the windward side, is presented.
- Section *Morphology and field work*, presents the work done in the new Digital Elevation Model (IGM, 2014) complemented with field work.
- In section *Experimental site*, a brief description of the study zone is presented followed by a description of the hydrological network installed in San Cristobal.
- Finally, section *Comparison of deep percolation rates below contrasting land covers with a joint canopy and soil model*, presents a methodology to estimate deep percolation rates (groundwater recharge) which is a fundamental hydrodynamic boundary conditions for hydrogeological modeling.

To avoid any confusions in this chapter and following chapters surrounding the term *Cerro Gato*, a clarification of this term is presented. *Cerro Gato* is a

small hill in the windward side named by the locals after the quantity of cats observed in it. Being the only feature in the area, the whole area was named *Cerro Gato*. In this thesis, the term *Cerro Gato* is referred basically in three different ways (section A 1):

- *Area, zone or sector:* which refers to the central southern area of the islands, from the coast to *El Junco* lake, and which includes several watersheds.

- *Big watershed:* which refers to the watershed in which the hill is located, in which its outlet reaches the coast (2.47 km^2).

- *Watershed:* which is a sub-watershed of the *Cerro Gato* big watershed and which outlet is the municipal water catchment (0.69 km2). This is the most referred throughout the text.

Occasionally *Cerro Gato* is also referred to the hill, which is in fact a pyroclastic cone, but it is clarified in the text.

2.1 Background knowledge of San Cristobal

2.1.1 Geology, geomorphology and weathering

San Cristobal can be divided into two sub-regions: The older southwestern sub-region, characterized by a major shield that emerged ca. 2.35 Ma ago; and the younger flat and arid northeastern sub-region (Geist et al., 1986). The southwestern sub-region has an elongated NE-SW shape with satellite cinder cones organized into two major alignments (Fig. 2.1). The highest point is *Cerro San Joaquin* at 725 m a.s.l. The base of the shield is composed by lava flows older than 0.78 Ma, but most of it is covered by younger flows (0.78 Ma) (Geist et al., 1986). Eruptions were characterized by *pahoehoe* and *aa'* lava flows (Geist et al., 1986). At several locations, paleosols can be observed between these flows. At the end of the volcanic activity, the shield was covered by at least 10 m of pyroclastic deposits (ca. 0.6 Ma) (Geist et al., 1986). However, in recent observations its thickness seems to be thinner (T. Izquierdo, personal communication, 2014). Due to the humid weather conditions on the windward side, the pyroclastic material was weathered to form a thick soil cover (Laruelle, 1967; Pryet, 2011; Violette et al., 2014). The permanent existence of flowing surface promote the weathering process. The thick weathered cover has been dissected by a drainage network, in which deep incisions can be observed. The hydrodynamic properties and mineralogical composition of the soils have suggested that soils have evolved along the orographic gradient (Adelinet et al., 2007; Violette et al., 2014). At the highlands, the weathering process is the consequence of chemical alterations; while at the lowlands, the weathering is driven by mechanical processes (Adelinet et al., 2007; Violette et al., 2014).

2.1.1.1 Climatic conditions

On the windward side of San Cristobal there is no available data about the meteorological conditions on a long term basis. Using the available data from the long-term records at Puerto Baquerizo Moreno (6 m a.s.l.), the average annual temperature is 24.8 °C. During the cool season, the average temperature is 23.5 °C, while it is 26.5 °C during the hot season. The annual rainfall at this location is 343 mm. Because of the similarity on the climatic conditions with Santa Cruz, Pryet (2011) applied the estimated rainfall orographic gradient of Santa Cruz at the windward side of San Cristobal, the median annual rainfall is predicted to be 1580 mm (Fig. 2.2), reaching 2960 mm above 650 m of elevation (Violette et al., 2014). During the cool season, fog can be observed above 300 m of elevation.

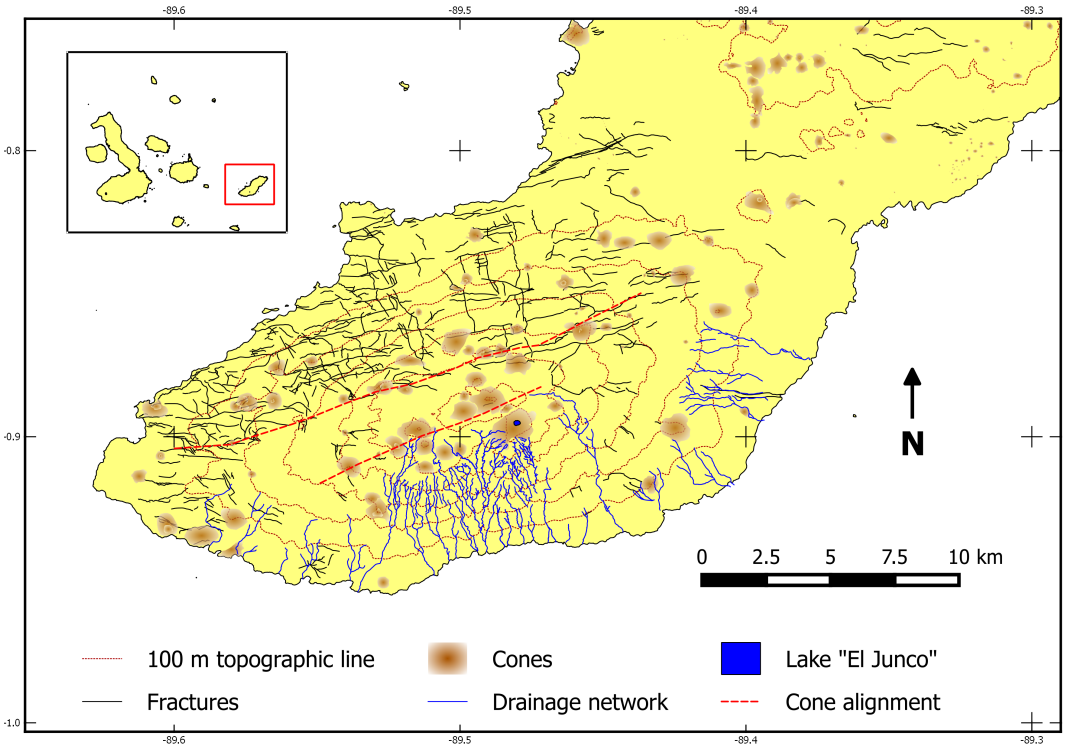

Figure 2.1: Surface morphology of the southwestern sub-region of San Cristobal.

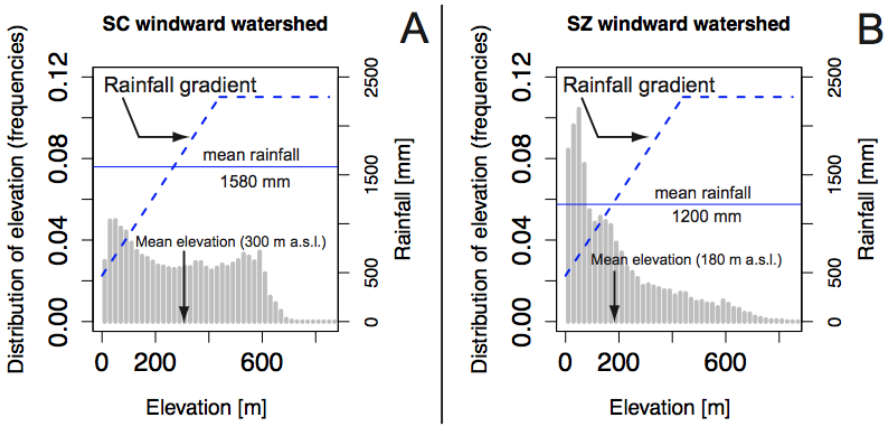

Figure 2.2: Distribution of elevations and rainfall gradient on the windward side of: A) San Cristobal and B) Santa Cruz (Pryet, 2011; Violette et al., 2014).

2.1.1.2 Hydrology and hydrogeology

The southern side of San Cristobal presents a complex hydrological system. At the highlands, wide grasslands with gentle slopes allow the ponding of rainfall, such as "El Colorado" pond which is a big seasonal pond (ca. 0.05 km^2) and, "El Junco" lake, a permanent lake at a high altitude cone (660 m a.s.l.) with a mean surface of 0.04 km^2 and at least 5 m depth. At mid-slope, between 200 and 500 m of elevation, a well-developed drainage network can be observed (Fig. 2.1). Due to the presence of clay minerals at the weathered cover, the occurrence of runoff is regular favoring erosive processes where runoff concentrates. Several ravines are dry, but others are fed by perennial springs that outcrop of impermeable layers. In some of them, the streamflow presents considerable variations along its course disappearing and reappearing downstream. Springs above 420 m a.s.l. seems to be recharged during both the garua and hot seasons (Warrier et al., 2012). During five months of weekly monitoring of several streams in 2005 by Adelinet (2005), for most of the streams, the water discharge was weak (< 5 l/s) (Adelinet, 2005), except for one stream in *Cerro Gato* watershed ($15 - 25$ l/s). At the lowlands, due to infiltration losses on the riverbeds, only four ravines have been identified to have streams that reach the sea (d'Ozouville, 2007). One of these ravines has a waterfall when it reaches the coast, showing that the water flow in the ravine is suspended by a weakly impermeable scoria layer (d'Ozouville, 2007; Violette et al., 2014).

The AEM SkyTEM survey performed over San Cristobal provided a 3-D resistivity map of the internal structure of the island (d'Ozouville, 2007; Pryet et al., 2012b). The first hydrogeological conceptual model was proposed by Pryet et al. (2012b) after the interpretation of this resistivity map and field observations. The model configuration can be associated to the Hawaiian model (Peterson, 1972; Macdonald et al., 1983), which have been identified in similar volcanic islands such as: Azores (Cruz and França, 2006), Madeira (Prada et al., 2005), La Réunion (Violette et al., 1997) and Cape Vert Island (Heilweil et al., 2009). The model suggest that springs are originated from perched aquifers formed over impervious layers, which are disconnected from the basal aquifer because its water table remains at low elevation. The impervious layer can be formed from ash deposits or red "baked" soils. These springs are originated when the water level of the perched aquifer intersects the topography or when the impermeable sustaining layer intersects with the topography. Additionally, the existence of a buried low resistivity channel in the summit zone have been interpreted as a dike-impounded aquifer formed between two volcanic cones line ups towards the west-east. Its location is favorable to groundwater recharge given the considerable input of rainfall and fog interception at the highlands.

2.2 Morphology and field work

2.2.1 DEM, extracted drainage network and watersheds

The SRTM DEM (30 m resolution) available (Rabus et al., 2003) is too coarse for an appropriate definition of the watersheds and the extraction of the drainage network. Thanks to an agreement between the *National Polytechnic School* (EPN) of Quito and the *Ministry of agriculture, fishing and ranching* (MAGAP), we could have access to a new DEM developed by the *Instituto Geofísico Militar* (IGM) using aerophotogrammetric digital restitution from 50 cm resolution ortophotos taken on 2011 (IGM, 2014). The DEM has a horizontal and vertical resolution of 10 and 5 m, respectively. It offers a detailed view of the morphology of the island, especially in the windward side (Fig. 2.3, Fig. 2.4 and Fig. 2.5). The cone of *El Junco* can be easily distinguish along with three zones: i) a relative plane zone at the western side of *El Junco*, ii) the mid-elevation zone dissected with a large number of incisions (some of them really deep, up to 65 °C in their slopes) and iii) the relative plane zone near the coast with just few incisions.

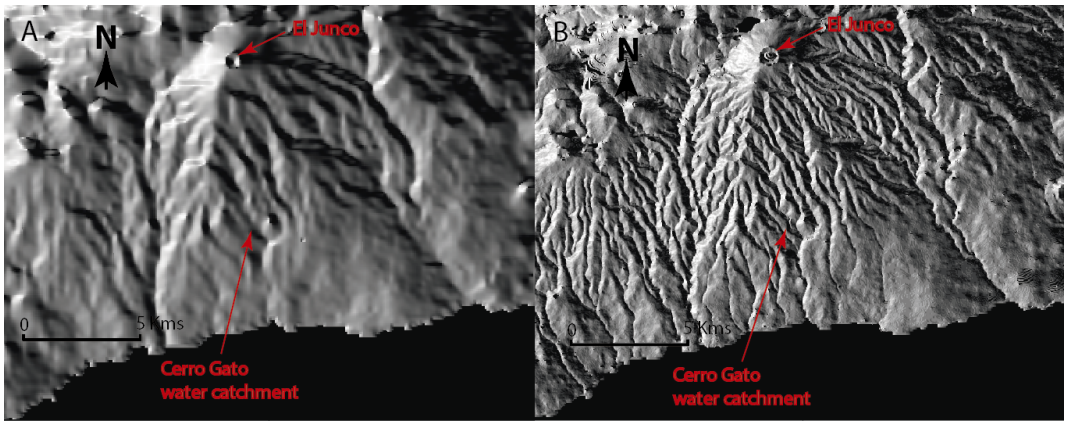

Figure 2.3: Aspect view of the Digital Elevation Model at the windward side of San Cristobal. (A) is the SRTM-DEM 30 m resolution (Rabus et al., 2003). (B) is the IGM-DEM 10 m resolution (IGM, 2014).

The extraction of the watersheds and drainage network was performed using the *GRASS* tools in *QGIS*. Similar to the methodology proposed by (d'Ozouville et al., 2008b), depressions were filled, the flow direction and accumulation were estimated and the stream threshold was defined. The minimum size of the watershed used was 0.4 km^2. Visual validation of the drainage network was performed using the high resolution (50 cm) images from aerophotogrametry supplied by the MAGAP (Fig. 2.6). Also, field validation was performed with a regular GPS on several points of the road, on the limits of some watersheds and at the outlet

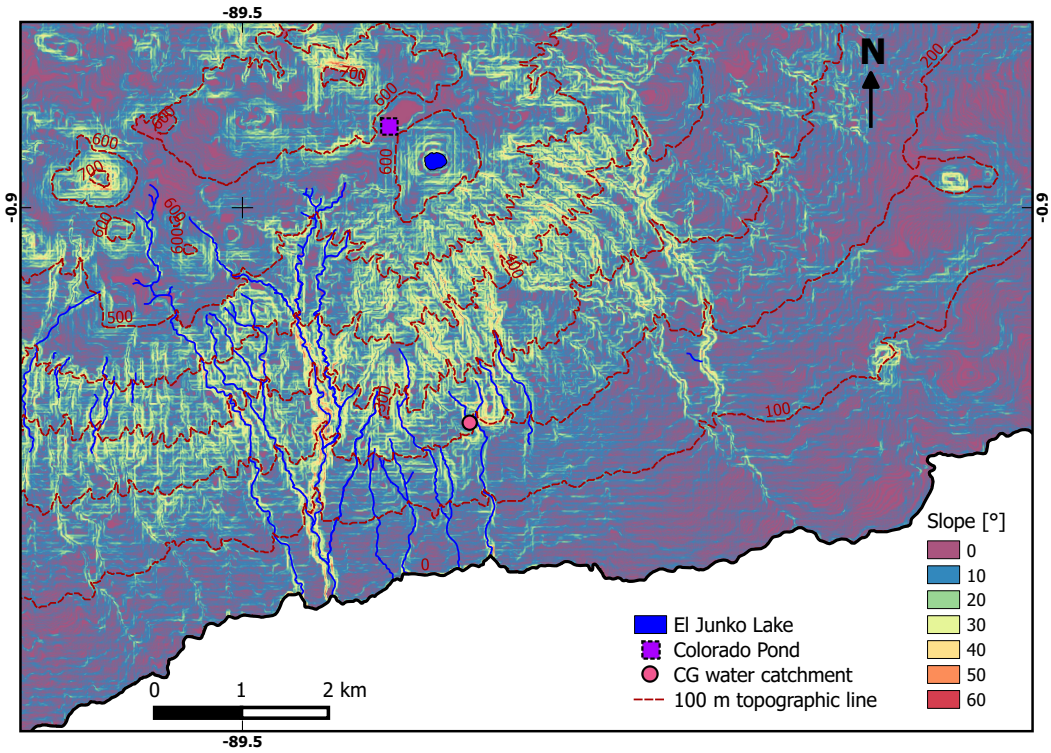

Figure 2.4: Map of the terrain inclination of the windward side on San Cristobal from the IGM-DEM (IGM, 2014). Slopes are relative gently at the highlands and near the coast. At mid-elevation the topography is dissected with several incisions.

of *Cerro Gato* watershed.

11 watersheds were defined in the windward side with surfaces between 0.42 and 12.34 km^2. From the several watersheds, one of interest is *Cerro Gato* big watershed, the one in which the municipal water catchment was build to provide fresh water to the population of Puerto Baquerizo Moreno, located at a distance of 18 km far west. Its surface is 2.5 km^2. The highest point reaches 625 m of elevation. This watershed has a particular morphology. At several locations, the course of the drainage is not straightforward to the coast. It is probably a result of the presence of volcanic edifices and structures (such as cones or lava flow barriers). The municipal water catchment is located at 190 m of elevation.

Using the DEM, it was also possible to define the limits of the three watersheds that will be studied throughout this thesis: *El Bayo*, *Chuki Marka* and *Cerro Gato* watershed. The drainage surface of each watershed was obtained with the program *HydroSIG*, which estimates the flow direction and slopes from a given treated DEM. The DEM must be first corrected to avoid sinks or non-flux directions. Once maps of flow direction and slope are obtained, the coordinates of the control sections are given and *HydroSIG* defines the surface that drains into this point. The main features of this watersheds are summarized in table 2.1.

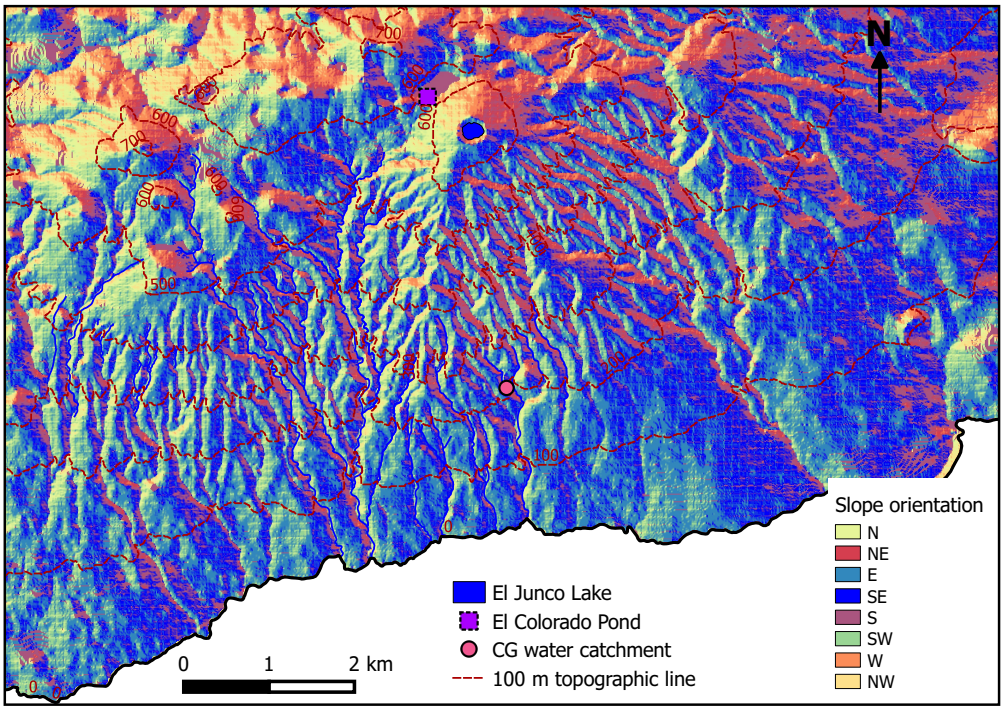

Figure 2.5: Map of the terrain orientation on the windward side of San Cristobal from the IGM-DEM (IGM, 2014). The terrain is mainly oirentated towards the south and south-east. At mid-elevation, portions orientated towards the North are consequence of the deep incisions.

Table 2.1: Main features of the studied watersheds

	El Bayo	*Chuki Marka*	*Cerro Gato*
Surface [km^2]	1.78	0.33	0.69
Median elevation [m a.s.l.]	607	320	373
Maximum altitude [m a.s.l.]	712	445	532
Minimum altitude [m a.s.l.]	520	239	220
Orientation	SW	S	S
Mean slope [%]	5	17	16

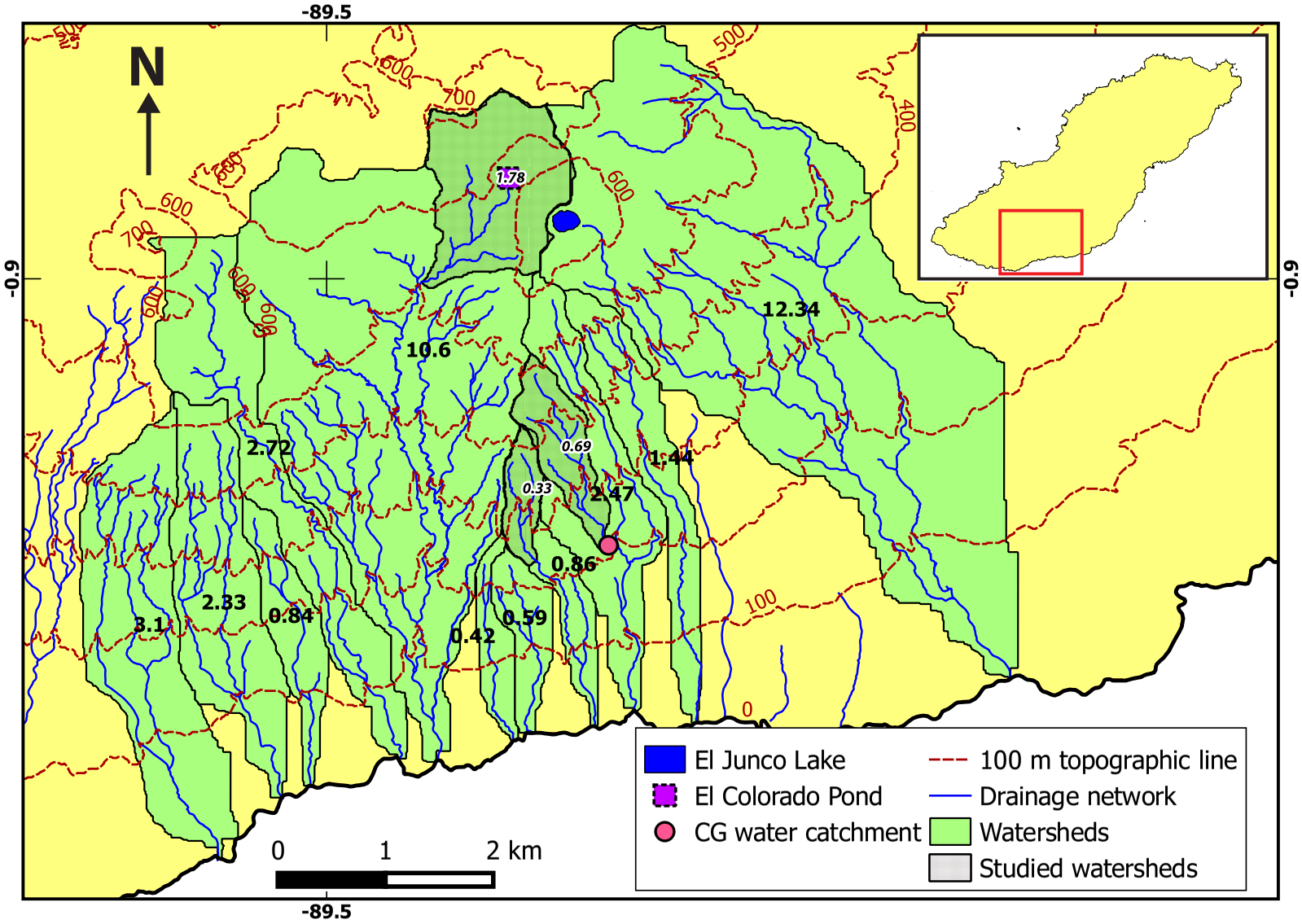

Figure 2.6: Drainage network and watershed extraction of the windward side of San Cristobal from the IGM-DEM (IGM, 2014). Studied watersheds, *El Bayo* (0.33 km^2), *Chuki Marka* (0.69 km^2) and *Cerro Gato* (1.78 km^2), are sub-watersheds of larger watersheds in which its outlet reaches the ocean. The surface of watershed is expressed in km^2.

2.2.2 Spring and stream surveys

A first intent to cartography the rivers and to inventory the springs on the windward side of San Cristobal was performed by Adelinet (2005). The cartography of drainage network was completed from the interpretation of Google Earth images performed by Ramdani and Fauchet (2010). The mapped springs were reduced and scattered distributed. The mapped ravines presented various incongruences compared to the drainage network derived from the new high resolution DEM, dry ravines are not distinguished and the course of the streams is unknown. In consequence a new survey have been performed during 2013 and 2014 in collaboration with *SENAGUA*. It should be highlighted the tough field conditions to perform this job.

Efforts were concentrated in *Cerro Gato* and surrounding watersheds, but still several springs and rivers were mapped in other zones. A total of 68 springs and several ravines with streamflow were mapped to obtain a comprehensive and extensive map of the water resources (Fig. 2.7). Several springs were identified into two types: i) depression springs, where the incised topography intersects the water level of a perched aquifer body, and ii) contact springs, where the impervious layer of the perched aquifer and its water level intersects the incised topography. In the first type of springs, their existence depends of the fluctuation of the water level of the aquifer, while contact springs will always exist unless the entire perched aquifer dries. Overall contact springs could be observed, in which the impervious layer has been seen to be red baked soils or clayed material, and the overlying layer where water flows is whether fractured basalt or scoria deposits.

In *Cerro Gato* watershed, at least six springs form its stream. These springs are located at ca. 240 m of elevation. Only one of them allows the identification of the type of spring. Figure 2.8 shows the spring of *Cerro Gato* that have been identified as a contact spring. It is located ca. 200 m upstream of the watershed outlet. As observed in the figure, water outcrops above a brown clayed material which acts as the impervious layer. Water seems to flow through fractured unweathered basalt until the clayed material intersects the topography. The spring of *Chuki Marka* could not be identified but it is expected to be similar to the ones of its neighbor (*Cerro Gato*). Contrary to springs of *Cerro Gato*, the spring of *El Bayo* is a depression-type, which forms a relative large swamp. It is located ca. 100 m upstream of the watershed outlet.

Measurements of electrical conductivity on springs in the *Cerro Gato* area show that they are poorly mineralized ($30 - 110$ μS/cm). Similar values were found by Adelinet (2005) ($30 - 170$ μS/cm). Springs located at lower elevations, such as *Cerro Gato* (100 μS/cm) and *Chuki Marka* (100 μS/cm), show

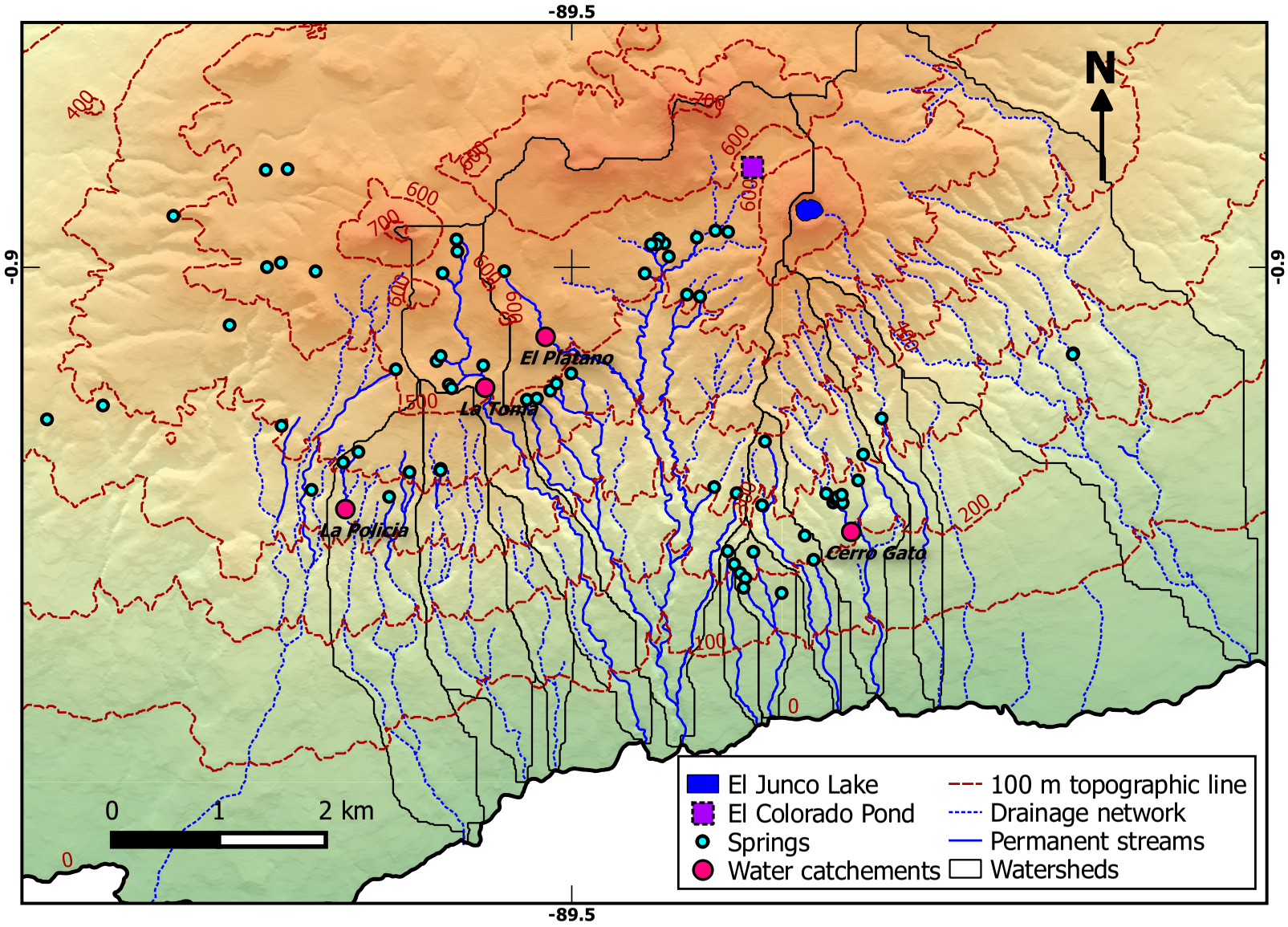

Figure 2.7: Map of water resources on the south-side of San Cristobal from: extraction of IGM-DEM (IGM, 2014), interpretation of aerial photographies and field observations.

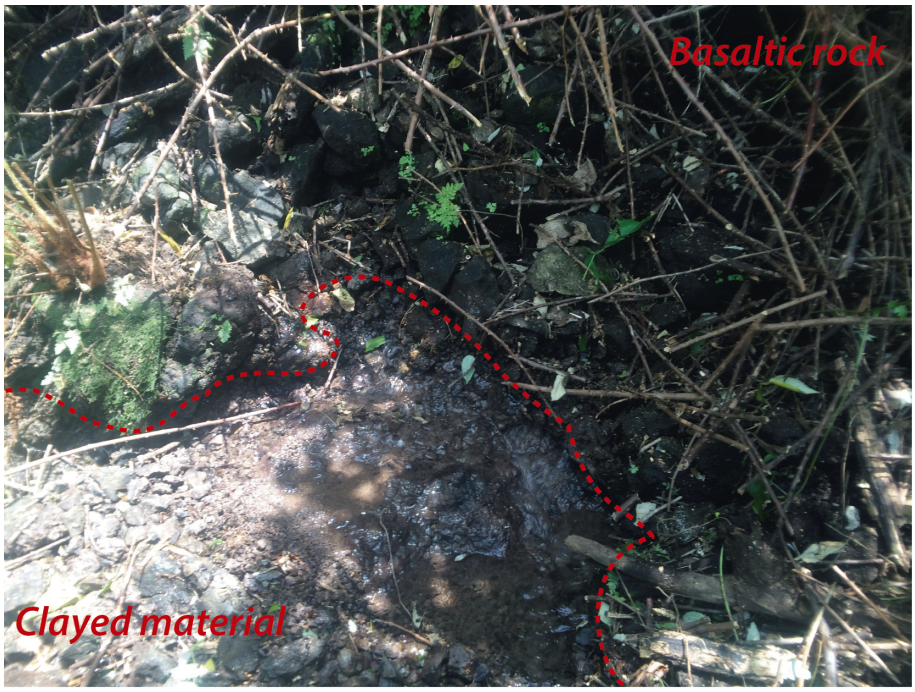

Figure 2.8: Image of one of the springs of *Cerro Gato*. Water outcrops through the basaltic rock above the sustaining unit identified as clayed material.

higher electric conductivity than the ones on the highlands, such as *El Bayo* (40 μS/cm). It suggests that the residence time of groundwater on the lower springs is significant higher than the springs at higher elevations.

2.3 Experimental site

2.3.1 Cerro Gato

The zone of study is surrounding *Cerro Gato* watershed. It is located on the exposed southern windward side of the island, beneath *El Junco* lake (Fig. 2.9). This watershed has particular hydrogeological interest. As mentioned before, the relative large streamflow suggests that the outflow may be larger than the input within its drainage surface, which implies that its hydrogeological watershed may be larger than the surface watershed. Furthermore, the population of Puerto Baquerizo Moreno (PBM), located 18 km far land from the water catchment, is entirely dependent on this stream. A municipal water catchment system located at mid-slope is used for water supply (50% of the total water supply for PBM is taken from this catchment). On this context, the study of this watershed in terms of water management is of great interest. Watershed surrounding *Cerro Gato* are also of interest. They can be useful to place *Cerro Gato* at a regional scale and for comparison purposes. Due to difficulty of access to the interior sector of *Cerro Gato* watershed, some of the measurements and surveys have been carried out on the adjacent watersheds; nevertheless, conditions are expected to be similar.

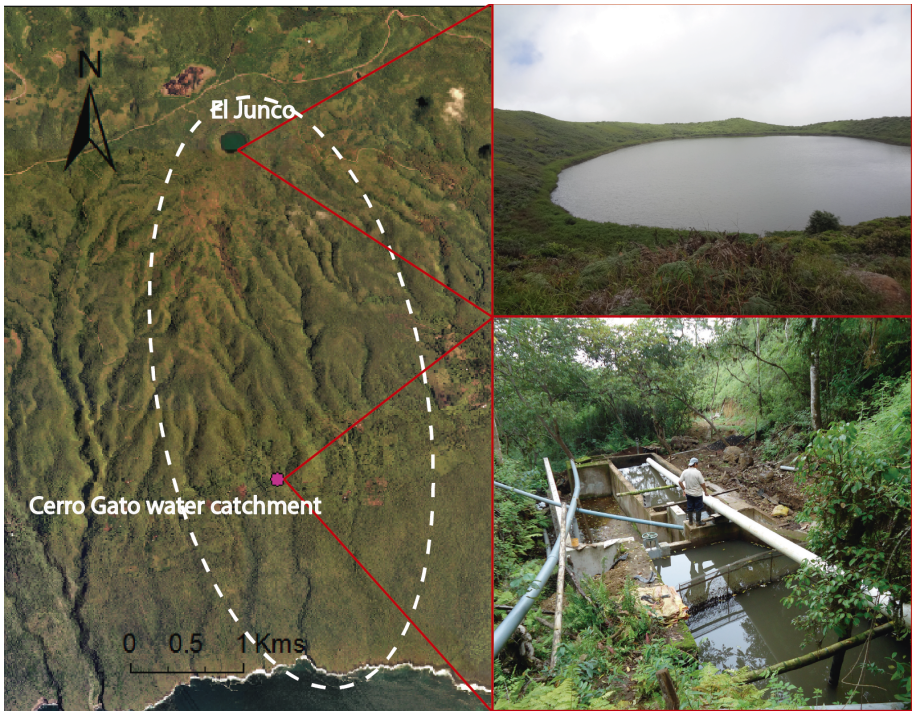

Figure 2.9: Image of the study area located in *Cerro Gato* watershed and surrounding watersheds (IGM, 2014). *Cerro Gato* watershed extends along the windward side of San Cristobal from the coast to the highlands, below *El Junco* lake. 50% of the water supply of Puerto Baquerizo Moreno is taken from the stream of Cerro Gato.

Figure 2.10: Photographies taken at the end of the hot "Invierno" season (May-2013) along *Cerro Gato* watershed. (A) at lowlands (40 m a.s.l.), cactuses and shrubs are visible. (B) on a ravine at mid elevation (250 m a.s.l.), in which pasture, blackberry and guayabas can be identified. (C) at the highlands (620 m a.s.l.), grassland and miconias on the sight.

A brief description of the vegetation and soil on this area is presented as follows (Fig. 2.10):

- At the lowlands (< 200 m a.s.l.), cactuses and shrubs are the dominant species as a consequence of the arid conditions. The soil cover near the coast is ca. 50 cm, it is brown and has a clayey composition.
- At mid elevation (200 - 500 m a.s.l.), the soil has several meters of depth, it is a brown-yellow clayed soil. Because of the diversity of the agriculture (yet, the crop areas are limited) and the presence of invasive species (*Guayaba* and *Blackberry*), a dominant species is difficult to identify.
- The highlands (> 500 m a.s.l.) are covered by forest of the endemic *Miconia* and vast grassland. The soil can be characterized as brown red clayed soil, with several meters of depth.

2.3.2 Hydrological monitoring

Hydrological monitoring was performed in the study zone in order to measure water inputs and outputs. The installation of the different equipment was performed in May 2013. Records used in this thesis correspond to the period from June 2013 to May 2015, which corresponds to two hydrological years. Measurements included both automatic and manual methods. The monitoring was performed by the *Secretary of Water* (SENAGUA) during the first hydrological year thanks to an agreement, and by a private employee of the *GIIWS* project during the second year. Installation, maintenance and change of equipment required several field missions by the author throughout the two years. Recorded data is summarize in section A 2. A detail description of the equipment and monitoring can be found in the following sections.

2.3.2.1 Weather monitoring

Continuous records of the meteorological variables are necessary to water balance estimations. As an orographic gradient is expected on the study area, three weather stations have been installed along the windward slope at 30, 300 and 600 m of elevation (Fig. 2.11). Location of the stations was carefully chosen so it is both representative of the study zone and the access is relative simple. At the mid and high elevation stations (SC300 and SC600), weather data is recorded at 15-minutes time steps with measurements of: atmospheric pressure, solar radiation, air temperature, relative humidity, wind speed and direction, and rainfall (Tb. 2.2). Atmospheric pressure is measured with an independent barodiver. Solar radiation, relative humidity, temperature and wind speed and direction are measured at 2 m above the ground. Rainfall is measured with a tipping bucket rain gauge, placed at 1.5 m above the ground.

Given the semi-presence of fog at the highlands and reports of non-negligible fog interception in Santa Cruz (Pryet et al., 2012a), station SC600 includes a cylindrical fog gauge (height 40 cm, 12 cm in diameter) made of a fine plastic mesh (1 mm). It is placed at 2 m above the ground (same height as Santa Cruz). At the low-elevation station (SC000), only measurements of temperature and rainfall (both at 1.5 m above the ground) are recorded at a 30-minutes time step. Station SC000 is used to complete the orographic gradient. However, the zone of interest is above ca. 200 m of elevation supposed to be the recharge area of the system studied, thus, a more complete set of measurements are unnecessary at this station.

2.3.2.2 Below canopy monitoring

During the cool season, above 300 - 400 m of elevation, an inversion layer is formed leading to the formation of fog. On the highlands of Santa Cruz, cloud water interception by endemic *Miconias* has been reported to be an added input to the hydrological balance (Pryet et al., 2012a). Vast regions of the highlands of San Cristobal are covered by *Miconias*, thus its influence on the groundwater recharge deserves to be assess. At 50 m from the station SC600, throughfall and stemflow measurements are performed within a 6×6 m plot beneath a *Miconias* forest.

Throughfall is measured using two sampling designs (Fig. 2.12): (1) a continuous record from a set of troughs draining into a tipping bucket gauge, and (2) manually read small collectors (Thimonier, 1998; Holwerda et al., 2006; Ziegler et al., 2009). Collected water is directed to an automatic tipping bucket rain gauge. Small collectors were built from funnels placed over 2 L containers. 30

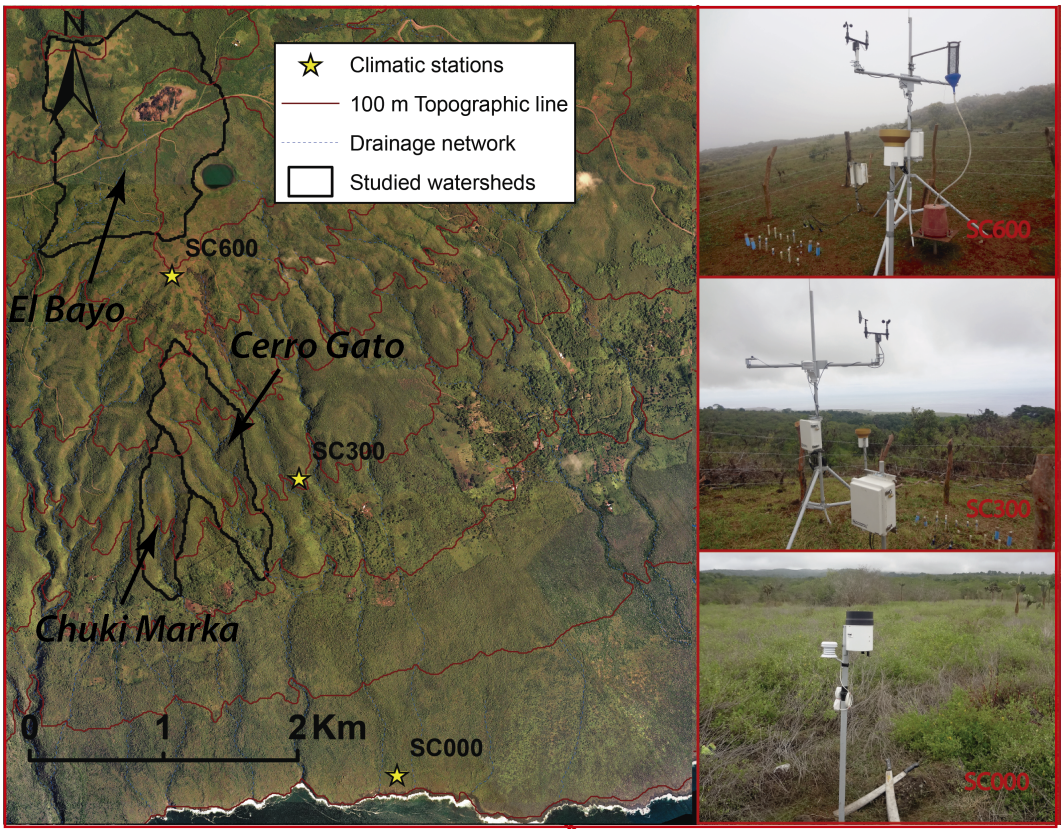

Figure 2.11: Location of the three monitoring stations installed along the windward side of San Cristobal (Aerial photography (IGM, 2014)). Station SC000 consists of a rain gauge and a temperature probe. Station SC300 and SC600 have the instrumentation for weather and soil monitoring.

Table 2.2: List of the monitoring equipment installed on the experimental sites.

	Equipment	**Brand**	**Model**
Station SC000 *North:-0.935652 Est:-89.467977 Altitude: 30 m a.s.l.*	Rain gauge	HOBO	RG3M
	Temperature and relative humidity sensor	HOBO	U23-002
Station SC300 *North:-0.915638 Est:-89.474560 Altitude: 315 m a.s.l.*	DataLogger (x2)	Campbell	CR1000
	Rain gauge	Texas	TE525MM
	Temperature and relative humidity sensor	Campbell	CS215
	Anemometer	Young	03002-5
	Pyranometer	Campbell	CS300
	Automatic tensiometer (x3)	UMS	T8
	Tensiometer probe (x16)	SDEC	SMSxxx
	Pressure sensor	Schlumberger	Baro
Station SC600 *North:-0.901932 Est:-89.483088 Altitude: 595 m a.s.l.*	DataLogger (x2)	Campbell	CR1000
	Rain gauge	Texas	TE525MM
	Rain gauge (x2)	Precis	R307A0
	Temperature and relative humidity sensor	Campbell	CS215
	Anemometer	Young	03002-5
	Pyranometer	Campbell	CS300
	Automatic tensiometer (x3)	UMS	T8
	Tensiometer probe (x16)	SDEC	SMSxxx
	Pressure sensor	Schlumberger	Baro

Figure 2.12: Throughfall and stemflow monitoring at station SC600. Monitoring is performed below the canopy of the *Miconia* forest located at a distance of 50 m from station SC600. Throughfall is measured with troughs and individual collectors, while stemflow is measured with small collection funnels.

collectors are randomly distributed within the plot. Measurements are performed manually bi-weekly by weighting the container with a portable scale. Stemflow is measured on 6 trunks within the plot. Collection funnels connected to a 2 L container were installed at these trunks. Manual measurements are performed similar to the manual throughfall measurements. A detailed description of the monitoring can be seen in section 3.2.

2.3.2.3 Soil monitoring

Investigations on the unsaturated zone of the soil can be integrated to several hydrological processes at the surface, mainly evapotranspiration, which can be modified under the presence of fog. In order to have a more accurate estimation of deep percolation rates that affect the groundwater recharge, the unsaturated soil is monitored by means of tensiometers (Fig. 2.13). At the grassland of the station SC300 and SC600, soil water suction is monitored on a vertical profile with: 1) three automatic UMS T8 tensiometer probes connected to a datalogger with 15-minutes time steps records at 25, 40 and 55 cm of depth and; 2) weekly manual measurements with 16 SDEC SMS tensiometer probes. The tensiometers reach 8 different depths (15, 25, 40, 50, 70, 100, 150, 200 cm) and are split in two series to duplicate the measure at each depth. At the plot under the *Miconia*

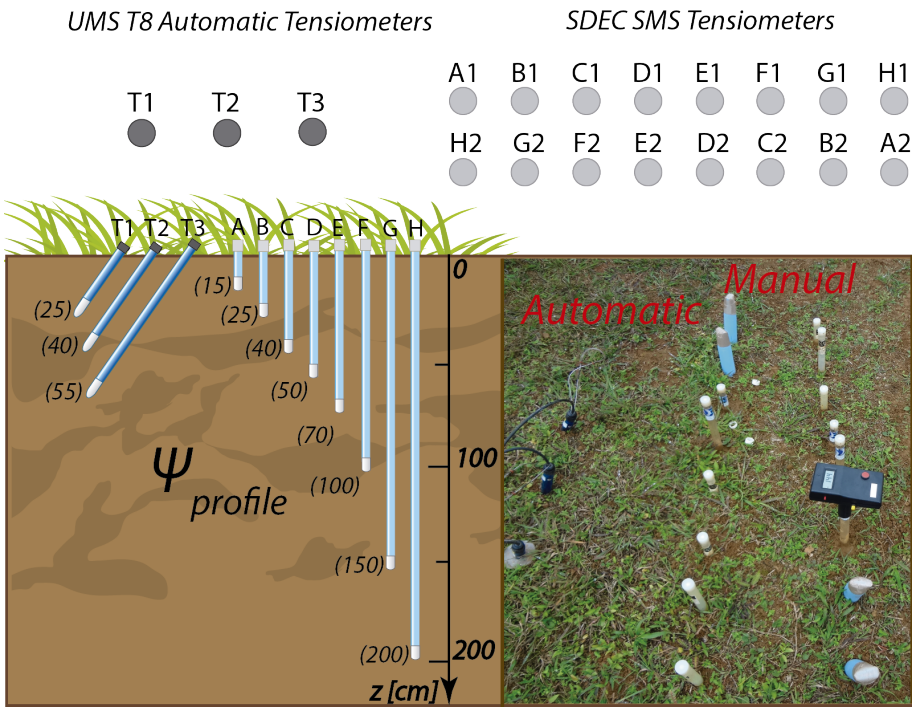

Figure 2.13: Schematic view of the soil monitoring at stations SC300 and SC600. Three automatic tensiometers and 16 tensiometer probes were installed at different depths. Tensiometer probes have 8 lengths into two aligments.

forest, 8 tensiometer probes were also installed at 4 depths (15, 25, 40, 50 cm). Soil, below canopy and weather monitoring completes the monitoring at station SC600 (Fig. 2.14). Automatic measurements are calibrated with several manual measurements during relative dry conditions (to avoid errors for infiltration in preferential pathways) using a linear interpolation.

Soil water suction measurements in stations SC300 and SC600 were complemented with soil samples taken at different depths. Samples were taken to the laboratory for hydrophysical testing. Results from the laboratory are summarize in table 2.3 and show that soil at SC600 is less permeable than soil at SC300. These results are in accordance to the ones reported by Adelinet et al. (2007), in which permeability is lower at the highlands, increasing at lower elevations. A detailed description of the influence of the hydrophysical properties of the soil in the recharge can be seen in section 2.4 and section 3.3.

2.3.2.4 Water level and streamflow monitoring

Continuous records of streamflow on the watershed of interest and surrounding watersheds are fundamental to the interpretation of their hydrological processes. Three sections of control on ravines have been equipped with divers (Fig. 2.15). Measurements were performed at these points because they have the most homo-

Table 2.3: Hydrophysical properties of soils in stations SC300 and SC600. Properties were obtained from laboratory experiments on samples taken from the stations at different depths.

	SC300			SC600		
Parameter	0-25 cm	25-50 cm	> 50 cm	0-30 cm	30-60 cm	> 50 cm
Mineralogy						
Sand[a] [%]	11	15	16	8	13	12
Clay[a] [%]	29	41	25	22	20	13
Silt[a] [%]	60	44	59	70	67	75
Hydrophysical						
Dry bulk density [gr/cm^3]	1.08	1.01	1.16	1.28	1.64	1.17
Organic content[b] [%]	16.63	15.02	18.23	19.30	18.23	17.83
Hydraulic conductivity [m/s]	2.03×10^{-4}	1.34×10^{-4}	-	1.78×10^{-5}	9.02×10^{-6}	4.45×10^{-6}
$VSWC_{sat}$[c,e] [%]	0.63	0.64	0.54	0.55	0.45	0.57
$VSWC_{dry}$[d,e] [%]	0.39	0.34	0.26	0.25	0.31	0.42
n[e]	1.64	1.20	1.52	1.40	1.14	1.41
α[e] [m^{-1}]	20.28	32.35	1.35	9.04	10.79	12.77

[a] Granulometry using sieves and hydrometer

[b] Obtained by loss of ignition method

[c] Volumic soil water content at saturation

[d] Volumic soil water content at pF 4.2

[e] Van Genuchten parameters obtain from the soil mositure retention curve (pF curve)

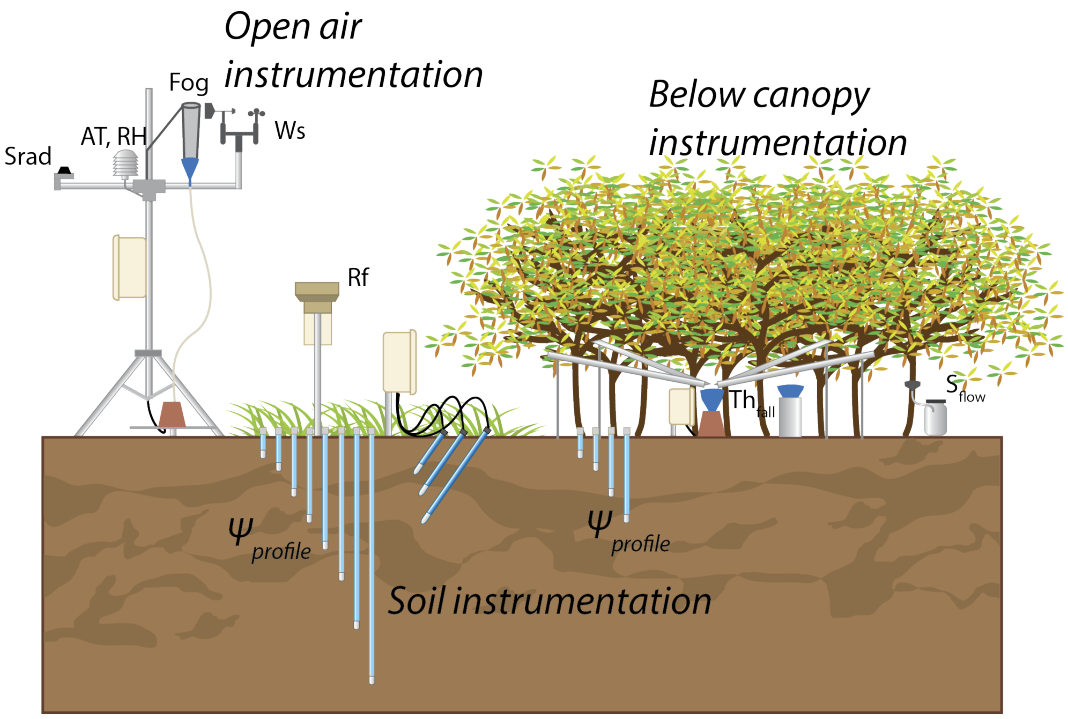

Figure 2.14: Schematic representation of the monitoring at station SC600. At a grassland, a weather station was placed on the open area. At the *Miconia* forest, net precipitation instrumentation was installed under the canopy. At both sites, soil water suction instrumentation was positioned under the vegetation.

geneous section possible and they are close to the road. Streamflow monitoring complete the measurements made in the study zone. Figure 2.16 shows a comprehensive map of the water resources of the windward side of San Cristobal and the hydrological monitoring performed in the frame of the *GIIWS* project. Additionally, at the shore of *El Junco* lake, one diver have been installed in order to assess the seasonal variations of its water level. The divers record pressure and temperature at a 15-minutes time step. Pressure is compensated with a barodiver in order to have estimates of the absolute water level fluctuation. The three sections of control on the ravines are:

- *Cerro Gato*, which is located at 30 m upstream of the municipal water catchment (220 m a.s.l.). In this section, a V-notch weir was already installed favoring the accuracy of the measurements. Water discharge range from $15 - 25$ l/s (between March to July of 2005, reported by Adelinet (2005)).

- *Chuki Marka*, which is located few meters from the road (239 m a.s.l.), the water discharge range from 5 to 11 l/s (Adelinet, 2005). The lack of a weir and the irregularity of the section jeopardize the accuracy of the measurements, but the water level measurements can still be related to the

drain pipe upstream.

- *El Bayo*, which is located at the highlands (520 m a.s.l.). Similar to *Chuki Marka*, this is an irregular section at the exit of a drainpipe under the road.

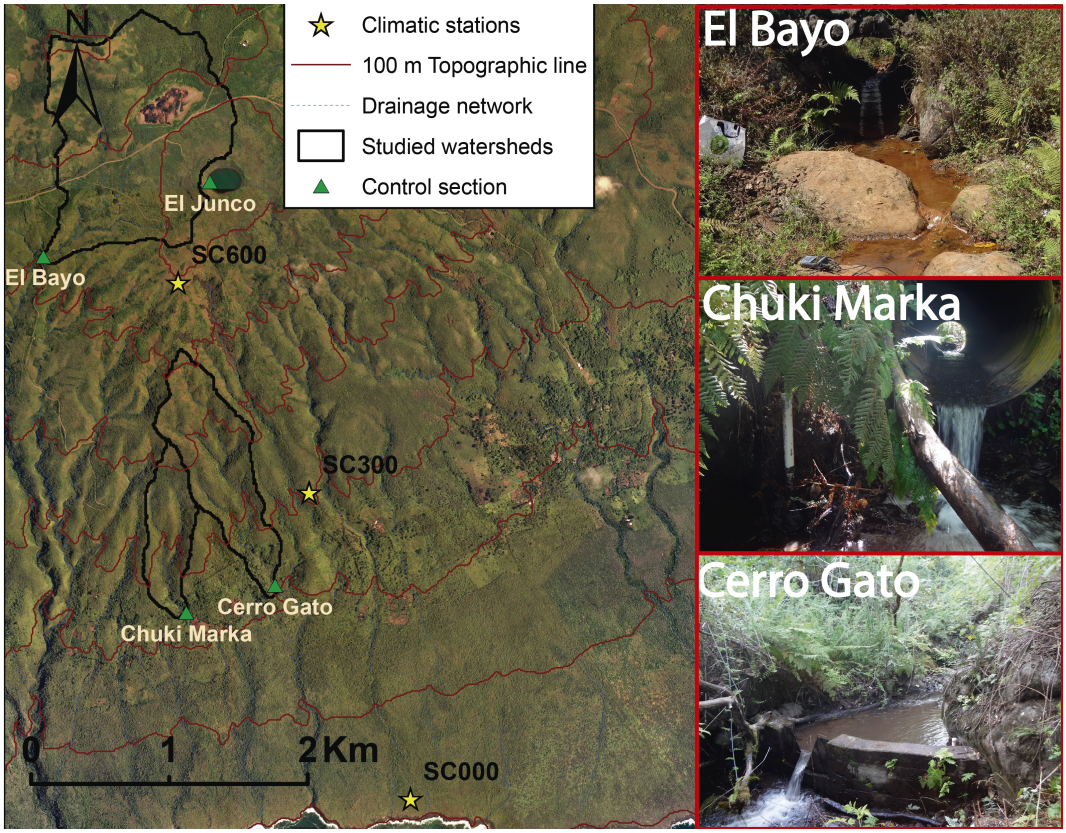

Figure 2.15: Location of water level monitoring on the study zone (Aerial photography (IGM, 2014)). Three divers were installed on sections of control of ravines and one diver on the shore of *El Junco* lake. Drainage surface was estimated with the program *HydroSIG*. Streamflow of ravines is derived from the relation water level - discharge.

Punctual measurements of streamflow at these sections are performed with the mass balance method (Moore, 2005; Hudson and Fraser, 2005). The punctual streamflow measurements are performed on a regular basis (2-3 weeks). The water level is correlated with the water flow rate resulting in a calibration equation that gives water flow rate as a function of the water height (rating curve). Thus, streamflow is estimated at 15-minutes time step using the records from the water level divers. A detailed description of the streamflow measurements can be seen in section 4.1.1.

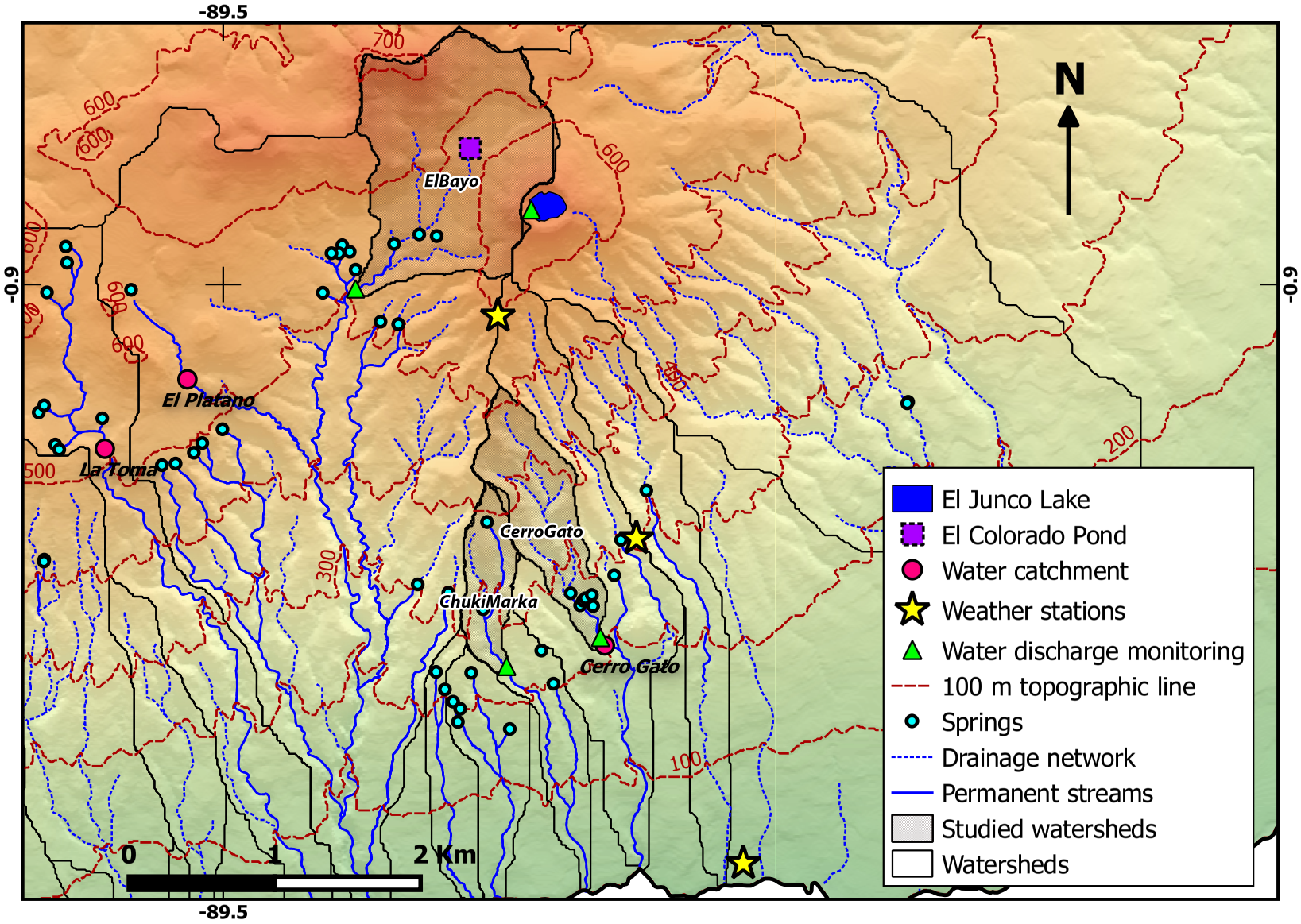

Figure 2.16: Map of water resources and the hydrological monitoring network performed by the *GIIWS* on the south-side of San Cristobal. The shaded relief is extracted from the IGM-DEM.

2.4 Comparison of deep percolation rates below contrasting land covers with a joint canopy and soil model*

Abstract

A Rutter-type canopy interception model is combined with a 1-D physically-based soil water flow model to compare deep percolation rates below distinct land covers. The joint model allows the quantification of both evaporation and transpiration rates as well as deep percolation from vegetation and soil characteristics. Experimental observations are required to constitute the input and calibration datasets. An appropriate monitoring design is described which consists in meteorological monitoring together with throughfall and soil water tension measurements. The methodology is illustrated in Santa Cruz Island in the Galapagos Archipelago, which has been affected by significant land use changes. Two adjacent study plots are investigated: a secondary forest and a pasture. The results of the model reveal that total evaporation is higher in the pasture due to the bigger canopy storage capacity, which promotes evaporation against canopy drainage. This is however compensated by higher transpiration in the secondary forest, due to the smaller surface resistance. As a consequence, total evapotranspiration is similar for the two plots and no marked difference in deep percolation can be observed. In both cases, it reaches ca. 2 m/year which corresponds to 80% of the incoming rainfall. This methodology not only allows the quantification of deep percolation, but can also be used to identify the controlling factors of deep percolation under contrasting land covers.

* In collaboration with Alexandre Pryet[1], Miguel García Vera[2], Andres Gonzalez[3], Cedric Chaumont[4], Julien Tournebize[4], Marcos Villacis[3], Noemi d'Ozouville[5], Sophie Violette[6,7]. Published in *Journal of Hydrology*, Volume 532, January 2016. Pages 65-79, `http://dx.doi.org/10.1016/j.jhydrol.2015.11.022`.

2.4.1 Introduction

The estimation of groundwater recharge is fundamental for the efficient management of water resources and the application of conservation policies. It is of particular interest in locations where surface water resources are limited, and groundwater is essential for water supply. The determination of groundwater recharge (referred as "deep percolation" in this paper) is challenging because it is dependent on several variables such as meteorological conditions, vegetation and soil characteristics.

Land cover controls deep percolation rates, affecting the amount of rainfall that reaches the canopy floor, transferring the available soil water to the atmosphere and influencing the hydrophysical properties of the soil (Alegre and Cassel, 1996; Ziegler et al., 2006; Zimmermann et al., 2006). The impact of land use change over the hydrological processes has been evaluated in various contexts (Bosch and Hewlett, 1982; Johnson, 2012; Zimmermann et al., 2010). Bosch and Hewlett (1982) reported significant difference in soil water yield depending on the vegetation cover and related it to the vegetation water use. Dean et al. (2014) suggested that in order to reduce the high evapotranspiration of tree plantation, forests should be placed in locations with limited water, so the plant water demand will have a minimum impact. Taniguchi and Sharma (1993) reported variable recharge rates in different zones of the same forest, because of the difference in rainfall interception at these zones related to their density. Soil characteristics are also affected by land cover and land use, Dörner et al. (2010) reported that the saturated soil hydraulic conductivity was a function of the land use, and Bormann et al. (2007) concluded that different hydrological catchment models showed sensitivity to soil parameterization related to the land use even with similar evapotranspiration and discharge rates. Focusing on the comparison between a forest and a pasture, several studies (e.g. Bosch and Hewlett (1982); Hibbert (1969); Thorburn et al. (1991)) have shown that replacing forests with herbaceous vegetation increases the groundwater recharge, as a consequence of the decrease in plant water use. German scientists (ATV-DVWK, 2002) estimated evapotranspiration of different plants species with weighable lysimeters

[1] *EA 4592, Institut Polytechnique de Bordeaux et Université Bordeaux Montaigne. 1, Allée Fernand Daguin, 33607 Pessac, France*

[2] *Department of Physics, National Polytechnic School, Quito, Ecuador*

[3] *Department of Civil and Environmental Engineering, National Polytechnic School, Quito, Ecuador*

[4] *IRSTEA UR HBAN, 1 rue Pierre Gilles de Gennes, 92761 Antony cedex, France*

[5] *Charles Darwin Foundation, Puerto Ayora, Galapagos Islands, Ecuador*

[6] *UPMC-Sorbonne Universités, 4 Place Jussieu, 75252 Paris Cedex 05, France*

[7] *ENS-PSL Research University & CNRS, UMR.8538-Laboratoire de Geologie, 24 rue Lhomond, 75231 Paris Cedex 05, France*

on conditions of optimized water supply. They compared their measurements with the reference evapotranspiration (ETo) (Allen et al., 1998) and deduced a plant specific coefficient from their ratio. Comparing the coefficients, their results show that evapotranspiration of forests (1.13, 1.23 and 1.34 for a deciduous, mixed and coniferous forest respectively) are higher than a grassland (0.98). Nevertheless, when a forest and a pasture land were compared in wet regions, Kelliher et al. (1993) estimated similar rates in evapotranspiration and Brauman et al. (2012) concluded that evapotranspiration was higher at the pasture than at the forest. In the case of conversion from forest to pasture, infiltration rates could be reduced as a result of a reduction in hydraulic conductivity caused by compaction (Dörner et al., 2010; Zimmermann et al., 2010).

Several methods can be used to estimate recharge rates such as the water table fluctuations analysis, tracer experiments and lysimeters. The drawback of these methods is that they are not suitable for regular basis estimations over long time periods because they are based on relatively heavy experimental designs and require access to observation wells. In addition, they cannot describe the different processes involved in water transfers. Another common approach is the use of soil-plant-atmosphere models in which the water transfer processes are assessed through the canopy and soil (e.g. Finch (1998); Klinge et al. (2001); Panigrahi and Panda (2003); Rushton et al. (2006); Simunek et al. (2013); Williams et al. (1985)). In some of these models, only the soil compartment is evaluated and processes such as interception losses may not be considered. Johnson (2012) highlighted the importance of considering interception losses over the canopy for the estimation of groundwater recharge. In the case where interception losses are considered, they are usually estimated with empirical formulas, in which the results are highly dependent on the characteristic of the species and atmospheric conditions (Kozak et al., 2007; Muzylo et al., 2009). At the soil compartment, reliable inflow and root water uptake rates are necessary to properly describe soil water tranfers. Several studies reported a reduction of transpiration under wet canopy conditions (e.g. Bosveld and Bouten (2003); Kozlowski (1983); Larsson (1981)), affecting the soil water content by the root water uptake. Thus, a suitable strategy to evaluate deep percolation under different canopy covers could be the joint modeling of the canopy and the soil.

Interception models most commonly redistribute rainfall using a mass balance equation. Muzylo et al. (2009) provided a review of more than 15 physically-based interception models and makes the distinction between: 1) Rutter-type models (e.g. Liu (1997); Rutter et al. (1975)), based on the running canopy water budget, and 2) Gash-type models (e.g. Gash (1979); Zeng et al. (2000)), based on discrete rainfall events. Even though Gash models are more frequently

chosen because of their simplicity, they are limited to relatively large temporal resolutions and require the tedious task of separating individual rainfall events.

Two main approaches are commonly used for the modeling soil water transfer (Gandolfi et al., 2006; Panigrahi and Panda, 2003): 1) Simple conceptual reservoir models (e.g. Rushton et al. (2006); Williams et al. (1985)) based on the principle of mass conservation, where the soil is assumed as a reservoir, the recharge is estimated as the drainage from the excess of water when the soil moisture content reaches the field capacity. 2) Physically based models (e.g. Herrada et al. (2014); Simunek et al. (2013)) that use either analytical or numerical solutions of the Richards equation (Richards, 1931), where the water movement is described from differences in the hydraulic potential along the soil profile. The latter approach provides detailed information about the infiltration and outflow dynamics from the soil profile and can be used in several contexts (Herrada et al., 2014; Moukandi-N et al., 2011; Rushton et al., 2006).

In this study we describe a methodology to assess the impact of land use change over deep percolation. The approach is composed of (i) a joint model, in which we combined a Rutter-type canopy interception model with a 1-D physically-based variably saturated flow model and (ii) an experimental monitoring design providing the necessary input and calibration datasets. This methodology is illustrated on Santa Cruz Island (Galápagos Archipelago), an example of land use change, where deep percolation rates are compared and quantified between a secondary forest and a pasture, which are the two most representative land covers of the highlands of this island. We first detail theoretical background of the interception and soil water transfer model and describe the hydrological monitoring. We then provide a description of the study site and the main results are presented. The relevance of the method and results are eventually discussed.

2.4.2 Methods

2.4.2.1 Interception model

We used a modified sparse version of the original *Rutter* model to estimate canopy interception losses, net precipitation and transpiration (Fig. 2.17) (Rutter et al., 1971, 1975; Valente et al., 1997). The model requires parameters describing the canopy structure (Schellekens et al., 1999). Stemflow is not considered explicitly in the current model version (since stemflow is less than 1% of rainfall, see section 2.4.3.2), but it could easily be extended for cases where it is relevant. For each time step, changes in the canopy water storage (C) is computed from the amount of rainfall (RF) intercepted by the canopy, and the outputs of drainage

from the canopy (D) and actual evaporation of the intercepted water (E):

$$\Delta C/\Delta t = (1-p) \times RF - D - E \tag{2.1}$$

where p is the free throughfall coefficient. The drainage from the canopy is calculated using an exponential function (Gash and Morton, 1978; Schellekens et al., 1999; Valente et al., 1997):

$$D = \begin{cases} D_s \times exp(b(C-S)) & \text{if} \quad C > S \\ \\ 0 & \text{if} \quad C \leq S \end{cases} \tag{2.2}$$

where D_s [LT^{-1}] is the drainage rate for $C = S$, b [L^{-1}] is an empirical parameter and S [L] is the maximum amount of water stored by the canopy that will not drip to the canopy floor, defined as *adherent storage capacity* by Liu (2001). Thus, D is set to zero when $C \leq S$ (Gash and Morton, 1978; Schellekens et al., 1999). Understory evaporation is neglected (Valente et al., 1997). The actual evaporation of canopy interception rate (E_a) depends on the amount of water stored by the canopy:

$$E_a = \begin{cases} (1-p) \times E_p & \text{if} \quad C \geq S \\ \\ (1-p) \times C/S \times E_p & \text{if} \quad C < S \end{cases} \tag{2.3}$$

where E_p [LT^{-1}] is the potential evaporation rate. When the canopy is saturated ($C \geq S$), E_a reaches the potential evaporation rate. For unsaturated canopy ($C < S$), E_a is proportional to the C/S ratio (Rutter et al., 1975; Valente et al., 1997). Similarly, the transpiration rate T [LT^{-1}] also depends on C. When the canopy is unsaturated, T is considered to be proportional to the fraction of dry canopy (Whitehead and Kelliher, 1991):

$$T = \begin{cases} 0 & \text{if} \quad C \geq S \\ \\ (1-p) \times (1 - C/S) \times T_p & \text{if} \quad C < S \end{cases} \tag{2.4}$$

where T_p [LT^{-1}] is the potential transpiration rate. T_p and E_p are estimated using the Penman-Monteith (P-M) equation (Monteith, J.L., 1965). In the case of T_p, surface resistance (r_s) is used as a constant value in the P-M equation, while r_s is set to zero in the case of E_p (Kelliher et al., 1993; Muzylo et al., 2009; Pryet et al., 2012a; Rutter et al., 1975; Whitehead and Kelliher, 1991).

The aerodynamic resistance r_a is calculated with the equation from Rutter et al. (1971, 1975) valid for moderate wind speeds:

$$r_a = \frac{1}{k^2 u_z} \cdot \left(\ln(\frac{z-d}{z_0}) \right)^2 \tag{2.5}$$

where k is the *von Karman* constant, u_z is wind speed measured at height z, z_0 is the roughness length and d is the zero plane displacement. The net precipitation (P_{net}) constitutes the input of water to the soil. It is estimated as the sum of free throughfall and canopy drainage:

$$P_{net} = p \times RF + D \tag{2.6}$$

It should be noted that the transpiration term does not affect the canopy water balance, it is only used at the soil compartment.

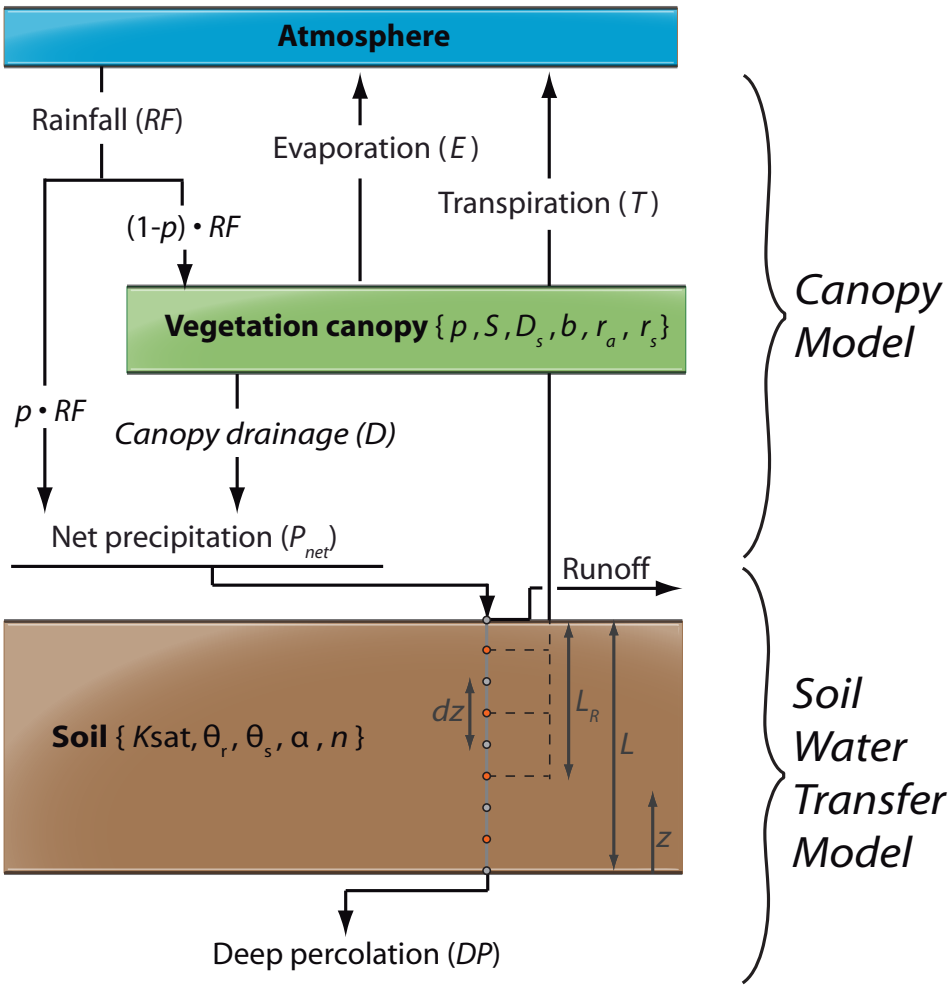

Figure 2.17: The joint interception and soil water transfer model. p, S, D_s, b, r_a and r_s correspond to canopy characteristics. K_{sat}, θ_r, θ_s, α and n correspond to soil characteristics. L, L_R, dz and z are variables used in the spatial discretization of the physical soil water transfer model.

2.4.2.2 Soil water transfer model

We used a physically based model that solves numerically the mixed-form of the *Richards'* equation for one-dimensional variable saturated flow (Fig. 2.17). This approach not only allows the quantification of the soil water budget, but also provides simulated values of pressure head and water content, thus it is possible to have insights about the redistribution of the infiltration along the soil profile (Gandolfi et al., 2006; Herrada et al., 2014; Rushton et al., 2006).

Soil water flow can be described by the mixed-form of the *Richards'* equation with a source term along the vertical upward axis:

$$\frac{\partial \theta}{\partial t} = \frac{\partial}{\partial z}\left(K(h)\frac{\partial h}{\partial z}\right) + \frac{\partial K(h)}{\partial z} + q \tag{2.7}$$

where h [L] is the soil pressure head, θ [-] is the water content, $K(h)$ [LT^{-1}] is the hydraulic conductivity, q [T^{-1}] the sink term and z [L^{-1}] is the coordinate along the vertical upward axis. The discretization of this equation is based on a fully implicit finite-difference scheme for time derivatives and a central differences scheme for spatial derivatives (section A 3). h is estimated using a modified *Picard* iterative scheme (Celia et al., 1990; Clement et al., 1994). The entire method ensures mass balance conservancy, is computationally efficient and has no limitation when applied to field problems (Celia et al., 1990; Clement et al., 1994; Hendriks, 2010). The relation between θ and K is described with the analytical models proposed by Van Genuchten (1980):

$$\theta(h) = \theta_r + (\theta_s - \theta_r)\left(1 + |\alpha h|^n\right)^{-m} \tag{2.8}$$

$$K(h) = K_{sat} \times \frac{\left((1 - |\alpha h|^{n-1})\left(1 + |\alpha h|^n\right)^{-m}\right)^2}{\left(1 + |\alpha h|^n\right)^{m/2}} \tag{2.9}$$

where K_{sat} is the saturated hydraulic conductivity, θ_r is the residual water content, θ_s is the saturated water content, α [L^{-1}] is the inverse of the air entry pressure, n is a pore-size distribution index and $m = 1 - 1/n$. Plant water uptake is computed from potential transpiration rate but is reduced under water stress conditions. The sink term q in Eq. 2.7, is defined as the rate of water removed due to water uptake by the plants (Feddes et al., 1978). For this model, we use an equally distributed water uptake rate:

$$q = \begin{cases} 0 & \text{if} \quad z < (L - L_R) \\ \\ \beta(h) \times 1/L_R \times T & \text{if} \quad z \geq (L - L_R) \end{cases} \tag{2.10}$$

where L is the soil depth, L_R is the root depth, T is the transpiration rate calculated by the interception model and $\beta(h)$ is the dimensionless stress response

function defined in a similar way as Feddes et al. (1978):

$$\beta = \begin{cases} 1 & \text{if} \quad h \geq h_{fc} \\ 1 - \dfrac{h - h_{fc}}{h_{wp} - h_{fc}} & \text{if} \quad h_{wp} \leq h \leq h_{fc} \\ 0 & \text{if} \quad h < h_{wp} \end{cases} \tag{2.11}$$

where h_{fc} and h_{wp} are the pressure heads at the field capacity and wilting point, respectively. The actual transpiration rate T_a [LT^{-1}] is obtained by the integration of q along the soil profile:

$$T_a = \sum_{z=0}^{L} q(z) \tag{2.12}$$

The boundary conditions used in the soil model are: fixed flow at the top (P_{net}), and below either a fixed head (aquifer) or free drainage (unsaturated permeable unit).

Finally, the soil running water balance can be written as follows:

$$P_{net} = T_a + DP + RO + \Delta S/\Delta t \tag{2.13}$$

where DP [LT^{-1}] is deep percolation, RO [LT^{-1}] is runoff and ΔS is the change in water content of the soil column. DP and RO are derived from the solution of the pressure head profile in the model. Runoff occurs in the case when P_{net} exceeds the infiltration rate at the top surface, it is estimated similar to the methodology proposed by Herrada et al. (2014), where the top boundary condition change to a prescribed pressure head whenever the upper soil layer reaches saturation. The soil model has been validated with the *Hydrus-1D* software, simulating the pressure head at several depths using the same soil characteristics, boundary conditions, input rates and no water uptake ($RMSE = 1.25$ cm, $n = 960$).

2.4.2.3 Hydrological monitoring

The joint model described above requires meteorological variables as input over the whole simulation period. In addition, observed values of simulated variables are required for the calibration of model parameters. The monitoring design necessary for the implementation of the joint model consists in climatic, vegetation and soil measurements (Fig. 2.18). The instrumented plot must be representative of the land cover of interest in terms of vegetation species, tree density and size. Climatic monitoring is conducted with a weather station placed in an

open area. Similar climatic conditions should be expected at the weather station and the study plot, and therefore the distance between both should be short. Measurements at the open area include rainfall, solar radiation, air temperature, relative humidity and wind speed. These variables are necessary as the model input (rainfall) and for the computation of potential evaporation and transpiration rates. Climatic data should be recorded at short time intervals (e.g. 15 min) in order to estimate the canopy parameters for the interception model (Pryet et al., 2012a).

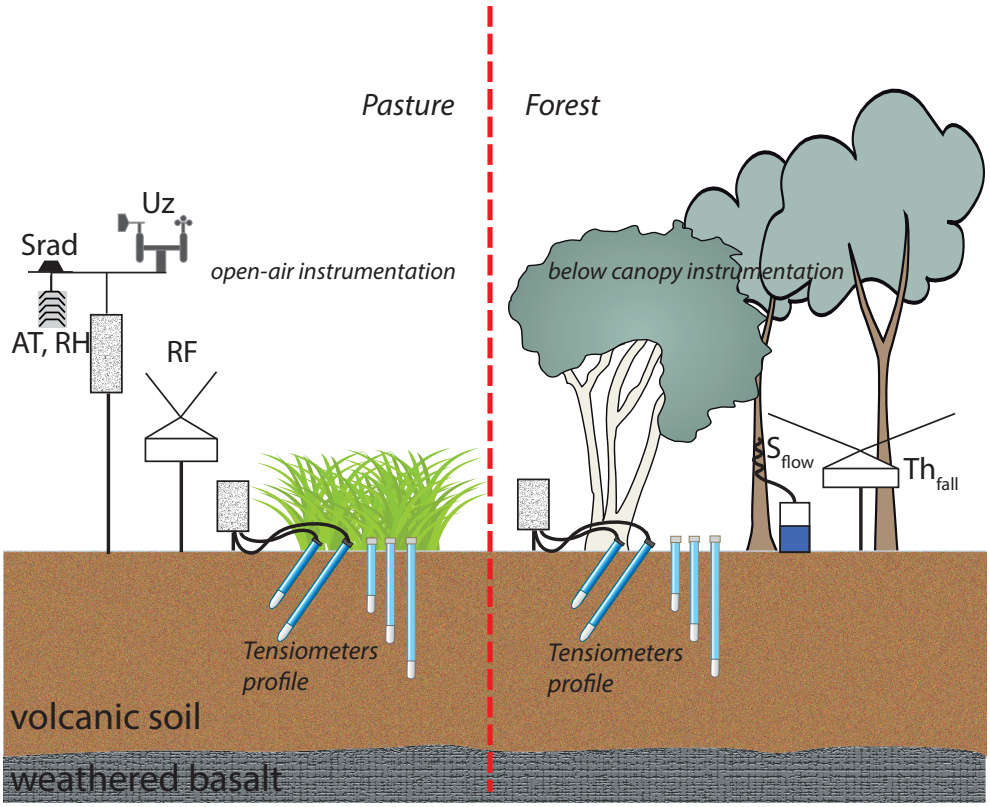

Figure 2.18: The hydrological monitoring at the two land covers: pasture and forest. At the pasture, we placed a weather station on the open area ($Srad$: solar radiation, Uz : wind speed, AT : air temperature, RH : relative humidity, RF : rainfall, S_{flow} : stemflow and Th_{fall} : throughfall). Net precipitation was measured below the forest. At both sites, automatic and manual soil water suction instrumentation was positioned under the vegetation along a vertical profile.

The vegetation monitoring consists in measurements of throughfall and stemflow below the canopy. The spatial representativity of throughfall measurements should be assessed due the existence of dripping points and shaded areas (Zimmermann et al., 2009). The soil monitoring consists of measurements of soil pressure head by means of tensiometers on a vertical profile distributed over the study plot. The advantage of using a soil pressure head monitoring instead

of a water content monitoring, is that these measurements are direct, they are relatively cost effective and they are more informative, as the pressure head is the driver of soil water movement. Automatic measurements at short time intervals are encouraged in order to have detail observations during storm events. Nevertheless, regular manual measurements are required to validate the spatial representativity of automatic tensiometers. Throughfall and soil pressure head measurements are not used as input variables in the model, instead they are used for the calibration and validation of the joint model.

2.4.2.4 Implementation of the joint canopy and soil model

The interception and soil water transfer models are associated using the net precipitation as the input for the soil model and the simulated soil water pressures are used to compute the actual transpiration rates. The model was implemented with the *Python* scripting language.

The calibration of model parameters is conducted with the *Guauss-Levenberg-Marquadt* algorithm (GLMA) implemented in the PEST software (Doherty, 2010) for the optimization of minimum weighted least square (OMWLS) between simulated and observed data. Inversion convergence was insured with a *Tikhonov regularization* scheme, based on initial parameter values (Aster et al., 2013; Doherty, 2010). These initial values were set to their expected values after literature review and field measurements.

The predictive uncertainties of model predicted values (evaporation, transpiration, runoff, deep percolation) can be computed from Bayes' equation with a linearized version of the joint model (Doherty, 2013). Confidence intervals for parameters and predicted values assume gaussian distributions of errors. The potential error of forcing variables, namely rainfall and potential evapotranspiration rates are not taken into account. Although they are based on relatively rough assumptions, the confidence intervals computed with this approach provide an indicator of the effectiveness of model calibration to constrain predicted values.

2.4.3 Case study in the Galapagos Islands

2.4.3.1 Study area

The Galapagos Islands are located in the Eastern Pacific, 1000 km west of the Ecuadorian mainland (Fig. 2.19). There are two distinct climatic seasons: 1) The cool "garua" season from June to December characterized by relative low temperatures and the ocurrence of orographic precipitations and the presence of a semi-permanent fog layer that covers the highlands of the main islands (Pryet

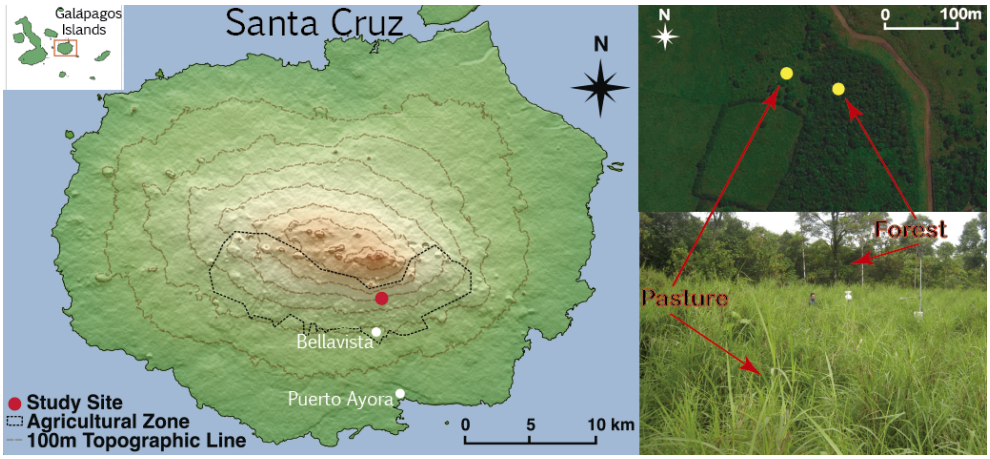

Figure 2.19: Digital elevation model of Santa Cruz Island, located at the center of the Galapagos Archipelago (Ecuador). The hydrological monitoring was set up at two adjacent land covers on the windward slope of the island (image from IGM (2014)): a secondary forest and a pasture.

et al., 2012a; Trueman and d'Ozouville, 2010). 2) The hot "invierno" season from January to May, characterized by high air temperatures, and high intensity convective precipitations (Dunbar et al., 1994; Grant and Boag, 1980; Trueman and d'Ozouville, 2010). The island of Santa Cruz is characterized by the absence of permanent surface freshwater, because the thin and relative high permeability of the soil layer ($0 - 100$ cm) enhance infiltration, and the water is rapidly drained through the fractured basaltic bedrock (Violette et al., 2014). The humid zone of Santa Cruz Island has suffered from dramatic anthropogenic disturbance (Trueman et al., 2013, 2014). It was originally covered by the endemic *Scalesia* tree (Hamann, 1984; Trueman et al., 2013), but the development of agriculture has been associated with the clearing of the native vegetation which has been replaced by an alternance of secondary forest and pasture that extend over a large area of the windward humid zone (currently known as the "agricultural zone"). Nowadays, the original *Scalesia* forests can only be found in patches of limited extends (Trueman et al., 2014) and the conversion of secondary forest to pasture is increasing.

We identified two sites representative of the contemporary vegetation of the agricultural zone (Fig. 2.19). They have been instrumented with soil, vegetation and weather monitoring: an open area pasture, and a secondary forest. The distance between plots is ca. 70 m, so that similar climatic conditions are expected at both sites. The canopy and soil characteristics of the two sites are presented in Tb. 2.4. At the pasture plot, the dominant species is the *Pennisetum purpureum*. Its leaves are long and cylindrical at the base. These species grow in small groups, increasing the canopy cover. At the base, dead tillers can be found, forming a

Table 2.4: Physical conditions, canopy and soil characteristics at the two study sites.

Parameter	Forest	Pasture
Height [m]	5.45	1.2
Altitude [m a.s.l.]	400	405
Slope	10°	12°
Vegetation type	Secondary forest	Pasture
Dominant species	*Psidium guajava*	*Pennisetum purpureum*
Basal area [m^2/ha]	29.8	-
LAI	4	-
Albedo	0.13[a]	0.23[b]
Canopy gap fraction (p)	30%[c]	-
Soil depth [cm]	44	39
Mean root depth [cm]	40	38
Soil bulk density[*] [g/cm^3]	0.61	0.63
Saturated water content[*]	70%	71%
Hydraulic conductivity[*] [m/s]	1.1×10^{-4}	3.4×10^{-5}

[*] Mean value measured on 6 samples between depths from 7 to 30 cm.
[a] See Pryet et al. (2012a).
[b] Value from Allen et al. (1998).
[c] Value estimated from photographical analysis.

standing dead leaf litter. At the forest plot, the dominant species are the *Psidium guajava*, *Cestrum auriculatum*, and *Cinchona pubescens*. Leaves have generally ovale-ellyptic shapes and are orientated towards the ground. Trunks and branches are generally horizontal with epiphytes and detaching bark pieces. The soil at both sites is similar. It is an andisol that developed from the weathering of the underlying basalts. Soil depth varies from 0.1 m to 1 m with three horizons before bedrock, which mostly consists of permeable fissured basalts.

2.4.3.2 Hydrological monitoring and model implementation

Climatic monitoring was conducted over the pasture plot with a weather station where data was recorded with 15-minutes time intervals using a Campbell CR100 datalogger. Rainfall was measured with a Campbell ARG100 tipping bucket rain gauge placed 1 m above the vegetation. Wind losses and slope corrections were not applied to the recorded rainfall data because of the relative low wind intensity and the negligible correction factor. Wind speed and direction were monitored with a Young WindSentry Kit positioned at 3.4 m above the ground. Solar radiation, relative humidity and temperature were measured at 2 m above the ground, with a Kipp&Zonen SPLite silicone pyranometer and a Campbell CS215 T&RH sensor, respectively. For evident reasons, it was not possible to measure throughfall and stemflow below the pasture. However, throughfall and

stemflow were measured below the forest within a 6 × 6 m plot using the same sampling design reported by Pryet et al. (2012a). Throughfall was collected with troughs draining into a funnel that redirects flow to an automatic tipping bucket rain gauge. Stemflow was collected with collecting spirals on stems that drained into water containers (for detailed information on the sample design see Pryet et al. (2012a)). Spatial representativity of the troughs measurements was assessed with manually read small collectors distributed randomly within the plot (Domínguez Gonzalez, 2011; Pryet et al., 2012a). The estimated sampling error at the 68% confidence level was 8.8% (Pryet et al., 2012a). Most stemflow records are not available for the observed period because of the difficulty to keep continuous monitoring. Nevertheless, stemflow has been shown to constitute less than 1% of total rainfall.

At both sites, tensiometers were installed along vertical profiles between depths of 10 to 45 cm with: weekly manual measurements with SDEC SMS tensiometer probes (five pairs); and automatic UMS T8 tensiometers (two pairs) probes connected to a datalogger with 15-minutes time steps records. The spatial representativity of tension measurements was assessed with tensiometers (manual) at the same depth. At each depth, we used records that were within a distance of one standard deviation from the mean of all tensiometer measurements at the same depth. Soil water suction and throughfall records were not considered in the analysis when measurements showed no representativity due to electronical and/or technical problems. It was observed especially when the funnel that redirects the collected throughfall from the troughs to the tipping bucket was completely filled up (e.g. when heavy rains occurred during the hot season, water spills over from the funnel).

The joint model is implemented using constant canopy and soil parameters during the investigation period (June 2011 to May 2012). As measurements of net precipitation were not available at the pasture plot, a simple drainage function ($D = C - S$) is considered, in which all water stored above S is immediately drained to the soil. This is a fair assumption considering the plant structure organization of the pasture, where the long leaves form a *funnel* shape, that once saturated enhances drainage. At the soil of both plots, considering the interception model and the very permeable basalts underlying the soil, we used as boundary conditions a fixed transient flow at the top (simulated P_{net}) and free drainage at the bottom. In consideration of the soil observations and the relative small physical differences between horizons, the total soil depth simulated was 0.65 m, divided into two layers: a 0.6 m top layer containing roots evenly distributed until 0.4 m depth, and a 0.05 m bottom soil layer (Fig. 2.19). The soil column was discretized into 65 slices (0.01 m each). Except for K_{sat},

we considered the same parameters (θ_r, θ_s, α, n) in the top and bottom simulated soil layers. The values of h_{wp} and h_{fc} (-15 m and -1.03 m), were taken from Van Genuchten (1980), and Armas-Espinel et al. (2003) for volcanic soils, respectively.

The calibration of the canopy parameters (p, S, D_s, b) at the forest is conducted: using a within-event analysis of a set of rainfall storms detailed by Pryet et al. (2012a) for p and S and with the OMWLS between the observed and simulated P_{net} during the whole study period for D_s and b. The soil parameters (K_{sat}, θ_r, θ_s, α, n) and the canopy surface resistance r_s are calibrated using the OMWLS method between the simulated and observed pressure head during a 98-days calibration period (July-October with rainfall of 518 mm). In the case of the pasture, the calibration using the OMWLS method also included the canopy parameters p and S. At both locations, we used the validated observed pressure head at three depths (15, 25, 35 cm).

2.4.3.3 Results

2.4.3.3.1 Meteorological conditions Considering the long term records of the *mid-elevation* weather station located in *Bellavista* (alt. 180 m a.s.l.) (Fig. 2.19), the hydrological year 2011-2012 (June to May) is characterized by relative high temperatures (daily average of 23 °C) and strong rainfall (total height of 1629 mm). Rainfall remained close to the median during the cool season but it was higher than the median during the hot season. During the 366-day observation period at the study site, mean air temperature was 21 °C. Solar radiation remained low (daily average 114 $\mathrm{Wm^{-2}}$) and wind speed was weak (0.9 $\mathrm{ms^{-1}}$). Relative humidity was close to, or at saturation for most part of the period, especially during the cool season. Total rainfall height was 2577 mm. When throughfall data was available (99% of time), total throughfall collected was 1884 mm, and relative throughfall with respect of total rainfall was 87%. Potential evaporation from the forest was 1322 mm, while E_p from the pasture was 960 mm.

2.4.3.3.2 Model calibration Calibrated values of canopy and soil parameters are detailed in table 2.5. Forest canopy parameters p and S were estimated with a linear regression from rainfall events with low relative throughfall (Pryet et al., 2012a). The value of p is in accordance with the value of canopy gap fraction estimated from vertical photographs under the canopy plot (0.29). p, S, D_s and b are relatively close to the values obtained for the same forest by Pryet et al. (2012a) during the 2010-cool season. We attribute the slight differences to a larger set of data used, which included the hot season with heavy rainfall

Table 2.5: Canopy and soil parameters used in the interception and soil water transfer models. p and S are estimated from *within event* analysis, while all other parameters are estimated from calibration using the *Guauss-Levenberg-Marquadt* algorithm. Estimated errors correspond to a 95% of confidence level.

Parameter	Forest	Pasture
p	0.29	0.15 (0.03)
S [mm]	0.62	1.15 (0.15)
D_s [mm s^{-1}]	3.30 (0.12) $\times 10^{-5}$	-
b [mm^{-1}]	2.70 (0.03)	-
r_s [s m^{-1}]	91 (3)	231 (6)
$Ksat_{(t)}$* [m s^{-1}]	9.6 (0.4)$\times 10^{-5}$	8.0 (0.6) $\times 10^{-5}$
$Ksat_{(b)}$* [m s^{-1}]	5.2 (0.4) $\times 10^{-6}$	1.4 (0.14) $\times 10^{-5}$
θ_s	0.70	0.71
θ_r	0.35 (0.01)	0.39 (0.02)
α [m^{-1}]	5.8 (0.1)	8.4 (0.2)
n	1.66 (0.04)	1.56 (0.09)

* (t) and (b) refers to top and bottom soil layer, respectively. The other soil parameters are for both layers.

events. At the forest plot, the interception model satisfactorily simulates net precipitation (only throughfall since stemflow is not considered) during most of the study period (Fig. 2.20). RMSE of simulated net precipitation is 0.12 mm ($n = 9975$). It is estimated between the simulated and available net precipitation disregarding data points where P_{net} was equal to zero simultaneously for both datasets. RMSE is 0.14 mm ($n = 7038$) and 0.23 mm ($n = 2937$) for the cool and hot seasons, respectively. Net precipitation is overestimated by 3.8% over the calibrated period. During the cool season, P_{net} is underestimated by 1.7%, while it is overestimated by 8.5% during the hot season. At the pasture, the calibrated values of parameter p and S are 0.15 and 1.15 mm, respectively.

Soil parameters and the canopy parameter r_s were estimated from a representative period of 98 days during the cool season. Despite the wet conditions that prevailed during this season, this period also included several days of drought where dry conditions were observed. Estimated r_s are 91 and 231 sm^{-1} for the forest and pasture, respectively. As expected for these vegetations, r_s at the pasture is significantly higher than r_s at the forest. Estimated soil parameters are similar at both locations, except for α and the lower layer K_{sat}.

The simulated pressure heads are in agreement with the observations during humid and dry conditions at both locations for the entire study period. In figure 2.21 we present the observed and simulated pressure heads for a representative period of each season. At a depth of 25 cm, where we have the larger set of observations, the range of pressure head for the whole study period is $(-341, -14)$

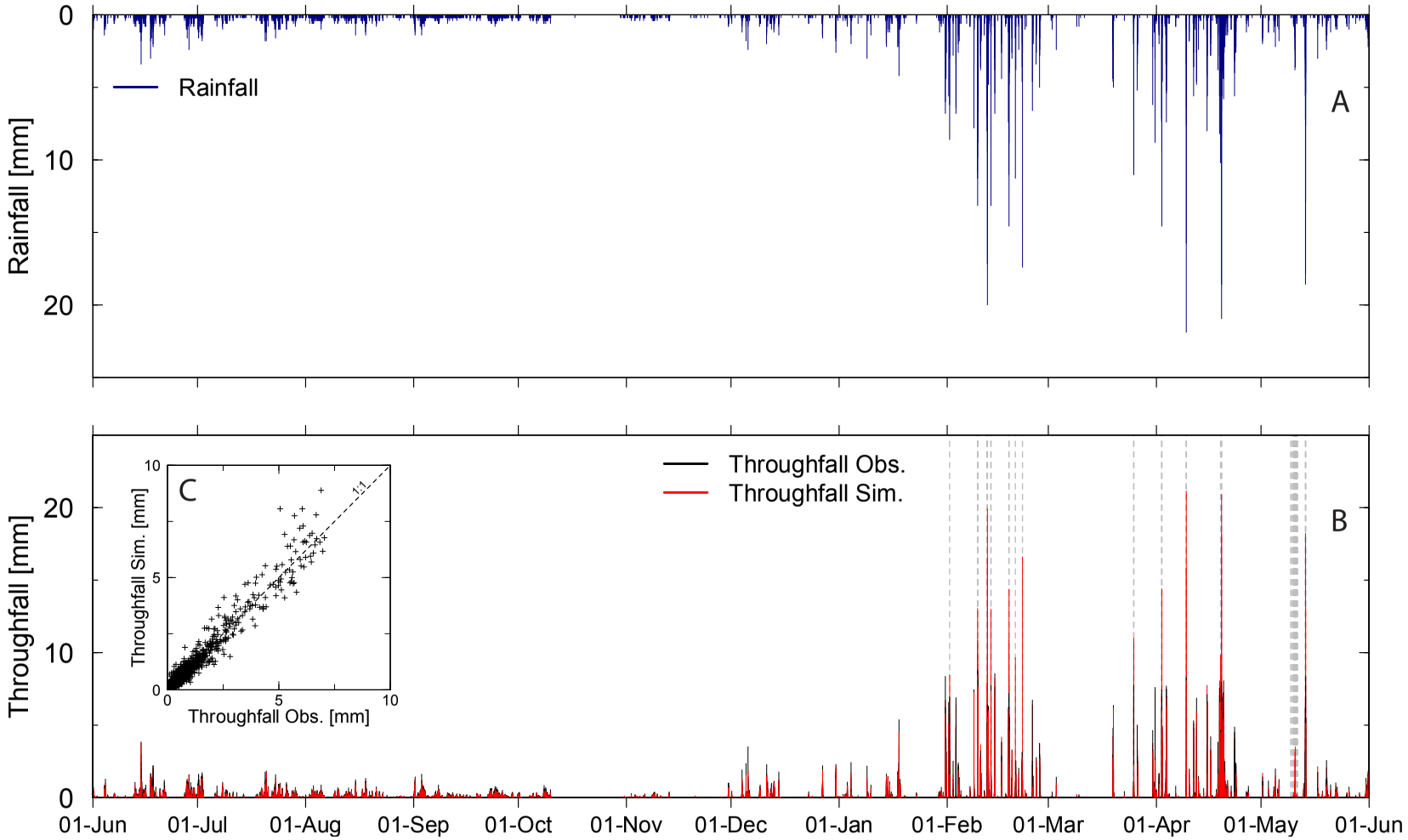

Figure 2.20: Results from the interception model at 15 minutes time step during the study period at the forest. (A) is the incident rainfall. (B) is the observed and simulated throughfall along the hydrological year. Dashed lines in gray indicate data gaps in throughfall monitoring. (C) is the comparison between observed and simulated throughfall.

Table 2.6: Cumulated water balance variables at the forest and pasture plots during the hydrological year 2011-2012. Estimated errors correspond to a 95% of confidence level.

Variable	Forest	Pasture
Rainfall RF [mm]	2577	2577
Potential evaporation E_p [mm]	1322	960
Actual evaporation E_a [mm]	220 (7.8)	263 (9.4)
Potential transpiration T_p* [mm]	516	398
Actual transpiration T_a [mm]	280 (11.7)	230 (13.1)
Deep percolation DP [mm]	2077 (19.1)	2084 (13.6)

* The reduction of transpiration is due to coditions of wet canopy (93%) and soil water stress (7%).

cm at the forest, and $(-458, -7)$ cm at the pasture. At this depth, RMSE was 8.1 cm ($n = 27313$) at the forest, and 6.9 cm at the pasture ($n = 29677$).

2.4.3.3.3 Water balance Cumulated values of soil and canopy water balance highlight negligible runoff (Tb. 2.6). Simulated runoff is always zero on both locations during the entire period because the soil water input is never above the infiltration capacity of the upper soil layer, even during the heavy rainfall events during the hot season. Actual evaporation is 220 mm at the forest, and 263 mm at the pasture. The estimated potential transpiration is 516 mm and 398 mm at the forest and pasture, respectively. Transpiration is markedly reduced from its potential due to the long periods when the canopy was saturated or partially saturated. In contrast, transpiration is barely reduced from soil water stress conditions (less than 5% approximately on both locations). Estimated T_a is 280 mm and 230 mm at the forest and pasture, respectively. Considering actual evapotranspiration (ETa) as the sum of E_a and T_a, then estimated ETa is similar at both locations: 500 mm at the forest and 493 mm at the pasture. Mean daily ETa is 1.37 mm at the forest and 1.35 mm at the pasture. Deep percolation was estimated from the free drainage boundary condition, as the flux at the bottom of the soil profile. Cumulated values of deep percolation are very similar at both locations: 2077 mm at the forest plot, and 2084 mm at the pasture plot (Fig. 2.22). At both locations, a major proportion (64%) of cumulated deep percolation occurs during the hot season. In both of the study plots, cumulated deep percolation notably increases after five days of intense rainfall (Fig. 2.22). Median daily deep percolation is 2.2 mm at the forest, and 2.3 mm at the pasture. Despite the uncertainty in the estimation of the parameters, the confidence intervals of the predicted water balance variables are relatively low according to the linear analysis (Tb. 2.6).

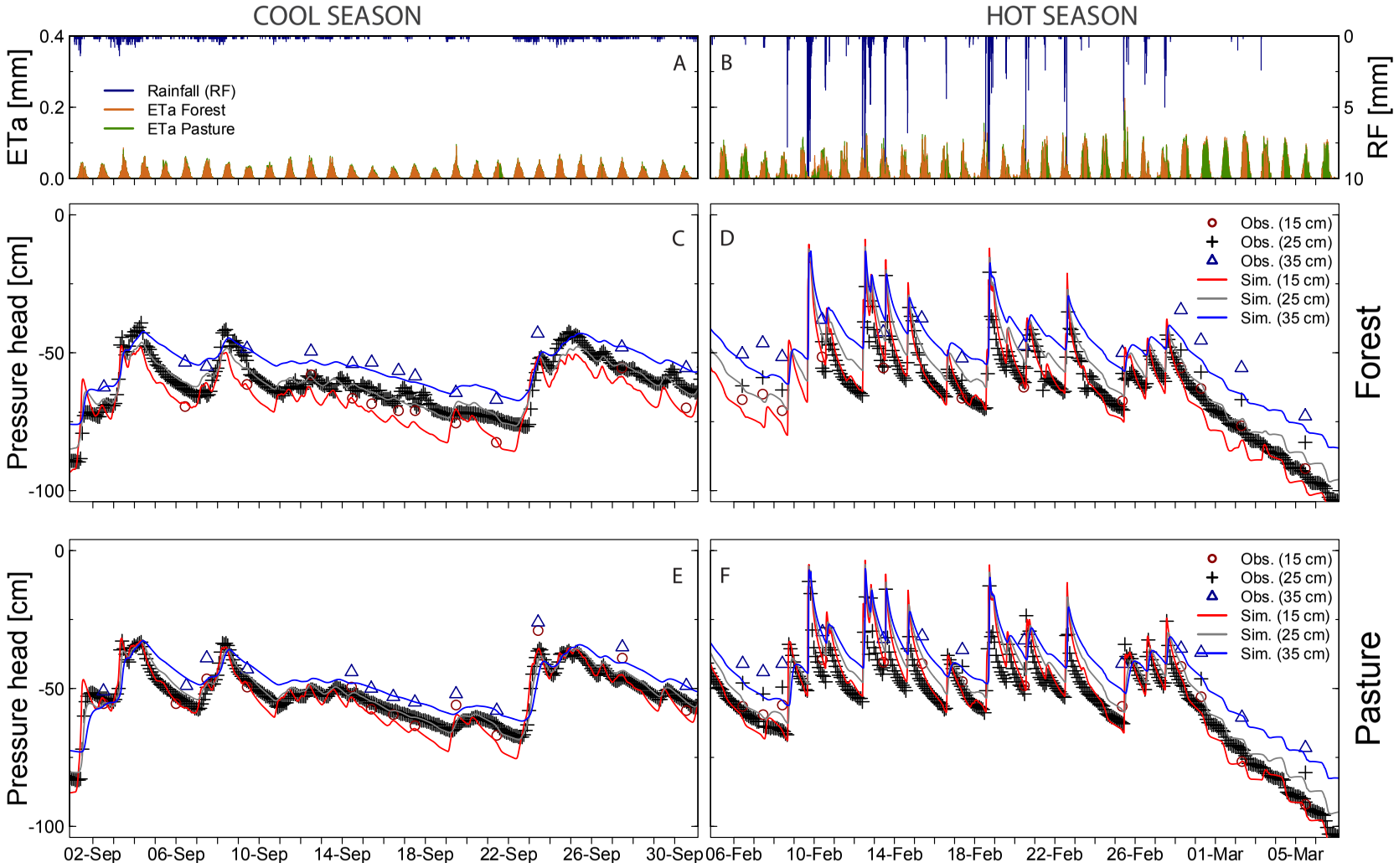

Figure 2.21: Results from the joint model at 15 minutes time step during 30 days representative of the cool (left) and hot seasons (right), respectively. (A, B) Water balance variables: incident rainfall (RF) and estimated actual evapotranspiration (ETa). (C, D, E, F) Observed and simulated pressure heads at the forest (C, D) and pasture (E, F). Observed pressure head are from both automatic (depth: 25 cm) and manual (depth: 15 and 35 cm) probes at the soil.

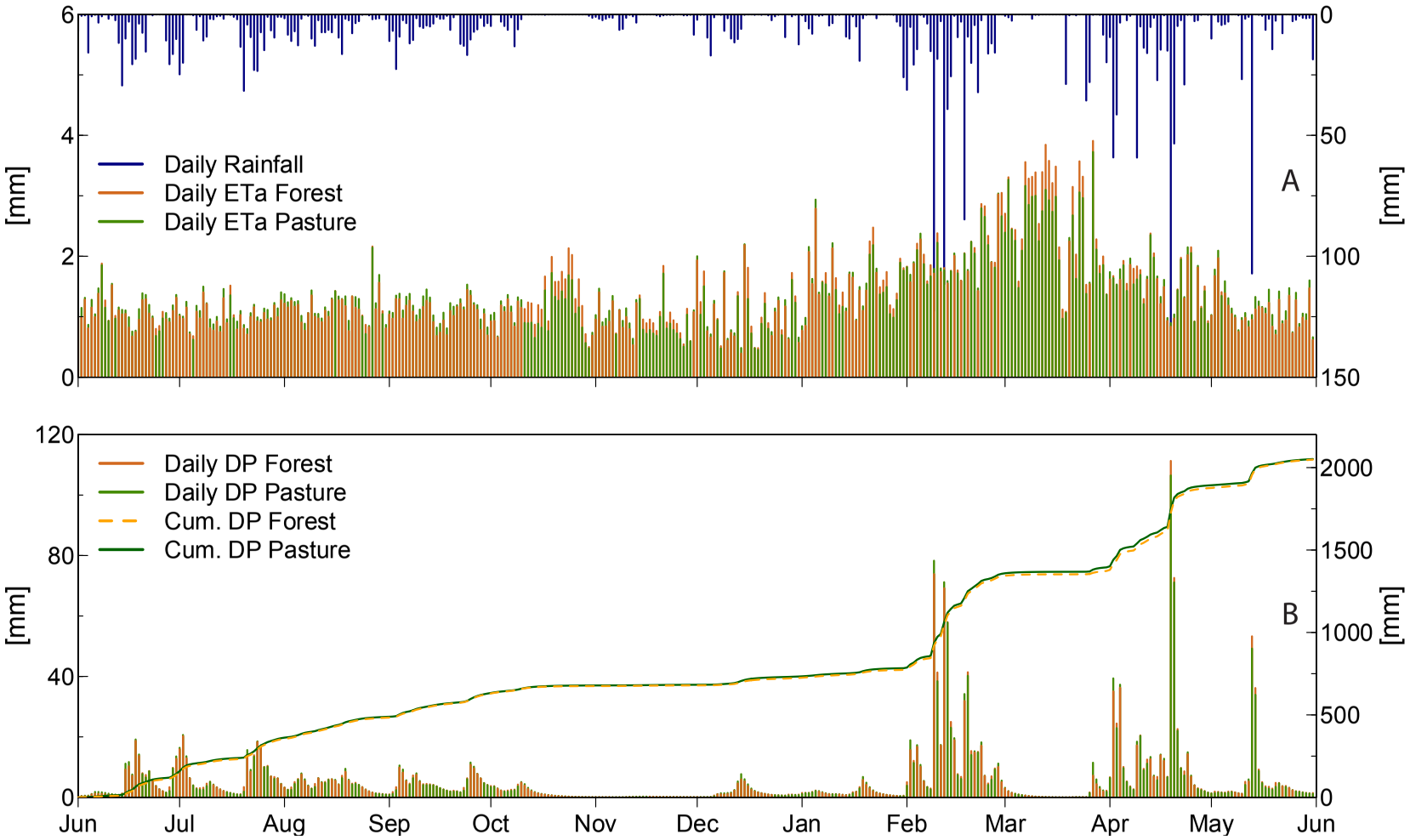

Figure 2.22: (A) Daily rainfall and actual evapotranspiration (ETa) at the forest and pasture along the hydrological year (June 2011 - May 2012). (B) Daily (bars) and cumulative (lines) deep percolation (DP) at the pasture and forest.

2.4.3.3.4 Comparison of soil hydrodynamics In order to observe the effects of the atmospheric conditions on the soil hydrodynamics under both land covers, we have taken one typical rainfall event per season. In figure 2.23 we show the pressure head profile of both events. It can be seen that soil hydrodynamic behavior is relatively similar at both sites. During the cool season, the pressure head profile presents slight variations because of the low intensity of rainfall events. The effect of the slow infiltration is only visible in the upper part of the profile while it is negligible in the lower part, as it remains nearly constant. This behavior is constantly reproduced throughout this season as a consequence of the permanent wet conditions. On the opposite, the high intensity rainfall events of the hot season strongly disturb the pressure head profile including its lower section. The disturbance can be seen soon after the storm event, suggesting a fast infiltration on both soils under these conditions. Throughout the hot season, the pressure head profiles have stronger fluctuations due to the alternations between heavy rainfall events and high atmosphere evaporative demand. During the study period, the soils remain relatively near saturation for most of the time under the forest and pasture, except for two dry periods (12% of the total study period).

Comparing the pressure head profiles under the two land covers, soil at the forest remains dryer than at the pasture at both seasons (Fig. 2.23). This is observed moslty during wet canopy conditions in which transpiration has a negligable effect on the soil. The profile of the forest is affected faster than the one of the pasture at deeper levels. This occurs because the hydraulic conductivity of the soil at the forest is higher than the pasture, thus promoting a relative faster infiltration. The soil at the pasture is the most sensitive to the variability of the atmospheric boundary conditions, especially near the surface. Low intensity rainfall events produce more distinctive changes in the pressure head profiles near the surface. But this effect is more apparent during dry conditions, when the effect of transpiration is marked in the soil and the drainage is negligible. Under these conditions, given that the soil water storage capacity at the pasture is smaller than at the forest ($\theta_s - \theta_r$ is 0.32 and 0.35 at the pasture and forest respectively), and water removed by plants at both locations may somehow be comparable; small changes in the soil water content lead to large changes in the pressure head, therefore the pressure head will decrease more rapidly at the pasture. We associate the faster infiltration capacity of the soil at the forest, as the main cause to have lower pressure heads compared to the pasture and not its higher transpiration. However, during long periods of stress conditions, pressure heads at the pasture can be lower than the forest because of its smaller water storage capacity.

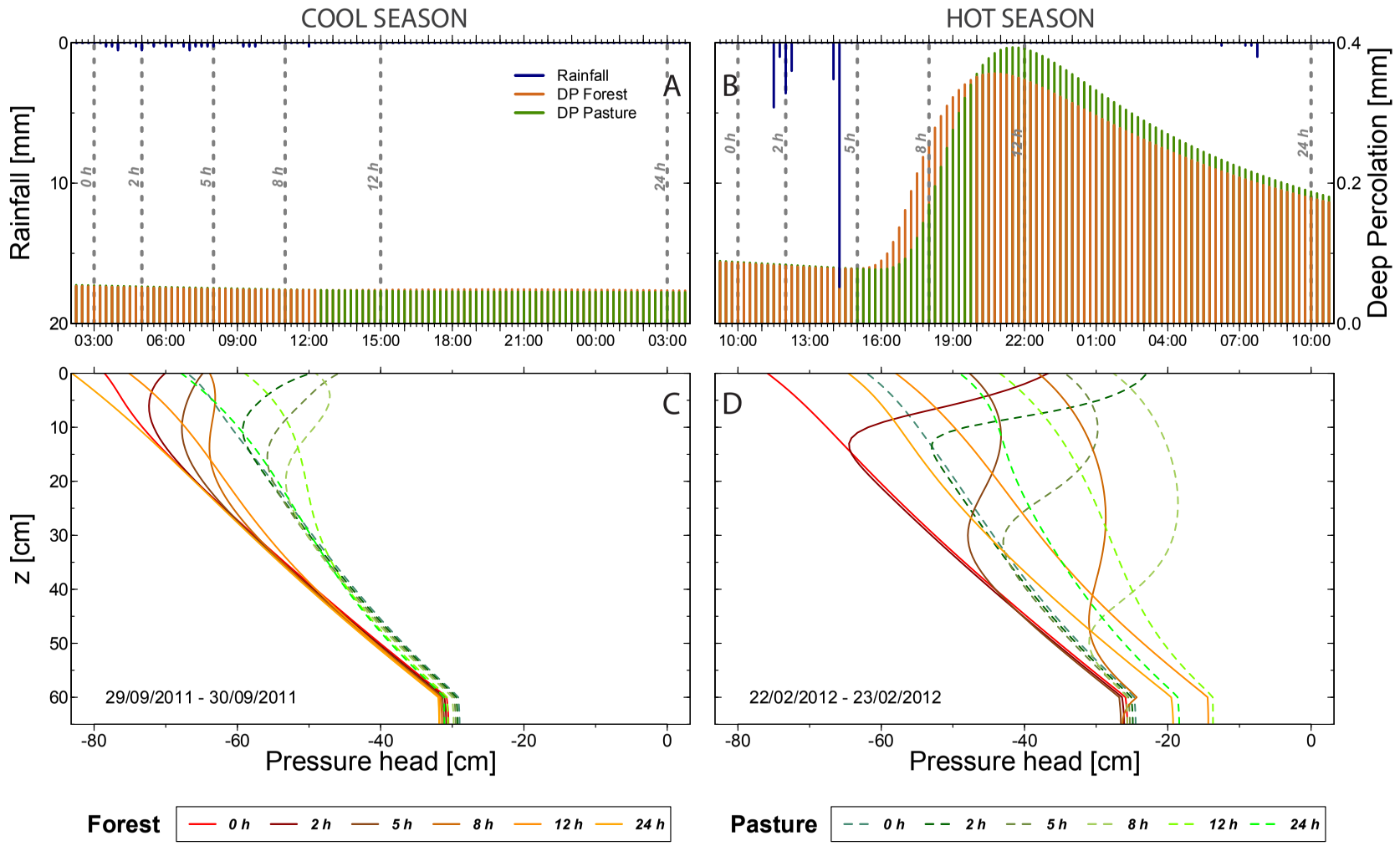

Figure 2.23: Deep percolation (DP) and pressure head profiles before, during and after a rainfall event at the forest and pasture. (A,C) correspond to a typical rainfall event of the cool season (4.2 mm). (B,D) correspond to a typical rainfall event of the hot season (31.2 mm). Solid and dashed lines correspond to forest and pasture, respectively.

2.4.4 Discussion

2.4.4.1 Uncertainties in the evaporation estimates

Predicted net precipitation obtained from the interception model is overestimated at the forest by 3.8% over the calibration period. However, this apparent underestimation of the simulated canopy interception might be attributed to an error in its observed value, inferred from net precipitation measurements. Throughfall patterns have been shown to present a substantial spatial and temporal variability related to the canopy structure, rainfall intensity and seasonality (Staelens et al., 2006; Ziegler et al., 2009; Zimmermann et al., 2009). Zimmermann and Zimmermann (2014) conducted sampling experiments using simulated fields and reported that depending on the sampling strategy adapted, errors in the mean throughfall estimates can be significantly large. Pryet et al. (2012a) estimated a sampling error of 8.8% during the 2010-cool season at the same forest plot. In our case, we are not free from these types of errors and we have direct evidences of splash losses on the troughs and water spilling out of the collecting funnel in some ocassions when rainfall was intense. These effects alone could easily explain the misfit between observed and simulated values.

The underestimation of wet canopy evaporation can also be associated to several factors, measurement errors (e.g. overestimation of relative humidity with permittivity sensors (Frumau et al., 2006; Holwerda et al., 2010; Pryet et al., 2012a)), overestimation of the aerodynamic resistance (discussed in Limousin et al. (2008) and reported by Holwerda et al. (2012)), processes not considered in the P-M equation (effect of advection of the warm air from the nearby ocean (Scatena, 1990; Schellekens et al., 1999; van Dijk and Bruijnzeel, 2001) or heat released upon the condensation of the water vapor above the vegetation canopy (Holwerda et al., 2010; Schellekens et al., 1999)) or processes not considered in the interception model (evaporation of splash droplets produced on the canopy, especially during heavy storms (Dunkerley, 2009; Murakami, 2007; Saito et al., 2013)). Given the instrumentation used and the purpose of this study, to consider the actual significance of these factors is challenging and of limited interest. Even if these factors have an effect on the calculation of net precipitation, they would contribute similarly in both land covers, and would not change our conclusions.

Moreover, if there are uncertainties on the evaporation estimates, the total value of deep percolation, which constitutes the main result of this study, will show a marginal variation because deep percolation is controlled mainly by the rainfall and evaporation has a much smaller contribution.

2.4.4.2 Canopy and soil parameters

Calibrated canopy and soil parameter values are within the range found in the literature. The canopy parameters estimated at the forest are related to its single-storey tree architecture and its sparse understory vegetation (see Pryet et al. (2012a) for a wider discussion on these parameters). At the pasture, the estimated value of p agrees with dense vegetation, and the relative high value of S may be related to the storage capacity of litter. Domingo et al. (1998) estimated p of 0.1 from photographical analysis and S of 2.44 mm for a 1.5 m perennial tussock grass. The same authors also related the higher canopy capacity found at the tussock grass to the rigid mat of leaf litter at its base. Complementary to that, Guevara-Escobar et al. (2007) found S in the range of 0.3 and 0.7 mm for litter from a lodged tall grass. The estimated values of surface resistance at both locations are also in the range of values encountered in the literature (Adams et al., 1991; Brauman et al., 2012; Gavin and Agnew, 2000; Kelliher et al., 1995; Körner, 1995). Estimated r_s at the pasture is relative close to the mean daily r_s of 200 sm^{-1} in a short grass steppe and 175 sm^{-1} in a tussock grass found by Parton et al. (1981) and Campbell (1989), respectively. At the forest, the value is similar to r_s of 77 sm^{-1} in an Amazonian tropical rainforest found by Shuttleworth (1988).

Soil at both locations present relative high values of K_{sat} and α, and low values of n. These parameter values are classical for andisols (Armas-Espinel et al., 2003; Fontes et al., 2004). Calibrated K_{sat} values on all layers, are found within the range of K_{sat} reported by Adelinet et al. (2007) at similar altitudes on this island. Soils seem to present sandy behavior when they reach near saturation conditions and large water holding when they are under water stress conditions. This behavior is reported by El-Swaify, S. (1980) in andisols, and has been described in soils of: Hawaii (Warkentin and Maeda, 1980), Tenerife (Armas-Espinel et al., 2003), and Japan (Hamamoto et al., 2008).

2.4.4.3 Driving factors for the similar deep percolation rates between forest and pasture

Our results show that deep percolation rates were similar at a pasture and a forest plot because of the similar evapotranspiration rates for both land covers. Similar values of evapotranspiration between forest and grass have been reported in wet regions (Brauman et al., 2012; Kelliher et al., 1993, 1995). Kelliher et al. (1995) found close values of the maximum rates of ETp and median daily ETp between pasture and coniferous forest. Brauman et al. (2012) found that in Hawaii, the mean daily ETp was higher in the pasture than over a mature en-

demic forest, and attributed this difference to the low relative contribution of stomatally-controlled evapotranspiration compared to the radiation-controlled evapotranspiration when low vapor pressure deficit (VPD) and low wind conditions are present. Similar conditions are observed in our study site, especially during the wet cool season. However dry periods are also observed. In these cases VPD is high, and the vegetation with the lower r_s will enhance the contribution of the VPD term in the P-M equation. As a consequence, the transpiration rates are more contrasting. Under these conditions, potential transpiration of the forest is significantly higher than in the pasture (when $RH < 90\%$, $T_{p\ forest}/T_{p\ pasture} = 1.39$; when $90\% \leq RH < 100\%$, $T_{p\ forest}/T_{p\ pasture} = 1.20$ and when $RH = 100\%$, $T_{p\ forest}/T_{p\ pasture} = 1.08$). In constrast to Brauman et al. (2012), potential transpiration is also higher at the forest when VPD is low. On both of our study plots, the radiation term of the P-M equation is the most influential, but the difference in the aerodynamic resistance are not as contrasting as the difference between pasture and forest reported by Brauman et al. (2012). Thus, at both vegetations, the influence of r_a is relatively similar on the P-M equation, so transpiration on the pasture does not become larger than the one on the forest. Even though, estimated ETa is similar at both plots, there are contrasting evaporation and transpiration rates. The ratio between actual transpiration and actual evaporation is 1.27 and 0.87 at the forest and pasture, respectively. Those differences can be related to the differences in the canopy structure and the surface resistance.

Estimated E_a is higher at the pasture than at the forest, despite the fact that E_p at the pasture is 38% lower. The canopy storage capacity (C_{max}) at the pasture is considered to be equal to the adherent canopy capacity, thus water is instantly drained above S. At the forest, C depends on the rainfall intensity and can be much larger than S (estimated C_{max} is 2.9 mm). When C is above S, in the absence of rainfall, due to the canopy fast drainage, C is rapidly reduced until it reaches S. A slight difference is observed between the time the canopy was completely saturated between both sites (21% of the time during the study period at the forest and 18% at the pasture). While, C is either completely or partially saturated during 64% and 74% of time at the forest and the pasture, respectively. Thus, the larger range of C at the forest seems to have a small effect on the difference of net precipitation between both sites, which justifies the absence of a drainage function at the pasture. Then, the fact that the amount of E_a is higher at the pasture than at the forest is related to its larger adherent canopy capacity and its larger canopy cover. The difference in the canopy saturation has also an effect over T_a. At the pasture, transpiration occurs more recurrently because more water is necessary to saturate the canopy

and the transpiration can occur immediately after rainfall ceases. Nevertheless, total T_a is higher at the forest because the T_p rate is higher, and a considerable part of the total transpiration occurs when the canopy is barely or completely dry. In this case, T_a reaches T_p and the difference of the transpiration rate between both land covers is more contrasted.

At the soil compartment, the lower layer is less permeable than the upper layer at both plots. As a consequence, the infiltration is slower and the upper soil layer water storage is extended, thus more water may be available for the vegetation demand. At the forest, the soil is slightly more permeable than the soil at the pasture, which agrees with the observations and the properties of the samples taken at these sites. The slightly high permeability at the forest could be associated to the effect of bioturbation (Wilkinson et al., 2009; Zimmermann et al., 2010). Neris et al. (2012) reported higher infiltration rates on andisols under a green forest than andisol under herbaceous vegetation and related this difference to the vulnerability of this type of soils to land use modifications.

The soil hydraulic properties seem to have a small effect over the cumulated deep percolation along the year under both land covers. When the soil parameters at the forest are used in the pasture and vice versa, the difference of cumulated deep percolation is less than 0.1% compared to the original values. Because the soils are in or close to optimal moisture conditions during the study period, evapotranspiration is mainly affected by the meteorological conditions and the canopy characteristics, not by water stress (Eq. 2.11). The soil characteristics may have an influence over deep percolation rates with longer droughts when soils reach very dry conditions. Indeed, the reduction of transpiration under stress conditions depends on the available water storage of each soil.

2.4.4.4 Relevance of the methodology

The proposed methodology is established on physically based models with parameter and simulated values that can be confronted to real observations. It can be applied either on a single study plot so as to provide an estimate of e.g. deep percolation or in a comparative study, where several canopy covers are investigated. In the latter case, if land use change is the topic of interest, then the land covers investigated should be the original and future states.

The methodology applied on the forest and pasture plots of Santa Cruz Island has not only shown to succesfully simulate the observed pressure heads and quantify deep percolation, evaporation and transpiration fluxes, but considering the extensive information offered by the model; this methodology is also an analysis tool to explain the differences or similarities of the components involved in the water balance between the two land covers. This information allows to

evaluate the conditions in which deep percolation is affected by each land cover, hence it has a practical use for conservation and water management policies (e.g. a change in the ratio between pasture and forest may have a limited effect on the regional grondwater recharge).

In this case study, it could be possible to apply other simple approaches, such as a simple conceptual reservoir models. However, they can only provide the quantification of the water balance variables and their simulations could not be validated given that only pressure head measurements are available. Because the potential uncertainty in the soil water retention curve can lead to uncertainties in the deep percolation fluxes, water content or bottom flux measurements should be required on these cases. Ritter et al. (2004) reported that uncertainties on the estimation of the soil hydraulic parameters by inverse optimization can be significant if the number of observations are limited. In our case, despite the uncertainty on some of the parameters, we show by linear analysis, that only a limited set of observations of pressure head appears to be sufficient to constrain the predicted value and that these uncertainties have a small effect on the percolation fluxes. Thus, in terms of cost and efforts, this methodology is also convenient as it does not rely on soil water content monitoring, which is expensive and might not be reliable if properly calibrated.

2.4.5 Conclusions

We have developed a methodology to compare deep percolation rates below contrasting land covers using a physically-based joint canopy and soil model. In addition, we describe the appropriate monitoring design necessary for the acquisition of observed field values. We use a Rutter-type canopy interception model to partition evaporation and transpiration. A 1-D variably saturated flow model is used to estimate deep percolation and actual transpiration. The methodology requires the acquisition of input and calibration datasets. They consists in continuous records of meteorological variables, sampling of throughfall and measurements of soil water pressure.

This model has been implemented for two representative land covers of the humid zone of Santa Cruz Island in the Galapagos Archipelago: a secondary forest and a pasture. At both land covers, the model successfully simulates the observed pressure head during the majority of the study period; and the calibrated canopy and soil parameters are within the range of values reported in the literature. Results show that evaporation and transpiration rates are contrasting but result in similar deep percolation rates below the forest and pasture. As expected, the potential evaporation and transpiration rates are higher at the forest than at the pasture. However, the actual evaporation at the

pasture is higher, increasing the pasture overall actual evapotranspiration and reaching the value obtained in the forest. This can be explained with the pasture canopy characteristics that enhance evaporation with respect to the forest. In both land covers, deep percolation reaches ca. 2080 mm which corresponds to 80% of the incoming rainfall. Differences in the soil parameters between the two sites influence soil hydrodynamics, but have small effect over the total deep percolation.

The estimation of groundwater recharge is challenging when there are alterations on land use. Understanding the combined role of vegetation and soil is necessary to assess the impact of land use change over deep percolation. This study provides a cost-effective methodology that not only quantifies the components of the canopy and soil water budget, but also identifies the influence of soil and canopy characteristics of contrasting land covers. On this case study, we determinate that under the current conditions, land use change is likely to have no or limited effect over deep percolation. However, we identified the conditions under which land cover may have a major impact on the groundwater recharge.

Acknowledgement

This study has been conducted in the frame of the project *Galapagos Islands Integrated Water Studies* (GIIWS). The GIIWS team would like to thank the *Agence Nationale de la Recherche* (ANR-blanc 2010 GIIWS Ref. 601-01) and *Galapagos Conservancy* for fundings. Christian Domínguez participation was supported by a PhD Scholarship from the Ecuadorian Government through the *Secretaría Nacional de Educación Superior, Ciencia y Tecnología* (SENESCYT). We also want to thank our local partners in the Galapagos: the Charles Darwin Research Station, the Galapagos National Park, and private land owners who allowed the installation of weather stations. Finally, we thank for the valuable comments by Steffi Knoblauch and another anonymous reviewer. This publication is contribution number 2113 of the Charles Darwin Foundation for the Galapagos Islands.

Conclusions

The new DEM of 10 m of horizontal resolution allowed the definition of watersheds and the extraction of the drainage network on the windward side of San Cristobal. It was complemented with field work, which included springs and stream survey, to have a water resources map of this zone. One of the springs of *Cerro Gato* watershed was defined as a contact spring, in which water outcrops through fractured unweathered basalt above a brow clayed material that acts like a sustainable layer.

The study zone is located in *Cerro Gato* and surrounding watersheds. In this zone, an hydrological network was installed to estimate the inputs and outputs variables of the water balance. The network includes three weather stations at different altitudes along the windward side (30, 300 and 600 m a.s.l.). Station at the highlands includes throughfall and stemflow monitoring. Soil monitoring is performed at mid and high elevations. The network is complemented with streamflow monitoring with three sections of control in three watersheds: one at the highlands (*El Bayo*) and two at mid elevation (*Chuki Marka* and *Cerro Gato*).

A methodology to compare deep percolation rates below contrasting land covers using a physically-based joint canopy and soil water transfer model was presented. This is a cost-effective methodology that not only quantifies the components of the canopy and soil water budget, but also identifies the influence of soil and canopy characteristics of contrasting land covers. This methodology will be complemented with fog interception estimations to estimate groundwater recharge rates in the study zone.

Chapter 3

Climatic monitoring and recharge processes

Introduction

This chapter, **Climatic monitoring and recharge processes**, is about an important factor in hydrology and hydrogeology, which is the water input to the system.

Similar to other islands, Galapagos climate is affected by seasonality. Rainfall distribution is affected by a positive gradient related to altitude, while evapotranspiration estimations are still missing. Moreover, the semi-permanent presence of fog at the highlands leads to an additional water input.

From several methods to estimate groundwater recharge, given the context of this study, a soil water budget is the most promising because it can be used for any spatial scale and any time period.

In this chapter, we intend to estimate recharge from plot to a watershed scale using a soil water budget approach, in which fog interception is considered. Estimations of actual evapotranspiration are improved from a soil water transfer model.

This chapter is organized as follows.

- In section *Monitoring*, the representativy of the hydrological years of monitoring during this study is analyzed using the inter-annual long-term records of a historic station. Results from the climatic monitoring of the stations along the windward side of the island are shown. Then, a first estimation of the rainfall and evapotranspiration gradients are presented.

- In section *Quantification of cloud water interception at the windward slope highlands of San Cristobal Island*, a method to estimate fog interception by

the vegetation from climatic monitoring based in a canopy water balance is proposed.

- Section *Analysis of soil water transfer along the windward slope of San Cristobal* deals with the estimation of deep percolation using a physically based soil water transfer model. In the forest, in which fog interception was estimated, the soil model is combined with the canopy model. At the end, a water balance at plot scale is presented and discussed.

- In section *Spatialization of recharge/deep percolation at watershed scale*, a spatialization of results of the former section is presented and discussed.

3.1 Climatic monitoring

3.1.1 Hydrological years 2013-2014 and 2014-2015

Climate variables are being monitored during several decades by two weather stations located in the two main islands: i) weather station operated by the *Charles Darwin Foundation* (CDF) at the coast of Puerto Ayora in Santa Cruz Island (alt. 6 m a.s.l.) with continuous records since 1965, and ii) weather station operated by the *Instituto Nacional de Meteorología e Hidrología* (INAMHI) at the coast of Puerto Baquerizo Moreno in San Cristobal Island (alt. 10 m a.s.l.) with discontinuous records since 1951. Despite data from station operated by the INAMHI would be more suitable for this study on San Cristobal Island, unfortunately it was not provided by them or any other national institution. For this reason, we only use data from the weather station operated by CDF. However, we expect similar conditions given the proximity between islands (at least to compare the years of study with the long term records).

Given the long term records, the median annual rainfall (from June to May) is 278 mm and the average air temperature is 24 °C at the coast of Santa Cruz Island (Fig. 3.1). The hydrological year 2013-2014 can be characterized as an average year in terms of rainfall (234 mm) and temperature (24.1 °C). However, year 2014-2015 could be consider a wet and hot year. Cumulative rainfall reaches 484 mm, which locate this year near the top quantile. While in terms of temperature it reaches the top octile (25.1 °C). Hot years are trending in the last 10 years, with 8 out of 10 above the average, in which half of them are located in the top quantile. Seasonally, rainfall in both years are near the median during the cool season (from June to December) (57 mm and 71 mm in the first and second year, respectively), while the second hot season (from January to May) is the one with high rainfall (413 mm). Average temperature is high in both hot seasons, while during the cool season it is low and high for the first and second year, respectively. Therefore, in both years the cool seasons are average, whereas the first hot season is near average and the second is relative wet.

Despite several indicators showed that El Niño event should be marked in the last years (Ludescher et al., 2014; Min et al., 2015; Song et al., 2015), the annual rainfall measured in the two last years from this station, show that the absence of El Niño event in Galapagos (Fig. 1.4). Nevertheless, El Niño event is a fact in the hydrological year 2015-2016 (Song et al., 2015), which presents an opportunity to assess its effect in Galapagos with the current hydrological monitoring network of the *GIIWS* team (unfortunately, not part of this thesis).

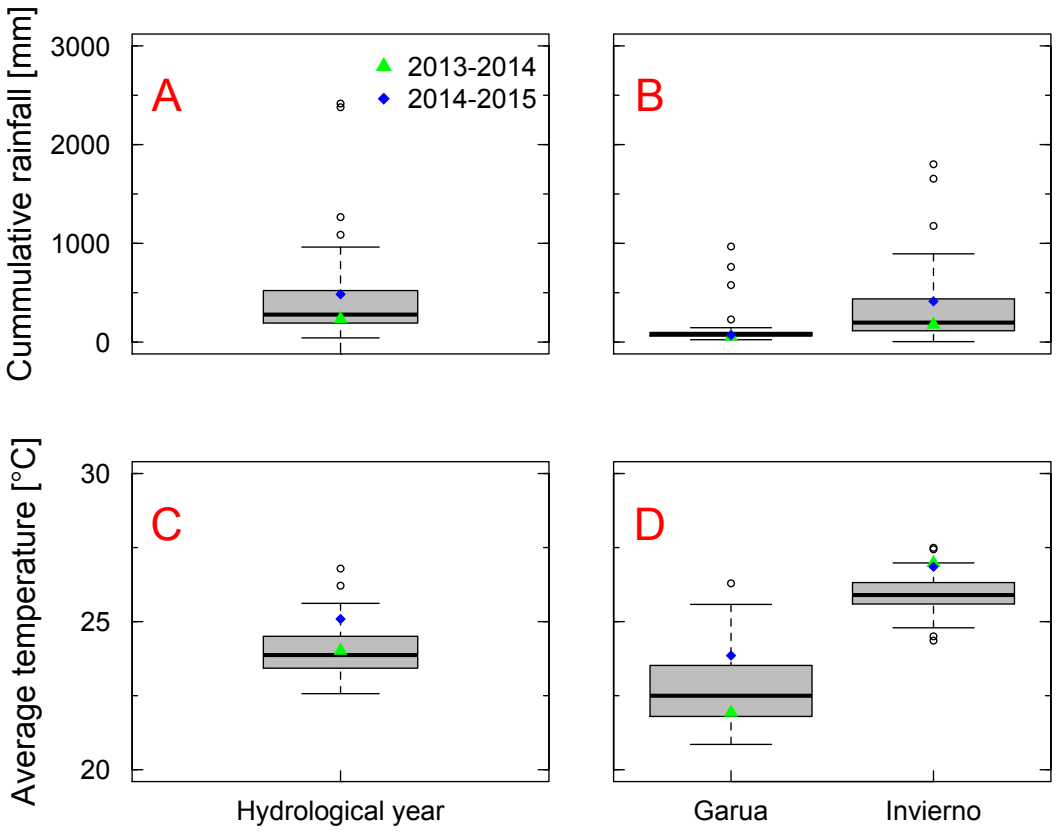

Figure 3.1: Boxplots of rainfall and temperature from the long-term record of the weather station operated by the CDF (6 m a.s.l.) at Puerto Ayora in Santa Cruz Island. (a) and (c) are the cumulative annual rainfall and mean annual air temperature form June to May, respectively. (b) and (d) are seasonal rainfall and air temperature Garua from June to December and Invierno from January to May, respectively. Color dots represent the hydrological years of study.

3.1.2 San Cristobal climatic records

3.1.2.1 Monitoring

After the quality check of all records from the three monitored weather stations set up on the experimental site, less than 6% of the data was discarded due to missing information or poor quality. In fact, most of the climatic records are complete (section A 2). Most of loss data belong to throughfall measurements, but it is understandable since its continuous acquisition is challenging. The short data gaps were filled with a linear interpolation (except for throughfall, which would require an improved approach); no loss in statistical accuracy is expected on the final results. Using the data from the hydrological years 2013-2014 and 2014-2015, a summary of the climatic conditions is shown in table 3.1 and monthly comparisons between stations on figure 3.2.

The orographic effect and seasonality are marked on the temperature and rainfall. Rainfall is significantly lower at SC000 comparing to SC300 and SC600 in all seasons. Rainfall between SC300 and SC600 do not have a clear pattern. There is a marked difference on some months while it is similar in others. However, it seems that rainfall is similar in the wet months of the cool season (August, September and October). During the hot seasons, the difference is more noticeable. May of both years have the highest rainfall height, especially on May 2015 (561 and 853 mm reported in stations SC300 and SC600, respectively).

Temperature follows a stable orographic gradient between the three stations, except during the wet months of the cool season, in which temperature in SC000 do not follow the tendency of the other two stations and remain higher. It seems that during the wet months of the cool season, conditions are similar from midland to the highlands, while conditions are more contrasted with the coast.

During the cool season, as expected, relative humidity was close to/or at saturation on the highlands and even at mid-elevation. While solar radiation and wind direction was similar at SC300 and SC600, wind speed was significantly higher at SC600. At each season, there is not significant difference between years, except for rainfall and temperature.

From the available records below the canopy, throughfall was recorded during 265 rainfall events. Throughfall was constantly higher than rainfall during both cool seasons, and lower than rainfall during both hot seasons (Fig. 3.3). As a consequence of the presence of fog during the cool seasons, it seems there is an additional input of cloud water interception by the vegetation. This is a phenomenon widely reported in the literature (Hutley et al., 1997; Holwerda et al., 2006; McJannet et al., 2007; Holwerda et al., 2010; Uehara and Kume, 2012; Bruijnzeel et al., 2011; Giambelluca et al., 2011), and that has been already

Table 3.1: Daily summary of the weather variables at the three stations (30, 300 and 600 m a.s.l.) placed along the windward side of San Cristobal during the two hydrological years of study.

Variable	SC000	SC300	SC600
Rainfall[a] [mm]			
2013-2014	258 (31)	1084 (36)	1762 (68)
2014-2015	405 (41)	1927 (170)	2756 (131)
Temperature[b]			
2013-2014	23.0 (21.3-25.8)	20.4 (19.0-23.0)	18.6 (17.5-20.5)
2014-2015	23.6 (22.0-26.1)	21.6 (20.2-24.1)	19.8 (21.8-18.7)
Solar Radiation[c] [W/m^2]			
2013-2014	-	129 (116-154)	128 (118-151)
2014-2015	-	121 (108-156)	113 (100-135)
Relative Humidity[d] [%]			
2013-2014	-	97.7 (176)	99 (269)
2014-2015	-	98.1 (199)	99 (269)
Wind speed[c] [m/s]			
2013-2014	-	1.3 (1.1-1.5)	2.9 (2.4-3.3)
2014-2015	-	1.2 (1.0-1.4)	2.7 (2.2-3.3)
Wind direction[c] [°]			
2013-2014	-	185 (147-212)	200 (184-214)
2014-2015	-	178 (145-204)	197 (182-210)

[a] Annual *rainfall*. In parenthesis maximum daily value.

[b] Mean daily *temperature*. In parenthesis: daily mean minimum and maximum *temperature*.

[c] Mean daily value. In parenthesis: first and third quantile.

[d] Mean daily value. Numbers of days in which *Relative humidity* > *99%*.

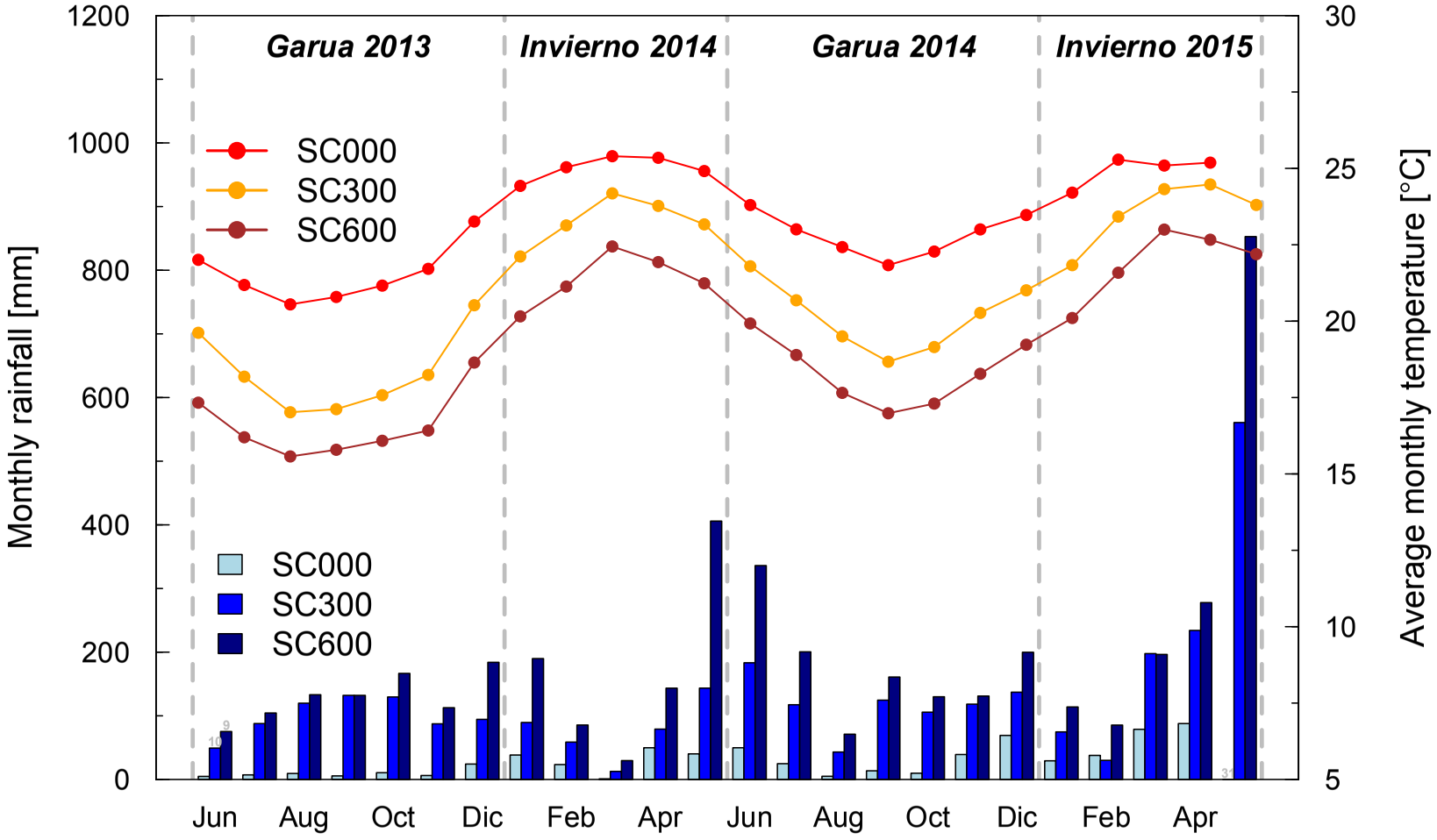

Figure 3.2: Monthly total rainfall and mean temperature of the three stations placed along the windward side of San Cristobal during the hydrological years 2013-2014 and 2014-2015. Rainfall is markedly different comparing SC000 to SC300 or SC600 consequence of the orographic gradient and seasonality, especially during the cool seasons.

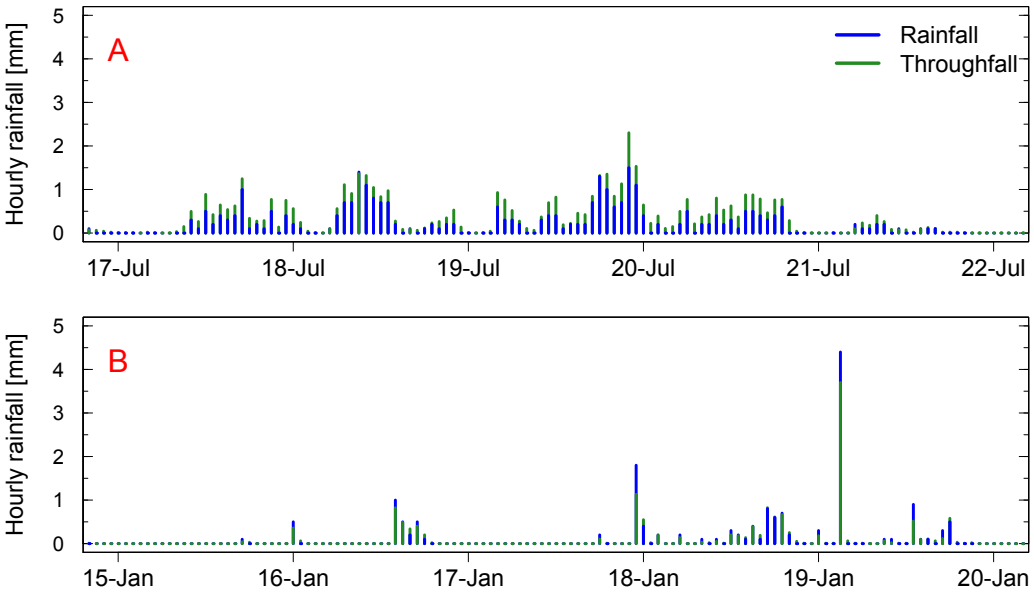

Figure 3.3: Height of rainfall and throughfall at a 1-hour time step at station SC600. Height of throughfall is estimated from the entire surface of troughs (1.8 m^2). (A) and (B) during the cool and hot seasons of the first hydrological year, respectively. Notice that height of throughfall is larger than rainfall during the cool season.

studied in the highlands of Santa Cruz by (Pryet et al., 2012a). In such case, records of throughfall require further analysis (section 3.2).

3.1.2.2 Rainfall orographic gradient

Seasonally, rainfall seems to follow a similar gradient between stations, particularly on the cool season (Fig. 3.4). However, differences in rainfall inputs are contrasting between the two years, it is noticeable in the hot season. Mean gradient from the two observations years is 336 mm/100 m of elevation starting from 323 mm at the coast. It means that at 600 m of elevation, rainfall reaches 2304 mm. However, the hydrological year 2014-2015 is a wet year and estimations might be biased. Therefore, it would be better to use the gradient from the first year which appears to be an average year in terms of rainfall. The gradient for the first year is 270 mm/100 m of elevation starting from 186 mm at the coast. Then, at 600 m of elevation, rainfall reaches 1804 mm. Given that median elevation at the windward side of the island is 305 m a.s.l., then rainfall at station SC300 can be considered as the median rainfall of the windward side of San Cristobal. Precipitation input is high at highlands and increased by fog interception above 300 to 400 m of elevation, which is not yet considered.

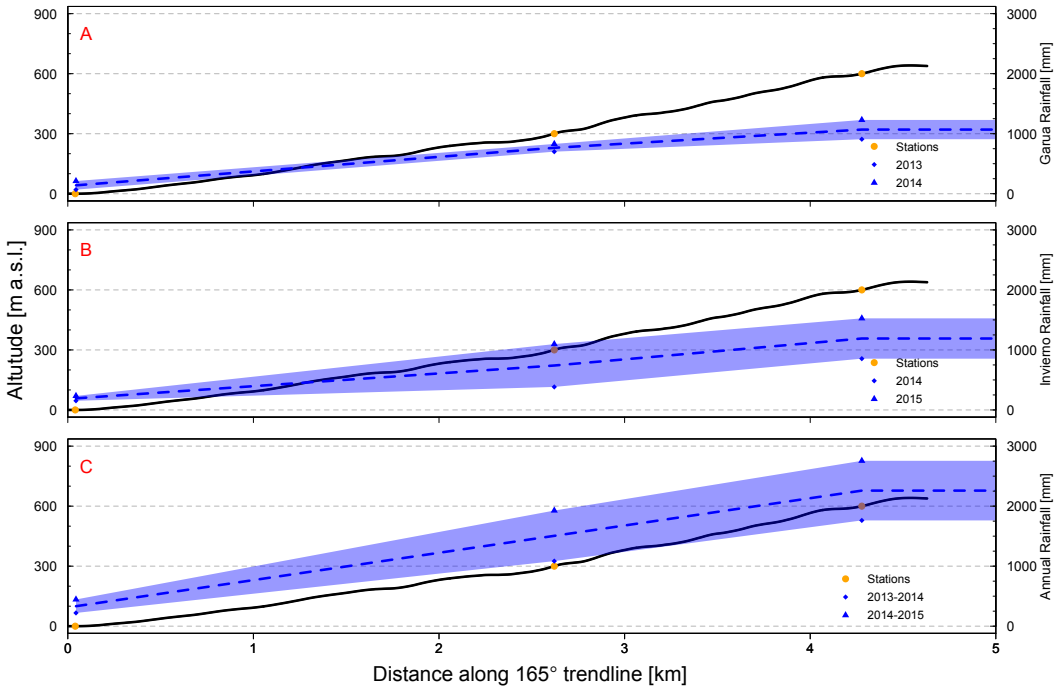

Figure 3.4: Seasonal, (A) cool garua season and (B) hot invierno season, and annual (C) rainfall gradient along the windward side estimated from stations SC000, SC300 and SC600 during the two hydrological years of study. The topographic cross section (black line) is exported from the IGM-DEM (10 m resolution).

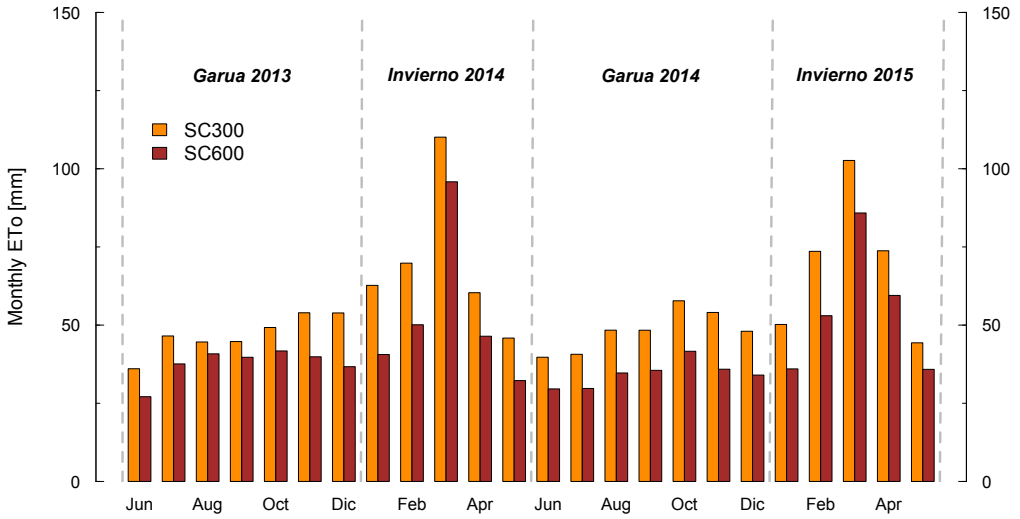

Figure 3.5: Monthly ETo from stations SC300 and SC600. ETo is estimated using the FAO-PM equation at stations.

3.1.2.3 Referential evapotranspiration and gradient

On the basis of the available data, a first estimation of the referential potential evapotranspiration (ETo), the evaporative demand of the atmosphere independently of crop type and soil water availability, is calculated with the FAO *Penmann-Monteith* equation (FAO-PM) (Allen et al., 1998) at stations SC300 and SC600. As expected ETo is lower at the highlands, particularly during the cool seasons (Fig. 3.5). The highest values are observed during the hot season, in which March has the highest values. ETo is similar between years. Mean estimated annual ETo is 680 and 519 mm at SC300 and SC600, respectively.

At SC000, the FAO-PM could not be applied due to missing data (solar radiation, wind speed and relative humidity). In such cases, the FAO recommends the use of the *Hargreaves* equation based on the temperature and extraterrestrial radiation (Allen et al., 1998):

$$ETo = 0.0023 \times (T_{mean} + 17.8) \times (T_{max} - T_{min})^{0.5} \times R_a \tag{3.1}$$

where T is the temperature and R_a is the extraterrestrial radiation. Eq. 3.1 tends to underestimate the value of ETo under strong wind conditions and overestimate ETo under high humidity conditions (Allen et al., 1998). However, estimations are expected to be fair given the mild winds and relative low humidity conditions expected at the coast. In any case, ETo estimations with this equation can be calibrated by means of determining empirical coefficients of a linear regression between the ETo calculated by the FAO-PM and Hargreaves equation on a neighboring weather station. The coefficients are obtained from the SC300 station. Estimated ETo at SC000 is 812 mm and 714 mm at the first and second year,

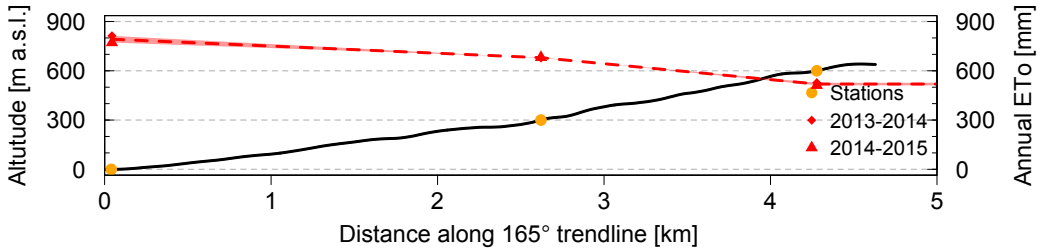

Figure 3.6: Annual ETo orographic gradient along the windward side estimated from station SC000, SC300 and SC600. At station SC300 and SC600, ETo is estimated using the FAO-PM equation, while ETo in station SC000 is derived from the Hargreaves equation. The topographic cross section (black line) is exported from the IGM-DEM (10 m resolution).

respectively. Contrary to rainfall, ETo gradient follows different slopes between stations (Fig. 3.6). ETo remains similar at stations SC300 and SC600. Because in terms of temperature, both years are similar, the gradient is estimated as the mean of both years. In such case, ETo gradient is -53 mm/100 m of altitude, starting with 840 mm at the coast and reaching 522 mm at 600 m of elevation.

It should be noticed that the use of the PM equation for estimations of potential evapotranspiration on region under wet conditions is still under debate. Loescher et al. (2005) and Langensiepen et al. (2009) studied the PM equation in wet tropical forest concluding that PM is suitable for those conditions. García-Santos et al. (2009) studied PM under very humid conditions showing slightly fair estimates and that transpiration under fog occurrence can be notably reduced compared to clear-sky conditions. Also, land use is an important factor to be consider as several authors have reported significant differences in transpiration depending of the vegetation cover (Bosch and Hewlett, 1982; Taniguchi and Sharma, 1993; Johnson, 2012; Zimmermann et al., 2010). Under these considerations, these estimates should be consider only as references and actual evapotranspiration (ETa) of the representative land covers should be evaluated, especially on the highlands.

3.2 Quantification of cloud water interception at the windward slope highlands of San Cristobal Island

Abstract Cloud water interception (CWI) by the vegetation can be an important water input to ecosystems subject to fog occurrence. In this work, we propose a methodology to estimate CWI by a forest using a Rutter-type interception model. The approach requires the acquisition of experimental observations. Continuous records of meteorological variables, including fog interception that is measured using a fog gauge system, are used as the input dataset of the model. Additionally, throughfall measurements performed below the forest are required only for the calibration and validation of the model, which constitutes a significant advantage considering the difficulties to obtain continuous records of throughfall. This methodology is applied in San Cristobal Island (Galapagos), where a semi-permanent fog layer covers the windward highlands during six months of a year. A study plot in an endemic forest in the highlands has been monitored during two years. Results show that CWI reaches 23% and 10% of the total water input of the first and second year, respectively. During the hot seasons, where fog is absent, CWI is negligible as expected, while it represents 37% and 19% of the water inputs during the first and second cool seasons, respectively. The marked difference of CWI between both cool seasons is related to higher liquid water content in the air during the first season. This methodology provides an indirect quantification of CWI by the vegetation from artificial fog gauges, it identifies controlling factors of CWI and it could be used to compare CWI in contrasting land covers.

3.2.1 Introduction

Cloud water interception (CWI) by the vegetation subject to fog occurrence has been considered as an important hydrological process because it is an additional water input to the canopy water budget. Moreover, it has been associated with a reduction in the evapotranspiration (Hamilton et al., 1995; Bruijnzeel, 2001; Ritter et al., 2008). Its measurement is critical to establish suitable water management policies, especially in regions with limited water resources and subject to land use change.

Basically, three main factors influence CWI (Brauman et al., 2010; Villegas et al., 2008; Ritter et al., 2008): climatic conditions (air liquid content, fog drop size, wind speed), canopy structure (size, height, density, leave morphology and orientation) and location (elevation, terrain slope and orientation). Attempts to quantify CWI has been proposed in different locations around the world (Ingraham and Matthews, 1988; Cavelier and Goldstein, 1989; Hamilton et al., 1995; Holder, 2004; McJannet et al., 2007; Gabriel and Jauze, 2008; Gomez-Peralta et al., 2008; Ritter et al., 2008; Villegas et al., 2008; Holwerda et al., 2010; Uehara and Kume, 2012; Pryet et al., 2012a), reporting different results, which shows that CWI is highly dependable of the site. Methods to quantify CWI includes the use of fog gauges (Ingraham and Matthews, 1988; Aboal et al., 2000; Villegas et al., 2008), measurements of net precipitation (throughfall and stemflow) (Gabriel and Jauze, 2008; Prada et al., 2009; Pryet et al., 2012a) and other alternatives (Chang et al., 2002; Holwerda et al., 2006; Eugster et al., 2006). While fog gauge are relative easy to install, the fog estimates it provides is from their capacity to catch fog and not from the vegetation. Net precipitation measurements in that sens, provide estimations which are related to the canopy capacity to intercept fog, once the interception variable in the canopy water balance is known. However, few studies have related estimates of CWI from fog gauges with the ones of vegetation. Ritter et al. (2008) used data from fog gauges to derive fog characteristics, which are used in a physically based impaction model to quantify CWI of a subtropical elfin cloud forest in La Gomera (Canary Islands). Holwerda et al. (2011) found that estimates of CWI with a wet canopy water budget in a Puerto Rican elfin cloud forest, correlated significantly with measured CWI in fog gauges.

The most common approach used for CWI estimations is the use of interception models. These models not only provide estimates of the different water balance variables but also they can be used to assess the driving factors of CWI. The two most common approaches are: i) Rutter-type models (e.g. Liu (1997); Rutter et al. (1975)), based on the running canopy water budget, and 2) Gash-type models (e.g. Gash (1979); Zeng et al. (2000)), based on discrete rainfall

events. Generally, Gash models are preferred because of their simplicity, but they require the separation of individual rainfall events. In context of fog occurrence and continuous rainfall, this could be quite challenging. Moreover, van Dijk et al. (2015) studied sources of errors in the estimation of interception in canopy water budgets, and showed that the Rutter-type model with accurate estimations of evaporation provide the best results. In canopy water models, rainfall and net precipitation are measured, evaporation is estimated with an energy balance (most commonly Penman–Monteith theory) and CWI is estimated from the difference in the water balance. The drawback of this approach is that it requires continuous measurements of net precipitation, which is extremely challenging, especially in an equatorial context.

The objective of this section is to propose and validate an innovate methodology to estimate cloud water interception by a forest using a Rutter-type interception model, in which CWI in the forest is estimated from monitoring of climatic variables, including fog interception by a fog gauge system. CWI estimates in the forest are obtained from measurements in the fog gauge and not as the remaining variable in the canopy water balance. In this way, measurements of net precipitation are only used for calibration and validation purposes. We tested this methodology in an endemic forest in the highlands of San Cristobal Island (Galapagos Archipelago).

3.2.2 Study Area

3.2.2.1 Climatic and hydrological context

The Galapagos Archipelago is located in the Eastern Pacific, 1000 km west of the Ecuadorian mainland. The climatic conditions are atypical for its equatorial position. Essentially, there are two distinct seasons: 1) The cool "garua" season from June to December, where the sea surface and air temperature are relatively low (Palmer and Pyle, 1966; Dunbar et al., 1994), and it is characterized by the occurrence of orographic precipitations and the presence of a semi-permanent fog layer that covers the highlands of the main islands (Trueman and d'Ozouville, 2010; Pryet et al., 2012a). 2) The hot "invierno" season from January to May, characterized by high sea and air temperatures, and high intensity convective precipitations (Grant and Boag, 1980; Dunbar et al., 1994; Trueman and d'Ozouville, 2010). Considering the long term records (1965-2015) of the weather station operated by the *Charles Darwin Foundation* at the coast of Santa Cruz Island (alt. 6 m a.s.l.), the median annual rainfall is 278 mm and the average air temperature is 24 °C.

San Cristobal Island, located at the East of Galapagos, is the only island of the

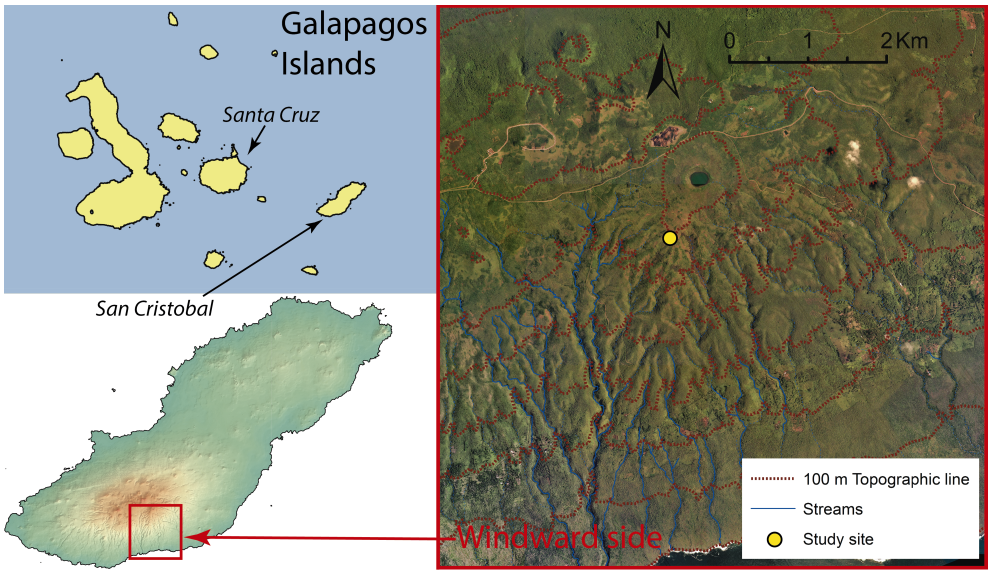

Figure 3.7: Location of the study site used for climatic and canopy monitoring in the windward side of San Cristobal Island. The hydrological monitoring was set up in an endemic forest at 600 m of elevation on the windward slope of the island (image from IGM (2014)).

Archipelago with permanent surface water resources (Fig. 3.7). This resources are located at the southern side of the island. The hydrological system is complex in this zone. Over the highlands, gentle slopes allow the pounding of rainfall. Over mid-slope, a well-developed drainage network can be observed. Several ravines are dry, but others are fed by perennial springs that outcrop of impermeable layers. The interpretation from the AEM SkyTEM dataset d'Ozouville (2007) suggests that the spring are originated from perched aquifers formed over impervious layers, which are disconnected from the basal aquifer (Pryet et al., 2012b; Violette et al., 2014). The population of the island is entirely dependent on the streams of this zone for water supply. At the lowlands, due to infiltration losses on the riverbeds, only four ravines have been identified to have streamflow reaching to the sea (d'Ozouville, 2007).

3.2.2.2 Highlands vegetation and study plot

The study area lies in the southern windward highlands, within the agricultural zone that extends from the midlands until the summit of the islands. Originally, highlands hosted mainly ferns and forest of endemic *Miconia Robinsoniana* shrub, which has been classified by Pryet et al. (2012a) as a low-elevation elfin cloud forest. The *Miconia* shrubs form small patches varying in height. They grow on steep slopes exposed to winds and fog. Due to the development of agriculture, endemic forest are being converted into pasture and secondary forests.

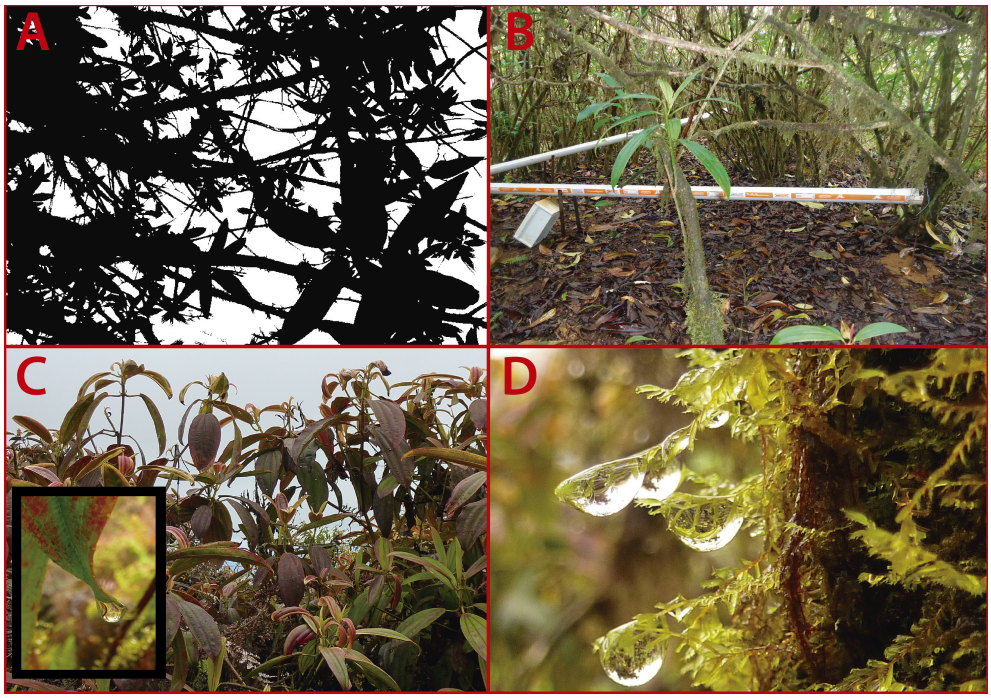

Figure 3.8: Morphological features of *Miconia* shrubs in the study site at the highlands of the windward side of San Cristobal. (A) Canopy coverage, (B) branches angle, (C) leaf shape and orientation and (D) flow path obstructions: epiphytes.

However, vast regions of the highlands are covered by the endemic forest, so they are still representative of the contemporary vegetation of the windward highlands. For this reason, we identified one study plot representative of the *Miconia* forest.

The study plot is characterized by a single-storied architecture of *Miconias* with similar morphological features (Tb. 3.2). However, sparse sections of small ferns have been observed. Even if height of the shrubs is homogeneous, the diameter of their stems is relatively diverse. Branches have different inclinations and many ramifications from the bottom (Fig. 3.8). These branches are characterized by the presence of abundant epiphytes. Leaves have broadly elongated elliptic shape with conical edges with inclination towards the ground.

3.2.3 Methodology

3.2.3.1 Climatic monitoring

Climatic monitoring was conducted with a weather station in the clearings close to the study plot (ca. 50 m) and consists of measurements of rainfall, solar radiation, air temperature, relative humidity, wind direction and speed and fog interception (Fig. 3.9). Data was recorded at a 15-minutes time step using a Campbell CR1000 datalogger. Rainfall was measured with a Texas TE525MM

Table 3.2: Features of the study plot.

Parameter	Value
Altitude [m a.s.l.]	610
Terrain slope	10°
Slope aspect	170°
Height [m]	3.0
Vegetation type	Elfin cloud forest
Dominant species	*Miconia Robinsoniana* shrub
Albedo	0.1[a]
Canopy gap fraction (p)[b]	41%

[a] Value from Pryet et al. (2012a).
[b] Value estimated from photographical analysis.

rain gauge placed at 1.5 m above the ground. Wind speed and direction were monitored with a Young WindSentry Kit positioned at 2 m above the ground. Solar radiation, relative humidity and temperature were measured at 2 m above the ground, with a Kipp&Zonen SPLite silicone pyranometer and a Campbell CS215 T&RH sensor, respectively. Fog interception was measured with a cylindrical fog gauge (height 40 cm, 12 cm in diameter) made of plastic mesh (1 mm) at 2 m above the ground. Intercepted water was collected with a funnel at the base of the cylinder and diverted to an automatic tipping bucket rain gauge. Using this system, fog interception and rainfall are collected, hence the partition into rainfall and fog interception is necessary.

Throughfall measurements were performed within 6m×6m plot beneath vegetation canopy (Fig. 3.10), using (Domínguez Gonzalez, 2011; Pryet et al., 2012a): i) a set of troughs draining into an automatic tipping bucket gauge (Ziegler et al., 2009; Holwerda et al., 2010; Zimmermann and Zimmermann, 2014), and ii) manually read small collectors distributed randomly within the plot (Keim et al., 2005; Staelens et al., 2006; Zimmermann et al., 2009). Troughs were made of 3 m long PVC pipes of diameter 10 cm cut in half. They have an average inclination of 25° to facilitate drainage. 6 troughs were used in this study corresponding to a collection area of 1.8 m^2. Manual collectors are used to assess the spatial representativity of the continuous troughs measurements. Collectors were made from funnels of diameter 16 cm placed over 2-L containers. A total of 30 collectors (total area of 0.6 m^2) were used in the plot. They remained fixed during the study period. Measurements were performed manually, but the number of measurements were limited due to difficulties of access to the field notably after rainfall events.

Stemflow was measured using a malleable plastic funnel adhered to the trunk

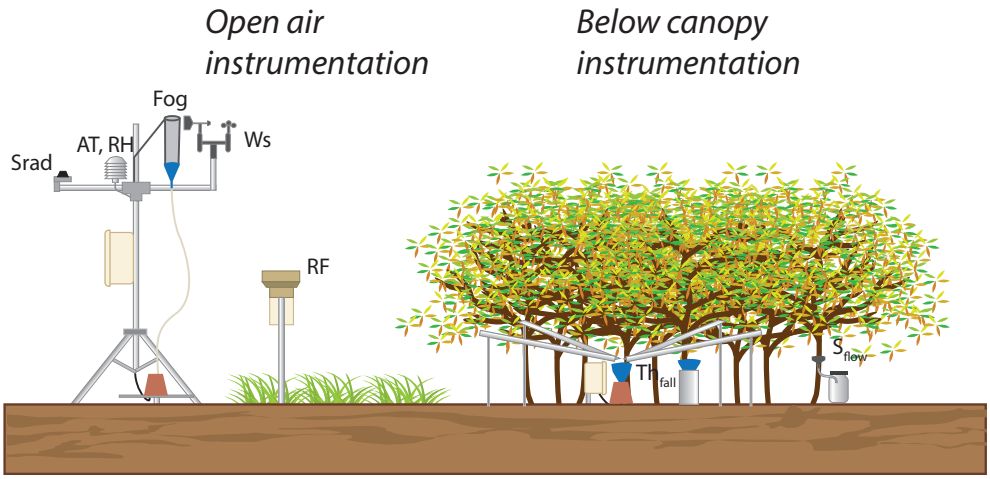

Figure 3.9: Representation of the hydrological monitoring at 600 m of elevation. A weather station is placed on the open area ($Srad$: solar radiation, WS: wind speed and direction, AT: air temperature, RH: relative humidity, RF: rainfall; and below the canopy: stemflow (S_{flow}) and throughfall(Th_{fall})).

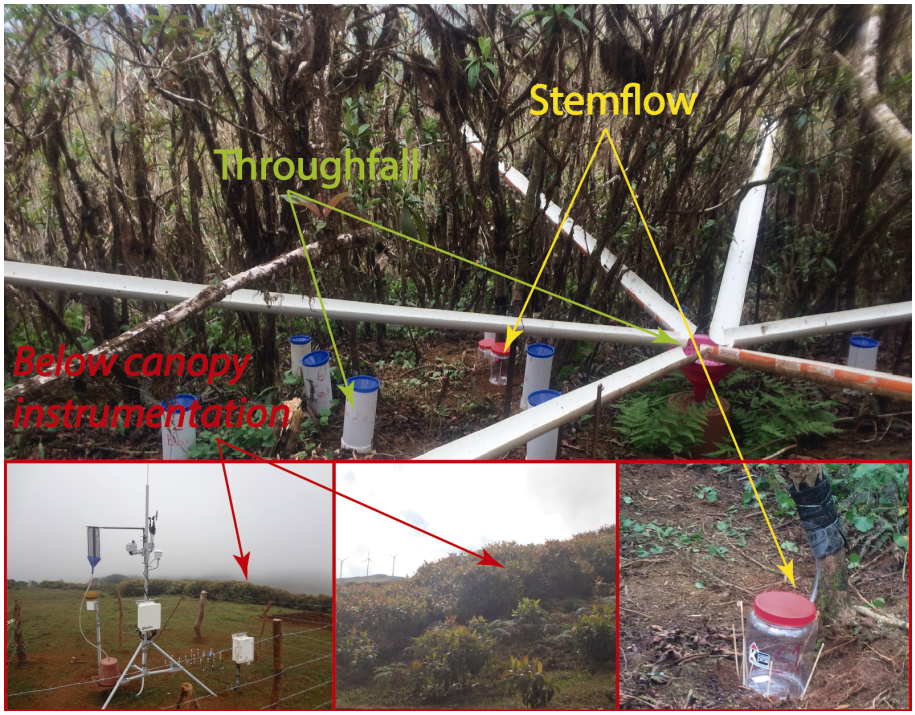

Figure 3.10: Throughfall and stemflow monitoring below the canopy of the *Miconia* forest. Throughfall is measured with troughs and collectors. Stemflow is measured with small collection funnels.

and connected to a hose that drips collected water into a 2-L capacity container. Funnels were made for each trunk with a diameter 1 cm larger than the one of the trunk. They were placed at 0.5 cm above the ground. Stemflow measurements were limited to 8 trunks with a diameter larger than 6 cm. We could not measure stemflow for the rest of the trunks within the plot (78). However, mean height of measured stemflow of the 8 trunks represented less than 0.5% of incident rainfall, even though we were generous limiting the incident surface of each trunk. In Santa Cruz Island, Pryet et al. (2012a) estimated stemflow of 0.6% of the incident rainfall for the same vegetation at a similar altitude. Thus, considering that errors of our throughfall measurements might be considerably larger than measured stemflow, we consider stemflow to be negligible.

All rain gauges used in the study were corrected for losses during bucket rotation using a dynamic calibration at the laboratory (Calder and Kidd, 1978). Measured throughfall reached a plateau of 20 mm/h despite measured rainfall was significantly higher. It seems that the capacity of throughfall measured by the troughs cannot be larger than this value, equivalent to 30 tips per minute.

3.2.3.2 Canopy model

Canopy evaporation, net precipitation and cloud water interception are estimated using a modified sparse version of the original Rutter model (Rutter et al., 1971, 1975). The model is based on a running water balance that requires parameters describing the structure, drainage and interception capacity of the canopy (Fig. 3.11). In contrast to Rutter et al. (1975) and Valente et al. (1997), the separation into a canopy and trunks compartment is not consider in the current model version (stemflow is negligible compared to the rainfall amount, see section 3.2.3.1), thus the water balance calculations are performed only for the canopy and net precipitation (P_{net}) is reduced to throughfall (Pryet et al., 2012a). However, in cases where stemflow amount is relevant, the trunk compartment can be easily included in this model.

All variables referring to a water storage, or flux, were expressed as depth of water over the whole plot area. The model considers changes in the water stored within the canopy compartment derived from the water balance for a plot area. In the absence of cloud water interception (CWI) the water budget can be written as follows:

$$\Delta C/\Delta t = (1-p) \times RF - D - E \tag{3.2}$$

where $\Delta C/\Delta t$ [LT^{-1}] is the variation of the canopy water storage (C), p is the free throughfall coefficient, RF [LT^{-1}] is the rainfall rate, D [LT^{-1}] is the drainage of the water from the canopy and E [LT^{-1}] is the wet canopy evaporation rate.

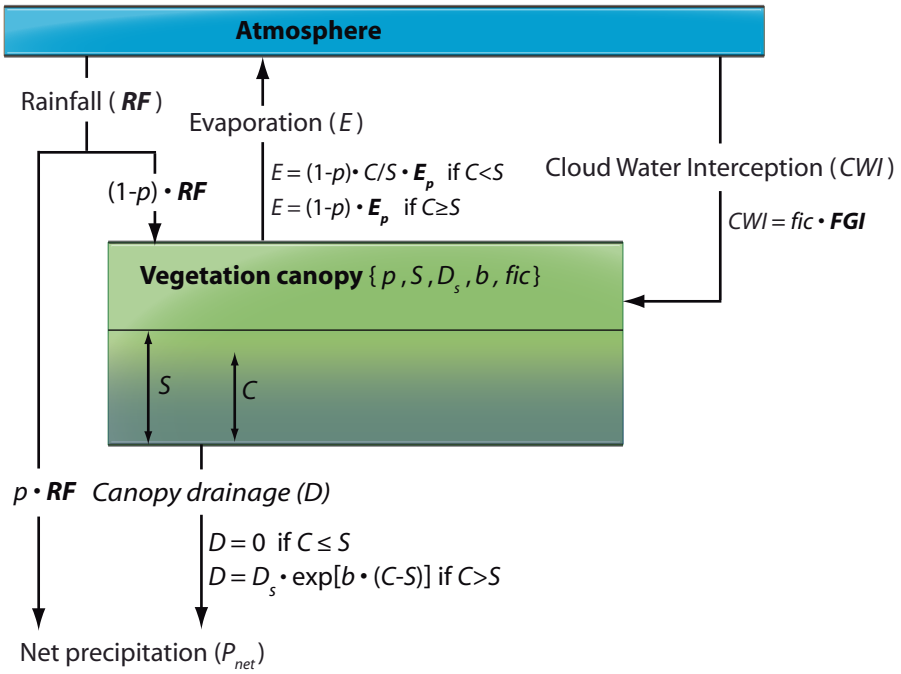

Figure 3.11: Interception model scheme. p, S, D, b and fic are canopy parameters. Bold variables are inputs of the model.

Notice that the rainfall input is a proportion of the canopy cover $(1-p)$. The canopy storage capacity (S) [L] must be satisfied before drainage occurs. It is calculated using an exponential function (Gash and Morton, 1978; Valente et al., 1997; Pryet et al., 2012a):

$$D = \begin{cases} D_s \times exp(b(C-S)) & \text{if} \quad C > S \\ \\ 0 & \text{if} \quad C \leq S \end{cases} \tag{3.3}$$

where D_s [LT^{-1}] and b are canopy characteristics.

Evaporation of canopy is scaled down from the potential evaporation rate of the plot area (E_p) in proportion to the canopy cover and the amount of water stored by the canopy (Pryet et al., 2012a):

$$E = \begin{cases} (1-p) \times E_p & \text{if} \quad C \geq S \\ \\ (1-p) \times C/S \times E_p & \text{if} \quad C < S \end{cases} \tag{3.4}$$

When the canopy is saturated $(C \geq S)$, E reaches the potential evaporation rate of the canopy. For unsaturated canopy $(C < S)$, E is proportional to the C/S ratio (Rutter et al., 1975; Whitehead and Kelliher, 1991; Valente et al., 1997). E_p is estimated using the Penman-Monteith (P-M) equation (Monteith, J.L., 1965)

with the surface resistance set to zero (Rutter et al., 1975; Kelliher et al., 1993; Muzylo et al., 2009). Parameters used in the P-M equation are obtained from Pryet et al. (2012a).

In this model, we consider cloud water intercepted by the canopy. Whereas intercepted rainfall depends of the proportion of the canopy cover, CWI depends basically on the fog properties, wind speed intensity and canopy characteristics (Bruijnzeel et al., 2006; Villegas et al., 2008; Holwerda et al., 2010; Pryet et al., 2012a). The first two factors can be assessed from the rate of intercepted water of a fog gauge (FGI). Indeed, water collected by the fog gauge will be influenced by the fog characteristics such as air liquid content, fog drop size and the atmospheric conditions such as the wind speed intensity. Then, CWI derived from FGI would only depend of the canopy characteristics. To simplify the effect of the canopy characteristics, a parameter called *fog interception capacity of the canopy* (fic) is used for the estimation of CWI. Then CWI can be expressed as:

$$CWI = fic \times FGI \tag{3.5}$$

Notice that CWI do not depend of the canopy cover but, rather, is only a proportion of FGI. Given that FGI would not be a vertical water input, we consider that an horizontal canopy cover would be different than $(1-p)$. However, we use CWI to increase the vertical canopy water storage which is a fair assumption considering that CWI will be stored by the canopy before dripping to the floor.

Considering cloud water interception, the wet canopy water budget equation is written as follows:

$$\Delta C/\Delta t = (1-p) \times RF + CWI - D - E \tag{3.6}$$

Net precipitation can be estimated from direct throughfall and drainage of canopy:

$$P_{net} = p \times RF + D \tag{3.7}$$

3.2.3.3 Model implementation and calibration

3.2.3.3.1 Estimation of intercepted water by the fog net Considering that the fog net collects the combine volume of incident rainfall and fog interception (VF_T), it is necessary to assess the height of fog interception from VF_T. To do this, we make two assumptions: i) intensity and direction at which rainfall is intercepted by the fog net and rain gauge are the same, and ii) cloud water incidence is horizontal, so the interception surface of the fog net is the vertical face of its cylinder. During windy conditions, the rain gauge measure vertical rainfall (RF_v), which is the vertical component of actual rainfall (RF_a) with an inclination angle (γ). γ is estimated at each time step from rainfall intensity,

raindrop size, terminal fall velocity of the raindrops and wind speed (Holwerda et al., 2006). Median raindrop diameter (RD) is calculated from the rainfall intensity (Laws and Parsons, 1943; Holwerda et al., 2006):

$$RD = 2.23 \times (0.03937 \times RF_v)^{0.102} \tag{3.8}$$

where RD and RF_v are in mm and mm/h, respectively.

The terminal fall velocity U_D (m/s) is estimated from D (Gunn and Kinzer, 1949; Holwerda et al., 2006):

$$U_D = 3.378 \times ln(RD) + 4.213 \tag{3.9}$$

Then, rainfall inclination angle is derived as (Herwitz and Slye, 1995; Holwerda et al., 2006):

$$tan(\gamma) = U/RD \tag{3.10}$$

RF_a can be estimated with a trigonometric relationship as follows:

$$RF_a = RF_v/cos(\gamma) \tag{3.11}$$

where RF_v is equivalent to the volume measured by the rain gauge divided by its horizontal circular surface. Therefore, RF_a can also be determined from the measured volume divided by the projection of the horizontal circular surface perpendicular to the direction of RF_a, which corresponds to an ellipse.

Given the above assumptions and equivalence, in the fog net, the volume corresponding to RF_a can be estimated as:

$$VF_r = RF_a \times S_{fp} \tag{3.12}$$

where VF_r is the volume of intercepted rainfall by the fog net and S_{fp} is the projected surface of the fog net perpendicular to the direction of RF_a (Fig. 3.12). S_{fp} decreases with the first couple of degrees, such as the rain gauge, until it reaches an inflection point, which corresponds to the appearance of the cylinder net, where S_{fp} starts to increase considerably. S_{fp} reaches a maximum value a couple of ten of degrees before the inclination of rainfall is horizontal, from this point its value starts to decline until it reaches the horizontal projection surface of the cylinder. Because, S_{fp} is a function of the inclination angle of RF_a and its geometry, then, the height of water from fog gauge interception (FGI) can be estimated as:

$$FGI = \pi \times h_c \times D_c/2 \times (VF_T - fe \times VF_r) \tag{3.13}$$

where h_c and D_c are the height and diameter of the cylinder, respectively, and fe is a coefficient of correction obtained from the bias when comparing volumes between the fog net and rain gauge during rainfall intensities with a low inclination angle.

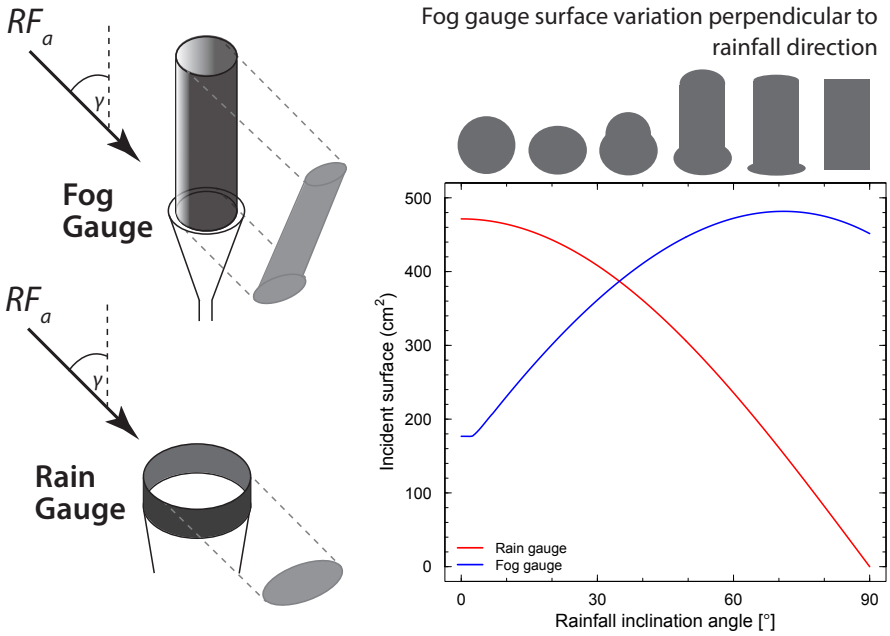

Figure 3.12: Fog gauge surface variation which is a function of rainfall inclination. An accurate surface estimation is necessary to estimate cloud water interception by the fog gauge.

3.2.3.3.2 Corrections and calibration of the model The canopy model is implemented using 15-minutes time step. Climatic variables measured at the weather station are assumed to be representative of the conditions at the top of the canopy. Corrected rainfall measured with the rain gauge is used as the incident rainfall at the canopy. When values of FGI estimated with Eq. 3.13 are negative related to measurement errors, they are set to zero. Given that the plot is located in sloping terrain with an angle ϕ, incident rainfall intercepted by the canopy (RF_c) is estimated using the relation proposed by Sharon (1980):

$$RF_v/RF_c = cos(\phi) + sin(\phi) \times tan(\gamma) \times cos(\Omega_a - \Omega_b) \tag{3.14}$$

where Ω_a is the slope aspect and Ω_b is the wind direction. Using this relation, we consider that the top canopy surface is parallel to the sloping ground.

Constant canopy parameters are assumed during the investigation period (June 2013 to May 2015). The calibration of the canopy parameters p and S is conducted using a within-event analysis of a set of rainfall storms detailed by Link et al. (2004). D_s, b and fic are calibrated with the *Guauss-Levenberg-Marquadt* algorithm implemented in the PEST software (Doherty, 2010) for the optimization of minimum weighted least square (OMWLS) between simulated and observed throughfall during the hydrological year 2013-2014 and validated during the hydrological year 2014-2015. Then, throughfall records are only used for validation purposes, not as inputs of the model for the estimation of CWI as

proposed by Pryet et al. (2012a).

3.2.4 Results

3.2.4.1 Meteorological and below canopy measurements

Long term records from the historical weather station operated by the *Charles Darwin Foundation* in Santa Cruz reveal that the hydrological year 2013-2014 (June to May) corresponds to an average year in terms of rainfall (234 mm) and temperature (24 °C), while the second year (2014-2015) is characterized by strong rainfall (484 mm) and relative high temperatures (25 °C). During the two-years observation period at the study site, daily average wind speed (2.7 m/s) and direction (195 °C) remained similar at all seasons. Relative humidity was close to, or at saturation for most part of the period. Solar radiation remained relatively low, however the daily average is lower during the cool seasons. Significant difference in temperatures can be seen between seasons, where the daily average during the 2013-cool season is especially low. Total height of annual measured rainfall at the study site reaches 1762.5 mm and 2755.5 mm, for the first and second hydrological year, respectively. Incident rainfall at the canopy is 1848 mm during the first year and 2857.2 mm during the second year. This corresponds, respectively, to 105% and 104% of the measured rainfall by the rain gauge.

In order to estimate FGI, a set of rainfall data ($n = 837$) from the rain gauge and fog net was selected when the angle of inclination of rainfall was lower than 2.5 °C (below this angle, the surface of the cylinder has no influence and measurements from both instruments should be equivalent). Then, equivalent height of water were compared. A relative bias of 0.12 was found between the height of water measured by the fog net and the rain gauge. This is associated to systematical errors in the fog net measurements. The estimated bias is used in Eq. 3.14 as $fe = 1.12$. Annual estimated FGI is 1066 mm and 613 mm at the first and second year, respectively. From the annual FGI for the first year, 96.4% correspond to the cool season and 3.6% to the hot season; while for the second year, 95.5% and 4.5%, respectively. FGI was registered during 21% of the first cool season and during 12% of the second cool season.

Due to the clogging of the throughfall tipping buckets and electronic issues with the instrumentation, 21% of the total throughfall data during the two hydrological years ($n = 69216$) is unavailable. Most part of the missed data is from the second year. During the calibration period (first hydrological year), available throughfall data available represents 87% ($n = 17453$) of the cool season and 82% ($n = 11884$) of the hot season. During the second year, it represents 74% ($n = 15274$) of the cool season and 67% ($n = 9711$) of the hot season. From

Table 3.3: Canopy parameters used in the interception model at the study plot. p is estimated from *within event* analysis, while all other parameters are estimated from calibration using the *Guauss-Levenberg-Marquadt* algorithm. Estimated errors correspond to a 95% of confidence level.

Parameter	Value
p	0.4
S [mm]	2.04 (0.03)
D_s [mm s^{-1}]	1.9 (0.15) $\times 10^{-5}$
b [mm^{-1}]	12.70 (0.5)
fic	0.52 (0.01)

the available throughfall observations, total collected throughfall reaches 121% and 105% of the incident rainfall at the canopy, during the first and second year, respectively. Difference of relative throughfall is marked between the cool and hot season at both years. During the first year, relative throughfall is 130% and 84% during the cool and hot seasons, respectively. While, it reaches 110% at the cool season and 88% at the hot season of the second year.

3.2.4.2 Model calibration and validation

Canopy parameters p and S were estimated with linear regressions from cumulative rainfall vs cumulative throughfall from a specific set of events with low relative throughfall values (Pryet et al., 2012a). Estimated p by this method is 0.4, while S is 1.5 mm. The value of p is in accordance with the value of canopy gap fraction estimated from vertical photographs under the canopy plot (0.41). However, the limited number of events is a constraint (9 out of 267). Therefore, we only used p from this methodology, and S was also calibrated with the OMWLS method as the rest of the canopy parameters (D_s, b and fic). Calibrated fic indicates that 52% of cloud water intercepted by the fog gauge is in fact intercepted by the vegetation (Tb. 3.3). This value is realistic, given that at similar conditions, we expect that the fog net capacity to intercept cloud water should be larger than the vegetation. Indeed, the fog net is placed at a similar height than the canopy height.

The model satisfactorily simulates throughfall along the study period (Fig. 3.13 and Fig. 3.14). During the calibration period (first year), RMSE of simulated throughfall is 0.06 mm ($n = 9365$), while it is 0.08 mm ($n = 4567$) at the second year. RMSE is estimated between the simulated and available throughfall of 15-min estimates disregarding data points where its value is equal to zero simultaneously for both datasets. Simulated cumulative throughfall is underestimated by 0.6% and overestimated by 0.7% over the first and second year, respectively.

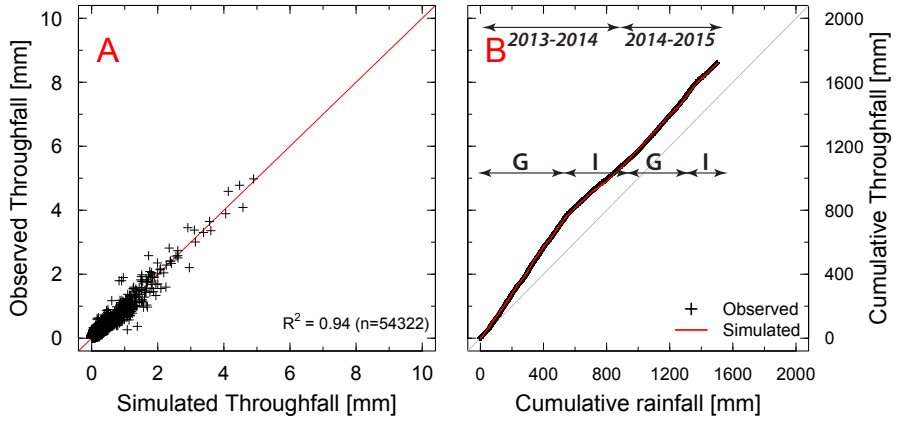

Figure 3.13: Simulated throughfall from the interception model. A) Comparison of simulated vs observed throughfall. B) Cumulative rainfall vs observed and simulated cumulative throughfall while observed throughfall is available. A seasonal change of slope can be seen between the cool garua season (G) and the hot invierno season (I).

3.2.4.3 Fog interception and canopy water budget

Cumulative CWI by the canopy is 555 mm during the first year and 319 mm during the second year (Tb. 3.4). These values represent 23% and 10% of the total water input of the first and second year, respectively. Seasonally, marked difference can be seen in the CWI quantities. It represents 36% and 19% of the water inputs at the first and second cool season, respectively (Fig. 3.15); while at the hot season, CWI represents 2% at the first year, and 1% at the second one. Clearly, contribution of CWI is significant during the cool season, while during the hot season it can be consider negligible. Cumulative evaporation reaches 318 mm during the first year and 297 mm during the second year. These values correspond to 15% and 10% of the total water outputs for the first and second year, respectively. Contribution of E during the cool seasons represent 72% of the yearly E for the first year and 62% for the second year. This is expected considering that, during the cool season the canopy remains wet for longer periods than during the hot season, hence more water is subject to evaporation.

3.2.5 Discussion

3.2.5.1 Interception model

Calibrated canopy parameters p and S values are comparable with values found in the literature (Aston, 1979; Lloyd et al., 1988; Holwerda et al., 2010; Takahashi et al., 2011; Wallace and McJannet, 2006). While the value of p may somehow be comparable with the one ($p = 0.3$) found by Pryet et al. (2012a) for the same type of vegetation, S is considerable higher in this study (S of 0.23 mm

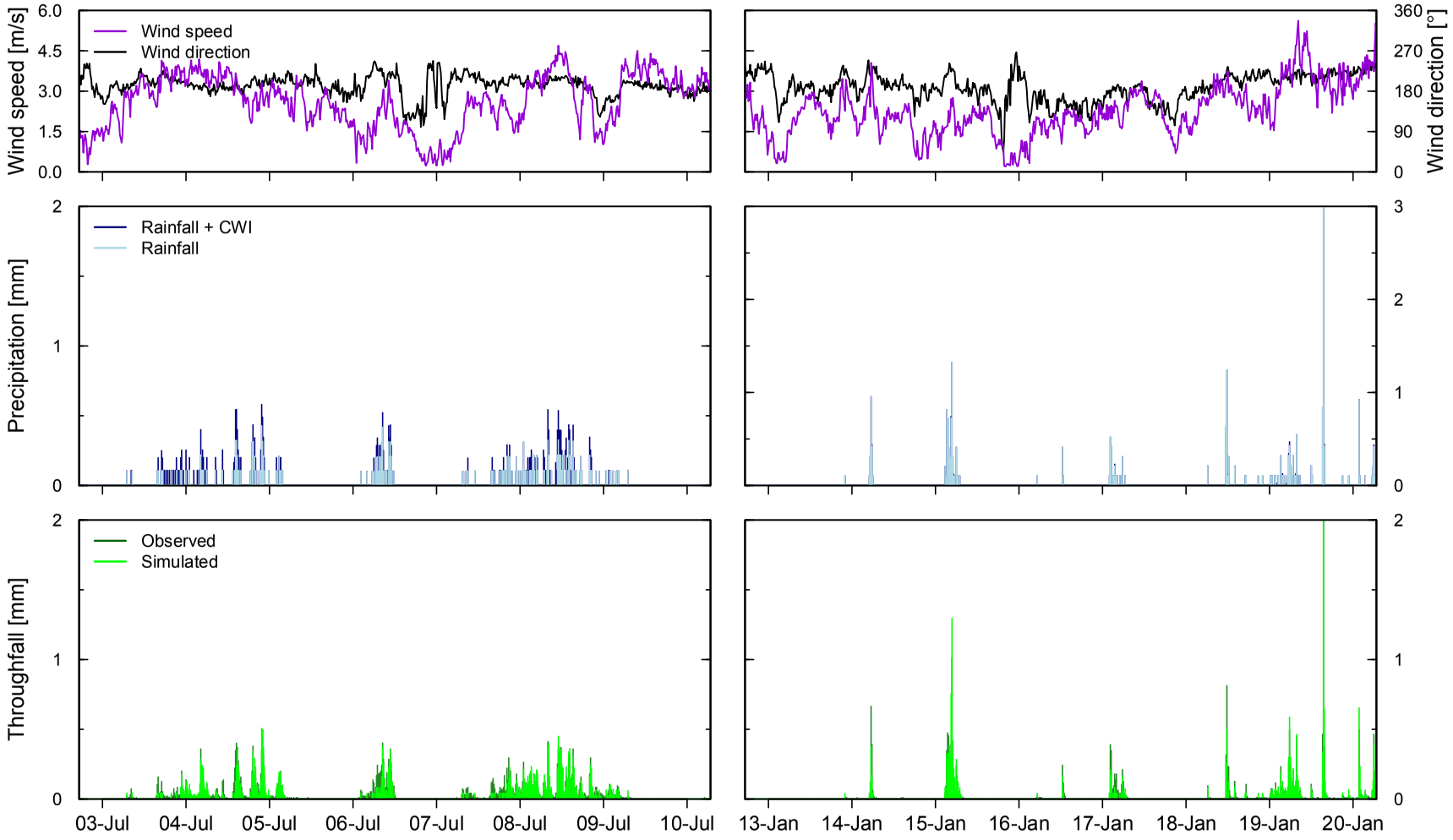

Figure 3.14: Climatic variables and modeled throughfall at 15-min time step during two months of the cool and hot seasons of the hydrological year 2013-2014.

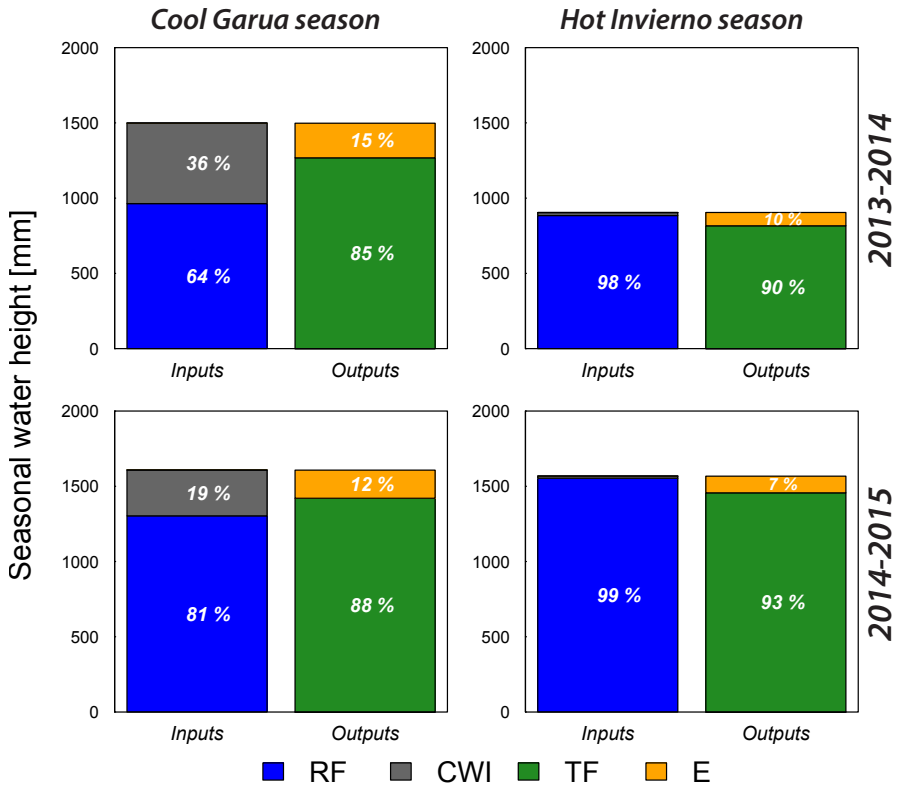

Figure 3.15: Seasonal canopy water balance summary during the two hydrological years of study 2013-2014 and 2014-2015. RF is rainfall corrected for sloping terrain, slope aspect and wind speed, CWI is cloud water interception by the canopy, TF is simulated throughfall and E is wet canopy evaporation.

Table 3.4: Canopy water balance variables at the study plots during the two hydrological years of study.

Variable	2013-2014	2014-2015
Rainfall* RF [mm]	1848	2857
Fog interception CWI [mm]	555	319
Wet canopy evaporation E [mm]	318	297
Throughfall TF [mm]	2085	2879

* Rainfall measured by rain gauge is corrected for sloping terrain, slope aspect and wind speed (Sharon, 1980).

reported by Pryet et al. (2012a)). However, the difference can be related to a larger dataset used in this study, which include both cool and hot seasons, difference in the methodology, and the larger presence of epiphytes observed in this forest. Despite small values of S associated with average values of p are attributed to a single storey tree architecture and sparse understorey vegetation (Pryet et al., 2012a), such as in the present study, the abundant presence of epiphytes may play an important role on the value of S. Indeed, they have a high water storage capacity, a slow drainage and their effect in throughfall differs to the structural components of the forest (Richardson et al., 2000; Villegas et al., 2008). The value of S found for the *Miconia* is comparable with the value of 1.92 mm reported by Holwerda et al. (2010) for a secondary cloud forest in Mexico and is the range (1.6-4.0 mm) reported by Herwitz (1985) for a tropical rainforest in Australia. Even though, cumulative throughfall might not be so sensitive to the drainage parameters (D_s and b), they provide a more accurate estimation of throughfall at such a small time step. Parameter fic shows the capacity of the canopy to intercept fog compared to artificial fog net. Despite this value is related to canopy characteristics such as height, size, orientation and leaves morphology; its significance remains related to the efficiency and capacity of the fog gauge to capture fog. Indeed, the efficiency of the fog gauge depends of the type, material and form (Villegas et al., 2008). Nevertheless, estimations of CWI by the vegetation would remain fair, because they are subject to the validation of the model.

3.2.5.2 Cloud water interception

Estimated CWI is negligible during the hot seasons while during the cool seasons it is significant. CWI represents 59% and 23% of the incident rainfall during the first and second cool season, respectively. These values are relative high comparing to studies reviewed by Bruijnzeel et al. (2011) (4% to 45%) and others reported by the literature (6%-31%) (Hutley et al., 1997; Holwerda et al., 2006; McJannet et al., 2007; Holwerda et al., 2010; Uehara and Kume, 2012). However, they are small compared to the value of 93% found by Cavelier and Goldstein (1989). Daily average CWI is 2.61 mm and 1.42 mm during the first and second cool seasons, respectively. Pryet et al. (2012a) estimated daily CWI of 1.18 mm for the same type of vegetation at a similar altitude (650 m a.s.l.) in another island of Galapagos during the 2010 cool season. This value can be comparable with the value found in the 2014 cool season of this study. Our estimates are within the range reported by the literature. Giambelluca et al. (2011) reported daily CWI of 0.43 mm for low shrubs and trees in Hawaii, Ritter et al. (2008) found values of 0.7 mm in a elfin laurel forest in Canary, Holwerda et al. (2006)

reported values of 2.14 mm for a 3 m tall Puerto Rican cloud forest, while Cavelier and Goldstein (1989) found values of 2.18 mm in a cloud forest in Colombia. Estimates of daily CWI reported by Uehara and Kume (2012), reach 3.26 mm for a dwarf coniferous shrub in the Japan Alps.

Estimates of CWI by the vegetation are contrasting between the two cool seasons. Difference between both seasons can be related to changes in the canopy structure or due to meteorological factors. Indeed, changes in the canopy structure are likely to happen between seasons. Aboal et al. (2000) found that heavy thinning of a pine forest in Tenerife (Canary Islands), led to a long-term decline in throghfall, in which throughfall showed to be significantly affected by its vegetation basal area and LAI. However, it should have a small effect on the CWI estimates of the vegetation given that CWI is a proportion of the quantity measured by the fog gauge and simulated cumulative throughfall remain close to the observed ones during both cool seasons. Given constant canopy characteristics, CWI is basically driven by the fog liquid water (LWC) content and wind speed intensity (Villegas et al., 2008). Villegas et al. (2008) reported that CWI is constraint at low LWC by limited fog availability and at high LWC by precipitation potential. The authors also concluded that optimal conditions for CWI are during medium values of LWC and wind speed. LWC was not measured in this study, nevertheless its presence can be assessed from wind speed measurements during CWI. Generally, for higher wind speeds, mean CWI increases at both cool seasons, but some difference can be identified (Fig. 3.16). At the first cool season, average CWI constantly increases with wind speed, even at high wind speed intensities. At the contrary, during the second cool season, the increasing reaches a plateau around 5 m/s and then it starts to decrease. CWI during the first season starts at lower values of wind speed than the second season. The plateau of CWI and its late start with lower wind speeds, suggest that LWC is lower than its optimal conditions, whereas LWC during the first seasons seems optimal, given that there is enough LWC at low wind speeds to be intercepted and at higher wind speeds it is still not reaches its peak. For this reason, we consider that the higher values of CWI during the first cool season are related to a higher presence of LWC that combined with the observed wind speeds enhances better conditions of CWI compared with the second season. Indeed, average values of meteorological variables of the two cool seasons are similar, except for temperature, which is significant lower during the first cool season (ca. 2 °C). Temperature could explain the difference in LWC, given that higher LWC is inversely related to the latent heat of condensation of water temperature (Thompson, 2007).

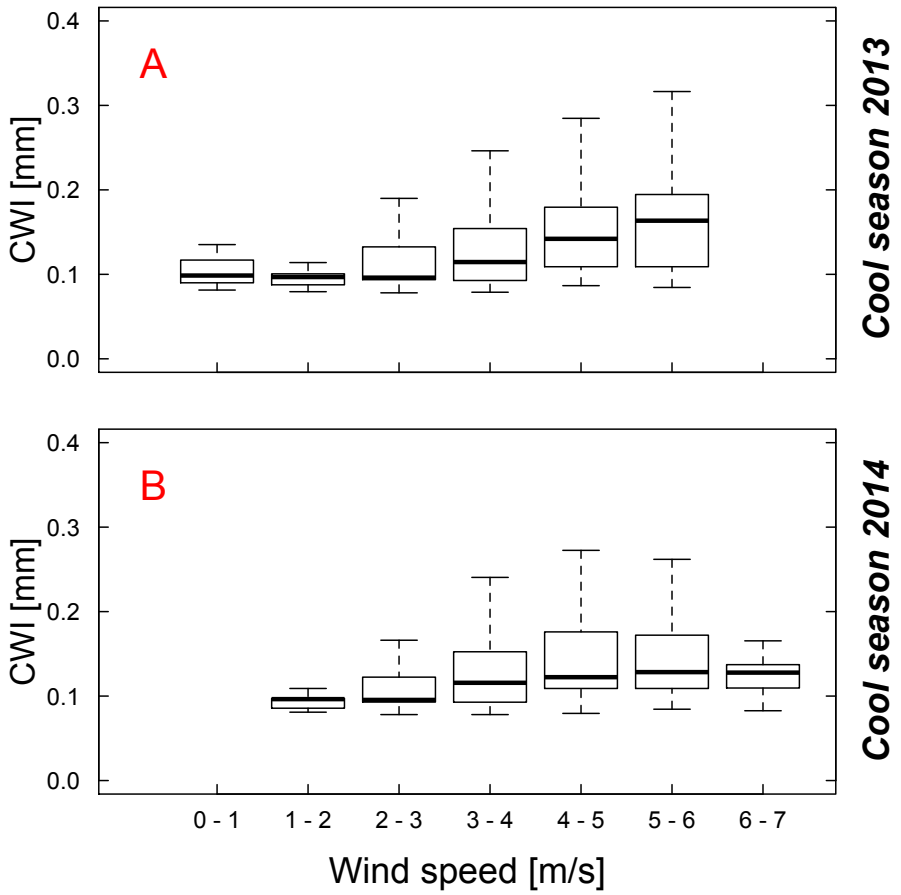

Figure 3.16: Statistic of CWI classified for wind speed intervals during the first (A) and second (B) cool seasons at the study site at 600 m of elevation.

3.2.5.3 Pertinence of the methodology

The proposed methodology is established on a physically based model, in which parameters and simulated values are confronted to real observations. Uncertainties in CWI should be highlighted, given that its estimation is subject to the propagation of errors from both sampling and modeling. It remains open the discussion about possible underestimation of wet canopy evaporation, which have been related to and underestimation of evaporation by the P-M equation caused by errors of measurement by the instrumentation (Frumau et al., 2006; Holwerda et al., 2010) and processes not considered in it (Scatena, 1990; Schellekens et al., 1999; Holwerda et al., 2010; van Dijk et al., 2015); or processes not considered in the canopy model (Murakami, 2007; Dunkerley, 2009). However these processes are difficult to overcome given the current instrumentation of this study. Indeed, an underestimation of evaporation will result in a reduction of the parameter fic in the calibration process, and therefore it would lead to an underestimation of CWI. Nevertheless, estimates of throughfall are consistent with observation in all seasons, including the hot season in which CWI is negligible. Given that estimates of evaporation by the model are consistent during all seasons, estimates of CWI should remain fair.

Fog inputs are introduced to the canopy model through a parameter (fic) that relates the capacity of fog interception between the canopy and the fog gauge. Though it might be a rough assumption it shows good results. Villegas et al. (2008) and Holwerda et al. (2011) reported that the amount of fog interception measured by fog gauges and by vegetation is significantly correlated. In this study we use throughfall only for validation purposes and not as inputs to estimate CWI (contrary to the methodology proposed by Pryet et al. (2012a)). This is a important advantage given that throughfall monitoring is challenging to maintain and continuous observations are hardly available. This method could be applied in a comparative study, in which estimates of CWI can be compared between different vegetation using the same fog gauge system. In this way, the canopy characteristics that influence CWI could be identified. Also a similar fog interception system in different areas in a region can lead to identification of the driving factors related to fog intensity.

3.2.6 Conclusions

We have proposed a methodology to estimate cloud water interception by the vegetation using a Rutter-type interception model. The approach requires the acquisition of input and calibration datasets. Inputs consist in continuous records of meteorological variables, which include cloud water interception using a fog

gauge system. Meanwhile, samples of throughfall are necessary for the calibration and validation of the model only and not as inputs in the model, which is an important advantage considering that continuous records of throughfall are challenging to obtain.

During two hydrological years (2013-2014 and 2014-2015), the model has been implemented in an endemic forest of the windward highlands of San Cristobal Island, in which the presence of fog is semi-permanent during half of the year. In these conditions, this is the first compiling approach for water balance estimation. Results show that CWI reaches 23% and 10% of the total water input of the first and second year, respectively. During the hot seasons, CWI is negligible (less than 1%), while it represents 37% and 19% of the water inputs during the first and second cool seasons, respectively. Despite similar wind speed intensities are observed in both cool seasons, the higher value of CWI in the first cool season compared to the second one (535 mm and 305 mm for the first and second year, respectively) is related to higher liquid water content in the air that combined with the observed wind speed intensities, leads to better conditions of CWI.

In this study we determined that CWI is a notably source of water in the highlands of the island, particularly during the first year which is consider to be an average year in terms of climate. Therefore, the role of vegetation in the highlands is important to the hydrology of the island. During the cool season, given the low intensity of throughfall contribution to the soil and the relative high infiltration capacity of it, CWI will most likely contribute to groundwater recharge. If climate change produces an increase in the temperature, and therefore a raise of the fog layer formation, which probably results in a reduction of fog occurrence, and land use change from the endemic forest to pasture still occurs on the highlands; it would most probably induce a reduction of net precipitation, and hence a reduction of discharge of the downwards rivers originated from springs.

3.3 Analysis of soil water transfer along the windward slope of San Cristobal

3.3.1 Soil water tranfer model in stations SC300 and SC600

3.3.1.1 Soil monitoring and model implementation

Soil water suction monitoring was performed below the grass next to weather stations SC300 and SC600 by means of tensiometers. At both sites, tensiometers were installed along a vertical profile (Fig. 3.17): i) three automatic UMS T8 tensiometer probes connected to a datalogger with 15-minutes time step records at 25, 40 and 55 cm of depth and; 2) weekly manual measurements with 16 SDEC SMS tensiometer probes. The manual tensiometers reach 8 different depths (15, 25, 40, 50, 70, 100, 150, 200 cm) and are split in two series to duplicate measure at each depth. Automatic tensiometers are used to have a detailed view of rainfall events and they are also used as constraints of the soil water transfer model. Depths of automatic tensiometers are related to the expected depth of roots. Manual tensiometers were used for the validation of the automatic ones and to measure deeper soil levels.

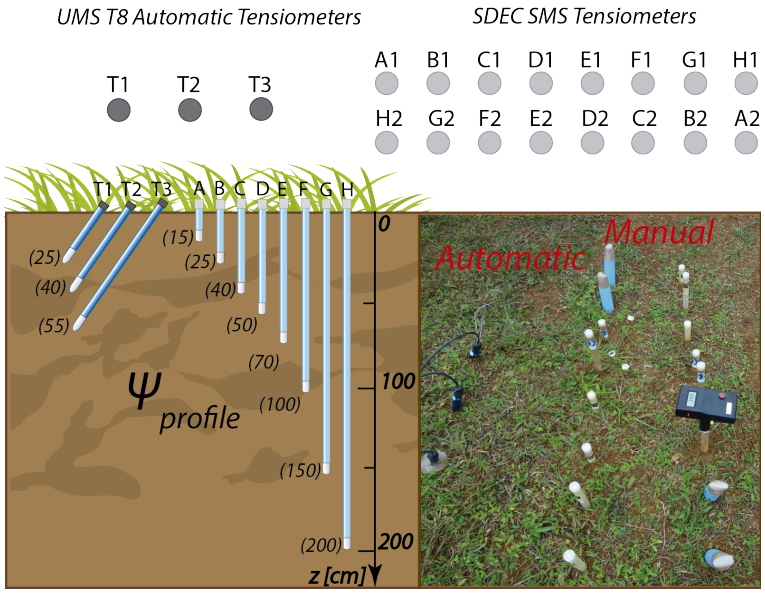

Figure 3.17: Schematic view of soil monitoring at stations SC300 and SC600. Three automatic tensiometers and 16 tensiometer probes were installed at different depths. Tensiometer probes have 8 lengths into two parallel aligments.

Given the small grass canopy cover, some assumptions are made during rainfall events contrary to the joint model in section 2.4: i) wet canopy evaporation rates in the grass should remain low given the small canopy cover and height

of grass (ca. 13 cm); ii) because of the small grass canopy cover, soil evaporation might be consider, but it should be somehow comparable to the wet canopy evaporation; and iii) given the PM equation, grass canopy evaporation should be driven mainly by the radiation term because of low vapor pressure deficit conditions (Brauman et al., 2012), in such case, the estimation of transpiration should be comparable to the one of evaporation. Given the above assumptions, we do not consider the canopy compartment in the grass, and the joint model is simplified to a soil model, in which rainfall is used as input and instead of evaporation of wet canopy during rainfall, the transpiration rate is used. Due to this simplification, canopy parameters are not used, except for r_s (which influence is related to the soil not to the canopy).

The soil model is implemented using constant soil parameters during the two hydrological years. Similar to section 2.4, a fixed transient flow at the top and free drainage at the bottom are used as boundary conditions. Soil depth is unknown at both sites, however it should be larger than 3 m (derived from observations). In the view that maximum depth of tensiometer is 2 m, soil depth used in the model is 2.2 m at both sites. The soil column is discretized into 110 slices (0.02 m each). Considering soil observations, four layers are used in the model (0-0.3 m, 0.3-0.5 m, 0.5-0.9 m, 0.9-2.2 m) with roots evenly distributed until 0.6 m of depth. The values of h_{wp} and h_{fc} (-15 m and -1.03 m), were taken from Van Genuchten (1980), and Armas-Espinel et al. (2003) for volcanic soils, respectively.

The soil parameters (K_{sat}, θ_r, α, n) and the canopy surface resistance r_s are calibrated using the OMWLS method between the simulated and observed pressure head during a 95-days calibration period. This period contains several rainfall events and a dry period. θ_s in all layers is used a fixed parameter to reduced the number of calibration parameters. Values are used from the soil samples taken on both stations. For a detailed description of the soil water transfer model and the calibration process see section 2.4.

3.3.1.2 Calibrated parameters and simulation

Calibrated values of soil parameters and r_s are detailed in table 3.5. Estimated r_s are 251 and 386 sm^{-1} at SC300 and SC600, respectively. r_s at SC300 is higher at SC300 than at SC600. It should be related to higher density of grass observed in SC300. It was also observed other species of small vegetation besides the grass that could increase the value of r_s. Compared to the pasture of Santa Cruz at 400 m of elevation (section 2.4), r_s at 300 m of elevation is similar. This is a consequence of different root depths used in the model at each location, and overall to the soil characteristics. Estimated r_s at both locations are within the

range reported in the literature for grass (Parton et al., 1981; Campbell, 1989; Brauman et al., 2012).

Soil parameters at each location have similar values between layers, except for α which is the more variable. Most importantly, calibrated parameters are similar to values derived from the pF curves analysis and permeability test of samples taken on both locations (Tb. 2.3). K_{sat} at SC300 is significantly higher than at SC600. It corresponds well to the results reported by Adelinet et al. (2007), in which reduced porosity and permeability are related to weathering process, which is more important at higher elevation. It was also reported by Taboada et al. (2016), where they included orientation as one of the factors affecting the degree of weathering.

The simulated pressure heads are in agreement with the observations at both locations during most of the study period (Fig. 3.18). This is especially seen with the observations from the automatic measurements (depth 25, 40 and 55 cm). Statistics are shown in table 3.6. Simulations are less accurate depending of the depth during dry periods (two observed in the two years). This could be related to several factors: change in vegetation, root movement to lower levels, root adhering to tensiometers, hysteresis effect or change in soil properties. However, given that these periods represent less than 10% of the two years, it is expected that any inaccuracy during this time has a weak effect on the general estimations. After the first dry period in March, simulations are biased in station SC300. This is also observed at depth of 25 cm in station SC600. Hysteris would be most likely be cause, however the discrepancy remains even after several storm events, and after a second dry period a new discrepancy is observed. Even though, these changes could be related to a change in transpiration demand due to changes in vegetation this is not the case because transpiration is influential when the soil is dry, but the bias occurs even in wet conditions. So this discrepancy is more likely related to changes in the soil properties. Indeed, given the clay content of these soils, it was observed shrinking of soil during the dry periods resulting in small fissures (more noticeable in SC300). Then, after rainfall soils swelled up. This behavior has been reported in other volcanic soils with high clay content (El-Swaify, S., 1980; Malik, 1990; Armas-Espinel et al., 2003; Dörner et al., 2009). The model cannot simulate this dynamic poro-elastic behavior and several calibrations would be necessary. However, this should not affect deep percolation estimations because it only occurs at the highest layers which have a small thickness comparing to the layers below. It was also reported in section 2.4 that despite soil hydrodynamic properties are influential in pressure head, they have a small effect on the cumulative deep percolation rates. It should be highlighted how two-years monitoring and the use of a model reveal

Table 3.5: Parameters used in the soil water transfer model in stations SC300 and SC600. Parameters are estimated from calibration using the *Guauss-Levenberg-Marquadt* algorithm. Estimated errors corresponding to a 95% of confidence level are not shown given their low values.

Depth [cm]	Parameter	SC300	SC600
	r_s [s m^{-1}]	251	386
	$Ksat$ [m s^{-1}]	1.1×10^{-4}	1.4×10^{-5}
	θ_s*	0.63	0.55
(0-30)	θ_r	0.39	0.42
	α [m^{-1}]	28.5	12.5
	n	1.1	2.3
	$Ksat$ [m s^{-1}]	1.6×10^{-4}	1.1×10^{-5}
	θ_s*	0.64	0.45
(30-50)	θ_r	0.44	0.35
	α [m^{-1}]	3.3	1.1
	n	3.5	1.7
	$Ksat$ [m s^{-1}]	7.2×10^{-5}	4.7×10^{-6}
	θ_s*	0.63	0.57
(50-90)	θ_r	0.39	0.31
	α [m^{-1}]	11.0	5.6
	n	1.7	3.0
	$Ksat$ [m s^{-1}]	7.5×10^{-5}	6.1×10^{-6}
	θ_s*	0.61	0.57
(>90)	θ_r	0.50	0.29
	α [m^{-1}]	12.3	9.6
	n	1.5	3.3

* Fixed parameter derived from soil samples (section 2.3.2.3).

Table 3.6: RMSE of simulated pressure heads from the soil water transfer model in stations SC300 and SC600.

	SC300		SC600	
Depth [cm]	n	RMSE [cm]	n	RMSE [cm]
0-200*	26657	7.0	25480	6.0
15	4	0.6	7	1.6
25	8881	4.8	8488	7.5
40	8881	5.7	8488	5.1
55	8881	9.6	8488	4.8
70	6	1.5	6	1.9
100	5	1.3	6	1.3
150	3	1.7	–	–
200	–	–	3	1.2

* Includes all depths below

the dynamic entity that the soil really is.

3.3.2 Joint canopy and soil model in station SC600

3.3.2.1 Monitoring and model implementation

Similar to section 2.4 in Santa Cruz, the joint model is used at SC600 in the plot below the *Miconia* forest. Simplifications used in section 3.3.1 were not used given the importance of the canopy compartment to intercept fog and to partionate evaporation and transpiration (in this case, both rates should be more contrasted). Soil water suction monitoring was performed with weekly manual measurements only, due to lack of automatic equipment. 8 SDEC SMS tensiometer probes were used at 4 depths: 15, 25, 40, 50 cm (Fig. 3.19).

Joint canopy and soil model is implemented using constant canopy and soil parameters during the two hydrological years. A fixed transient flow at the top and free drainage at the bottom are used as boundary conditions. However, the flux at the top is the output of throughfall from the canopy model. Given the reduced number of observations for calibration and expected similarities between the soil next to the weather station and the soil below the forest; the same geometry, number of layers and length of roots were used. Despite the length of roots in the forest might be expected to be larger than the one in the grass, given the wet climatic conditions in this zone, roots are expected to be shallow. Indeed, on the highlands of Santa Cruz island, given the slight deep of soils ($<$ 30 cm), the roots of these forest are very shallow, which probes that they do not need to reach deeper levels. Several soil parameters were fixed to the ones

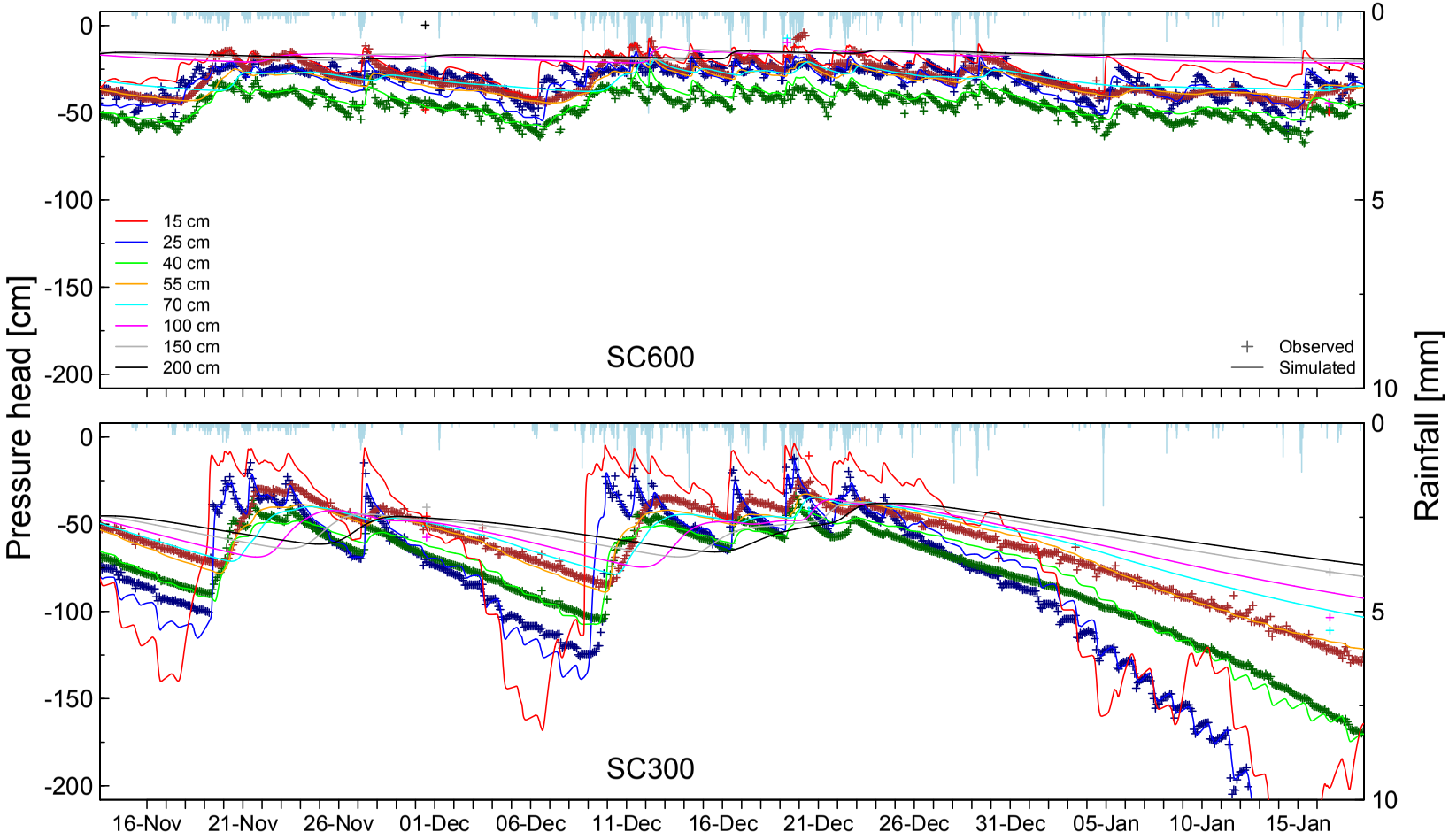

Figure 3.18: Results from the soil water transfer model at 15 minutes time step during 60 days representative of the cool and hot seasons at stations SC300 and SC600. Crosses represent observed pressure heads at different dephts, while lines are simulated values.

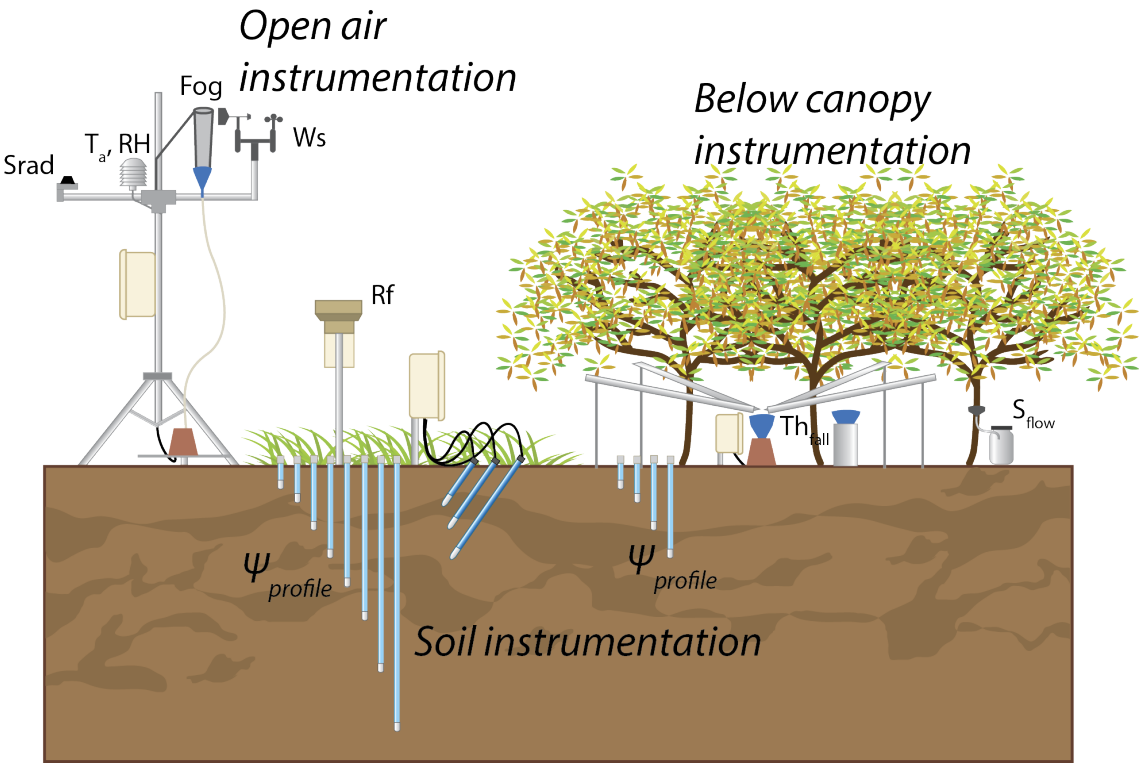

Figure 3.19: Diagram representing the instrumental device of monitoring at station SC600. At a grass land cover, a weather station was placed on the open area. At the *Miconia* forest, net precipitation instrumentation was installed under the canopy. At both sites, soil water suction instrumentation was positioned under the vegetation.

Table 3.7: Parameters calibration in the joint canopy and soil water transfer model in the forest at SC600. Parameters are estimated from calibration using the *Guauss-Levenberg-Marquadt* algorithm. Estimated errors correspond to a 95% of confidence level. The rest of parameters used in the model are from calibration in section 3.2 and section 3.3.1.

Depth [cm]	Parameter	SC600f
	r_s* [s m^{-1}]	108(55)
(0-30)	$Ksat$ [m s^{-1}]	1.43 (0.13)$\times 10^{-5}$
	θ_r	0.49 (0.03)
(30-50)	$Ksat$ [m s^{-1}]	1.11 (0.05)$\times 10^{-5}$
	θ_r	0.27 (0.03)
(50-90)	$Ksat$ [m s^{-1}]	5.19 (0.31)$\times 10^{-6}$
	θ_r	0.21 (0.10)

* Surface resistance of the *Miconia* forest

calibrated from the first soil. Besides the canopy parameter r_s, only parameters K_{sat} and θ_r from the first three layers were calibrated. The rest of parameters were used from the calibration in section 3.2 and section 3.3.1 for canopy and soil parameters, respectively.

3.3.2.2 Calibrated parameters and simulation

Calibrated soil parameters in the forest have similar values to the ones in the grass. Slight differences are expected given the proximity. Moreover, in section 2.4, it was also observed slight differences in soil parameters between a forest and pasture in Santa Cruz. Nevertheless, in section 3.3.1 changes in the soil properties are observed for the same soil after dry conditions. This might also affect the calibration given that the period used included one dry period. r_s for the *Miconia* forest is 108 s/m, which is significantly different to the value from the grass (396 s/m). The difference is also expected given the density and height of the forest. However, the error for the estimation of this parameter is significant.

Simulation of pressure heads is also poor (Fig. 3.20). RMSE is 284 cm ($n = 20$), 57 cm ($n = 24$), 119 cm ($n = 24$) and 56 cm ($n = 24$) at depths 15 cm, 25 cm, 40 cm and 55 cm, respectively. This is a consequence of the limited number of observations used in the calibration and because several observations were from the dry period where larger errors between simulations and observations are expected. Indeed, pressure head in the upper part of the soil is hard to fit due to the strong interaction of the soil with rainfall, evapotran-

spiration, wind and changes in the root distribution (Tournebize et al., 2012). Moreover, observations of pressure head from manual tensiometers are not quite reliable as automatic considering that they are subject to preferential flow during rainfall events (as they are installed vertically), difficulties during measurements and installation. Therefore, their tendencies should be considered rather than their absolute values. This shows evidence that a quite number of observations is necessary to properly characterize the soil with this methodology. Despite soil properties may have small influence over the cumulative deep percolation as reported in section 2.4 and thus their uncertainties may be overcome, this could not be the case for surface resistance. Indeed, r_s is the parameter controlling the transpiration rate, therefore affecting its quantity. In such case, the representativity of transpiration in the water balance should be evaluated.

3.3.3 Water balance and soil hydrodynamic

3.3.3.1 Water balance

Water balance is performed during the two hydrological years in the three sites of study (Fig. 3.21). Site SC300 in the grass at mid-elevation and at the highlands, sites SC600g and SC600f in the grass and endemic forest, respectively. Canopy water balance was already reported in section 3.2, while rainfall inputs in SC300 and SC600g were already reported in table 3.1. Water balance summary at three sites can be seen in table 3.8. As expected, transpiration is higher at SC300 due to a higher evaporative demand and its higher potential (result of a lower r_s). At 600 m of elevation, transpiration rates are contrasting between the grass and forest. At the forest, transpiration is reduced from its potential due to wet canopy conditions. However, wet canopy evaporation is important at the forest and its larger than transpiration at the grass. Therefore, evapotranspiration (sum of evaporation and transpiration) is higher than the one at the grass. Nevertheless, outputs of evapotranspiration (ETa) at the forest are compensated by inputs of fog interception, which results in higher deep percolation (DP) at the forest. Deep percolation at 600 m of elevation is considerable larger than at 300 m of elevation. At 600 m of elevation, DP is even higher at the forest than the grass, it is especially noticed during the months of the cool season (Fig. 3.22).

Between years, ETa remains similar while rainfall inputs are markedly different, which results in contrasting deep percolation rates between years. Analyzing the first year, which is considered the most representative compared to the long term records, transpiration and fog interception play a more significant role in the water balance. In this matter, a better estimation is essential to assess recharge rates. In section 3.1.2.3, ETo was estimated at 678 mm and 527 mm for the first

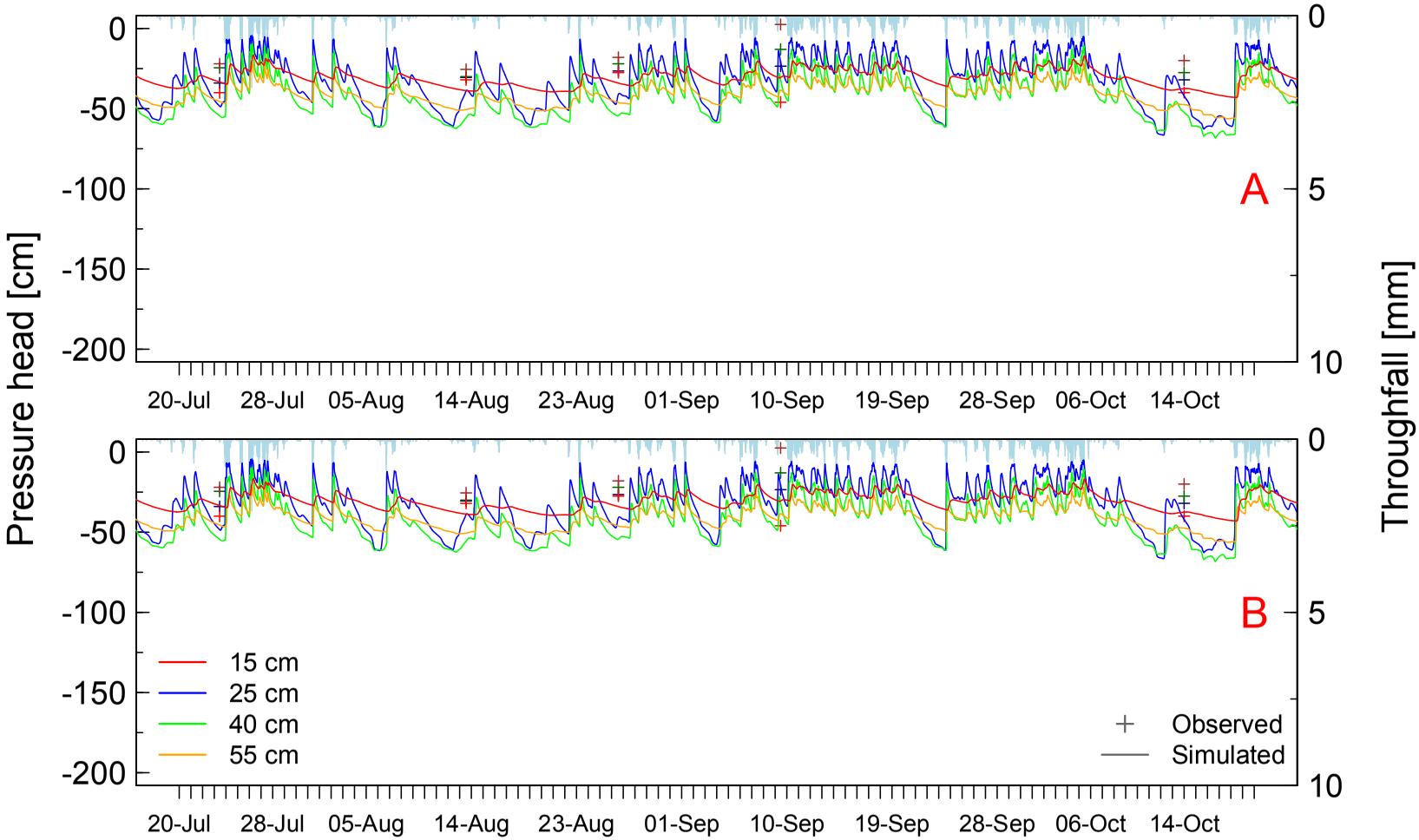

Figure 3.20: Results from the joint canopy and soil model at 15 minutes time step during 3 months of the hot (A) and cool (B) seasons under the endemic forest during the hydrological year 2013-2014. Crosses represent observed pressure heads at different dephts, while lines are simulated values.

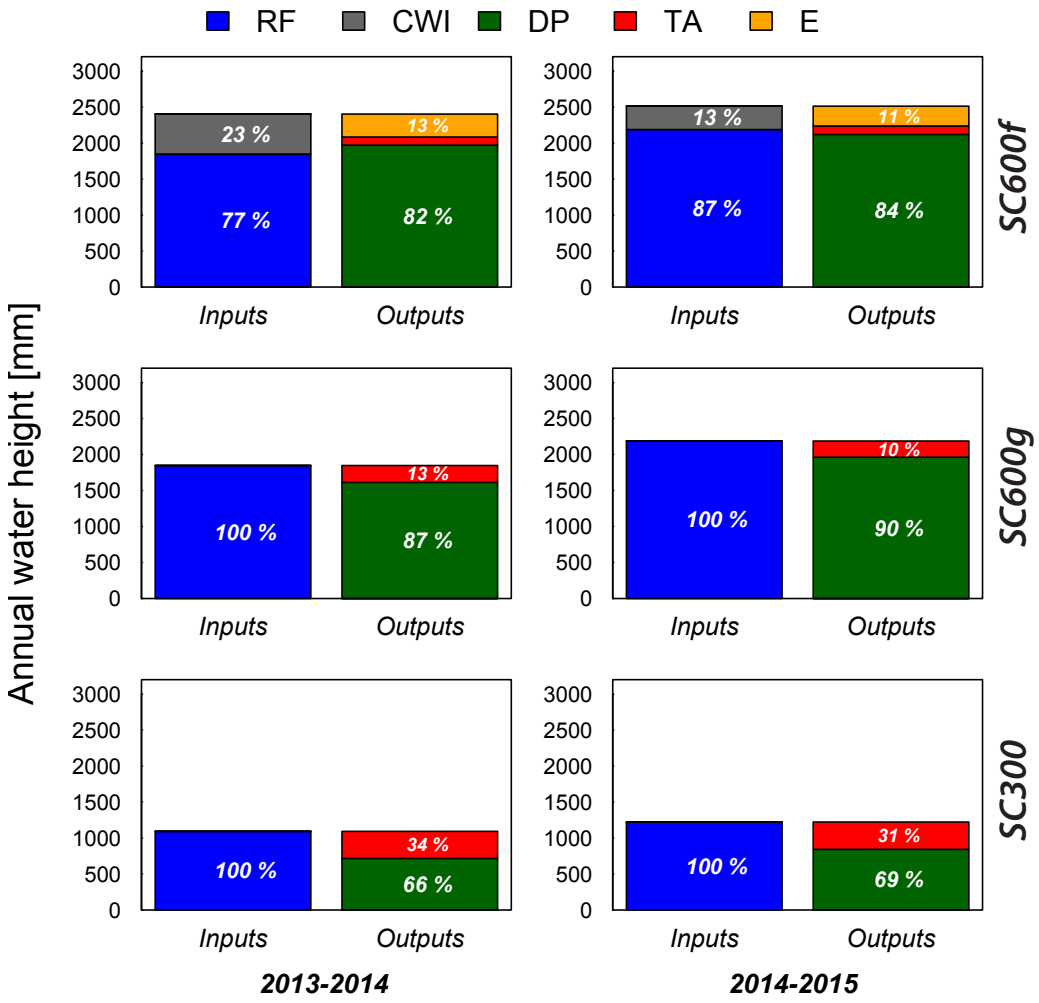

Figure 3.21: Annual canopy and soil water balance at stations SC300, SC600g and SC600f during two hydrological years (2013-2014 and 2014-2015). RF is rainfall corrected for sloping terrain, slope aspect and wind speed. CWI and E are cloud water interception by the canopy and wet canopy evaporation estimated from the interception model, respectively. TA is actual transpiration reduced from its potential due to wet canopy and soil stress water conditions. DP is deep percolation obtained from the water budget. CWI and E are neglected in the water budget at the grass (SC300 and SC600g). Runoff is negligible on all sites.

Table 3.8: Cumulated water balance variables at sites SC300, SC600g and SC600f during the two hydrological years of study. Site SC300 corresponds to grass at mid-elevation, while sites SC600g and SC600f correspond to grass and forest at the highlands, respectively.

	SC300		SC600g		SC600f	
Variable	2013-2014	2014-2015	2013-2014	2014-2015	2013-2014	2014-2015
Rainfall[a]	1093	1929	1848	2857	1848	2857
CWI[b]	0	0	0	0	555	319
Evaporation[c]	0	0	0	0	318	298
Runoff	0	0	0	3	0	7
transpiration[d]	376	436	233	252	77	80
Deep percolation	717	1493	1615	2605	2005	2791

[a] Rainfall measured by rain gauge is corrected for sloping terrain, slope aspect and wind speed (Sharon, 1980).
[b] Cloud water interception by the canopy is considered negligible at grass.
[c] Wet canopy evaporation at grass is considered negligible.
[d] Transpiration is reduced from its potential value due to wet canopy and soil water stress conditions.

year at SC300 and SC600, respectively. This means that ETo represents 182% of ETa at 300 m of elevation, resulting in an underestimation of deep percolation of 58%. It is still under discussion the representativity of grass transpiration at this elevation given other land covers which potentially have larger transpiration rates. At the highlands, the grass and forest studied are a fine representation of the vegetation at this altitude. At the grass, the use of ETo would represent an underestimation of 18% in deep percolation. At the forest, ETa is lower than ETo but the difference is not as significant as the one in the grass. However, fog interception is considerable. Using ETo and not considering CWI would represent an underestimation of 33% in deep percolation.

3.3.3.2 Soil hydrodynamics

Figure 3.18, figure 3.20 and figure 3.22 show the contrasting behavior in the soil hydrodynamic due to seasonality, altitude and land use. At the highlands, pressure heads show that the soil remains constantly wet along the whole soil profile during large wet periods. This is a consequence of the constant water input to the soil during the intense wet climatic conditions at this altitude, which is evidenced in the regularity of deep percolation rates. At mid-elevation, the soil is more reactive to the climatic conditions, which is observed in the variability of the pressure head along its profile (especially near the surface). The higher evapotranspiration and lower rainfall inputs, due to drier climatic conditions at this altitude, reduce deep percolation rates. During long-dry periods, there is not deep percolation in soils at mid-elevation, while soils in the highlands, maintain

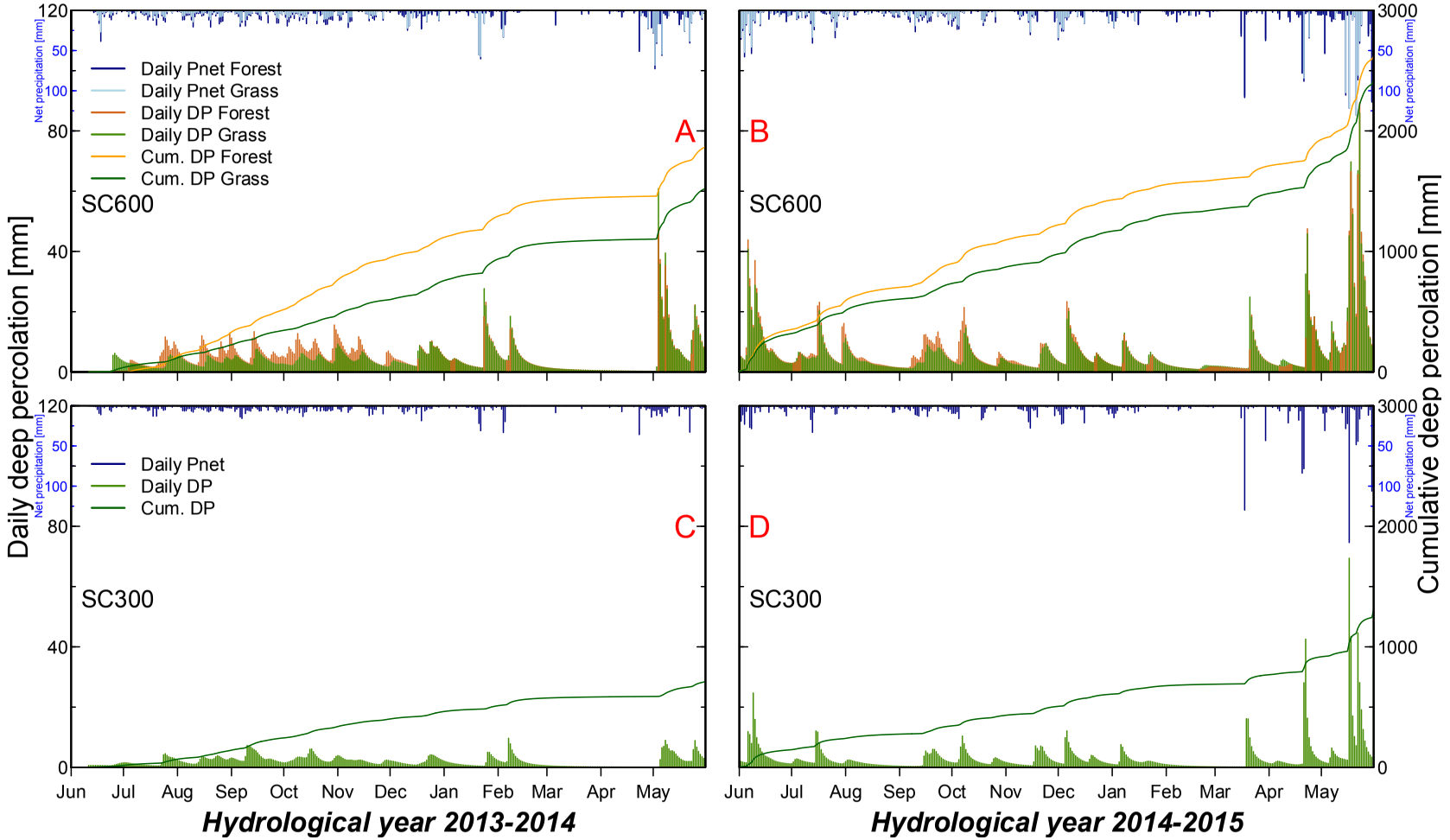

Figure 3.22: Daily (bars) and cumulative (lines) deep percolation (DP) at stations SC600g (A,B), SC600f (A,B) and SC300 (C,D) during the first 2013-2014 (A,C) and second 2014-2015 (B,D) year of study. Deep percolation reacts to net precipitation inputs, which is incident rainfall at SC300 and SC600g and simulated throughfall at SC600g.

a weak rate of deep percolation. This might be consequence of the higher storage capacity and lower hydraulic conductivity of these soils that yield a weak long-lasting drainage. Given the similar hydraulic properties of soils of the forest and grass at the highlands and similar evapotraspiration rates, the difference in the hydrodynamic behaviour of these soils is related to the water input, which only difference is fog interception. Indeed, fog interception increases the water input in the forest. This is noticeable in the slope of the cummulative deep percolation curve during the cool seasons (Fig. 3.22), whereas during the hot seasons these curves increases in a similar rate.

3.4 Spatialization of recharge/deep percolation at watershed scale

3.4.1 Method

Several methods have been used to estimate recharge at a regional scale. Levine and Salvucci (1999) estimated groundwater recharge distribution in a Canadian prairie using a regional groundwater model from measurements of the water table. Another complex approach is the one proposed by Adar et al. (1988), based on a mathematical model, Adar et al. (1988) estimate the spatial distribution of recharge rates into an aquifer in Arizona (USA) using environmental isotopes and hydrochemical measurements. Despite these methods have succeeded applied in relative plane regions, it would be difficult to assess their applicability in region with strong reliefs and with high rainfall spatial variability, such as islands. The most common approach to estimate regional recharge is through the spatialization of punctual soil water budgets. This method have been successfully applied in others islands such as Hawaii (Giambelluca, 1986; Engott and Vana, 2007; Izuka et al., 2010), La Gomera (Canary) (Izquierdo et al., 2010) and Taiwan (Lee et al., 2006). These methods use data from simple soil water balance at different points and then these values are extrapolated for the entire region usually using geostatistical tools such as kriging.

In the case of San Cristobal, an accurate regional spatialization of recharge is challenging given the limited number of spatial data (in this section recharge is still considered as deep percolation). However, at a smaller scale (e.g. small hydrological basins at the southern side of San Cristobal), it is more pertinent and results can remain fair because of the relative stable conditions observed (section 3.1.2.1). To make it simpler, spatial distribution of recharge in the windward side of San Cristobal is limited to altitude and a simple linear regression based on the orographic gradient of rainfall, fog and evapotranspiration is used.

However, in order to consider fog interception, two additional points are contemplated: i) slope aspect distribution, and ii) a spatial distribution of land cover based on two distinctive vegetation categories: forest and grass. The latter might be consider a rough categorization because in reality the heterogeneity of vegetation species is larger than just these two (especially a mid-elevation). However, we expect that the heterogeneity of vegetation species have a small effect on the overall calculation at the watershed scale, thus the additional work to identify several land covers might not be justified.

The three basins of study, (*El Bayo*, *Chuki Marka* and *Cerro Gato*) previously defined (section 2.2.1), located at the windward side are used for this case.

Elevation and slope aspect data are extracted from the DEM (IGM, 2014) as rasters. The two land cover categories are interpreted from high resolution images (IGM, 2014) and then it is rasterized with the same resolution as the rasters of elevation and slope aspect (Fig. 3.23).

Calculations at each point are performed based on the following considerations:

- Rainfall distribution is only a function of the altitude, and it is independent of the slope aspect and vegetation. At each point, it is calculated from a linear interpolation from rainfall data of stations SC300 and SC600 (to simplify, station SC000 is not considered because the watersheds are located between 200 and 650 m of elevation), reaching a plateau at 600 m of elevation.

- Actual evapotranspiration depends of vegetation, therefore two gradients are used (one for each vegetation type). ETa data from the soil water transfers and joint model used in stations SC300 and SC600 is used. However, ETa data from a forest at SC300 is missing. To consider the same approach, once more the soil water transfers model is performed at SC300 for a forest using the same soil calibrated parameters estimated for the grass but using a different surface resistance to estimate ETa. r_s estimated in section 2.4 for the secondary forest at Santa Cruz Island is used. This is a fair assumption considering that secondary forest in Santa Cruz are similar to the ones observed in San Cristobal. ETa has also a plateau at 600 m of elevation.

- Fog interception only occurs at the forest land cover (not in the grass) and when the slope aspect is between a range of 60° from the mean wind direction (which is 190° using data of SC300 and SC600). It also has a gradient (Pryet, 2011) which starts at 350 m of elevation (the lower boundary of fog has been observed between 300 and 400 m of elevation) and a plateau at 600 m of elevation.

Finally, recharge is considered as the difference between the inputs of rainfall and fog interception and the output which is evapotranspiration.

3.4.2 Results and discussion

Recharge distribution can be observed in figure 3.24. In the lower basins, *Chuki Marka* (outlet at 239 m a.s.l.) and *Cerro Gato* (outlet at 220 m a.s.l.), recharge is more affected by altitude, while the upper basin, *El Bayo* (outlet at 520 m a.s.l.), it is more influenced by the vegetation distribution and the slope aspect. The

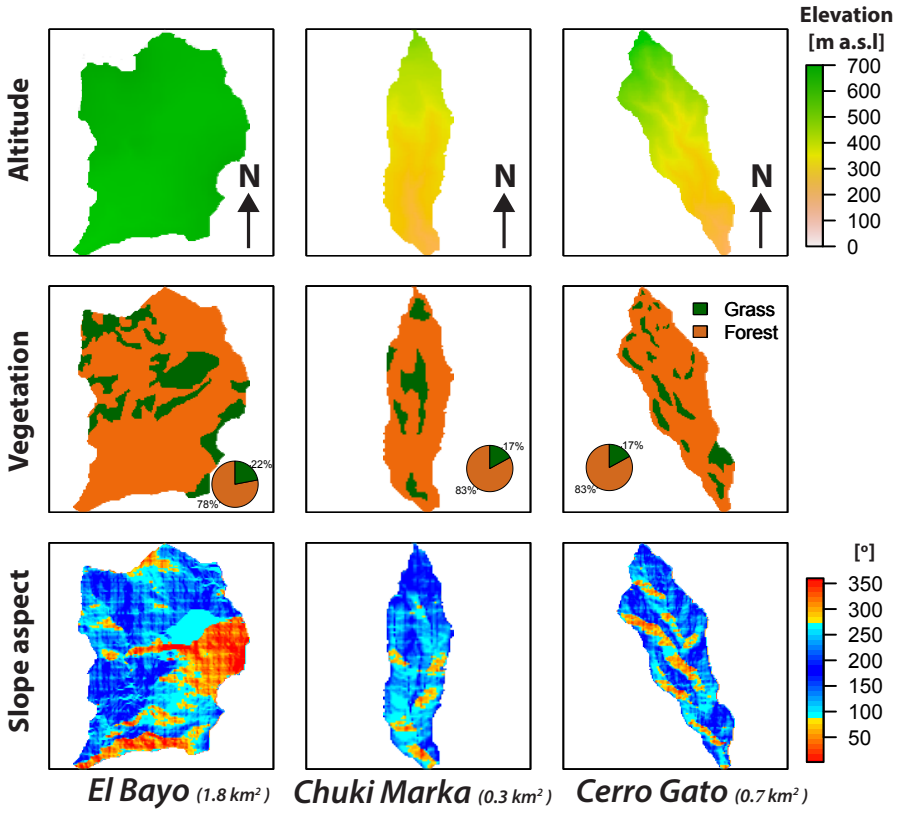

Figure 3.23: Spatial distribution of altitude, vegetation and slope aspect which are involved in the estimation of recharge at the basin scale. Fog interception is limited to zones higher than 350 m of elevation, with forest and with slope aspect in the blue range.

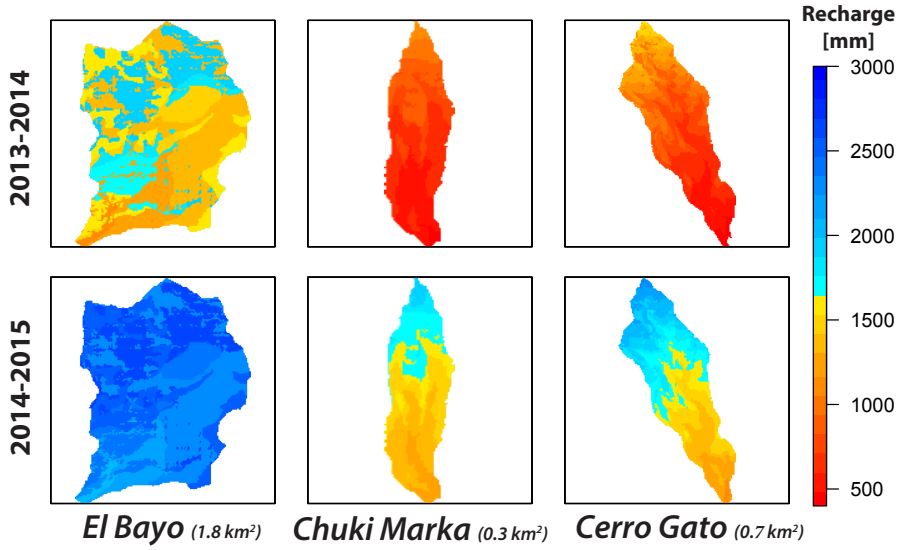

Figure 3.24: Annual recharge spatial distribution at three basins of study for the 2013-2014 hydrological year (uper-series) and the 2014-2015 hydrological year (lower series). Recharge at the second hydrological year is markedly higher than the first year in all basins.

latter is expected considering the small difference in altitude along this basin, and the marked difference observed in deep percolation between forest and pasture at SC600 (section 3.3.3.1). This difference can also be observed at the upper part of *Cerro Gato*. Mean recharge at each basin can be observed in table 3.9. As expected, the basins that reach higher altitudes are the ones with the higher recharge.

Comparing recharge estimates with this approach and a simple approach that considers only the rainfall and evapotranspiration gradients, and evapotranspiration is estimated as ETo (section 3.1.2.3); the difference is marked (Fig. 3.25 and

Table 3.9: Estimated mean water balance variables of three gauged basins during the two hydrological years of study.

Basin	Year[a]	Rainfall	CWI[b]	ETa[c]	Recharge
El Bayo	1	1735	180	390	1525
	2	2722	103	398	2427
Chuki Marka	1	1148	7	465	690
	2	2006	4	519	1491
Cerro Gato	1	1241	41	455	826
	2	2120	23	502	1641

[a] Year 1 and 2 correspond to the hydrological year 2013-2014 and 2014-2015, respectively.
[b] CWI corresponds to cloud water interception by the canopy.
[c] ETa corresponds to the sum of wet canopy evaporation and actual transpiration.

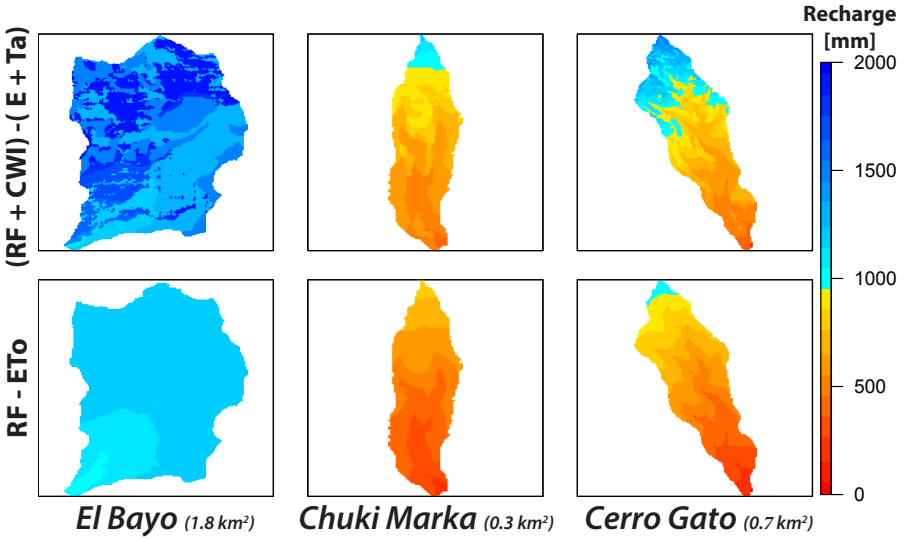

Figure 3.25: Comparison of recharge at three basins of study with two methods. In the upper maps, recharge is estimated using inputs of rainfall and cloud water interception, and outputs of wet canopy evaporation and actual transpiration. In the lower maps, recharge is estimated using rainfall and the referential evapotranspiration

Tb. 3.9). Taking the first year for example, with the simple approach compared to the one used, recharge is underestimated by 22%, 30% and 28% at *El Bayo*, *Chuki Marka* and *Cerro Gato*, respectively. This corresponds to ca. 260 mm less water input at each basin. This underestimation can have serious implications in an hydrogeological point of view. If a water balance at watershed scale is performed, and there is an underestimation of the water input, it can lead to an overestimation of the hydrogeological basin or to a misunderstanding of intercatchment groundwater flow. It should be noticed, that ETa estimates also include a reduction due to soil water stress conditions. Using potential transpiration estimated thanks to the soil water transfer model, the simple approach still underestimate recharge considerably (17%, 8% and 13% at *El Bayo*, *Chuki Marka* and *Cerro Gato*, respectively), especially at the basins that reach high elevations.

At watershed scale, fog interception input is not as big as expected. At the two lower basins, it is very low reaching 1% and 4% at *Chuki Marka* and *Cerro Gato* watersheds, respectively, while it reaches 9% of the total input at *El Bayo*. However, a relative large surface of *El Bayo* is covered by the large cone of *El Junco*, reducing the surface subject to fog interception. Another reason to the reduction of fog interception in these watersheds is the consideration of an elevation gradient, which starts at zero. Intensity of fog related to altitude is still not fully understood. Even though a fog interception gradient could be expected given a wind speed gradient, it might be smaller and starting from a higher value

rather than zero. Indeed, during the wet months of the cool season, a reduced gradient in rainfall between stations SC300 and SC600 is observed (Fig. 3.2), suggesting similar conditions between both altitudes. In terms of water management for this island, fog interception should be considered. It appears fog interception contribution for *Cerro Gato* basin is small. Thus, water supplied from this catchment might not suffer in case of land use change. However, this is not the case for the other two sources of water used to supply water to the inhabitants (*La Toma* and *El Platano*), which are located at the highlands (Fig. 2.16). Indeed, their watersheds are highly covered by *Miconias* and their surface are more exposed to the prevailing winds.

Finally, considering the surface of each watershed and a constant rate of recharge during the first year, the representative one, recharge rate at each basin is 86, 7 and 18 l/s at *El Bayo*, *Chuki Marka* and *Cerro Gato*, respectively. At the watershed scale, considering a simple water balance, the mean water discharge measured in the outlet of these watersheds should be close to the values of recharge rate estimated for each watershed if there are not losses or gains of water for groundwater inter-exchange with neighbors watersheds. If this difference is considerable in a watershed, then, groundwater inter-exchange should be evaluated.

Conclusion

In this chapter, we used the dataset from the climatic stations installed along the windward side of San Cristobal to estimate recharge from plot to watershed scale using a canopy-soil water budget approach. First at plot scale, fog interception was considered using a physically-based interception model (*Rutter-type*), in which fog interception estimates were validated with throughfall measurements. At the soil level, we used a soil water transfer model to quantify more precisely actual evapotranspiration of two land covers: forest and grass. This model is validated with measurements of pressure head at the soil. Results at plot scale were spatialized based on the land cover and an altitude gradient of rainfall, fog and evapotranspiration.

Given the long term records, the hydrological year 2013-2014 can be characterized as an average year in terms of rainfall and temperature, while the year 2014-2015 could be consider as a hot and relative wet year (near the top quantile in terms of rainfall).

Records from stations along the windward side of San Cristobal, reveal an orographic rainfall gradient of 270 mm/100 m of elevation and a referential potential evapotranspiration gradient of -53 mm/100 m of elevation for the hydrological year 2013-2014. At median elevation (300 m a.s.l.), rainfall is 1084 mm and potential evapotranspiration is 680 mm for the average year. Under these conditions, the average recharge reaches 440 mm.

Cloud water interception by the endemic vegetation at the windward highlands of San Cristobal is not negligible. It represents ca. 28% of the water input during the cool seasons, and it reaches 23% of the total water input for the representative year.

Deep percolation rates are markedly different depending of the altitude, land cover and seasonality. It is mainly affected by altitude due to the orographic effect of rainfall and evapotranspiration. However, at the highlands a marked difference of rates was estimated between different land covers (forest and grass) as a consequence of different transpiration rates, but mostly to the additional input of fog interception in the forest.

At a basin scale, recharge is more affected by altitude, in which fog interception has a reduced influence depending of the surface of land cover that can intercept fog and their exposure to the prevailing winds. Comparing a simple rainfall-evapotranspiration approach to estimate recharge with the methodology used, recharge can be underestimated ca. 25%, which has implications to the hydrological-hydrogeological analysis. Mean recharge estimated for the three watersheds of study reaches ca. 1530, 690 and 830 mm at *El Bayo*, *Chuki Marka* and *Cerro Gato*, respectively.

Chapter 4

Hydrological analysis

Introduction

This chapter, **Hydrological analysis**, deals with an hydrological approach to understand the hydrological behavior of the three basins gauged in this study.

From the work on the DEM, it is known that the high-elevation basin (*El Bayo*) has a larger surface compared to the two mid-elevation basins (*Chuki Marka* and *Cerro Gato*). The scarce measurements available on these streams from 2005-2006 show that mean streamflow in *El Bayo* is low (ca. 4 l/s), while it is relative high in *Chuki Marka* (ca. 8 l/s) and even higher in *Cerro Gato* (ca. 18 l/s). Compared with other watersheds, the latter has the larger streamflow in relation to its surface boundaries. This feature leads to think of the possibility that this watershed has groundwater contribution from surrounding basins.

Hydrological behaviour of these streams can be assess with: i) an analysis of the discharge measurements in the sections of control installed in the outlet of each watershed, and ii) applying a model, which could be physically based or conceptual. Considering it is a first approach to understand groundwater occurrence in these streams, a simple and robust method would be more desirable, such as lumped rainfall-runoff model.

In this chapter, we intend to make a first hydrological approach at the watershed scale to simulate streamflow in the three watersheds studied in order to analyze their hydrodynamic behavior and assess their groundwater contribution. Measurements of streamflow are analyzed, then simple lumped models are used to simulate streamflow. The hydrological behavior of these basins is assessed from the model.

This chapter is organized as follows:

- In section *Hydrological records*, monitoring of streams is described and the resulting hydrographs are presented and described.

- In section *Baseflow*, baseflow of streams is extracted from a graphical separation technique.
- In section *Hydrological modelling with a lumped conceptual model*, the GR4J model and modifications of it are used in the three basins of study. Results allows the possibility to present the water budget at watershed scale and an equivalent surface necessary to reach a balance.

4.1 Hydrological records

4.1.1 Monitoring

Given that the current metering on the streams of study is difficult and their flow rate is usually weak (< 25 l/s), punctual measurements of streamflow are performed with the mass balance method (Moore, 2005; Hudson and Fraser, 2005) on the three sections of control installed. A solution of salt with a known volume and electrical conductivity is injected on the stream, this solution disperses into the flow, where it gets completely mixed with it at a known length downstream. At this point, continuous measurements of electrical conductivity are performed with a conductivimeter (model WTW500). Dispersion of electrical conductivity along time forms a storm hydrograph shape, in which the flow is derived from the original mass of salt of the solution and the area under the graph of concentration over time. These punctual streamflow measurements were performed on a regular basis, each 1-4 weeks. It should be highlighted the tough conditions to perform this kind of measurements.

Sections of control are continuously monitored with water height sensors (Schlumberger diver-type) at a 15-min time step. Pressure records were compensated with barodivers (Schlumberger) located at stations SC300 and SC600 in order to have estimates of the absolute water level. Measurements are corrected due to temperature errors with an equation provided by the manufacturer. Then, the relationship between punctual measurements of streamflow and water level are described with a rating curve. A power function is used for this relationship. Parameters of the power functions are calibrated from a least square optimization for sections *El Bayo* and *Chuki Marka*. Given the weir at section *Cerro Gato*, parameters are obtained from its geometry.

Rating curves can be observed in figure 4.1. Equations can be seen in section A 4. Due to irregularity of sections *El Bayo* and *Chuki Marka*, the rating curve is adapted to the observations (e.g. at *El Bayo* a discontinuous function was used which is more adapted than a continuous one). Rating curve at *Cerro Gato* is discontinuous also given that after the height of the triangular weir is passed, another function is used derived from the combined geometry of the triangular weir and the rectangular section above it. From the three sections, *Chuki Marka* is the one with the higher uncertainties because its water level is very sensitive, small changes in it can lead to large changes in streamflow. Thus, any small obstruction, misplacement of the diver or local changes in air pressure that might be overlooked in the data treatment can lead to a change in the water level which is not a consequence of changes in streamflow. It should be highlighted the tough conditions to implement these devices and to perform measurements in a

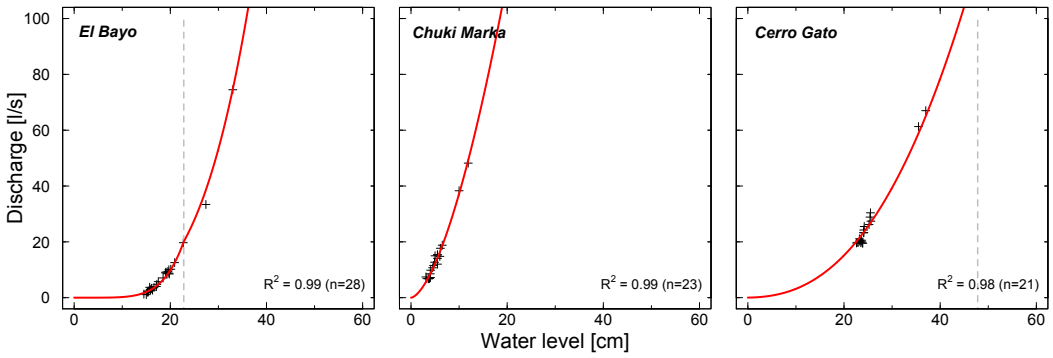

Figure 4.1: Rating curves of the three sections of control. Rating curves at *El Bayo* and *Cerro Gato* have a discontinuous function. Equations can be seen in section A 4

regular basis. To have this type of data in Galapagos regardless of the results is already an important achievement.

Given the instrumentation precision and the number and quality of measurements, uncertainties in streamflow values are expected in the three sections. Most of the measurements were performed at average discharge rates, while only few measurements are available at relative high rates. Therefore, even larger uncertainties are anticipated at high discharge rates. However, it would only occurs after heavy storm events which are not recurrently. Indeed, in each control section, less than 2% of the time estimated recharge from the rating curve is above of the maximum discharge measured. Given the scoop of this study, fair estimates of streamflow estimates from average water levels are enough, while accurate streamflow values during storm events are not so relevant.

4.1.1.1 Streamflow

The discharge from three sections of control is markedly different (Fig. 4.2 and Fig. 4.3). Median daily discharge reaches 8, 17 and 29 l/s at *El Bayo*, *Chuki Marka* and *Cerro Gato*, respectively, whereas the median specific recharge is 5, 52 and 42 l/s/km^2. At *El Bayo*, the drainage basin is the largest, however, discharge at the section of control is the smallest. *Chuki Marka* presents a large and medium discharge rates considering its drainage basin. On the contrary, *Cerro Gato* has constantly the largest discharge despite the topographical limits of this watershed has also a small size. Streamflow in *Chuki Marka* is the most irregular and it is the most sensitive, even during relative low rainfall days. The straightforward shape and slope of this watershed may explain its sensibility. Despite *El Bayo* presents the lowest streamflow rates, it has the largest peaks and long recessions after rainy days, which could be explain by its size. Streamflow in *Cerro Gato* is always considerable even in the dry months during both hot

seasons.

Streamflow is clearly affected by seasonality. Indeed, the hydrographs of these three sections reveal their sensitivity to strong rainfall events during the hot seasons, which is expected considering its small size. Streamflow from the three sections reacts strongly to the heavy rainfall days observed in the months of May and June (maximum daily streamflow during the study period is observed in mid-May 2015 and reaches 205 l/s, 110 l/s and 208 l/s at *El Bayo*, *Chuki Marka* and *Cerro Gato*, respectively). During the cool season, streamflow is less variable and increases slowly (first year mostly) or remains quasi-constant (second year). Except for *Cerro Gato*, the strong rainfall reported in May and June of 2015 had a marked effect in streamflow of the second season.

Average measurements made during the two years in the three sections reveal low values of electrical conductivity (38 μS/cm, 99 μS/cm and 100 μS/cm at *El Bayo*, *Chuki Marka* and *Cerro Gato*, respectively). Given the proximity of the section of control to the springs, these electrical conductivity measurements can be related to the ones of the springs. Indeed, measurements were similar along the study period (including dry and wet conditions). This means that springs are poorly mineralized, which was also reported in Adelinet (2005) during the hydrological year 2005-2006 (30 μS/cm to 170 μS/cm). Low values can be attributed to existence of clayey minerals (typical for andisols) produced by the weathering of basaltic rocks (Gislason et al., 1993), which have been observed in soil of San Cristobal (Adelinet et al., 2007). However, a marked difference in electrical conductivity is found between the mid-elevation watersheds (*Cerro Gato* and *Chuki Marka*) and the watershed in the highlands (*El Bayo*). The considerable specific discharge and the relative high electrical conductivity in the mid-elevation basins (*Cerro Gato* and *Chuki Marka*) may suggest that they have an important groundwater component which favors water-rock interaction and increases the mineralization of water. In section 4.2.3, a more comprehensive analysis of streamflow is presented.

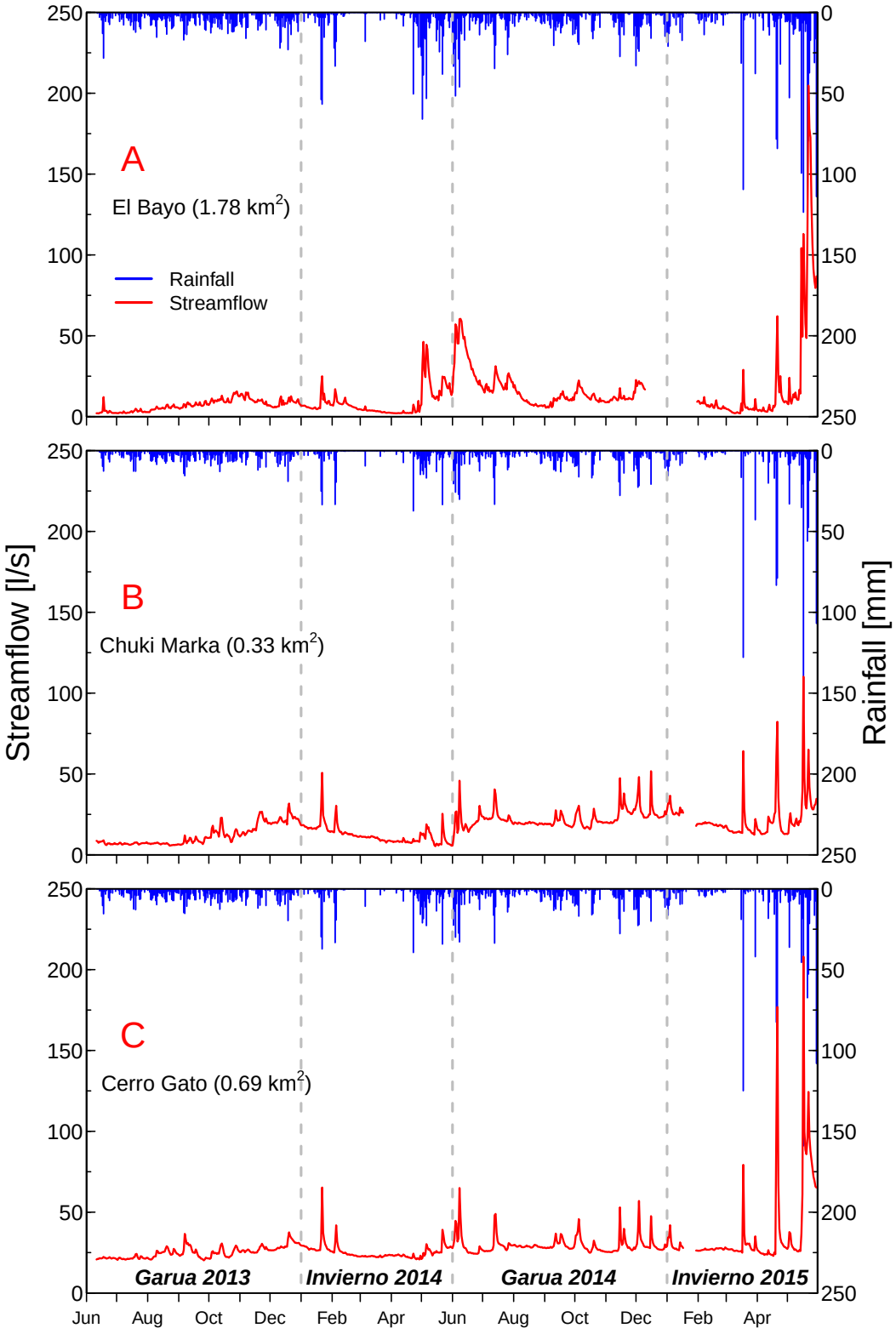

Figure 4.2: Temporal evolution of mean daily discharge on the three sections of control extracted from the relation height of water level-discharge. Daily rainfall is obtained from spatialisation of the rainfall orographic gradient at each basin.

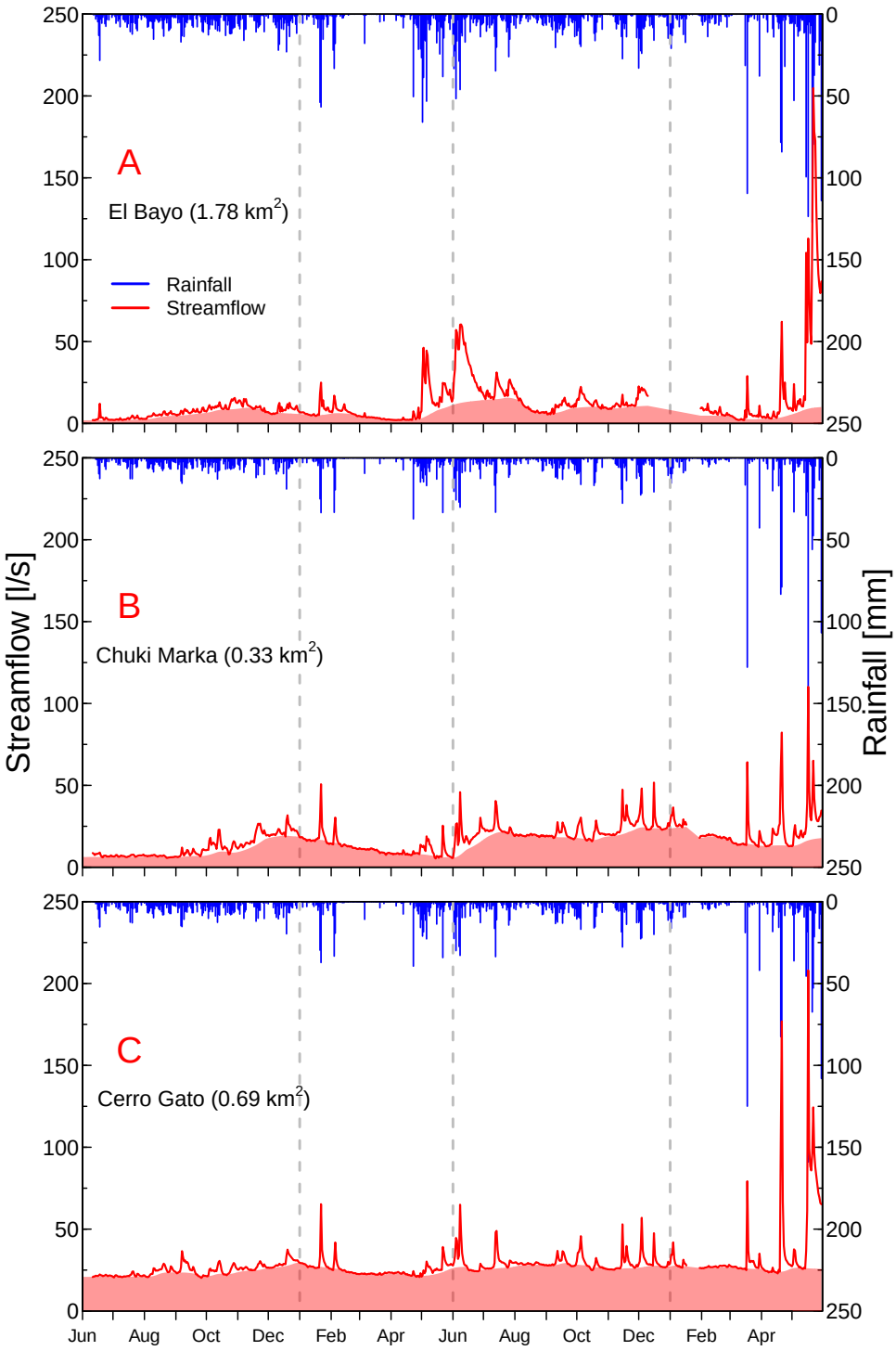

Figure 4.3: Temporal evolution of mean daily specific discharge on the three sections of control extracted from the relation height of water level-discharge. Specific discharge is obtained dividing discharge by the watershed surface. Daily rainfall is obtained from spatialisation of the rainfall orographic gradient at each basin.

4.2 Baseflow

4.2.1 Disaggregation of streamflow

Given that streamflow is the sum of directflow and baseflow, its separation is of many interest for several purposes. Graphical separation techniques are commonly applied for this matter. The most common approach are: i) UK smoothed minima approach (UKIH) (UKIH, 1980), in which daily flow is divided in non-overlapping blocks of five days and their minimas are evaluated to be considered or not as turning points of straight lines that represent the base flow; and ii) recursive digital filter (RDF) algorithm (Lyne and Hollick, 1979), which consists in a filter derived from the signal analysis studied.

In order to separate baseflow from the streamflow in the three sections studied, the FUKIH method (Aksoy et al., 2009) have been used. It consists to further filter the UKIH baseflow sequence by using the RDF method (for a wider description of this method, readers should see Aksoy et al. (2009)). The FUKIH method is applied in the streamflow of each control section in two different series (given missing data in January 2015), using the five-day blocking and parameters recommended in Aksoy et al. (2009). The result is shown in figure 4.4.

On the three sections during the first year, the highest baseflow values are reported between November/2014 and January/2015. Nevertheless the section at the highlands (*El Bayo*) has its peak at the beginning of November, while the mid-elevation sections present their peak at the end of December. On the second year (2014-2015), baseflow presents a peak in the three sections after the strong rainfall storms observed in May and June of 2015. However, its rising limb is different at each section. Sections *El Bayo* and *Chuki Marka* present a second peak at the end of the year 2014. It seems that the heavy rainfall of May and June disturbed the signal of baseflow, which might be similar to the one of the first year. In *Cerro Gato* the disturbance is barely seen and remains quasi-constant during the entire period. By the last months of the last year, baseflow in *Cerro Gato* and *Chuki Marka* does not return to the values observed at the beginning of the series. This could be related to the strong effect of the recharge produced by the rainfall storms of May and June 2014 and latter in May 2015.

4.2.2 Description and representativity of baseflow

Given the two years of study, baseflow represents 53% of the streamflow at *El Bayo*, while it represents 80% and 87% at *Chuki Marka* and *Cerro Gato*, respectively. The low direct flow (runoff) in these watersheds is consistent with results of section 3.3.3.1. Even though these values already show the considerate base-

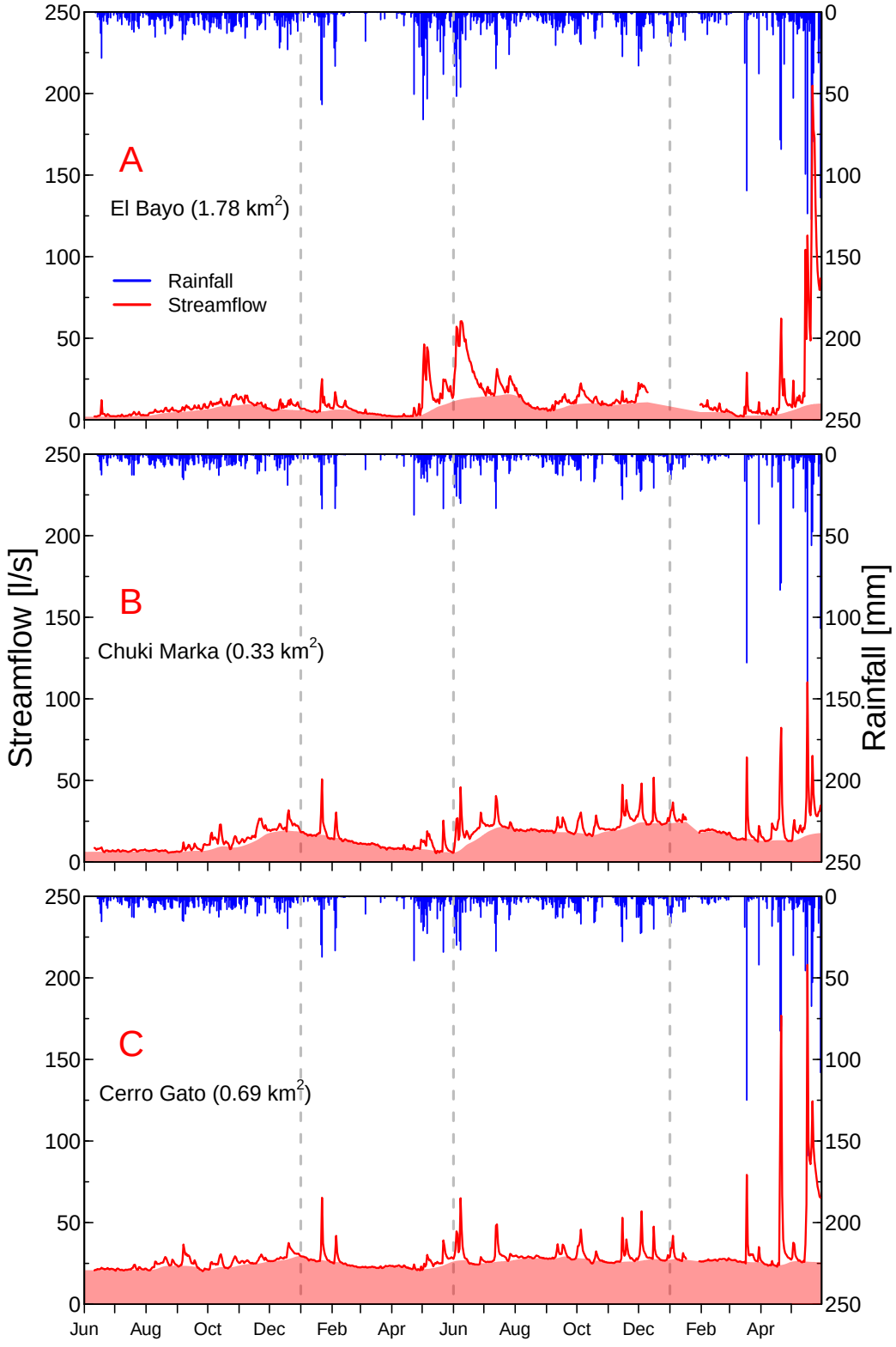

Figure 4.4: Temporal evolution of mean daily streamflow and baseflow on the three sections of control. Baseflow separation is made using the FUKIH method (Aksoy et al., 2009). Daily rainfall is obtained from spatialisation of the rainfall orographic gradient at each basin. The pink surface corresponds to baseflow.

flow component on these basins, they are somehow biased by the heavy rainfall storms on May and June of 2014 and the second hot season, in which directflow is predicted to be appreciable. Using data only from the first year, which is considered to be representative in terms of rainfall, the baseflow component reaches 68%, 84% and 94% of yearly streamflow at *El Bayo*, *Chuki Marka* and *Cerro Gato*, respectively.

The general appearance of baseflow shows the substantial groundwater component, which is influenced by seasonality. In general terms, it appears that recharge at the beginning of the cool season gradually feds the streams. The constant rainfall, low evaporation conditions and the probably fog presence of this season, enhance recharge and therefore baseflow starts to climb. At the month of transitions between seasons, the water input is reduced and a recession in baseflow starts. The evaporative demand and irregular rainfall during the hot season enhance decrease in baseflow reaching its lowest values. However, heavy rainfall events are observed during this season and despite its high intensity favors runoff, they also increase recharge, and thus markedly increasing baseflow.

Adelinet (2005) completed the measurements of several streams between March and July/2005 using the time/volume method. Yet, further measurements were performed until 2006 that have not been reported. After treating the data collected, the hydrological year 2005-2006 could be completed (Fig. 4.5). Despite these measurements were punctual, on a weekly basis, and might be inaccurate; the variation of the baseflow can be identified on most of them. During one year, flow of 10 out of 20 streams is similar in shape to an individual storm hydrograph. The rising limb starts between June and August (2005) and reaches its peak around November (2005), then a long recession limb can be observed until May and June (2006). Baseflow from the three sections of control also reveal this behavior and its magnitudes are also comparable; yet, a difference can be seen at *Cerro Gato*.

4.2.3 Hydrological and hydrogeological interpretation

Considering that baseflow is not restricted to groundwater flow but it also has sub-superfical component, physical characteristics of each basin affect their respective hydrographs (Gray, 1961; Thomas and Benson, 1970). Indeed, features that facilitate or delay runoff removal will produce short or long hydrographs. A first interpretation can be made using observations during the first year of study. *El Bayo* has the largest surface, but its drainage density is small compared to the other basins. Moreover, its drainage network is not straightforward and slopes are mild compared to the other basins. These characteristics can

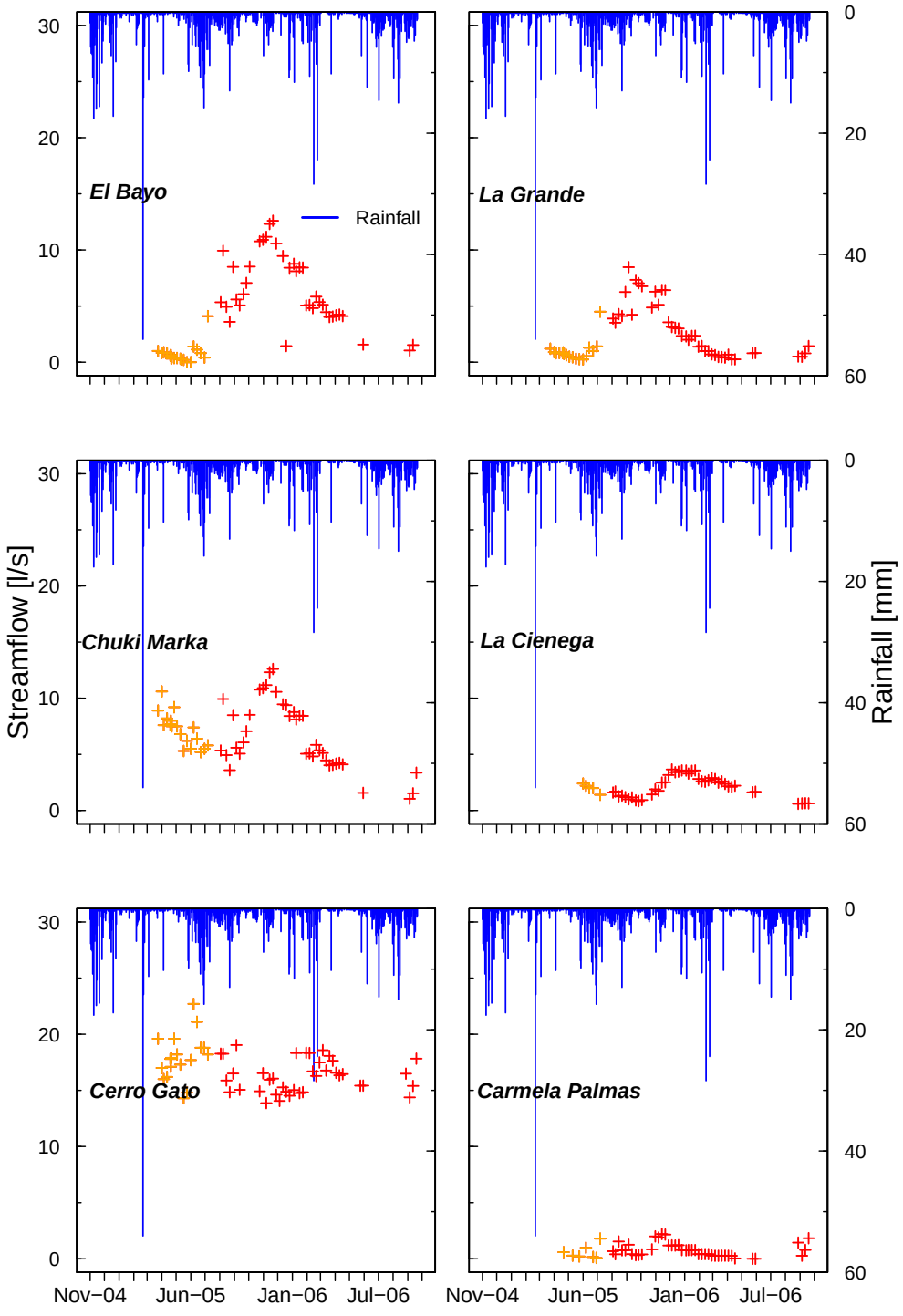

Figure 4.5: Temporal evolution of puntual water discharge on different ravines from March 2005 to August 2006. *El Bayo*, *Chuki Marka* and *Cerro Gato* correspond to the same section of control of the present study. The other three are ravines within the *Cerro Gato* area, which location can be seen in Fig. A.8. Orange crosses are values reported by (Adelinet, 2005; Violette et al., 2014). Red crosses are values from data treatment during the present. Blue lines correspond to daily rainfall from a weather station installed at *El Junco* (660 m a.s.l.) during those years.

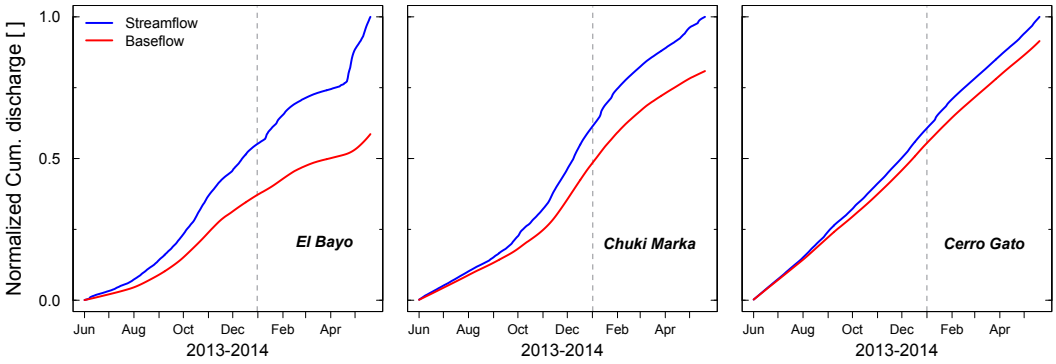

Figure 4.6: Normalized cumulative streamflow and baseflow with total streamflow in the three studied watersheds during the hydrological year 2013-2014. The curves show the hydrodynamic behaviour of each watershed to seasonality. The grey dashed line represents the change of season.

lead to a long rising limb (as seen between July and November of the first year). Low streamflow can be related to the gently slopes in this basin, which favors infiltration and temporary ponds. Mid elevation basins have a smaller surface and its drainage network is more straightforward given the steeper slopes, thus shorter hydrographs should be expected. Indeed, in these basins, the rising limb is shorter and its peak is more pronounced (especially in *Chuki Marka*).

Baseflow in the two mid-elevation basins starts rising around the month of October, contrary to the high-elevation basin in which the rising limb starts in late July. This could mean that the stream is fed with a lag of several months. This can be observed in figure 4.6, which shows the dynamic behavior of each watershed. Indeed, *Chuki Marka* show a lag in the discharge compared to *El Bayo*. However, *Cerro Gato* practically is invariable along the year. Figure 4.7 show the cumulative recharge against cumulative discharge at each basin during the first hydrological year (2013-2014). Several points can be analyzed with this graphic. First, it is evident that in the case of *El Bayo*, total discharge is significantly lower than its total recharge. On the contrary, in the two low-elevation watersheds (*Chuki Marka* and *Cerro Gato*), their total discharge is larger than their total recharge. Another interesting point in this figure is that recharge and discharge is almost balanced at the end of the cool garua season at the two mid-elevation watersheds. It is during the hot season where the difference between discharge and recharge is marked. It is caused because of the relative low rate of rainfall reported in this period which is evident in two dry periods. It could also be observed that streamflow and baseflow are similar during the cool season, whereas the difference growths during the hot season. This means, that most of the runoff occurs in strong rainfall events of the hot season and that the during the cool season is likely more favorable for the recharge of groundwater

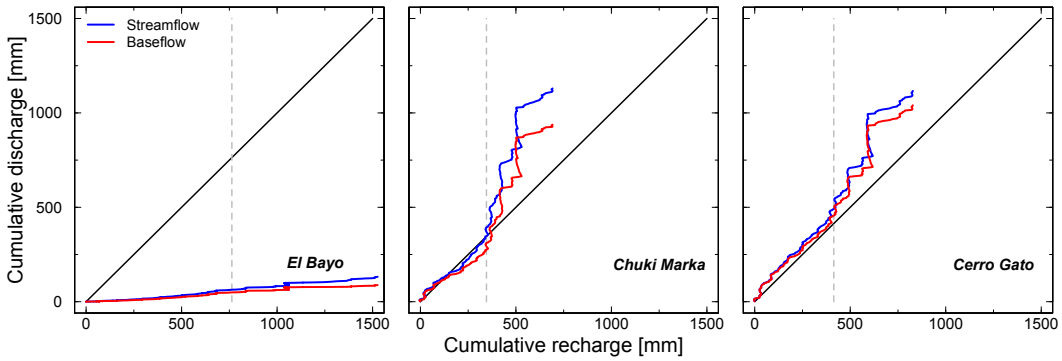

Figure 4.7: Recharge against discharge evolution of streamflow and baseflow in the three studied watersheds during the hydrological year 2013-2014. The grey dashed line represents the change of season.

bodies.

From the analysis of streamflow a first interpretation could be made about each basin. Given that *El Bayo* is strongly affected by the current climatic conditions and its discharge is relative low and significantly lower than its recharge, then it could be inferred that most of its recharge is either infiltrated or redirected to other watersheds, and only a small portion near the outlet of the watershed actually contributes to the stream, which could explain its sensibility to seasonality. The low-elevation basins have a different behavior. *Chuki Marka* has a discharge relatively high and its discharge is larger than its recharge. Its sensibility to strong rainfall events is related to its small size. Baseflow dynamics show seasonality but it has a lag. This could happen because the water input at the upper part of this basin flows in the unsaturated zone following the topography, and because its rate is low, it takes a long period until it reaches the stream. Indeed, given the recharge spatial distribution in these basins, a significant part of the input comes from the upper part of the basin. Rather than a slow sub-superficial flow, another possibility is that this rising is produced for the groundwater recharge of the perched aquifer which originates stream in the first place (as it could be interpreted from the geophysical data in chapter 5). In such case, water input, instead of flowing laterally, infiltrates until it reaches the aquifer increasing its level, which produces a rapidly rise of streamflow with a lag related to the infiltration time. To the author's opinion, a combination of both processes occurs in this basin. *Cerro Gato* presents similarities to *Chuki Marka*, in which its discharge is very high and larger than its recharge. Probably, the same scenario happens in this watershed, however their effects are diminish because most probably this watershed has a large reservoir. Indeed, the groundwater component of this watershed is significantly larger than direct flow. The fact that outputs are larger than inputs in the low-elevation watersheds could be

explain by two reasons: i) they have an additional contribution of groundwater from surrounding watersheds because their hydrogeological watershed is larger than the hydrological one, or ii) this groundwater component is the result of a huge recharge amount in previous years which filled the large reservoir of these watersheds. The latter option would imply a trend in which streamflow should be decreasing along the years, which cannot be seen with the two years of monitoring. However, the last strong rainy season was reported during El Niño event of 1998 and measurements of 2005 show that streamflow was similar to the first year monitored (2013-2014).

A watershed water balance would not be proper at this stage because the groundwater inter-exchange with other watersheds is not assessed yet. Any water balance at this point will increase positively or negatively the change of water storage in the watershed because the groundwater inter-exchange component will merge with it. Therefore, the water balance would not provide proper conclusions. Moreover, streamflow data from some days is missing, so a suitable method should be used to fill the gap. For these reasons, we propose the water balance after the hydrological model proposed for these watersheds.

4.3 Hydrological modeling with lumped conceptual models

4.3.1 Selection of the model

4.3.1.1 Lumped vs distributed models

Basically, two hydrological approaches can be used to simulate streamflow of a basin (Refsgaard, 1997; Beven, 1989; Carpenter and Georgakakos, 2006; Abbott and Refsgaard, 2012): i) lumped conceptual models, in which the entire basin is idealized as a single entity that depends of several parameters; and ii) distributed physically based models, which are structured to facilitate spatial variations in the catchment characteristics. The latter offers a better understanding of the functioning of the basin because is based in parameters that have a physical interpretation. However, these models manage a large number of parameters and their implementation and calibration is tedious. Given the background knowledge of the basins in San Cristobal, large groundwater component, different hydrological and hydrogeological basins, streams formed by perched aquifers; an hydrological approach might not be suitable. However, an hydrological model, can give further insights about the general behavior of these basins that leads to a better election of the next step: an hydrogeological approach. A lumped model is preferred in this case because it allows the understanding of the basin as a whole and mainly because it is based on few parameters.

4.3.1.2 GR4J model

For this study, we have chosen the four-parameter GR4J model (Perrin et al., 2003), a robust daily lumped rainfall-runoff model, that has been developed by the *IRSTEA* (formerly *Cemagref*) during several years and tested in a large set of catchments worldwide in different climate conditions, from semi-arid to temperate and tropical humid (Perrin et al., 2003), including France (Le Moine et al., 2007), China (Tian et al., 2013), Colombia (Carvajal and Roldan, 2007), Guinea (Traore, 2014), Indonesia (Harlan et al., 2010), Australia and United States (Oudin et al., 2005). The model is based on a standard soil moisture accounting approach with a production and routing modules (Fig. 4.8). A quick description is presented as follows (a detailed description of this model can be seen in Perrin et al. (2003)):

- First, an interception storage of zero is used to determine net precipitation P_n and evapotranspiration E_n.

- These estimations interact in a production store, in which rainfall input P_s and evapotranspiration output E_s are a non-linear function of the relative current level of the reservoir (S/x_1) in a first step, and then its production is a power function of the updated reservoir content.

- The total quantity of water (P_r) that reaches the routing functions is divided into two flow components with a fixed split, in which 10% of the flow is routed directly by a unit hydrograph $UH2$, while the 90% of the flow is rooted by another unit hydrograph $UH1$ with a base time (x_4) that corresponds to the half of the latter to a non-linear routing store.

- On both flows (Q_9 and Q_1), a catchment water exchange function (F) acts equally depending of the relative water level (R/x_3) in the routing store and a parameter x_2.

- Finally, the modified Q_1 (Q_d) is summed to the outflow of the routing reservoir Q_r to obtain the total streamflow (Q).

GR4J manages an intercatchment groundwater exchange (IGF) using F which is:

$$F = x_2 \times (R/x_3)^{5/2} \tag{4.1}$$

where x_2 is a magnitude that can be either positive or negative for water gains or losses, respectively. Because F acts equally in the quick and slow flow branches, IGF can be estimated as (Le Moine et al., 2007):

$$IGF = \begin{cases} 2 \times F & \text{if} \quad F > 0 \\ \\ -Min(|F|; R) - Min(|F|; Q_1) & \text{if} \quad F < 0 \end{cases} \tag{4.2}$$

Despite that IGF is an empirical formulation (usually it is never measured), its significance is supported by the vast number of catchment tested (Perrin et al., 2003; Le Moine et al., 2007, 2008). Thus, IGF will be used as a tool of analysis between the basins of study.

4.3.1.3 Improvement of GR4J into GR5J and GR7J

Despite GR4J has been tested in a large set of catchments and showed good performance (Perrin et al., 2003; Le Moine et al., 2007), the exchange function used (F), might be a limiting factor because it has a fixed amplitude and it is either positive or negative. Another point of discussion would be the routing scheme, in which it does account for a long term store that may play an important role. In order to account for these features, the current model structure

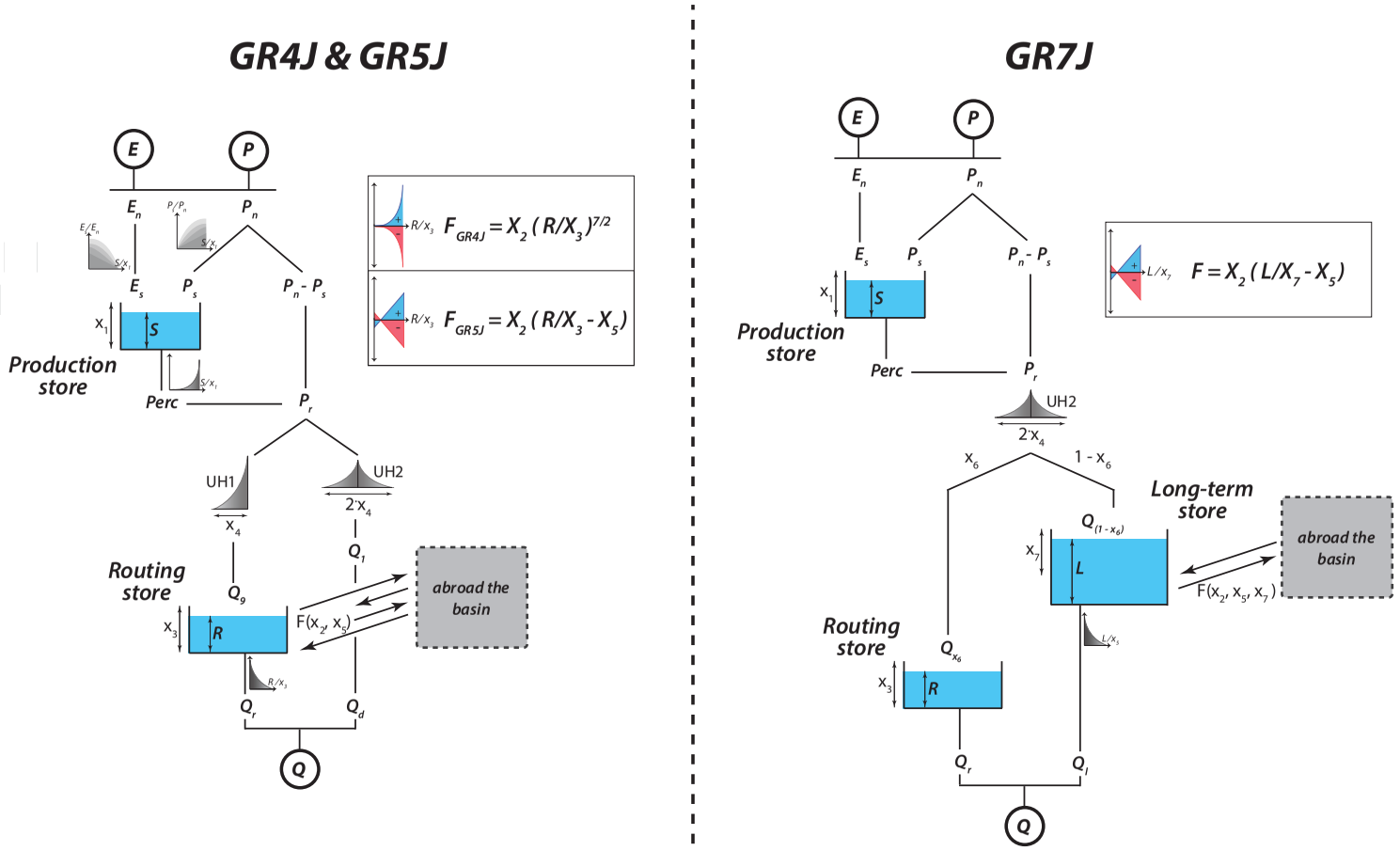

Figure 4.8: Schematic representation of the GR4J, GR5J and GR7J rainfall-runoff models. x_1 is the capacity of the production store. x_2 is intercatchment groundwater flow magnitude, which can be negative or positive. x_3 is the capacity of the nonlinear routing store. x_4 is unit hydrograph time base. x_5 is the constant intercatchment groundwater capacity. x_6 is the flow partition ratio. x_7 is the capacity of the nonlinear long-term store.

could be modified, leading or not to an improvement of flow simulations. Indeed, Le Moine (2008) performed a set of modifications to GR4J structure to improve flow simulations, incluiding groundwater contribution. These modifications embrace the use of extra parameters and stores. From the large set of tests, two models showed the best performance which address the limitations of F in the GR4J model mentioned above: GR5J and GR7J. However, GR5J and GR7J, respectively, handle 1 and 3 more parameters than GR4J. Given the characteristics of the three basins studied, IGF should play an important role. Therefore, GR5J and GR7J have also been applied with slight modifications (Fig. 4.8).

GR5J differs from GR4J only in the water exchange function (different from in Le Moine (2008) in which there is only one unit hydrograph), which is a linear function that requires an additional parameter (x_5). This function allows the positive or negative exchange of water depending of the relative level of the routing store. Another feature of this function is that if x_5 is large enough, it allows larger losses or gains of water. In such case, the routing store would be less influential.

In the case of GR7J, more changes to the structure have been performed. First, only one unit hydrograph is used before the separation into the two routing branches. Then, the partition of flow between branches is not longer fixed, and depends of a parameter (x_6). The left branch remains unchanged, while the second branch is not longer direct, instead another store is placed. This store is intended for long-term storage. It is nonlinear and has a maximum capacity of x_7. The exchange function is the same as in GR5J, it also acts on both stores equally but depends on the long-term store. With these changes, the branch of the routing store is intended to represent a more direct flow.

4.3.2 Implementation of the models

The three models are implemented in the three basins of study (*El Bayo*, *Chuki Marka* and *Cerro Gato*) using as inputs the recharge obtained in section 3.4, thus precipitation is the input of rainfall and fog interception minus wet canopy evaporation, and evapotranspiration is the potential transpiration (it should be noticed that it is not referential evapotranspiration, it is the potential transpiration obtained from the joint model and spatialized in each basin). In a first instance potential transpiration values are used because these models estimate actual evapotranspiration. However, actual transpiration from the soil transfer model would also be evaluated afterwards in the water balance section 4.3.5.

Parameters are calibrated with the *Guauss-Levenberg-Marquadt* algorithm (GLMA) implemented in the PEST software (Doherty, 2010), using as an objective function the Nash-Sutcliffe efficiency criterion (NS) for the daily square

root transformed streamflow ($\sqrt{Q}$):

$$NS = 1 - \frac{\sum_t (\sqrt{\hat{Q}_t} - \sqrt{Q_t})^2}{\sum_t (E[\sqrt{Q}] - \sqrt{Q_t})^2} \tag{4.3}$$

where Q is observed streamflow, $\hat{Q}$ is simulated streamflow and $E[\sqrt{Q}]$ is the mean of the square root observed streamflow. This criteria have shown to be the most adapted to several applications (Perrin et al., 2003; Oudin et al., 2005; Le Moine et al., 2007). It is the most adapted to our case because it reduces the effect of pick flows, which are not frequently observed and uncertainties in their estimation are relative large. Generally, the criteria is used with a standard split sample test scheme (Klemeš, 1986) for an evaluation of model performances in simulation mode. Nevertheless, given the reduced number of observations (only two years), if the total set is split into two parts, probably each part might not support an adequate calibration. For this reason, the full set is used for calibration (two hydrological years) with a 10-days warm up period. Initial conditions might represent an inconvenient for the calibration of the model with such a small period. For this reason, initial conditions are also calibrated, which include the initial water level of all stores in the model. Calibration process starts after a pre-optimization, in which a set of values are prescribed for each parameter, then all combinations are evaluated and the one with the best performance is chosen as the initial set of parameters for a local optimization (Fig. 4.9). In this way, the risk to encounter local optimums which are not the global optimum is reduced.

4.3.3 Results and interpretations

4.3.3.1 Performance of the models

Table 4.1 summarize the performance of the models at each basin. In general, all three models show a good performance (Fig. 4.10). However, in *Chuki Marka*, all models fail to simulate accurately streamflow during several periods. The model with the best performance is GR7J (Fig. 4.12), from 3 to 6 points better than the second model in performance which is GR5J. Apparently, modifications to GR4J have indeed improved its performance. However, the improvement is relatively small and GR4J already shows a good performance.

In terms of budget, an important criteria to assess is the total volume of streamflow. For this, the budget criteria (B_c) suggested by Perrin (2000) is used:

$$B_c = 1 - \left| \frac{\sum_t \hat{Q}_t}{\sum_t Q_t}^{0.5} - \frac{\sum_t Q_t}{\sum_t \hat{Q}_t}^{0.5} \right| \tag{4.4}$$

Notice that B_c does not distinguish if there is an overestimation or a underestimation of simulated streamflow. Using the best model (GR7J), B_c is 0.978,

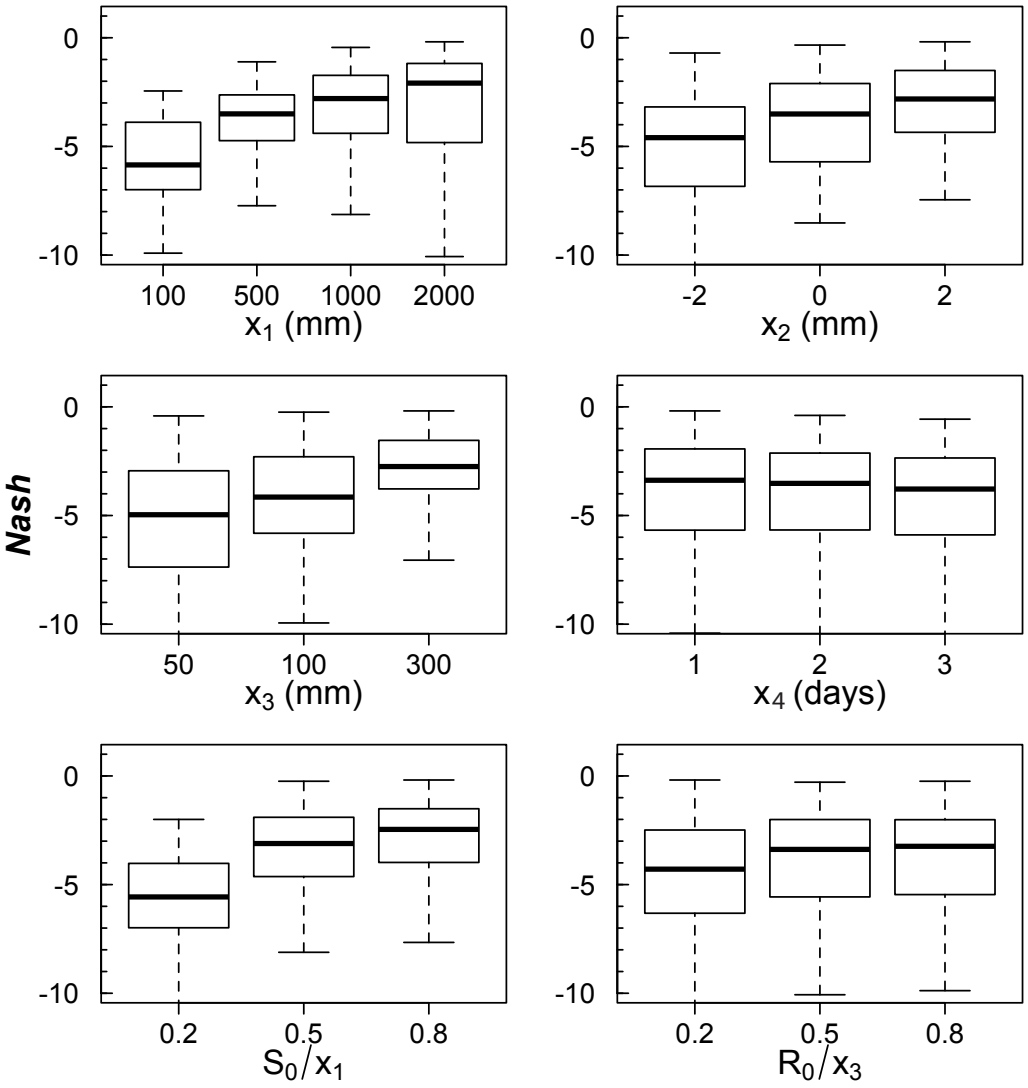

Figure 4.9: Set of values evaluated in the pre-optimization of the GR4J model in *Cerro Gato* basin. The combination with the highest NS is used as the starting parameter set in the PEST optimization (Doherty, 2010).

Table 4.1: Performance of the three rainfall-runoff models used in the three basins of study: *El Bayo*, *Chuki Marka* and *Cerro Gato*. Performance is evaluated with the Nash-Sutcliffe efficiency criterion of the square root streamflow.

$NS_{\sqrt{Q}}$	GR4J	GR5J	GR7J
El Bayo	0.84	0.87	0.90
Chuki Marka	0.55	0.64	0.68
Cerro Gato	0.77	0.77	0.83

0.984 and 0.996 at *El Bayo*, *Chuki Marka* and *Cerro Gato*, respectively. Which shows that simulated values can be used for the estimation of the water balance for all basins.

4.3.3.2 Interpretation of simulated streamflow

Given that GR7J model show the best performance, interpretations are restricted to the outputs of this model. From a general point of view, the behavior between the mid-elevation basins (*Chuki Marka* and *Cerro Gato*) are distinctive to the one at high-elevation (*El Bayo*). Parameter x_2 show that groundwater exchange in the two mid-elevation basins is positive, whereas the high-elevation basin loss water (Tb. 4.2). In all basins, the magnitude of this parameter is high, so either it is a negative or positive groundwater exchange, the quantity is large (especially in *El Bayo*). The partition of flow is also an interesting feature. In all cases, flow directed to the long-term reservoir is significant higher than the routing one (x_6), whereas the long-term store capacity is significant larger than the latter. Thus, in all cases the model is directing most of the flow to the long-term reservoir, in which the groundwater exchange takes place depending of its level. It means that the model is prioritizing the groundwater exchange. Indeed, the capacity of the long-term store is considerably higher than the others. This is especially seen in *Cerro Gato* where the groundwater component is supposed to be significant larger than direct flow. In figure 4.11, IGF can be seen for each basin along the two years of study. In the mid-elevation basins, IGF is always positive and almost constant (it barely changes at the of the series), while the high-elevation basin shows that IGF is always negative and more variable and influenced by the water input. This could be a consequence of the relative smaller capacity of the long-term store compared to the others and the recharge rate which is higher in this basin given the orographic gradient of recharge. This is also noticeable in the cumulative IGF graphic, in which in this basin, it can be observed a change of slope between years corresponding to the different magnitudes of recharge between the first and second year.

4.3.4 Another approach for mid-elevation basins

All models seem to have a relative bad performance in *Chuki Marka*. This could be a consequence of errors in the observations. Indeed, as reported in section 4.1.1, streamflow in this section is sensitive to small changes in the water level. The larger misfit encountered correspond to the months of the cool season in which manual monitoring and maintenance was limited. However, this should not be a reason why the dynamic of this basin is poorly represented by the

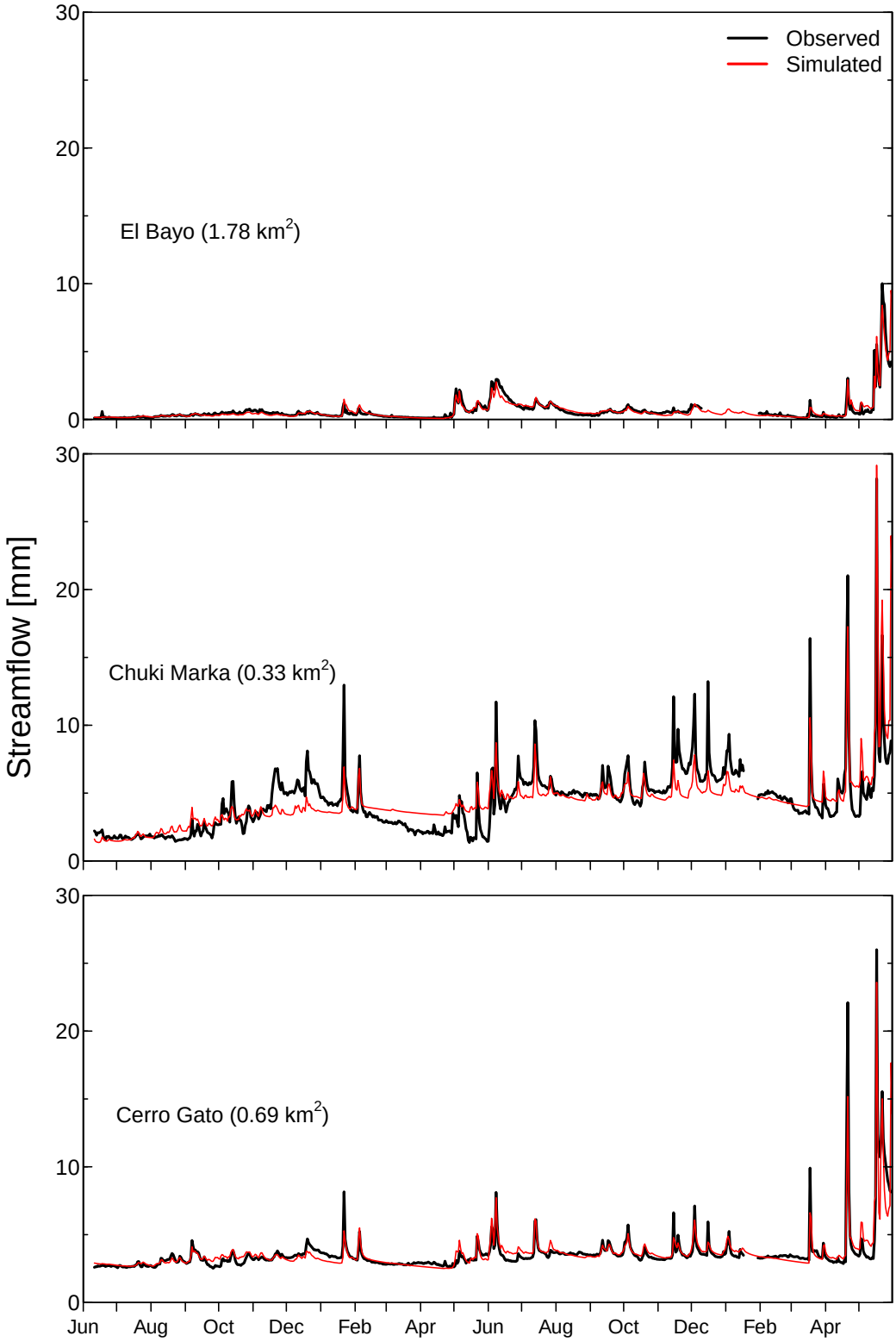

Figure 4.10: Simulated streamflow with the GR7J model for the three basins of study during the hydrological years 2013-2014 and 2014-2015.

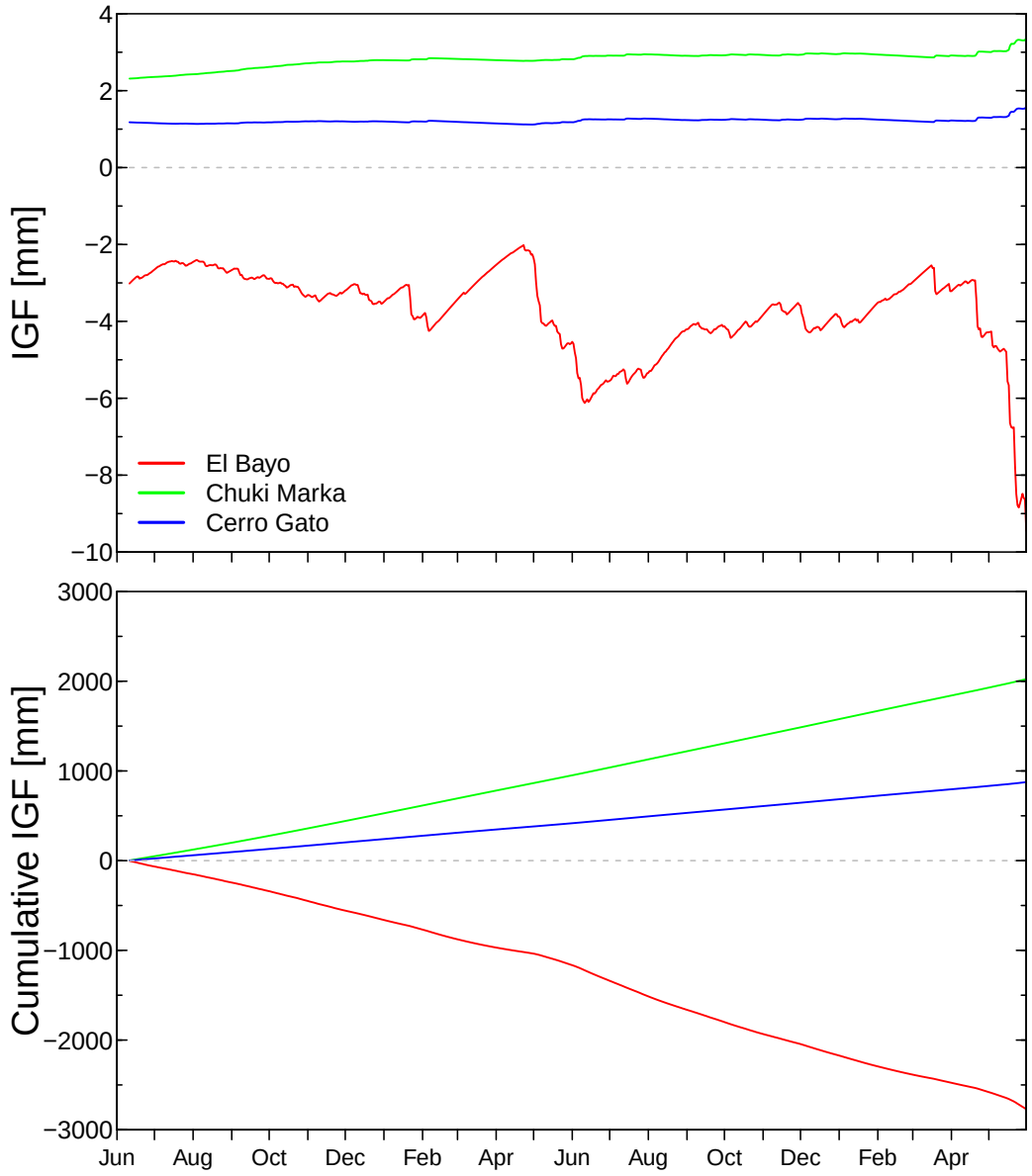

Figure 4.11: Daily and cumulative IGF at the three basins of study: *El Bayo*, *Chuki Marka* and *Cerro Gato*. The two mid-elevation basins have an almost constant IGF inputs, while at the high-elevation basin, IGF is an output which is more noticiable during the second hydrological year.

Table 4.2: Calibrated parameters and initial conditions of the GR7J model in the three basins of study: *El Bayo*, *Chuki Marka* and *Cerro Gato*.

parameter	*El Bayo*	*Chuki Marka*	*Cerro Gato*
x_1	162.4	291.0	113.6
x_2	-31.8	8.8	8.7
x_3	9.7	2.1	7.5
x_4	0.70	0.88	0.83
x_5	0.08	-0.02	0.12
x_6	0.05	0.23	0.17
x_7	2959.4	5835.6	10411.0
S_0/x_3	0.45	0.48	0.22
R_0/x_5	0.42	0.96	0.53
L_0/x_7	0.18	0.24	0.26

models. Streamflow is sensitive to rainfall and highly variable between seasons and years. The best performance of GR7J in *Chuki Marka* is when IGF is almost constant. However, the hydrograph in this basin shows seasonality with relative large amplitudes, thus IGF should be more sensitive. With the right combination of parameters, GR7J can produce a more sensitive IGF that can lead to represent the effect of seasonality in the hydrograph. Nevertheless, GR7J does it with a lag in the amplitude that produce larger errors. Thus, the sensitivity and seasonality of streamflow is replaced by a smoother simulation of it where the errors are lower.

The poor performance of the models might show that this basin cannot be correctly simulated by its own. Therefore another approach is tested. If we observe the hydrograph of this basin (Fig. 4.10), streamflow increases during the cool seasons, which could be related to an effect of fog interception. However, fog interception is very low on this basin. Another interesting hint might be in figure 4.11. IGF from the high-elevation basin has a tendency similar to streamflow in *Chuki Marka*. Given that the losses from high-elevation basins (in which fog interception is more influential) show a similar tendency with streamflow of this basin, it is plausible that this basin gains water from high-elevation basins. A simple relative semi-distributed approach has been used to test this hypothesis, in which losses from the top basins are used as groundwater input in the mid-elevation basins.

Several ways to introduce groundwater input from top basins to the model were tested, but to simplify the one that showed the best performance in *Chuki Marka* is presented. It is a simple modification to the GR7J model, in which a term is added (G_I) in the former exchange function F, that corresponds to the groundwater input from an upper basin. G_I is the output in the form of a unit hydrogram function with a base time (t_B) and exponent (p) that are calibrated

Table 4.3: Calibrated parameters and initial conditions of the modified GR7J model in the two mid-elevation basins: *Chuki Marka* and *Cerro Gato*.

parameter	*Chuki Marka*	*Cerro Gato*
x_1	255.4	97.3
x_2	-0.68	6.5
x_3	2.4	7.5
x_4	0.89	0.83
x_5	-4.97	0.21
x_6	0.27	0.16
x_7	6223.0	9684.8
S_0/x_3	0.10	0.56
R_0/x_5	0.98	0.96
L_0/x_7	0.26	0.26
t_B	33.0	98.1
p	15.1	22.0
f_{FOG}	3.9	9.2
f_{UB}	1.35	0.14

(even though a unit hydrograph might not represent the groundwater input, with a long base time and a high exponent it can be somehow comparable). The input to the unit hydrograph is IGF_{UB} from an upper basin. Precipitation input in the upper basin includes fog interception, which is multiplied by a calibration factor (f_{FOG}), in this way the effect of fog interception is assessed. Catchment surfaces above the mid-elevation basins are hard to define (at least with the ones IGF might occur) and they are not gauged for streamflow (except for *El Bayo* which is not really above the others two basins) and rainfall and evapotranspiration spatialisation is yet to be accomplished. In such case, a true IGF_{UB} is not possible to have. However, IGF_{UB} chronicles could be derived from *El Bayo*. Indeed, similar tendencies are expected in the high elevation basins given the similar climatic conditions. Possible different magnitudes are addressed with a scaling factor (f_{UB}). Thus, the IGF_{UB} used is actually $f_{UB} \times IGF_{ElBayo}$. In this way, IGF_{UB} inputs are from a virtual basin in which streamflow cannot be verified (it is purely theoretical).

Results show no improvement in the simulated hydrograph of *Cerro Gato* (does not change comparing with the former GR7J simulation), where $NS_{\sqrt{Q}}$ remains at 0.83. Basically, the model remains the same because the input from the virtual upper basin is heavily reduced by f_{UB} (Tb. 4.3). This might show that this basin more likely works by its own or with basins at a simliar altitude beside it. On the other hand, simulations in *Chuki Marka* show a significant improvement (Fig. 4.12), where $NS_{\sqrt{Q}}$ reaches 0.79. In this case, f_{UB} is larger than

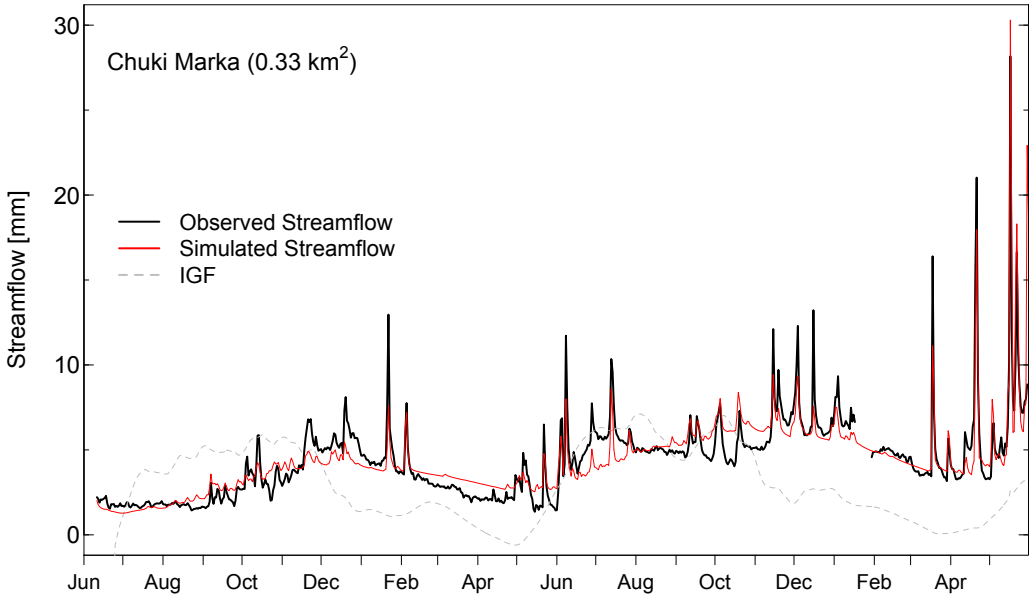

Figure 4.12: Simulated streamflow with the modified GR7J model in *Chuki Marka* basin during the hydrological years 2013-2014 and 2014-2015. Daily IGF shows positive and negative values.

1, considering the large IGF showed by *El Bayo*, the water quantity gained by this watershed is important. Another interesting point, is that fog interception is increased considerably, thus increasing even more IGB_{UB}. The other term of F, proper from the GR7J model is different. The combination of parameters x_2 and x_5 yields water losses which are almost independent of the store level (given the large value of x_5). Then, the combination of the two terms of F results in a large and variable groundwater inter-exchange component. Despite, the combined parameters to produce this large inter-exchange can be an artifact of the model to reach the amplitudes and seasonality of the measured streamflow, the arrangement shows a picture of the dynamic behavior of this basin, the link between runoff and groundwater and their seasonal interaction. Also parameters involving IGB_{UB} are not such unrealistic as they seem. Indeed, the surface above *Chuki Marka* does not have permanent streams (Fig. 2.16) and it is sufficiently large to produce such a groundwater input (given the small surface of *Chuki Marka*). Moreover, most of this surface is exposed to the prevailing winds (contrary to *El Bayo* where a considerable part of the catchment is protected from the wind by *El Junco* cone) and it is mostly covered by *Miconias*. As seen in section 3.3.3.1 and section 3.4, land cover in the highlands has an important effect in recharge, where forest, which intercept fog, can increase recharge considerably. Therefore, a large increase in fog interception can be justified.

4.3.5 Water balance and equivalent catchment surface

A water budget is performed at the basin scale. Results from the spatialization of recharge in each basins (Tb. 3.9) are completed with discharge outputs simulated by the hydrological model (given some missing data in streamflow measurements which corresponds to ca. 3% of the total records). Outputs from the GR7J model are used in *El Bayo* and *Cerro Gato*, whereas the modified GR7J model (GR7Jm) is used in *Chuki Marka*. In order to account with the actual transpiration estimated by the joint canopy and soil water transfer model, a small change is made in the structure of the GR7J and GR7Jm models. Instead of using the function within the model to estimate evapotranspiration, its value is given directly from the estimations in section 3.4. In this way, we used the same estimations than before, which are potentially more accurate. Even though it might not necessary, a new calibration was performed only to confirm that not significant difference was found neither in the parameters, $NS_{\sqrt{Q}}$ nor B_c. In fact, the two latter remained practically the same. Indeed, Oudin et al. (2005) reported that rainfall-runoff models are insensitive to detailed evapotranspiration and therefore not improvement was found in the efficiency of the model when using a better evaporative demand. However, this is important in terms of water budget.

The balance shows a contrasting behavior between all basins, even between the two mid-elevation basins (*Chuki Marka* and *Cerro Gato*). IGF is the value that is adjusted to reach the balance in each case. In the case of *El Bayo*, IGF reaches ca. 60% of the outputs, which means that most of the rainfall input is lost and infiltrated to deeper levels or/and to surrounding basins. In *Chuki Marka* the input of IGF is close to the input of precipitation, which is considerably large. It means that ca. 40% of the water in this basin is actually from another basin. *Cerro Gato* is the most balanced basin, IGF account for ca. 18% of the total input and evapotranspiration plus streamflow reaches similar values than precipitation. It is contrary to what was expected considering that it is the basin with the higher streamflow observed. In all basins, annual water height is similar, which shows an interesting fact about the equilibrium: even though high-elevation basins receive larger precipitation inputs because of its orographic gradient, mid-elevation basins can reach similar inputs because they are fed by other basins, where it is more likely that losses in the high-elevation basins become gains in the mid-elevation basins. A point to be highlighted are the high values in the term ΔS, which is the variation of the water storage at each basin. ΔS shows the seasonal connection between groundwater and streamflow. Large ΔS is related to the large storage capacity of these basins (indeed, x_7 is very high in all cases) and because the balance is made each year from the

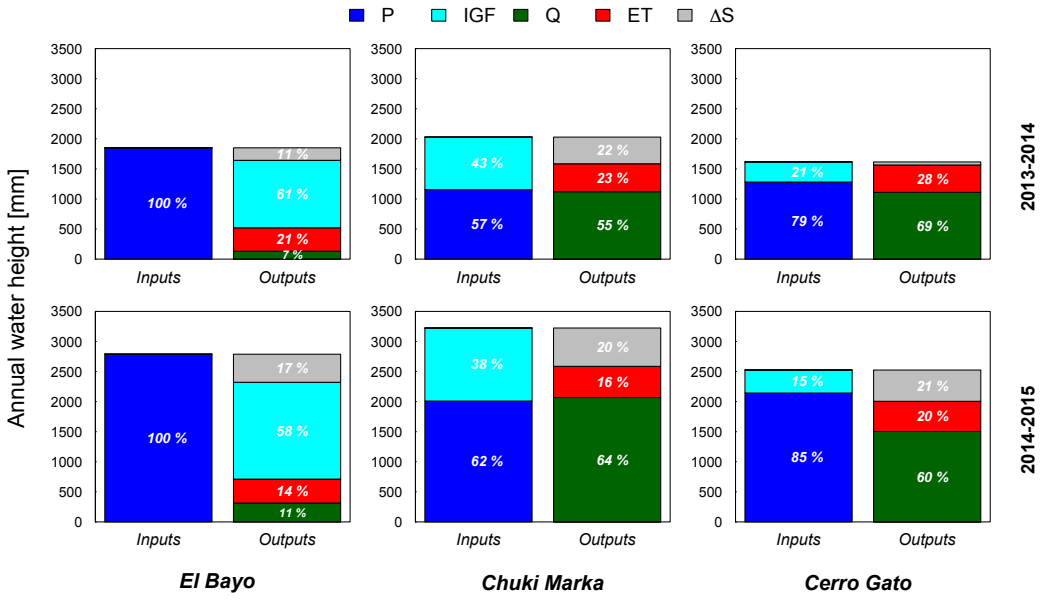

Figure 4.13: Annual water balance of each basin of study: *El Bayo*, *Chuki Marka* and *Cerro Gato*. P is precipitation that includes rainfall and fog interception. IGF is the interexchange groundwater between basins, which can be an input or output. Q is streamflow. ET is actual evapotranspiration. ΔS is change of storage at the basin. All values are cumulative heights of water in mm.

beginning of June to the end of May. During May of both years rainfall was particularly large (it accounts for ca. 17% and 30% of the total precipitation in the first and second year, respectively), which means that this input is still to be evacuated in form of streamflow.

Instead of using IGF to reach the water balance, Le Moine et al. (2007) proposed a different approach using the GR4J model, in which the exchange function is set to zero an the free parameter x_2 is used to correct either the precipitation, evapotranspiration or even the catchement surface. Assuming that our measurements of precipitation and evapotranspiration are fair, then the equivalent surface (S_E), which is the catchment surface necessary to reach the water balance (while streamflow is properly simulated), is estimated with this simple approach.

Using this approach, simulations remain fair. $NS_{\sqrt{Q}}$ reaches 0.90, 0.66 and 0.79 at *El Bayo*, *Chuki Marka* and *Cerro Gato*, respectively. The equivalent surface relative to the actual surface is 13%, 216% and 140% for *El Bayo*, *Chuki Marka* and *Cerro Gato*, respectively. As expected, the high-elevation basin needs a smaller surface while the two mid-elevation basins need a bigger one. The case of *Chuki Marka* is particularly interesting, it needs more than the double of surface to reach the relative high streamflow values observed in this basin.

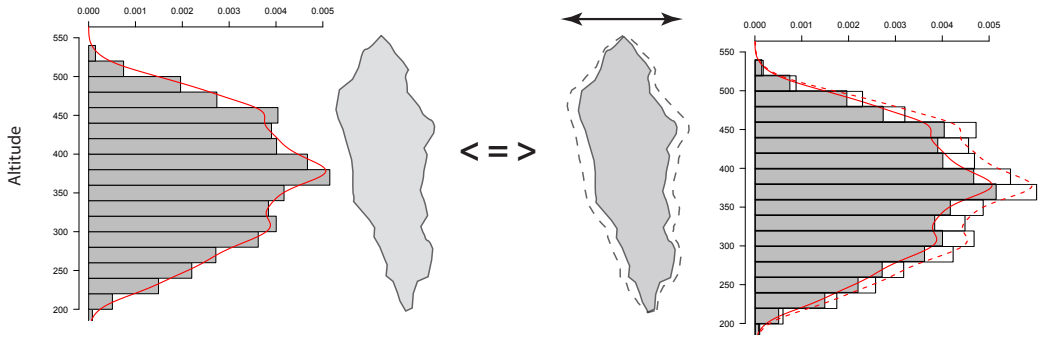

Figure 4.14: Exemple of a simple equivalent surface. Assuming that altitude is similar along the basin, the equivalent surface is an horizontal expansion of the original one.

4.3.6 Speculations about the recharge surface

The modified version of GR4J found an equivalent surface (S_E) to manage the water budget imbalance in each basin. In basins of *Chuki Marka* and *Cerro Gato*, this surface is larger than the catchment surface. But what does S_E means in a physical sense? Given that recharge is driven by the precipitation and evapotranspiration gradient, S_E would be a surface with the same original altitudinal distribution but with a different magnitude. Therefore, at a same altitude, the distribution of vegetation, fog interception is in the same proportion as the original surface. In a way, it is like stretching the width of the basin (Fig. 4.14). Given that S_E could be comparable with the hydrogeological basin of each catchment, then it might be interesting to know in which way the increased area is distributed. Indeed, it is unlikely that S_E is a wither version of the hydrological surface. It should also be noticed that if the distribution of the increased surface is larger at the upper part of the catchment, then the surface required to reach the water balance is smaller than the one necessary in the case the increased surface favors the lower part of the catchment. This is a consequence of the recharge gradient.

In order to assess the effect of the increased surface distribution (ISD), the modified version of the GR4J model is used to estimate S_E. However, the increased surface is tested with a different distribution along the catchment (to make it simpler, any increased surface remains within the altitudinal limits of the catchment). A simple linear function is used for an unit increased distribution

(ID_0):

$$ID_0(h) = \begin{cases} \frac{h \times 2B}{H_B} & \text{if} \quad h < H_B \\ \\ \frac{(\Delta H - h) \times 2B}{(\Delta H - H_B)} & \text{if} \quad h \geq H_B \end{cases} \tag{4.5}$$

where h is the elevation relative to the lower limit elevation of the basin, S_0 is the unit catchment surface distribution, ΔH is the difference between elevation limits of the basin, H_B is the altitude corresponding to $2B$, in which B corresponds to the value if ID_0 is uniform (Fig. 4.15). Given that the total surface of ID_0 is 1, then $B = 1/\Delta H$. The unit increased surface distribution (ISD_u) is extracted from the unit catchment surface (S_u):

$$(ISD_u)_h = \frac{(ID_0)_h \times (S_u)_h}{\sum_h (ID_u)_h \times (S_u)_h} \tag{4.6}$$

Finally, ISD is estimated from the catchment surface S_0:

$$ISD = S_0 \times (f_S - 1) \times ISD_u \tag{4.7}$$

where f_S is the equivalent surface ratio, which is the parameter x_2 used in the modified GR4J version. Different ISD_u are tested, with $H_B/\Delta H$ ranging between 0 to 1. For each ISD_u, a new calibration of the parameters of the model is performed with PEST using as the optimization criteria the minimum weighted least square (MWLS) because it would allow a larger distinction between the calibrated models for each ISD. During the calibration process, at each time PEST changes the value of the parameters (including x_2), a new set of mean daily precipitation and evapotranspiration are estimated, which correspond to the equivalent surface, and they are used as inputs of the models.

Results show that the range of f_S at *Cerro Gato* is between 1.35 and 1.52, while it is between 1.99 and 2.26 at *Chuki Marka*, which shows the influence of ISD in S_E. This results assume that precipitation and evapotranspiration are correctly observed. If we include an error of 10% in precipitation and evapotranspiration and if we use the most extreme values of $H_B/\Delta H$ with the most extreme combination of precipitation and evapotranspiration, then uncertainties in S_E increase considerably. In such case, the range of f_S is between 1.15 and 1.84 at *Cerro Gato* and between 1.74 and 2.84 at *Chuki Marka*. In any case, the necessity to have a bigger S_E is evident in both cases.

Another point to be evaluated can be fog interception. The magnitude of fog interception is increased by a set of factors (f_{fog}) to assess its influence. Also, to increase the effect of a different surface distribution, ISD is used directly from ID_O. Figure 4.16 shows the variation of f_S and MWLS depending of f_{fog} and $H_B/\Delta H$. In both basins, MWLS barely differs. This is a consequence of the

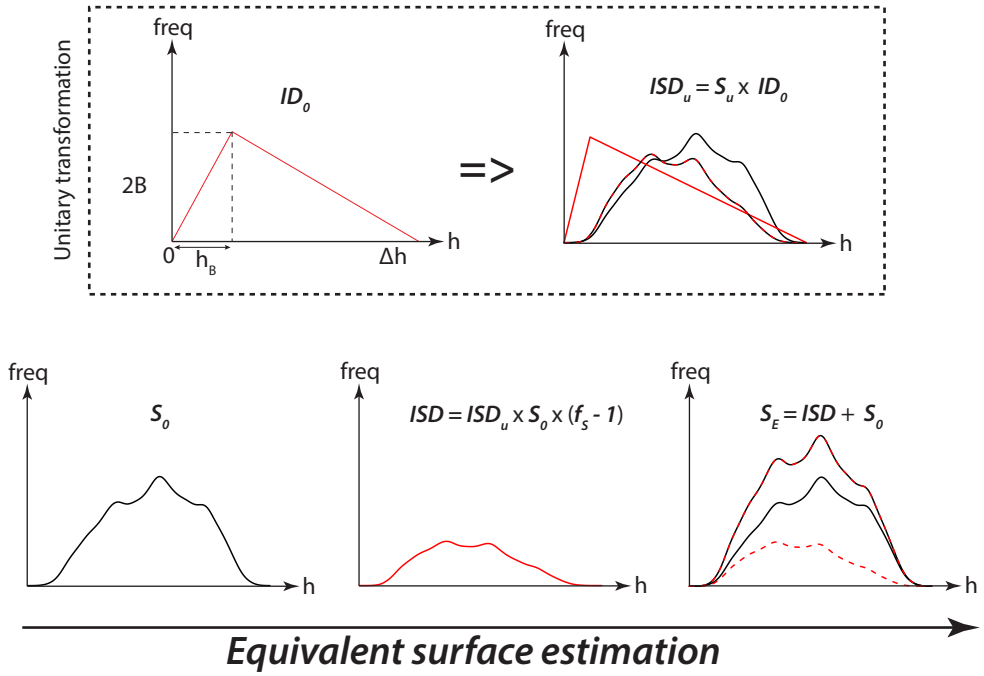

Figure 4.15: Scheme of the equivalent surface estimation.

robustness of the GR4J model. According to figure 4.16, the best optimization in *Chuki Marka* is when ISD favors the upper part of the basin. This makes sense considering the interpretation of GR7Jm in this basin. However, MWLS is significantly higher than the one of the GR7Jm (39 $mm^{0.5}$), which means that probably the use of a larger equivalent surface might not be a good approach. On the contrary, in *Cerro Gato* the lower values of MWLS are found when the catchment surface is increased in the lower part. MWLS is in the same order than the value obtained with GR7J (11.6 $mm^{0.5}$). It seems that *Cerro Gato* basin is more likely to have a larger hydrogeological surface that is not as big as expected and where its extension is more likely in the same altitude rather than at higher elevations.

It would be too pretentious to conclude that using a lumped hydrological approach, it is actually possible to define the extension and the possible distribution of the hydrogeological basin (indeed, the best fit is more likely related to a better simulation of the runoff component in the hydrograph). However, the tendencies presented can be considered as hints towards a proper hydrogeological approach.

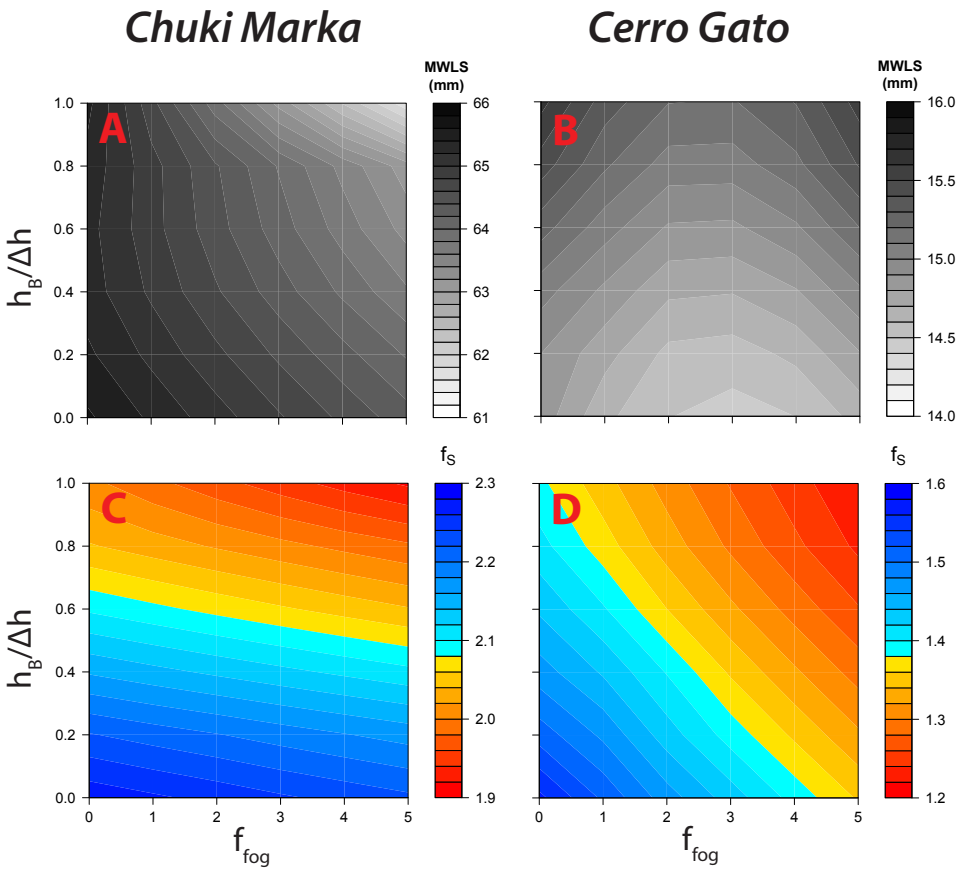

Figure 4.16: (A, B) Optimisation criteria (MWLS) and (C, D) equivalent surface ratio variation (f_S) according to the fog factor (f_{fog}) and $H_B/\Delta H$. in the mid-elevations basins: (A, C) *Chuki Marka* and (B, D) *Cerro Gato*. Higher values of f_S mean higher fog interception. Lower values in $H_B/\Delta H$ mean a higher increase of surface in the lower part of the basin and viceversa with high values.

Conclusions

Measurements performed in the outlet of the three studied basins show that their streamflow is markedly different. Median daily streamflow is ca. 8 l/s in the high-elevation basin (*El Bayo*), while it reaches 17 and 29 l/s in *Chuki Marka* and *Cerro Gato* (low-elevation basins), respectively.

Using a graphical separation technique (FUKIH method) in the streamflow records, baseflow represents 53%, 80% and 87% of streamflow at *El Bayo*, *Chuki Marka* and *Cerro Gato*, respectively.

From the analysis of recharge, streamflow and baseflow chronicles in each basin, it could be analyzed that: i) discharge in *El Bayo* watershed is significantly smaller than the recharge and it reacts rapidly to climatic conditions and seasonality, ii) discharge in *Chuki Marka* is very sensitive to rainfall events, it is larger than its recharge and it has a delay response to seasonality, iii) discharge in *Cerro Gato* is larger than recharge and it is quasi-constant along the study period which evidences the large size of the groundwater reservoir in the watershed.

The GR4J lumped model and modifications of it were used to simulate streamflow in the three basins. The best simulation was obtained using the GR7J model (7 parameters), where the Nash-Sutcliffe (NS) criteria for the square root streamflow reached 0.90 at *El Bayo* and 0.83 at *Cerro Gato*. In *Chuki Marka*, a modification of the exchange groundwater function in the GR7J was necessary to achieve a fair simulation of streamflow, in which NS reaches 0.79.

The simulation and parameters of the modeling reveal a striking difference in the behavior of the three basins. In *El Bayo*, most of the water input by precipitation (ca. 60%) is loss either by the inter-exchange with other basins or by deep infiltration. In *Chuki Marka*, a large groundwater inter-exchange occurs which influence the seasonality of the observed streamflow. The result of the inter-exchange is gains of groundwater that corresponds to the ca. 40% of the total input. Despite *Cerro Gato* has the highest streamflow of all basins, the groundwater income from other basins is ca. 18%, which shows it is the most balanced one.

From a general point of view, it seems that losses from the high-elevation basins (such as *El Bayo*) become groundwater inputs in the mid-elevation basins (such as *Chuki Marka*), while other mid-elevation basins have inputs from basins at the same altitude, such as *Cerro Gato*, where its hydrogeological watershed is larger than the catchment surface and its extension is more likely in the same elevation.

Chapter 5

Architecture and hydrodynamical properties of the internal structure

Introduction

In this chapter, the **Architecture and hydrodynamical properties of the internal structure** is deduced from geophysical methods.

Ground-based investigations about the internal structure of the island is extremely challenging due to the difficulty on the field (dense vegetation, steep slopes, restricted access, few number of geological outcrops and no boreholes). For this reason, indirect methods, such as geophysics, can be used to complement information about the hydrodynamical properties of the internal structure of the island.

Indirect geophysical method, such as the airborne electromagnetic survey with the SkyTEM system conducted in May 2006 in the Galapagos Islands (d'Ozouville et al., 2008a) and the 3-D models of resistivity (Pryet et al., 2012b), allow a more comprehensive view of the internal structure of San Cristobal. The model can be used to extract the extend of perched aquifers and define its geometry.

Ground-based geophysical methods, such as seismic of refraction, can be used to estimate the thickness of unsaturated basalts, the depth of the weathering zone, determine the groundwater level and extract hydrodynamic properties such as total porosity, fracture density and even permeability.

In this chapter, we intend to use two types of geophysical methods, airborne electromagnetics and seismic of refraction, to define the extension of the perched aquifer of *Cerro Gato* and to estimate hydrodynamic properties of the internal

structure of the island at a local scale.

This chapter is organized as follows.

- In section *Resistivity model*, a brief description about the construction of the 3D resistivity model is reported. Then, different resistivity models are shown and compared to determine the most adapted to the *Cerro Gato* area. Follows an interpretation of the origin of the springs of *Cerro Gato* from the interpretation of the resistivity model and field assessment. The extraction of the possible geometry of the perched aquifer deduced from the 3D model is described at the end of this section.

- In section *Seismic tomography*, the main concepts of seismic of refraction are mentioned, then the survey performed in San Cristobal is described. Results and interpretation of the tomographies are reported.

- In section *estimation of hydraulic properties*, we make a first intend to estimate some hydrodynamic properties of basaltic rocks from their effective elastic properties.

5.1 Resistivity model

5.1.1 3D resistivity model of San Cristobal

5.1.1.1 3D gridding of 1D resistivity models

Pryet et al. (2011) developed a technique that allows 3D visualization of extensive airborne electromagnetic (AEM) datasets. The technique is based in the interpolation of geophysical model parameters of 1D models, such as layer resistivity or layer thickness, in the 2D horizontal space (Fig. 5.1). The construction of the 3D grid is as follows (for a wider description of the technique see Pryet et al. (2011)): i) First, the set of 1D models, which are vectors of the vertical resistivity model obtained from the inverted electrical soundings and describe the resistivity and geometry of a layer (thickness, elevation, depth), are interpolated in the 2D horizontal space into matrices (resistivity and geometry) whose size is equal to the number of cells discretizing in the 2D domain. ii) Then, the 3D resistivity field, which is represented by a 3D grid composed by hexahedral cells, is obtained from the matrices.

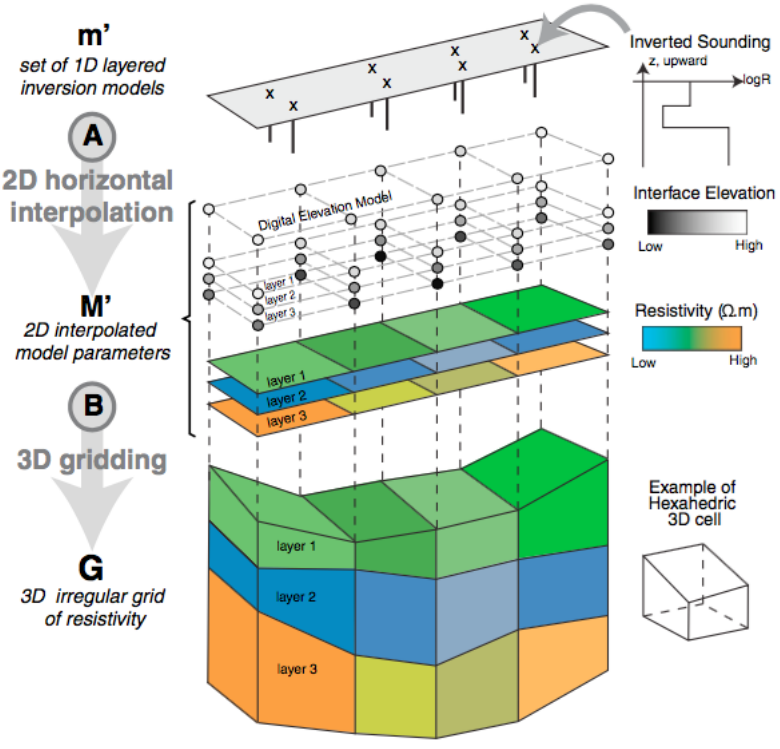

Figure 5.1: 3D gridding of resistivity from 1D inversion models (Pryet et al., 2011). (A) From the set of 1D vertical inversion models, geophysical model parameters are interpolated in the 2D horizontal space. (B) The 3D grid is constructed from 3D vertex positions and filled with resistivity values from corresponding resistivity maps.

The interpolation of the model parameters are made by kriging, which re-

quires variables whose histogram are close to a normal distribution. In the case of the parameter describing the geometry, its histogram is frequently normal. However, resistivity is far from normality and a log-transformation of the data is required. The horizontal resolution of the grid is the same as the 2D matrices. In the case of vertical resolution, the 3D grid has one cell per geophysical layer. The vertical coordinates of each cell vertices are deduced from the elevation model (DEM) and the thickness of each layer. Its thickness is either fixed in the case of numerous layers or interpolated in the case of few layers.

5.1.1.2 Airborne electromagnetic survey in San Cristobal

A time-domain AEM survey was conducted in May 2006 using the SkyTEM helicopter-borne system (Sørensen and Auken, 2004). SkyTEM consist in a transient electromagnetic system in which subsurface currents induced by a transmitter coil, diffuse into the ground with a magnitude and decay related to the electrical conductivity of the geological layers (d'Ozouville et al., 2008a). The system transmits two magnetic moments, a low moment for resolution of the near surface layers and a high moment for resolution of the deeper layers (Auken et al., 2009). The measured data is the time derivative of the magnetic field from the decaying subsurface currents. Data is filtered in way that early-time data is not smoothed to enhance near-surface resistivity variations, while late-time data is gradually filtered to obtain as much penetration as possible (Auken et al., 2009; Pryet et al., 2012b). After filtering, data are gathered into soundings. Then, the inversion model is described by a number of layers, each with a thickness and a resistivity (Auken et al., 2009).

The exploratory survey in San Cristobal was performed during 4 days. 23000 1D soundings were made along ca. 900 km of flight lines, with a sounding every 25-50 m (Pryet et al., 2012b). Average flight speed of the helicopter was 45 km/h and the flight altitude of the rig was 35-45 m above the ground surface. Flight lines were generally orientated N-S, where the average spacing between two parallel flight lines was 200 m. Vertical penetration is typically between 200 and 300 m depending of the geological layers.

1D soundings were inverted to both smooth and layered inversion models. A 4-layer and a 19-layer 1-D vertical models were obtained with the spatially constrained inversion scheme, in which local resisitivity models are constrained by neighboring soundings allowing the enhancement of the resolution of the model parameters (Pryet et al., 2012b).

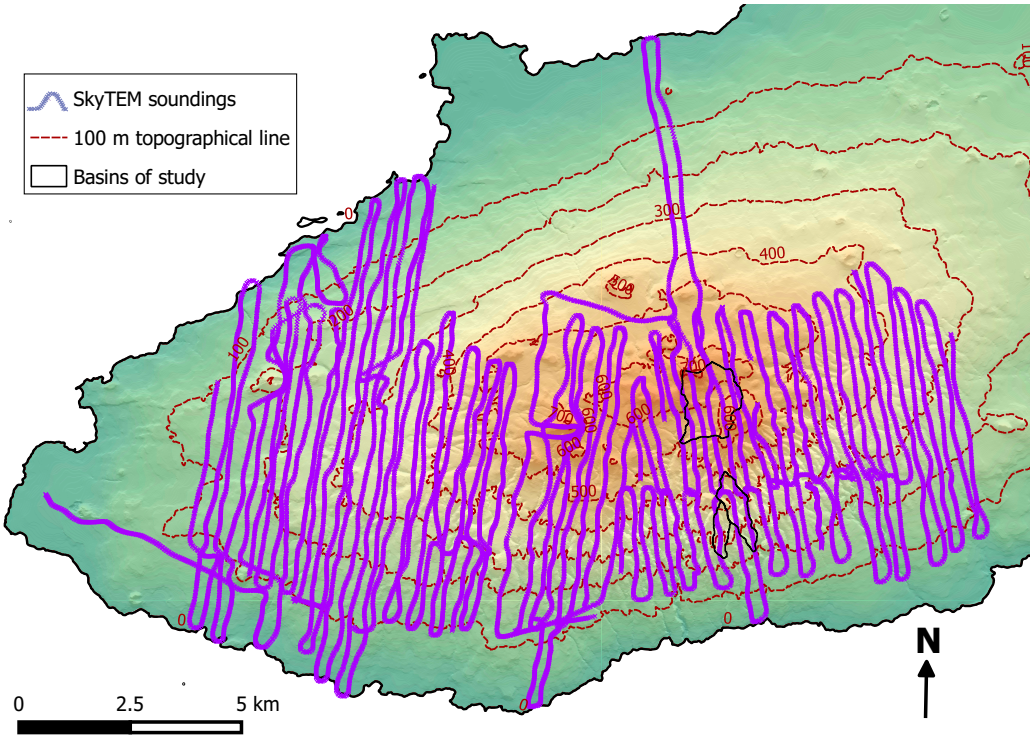

Figure 5.2: AEM SkyTEM survey in San Cristobal. Violet cruises represent each sounding. DEM from the IGM-DEM of 10 m horizontal resolution (IGM, 2014).

5.1.1.3 4-layer 3D resistivity model of San Cristobal

The 1D 4-layer inversions from the AEM survey were interpolated to form a 3D grid of resistivity with the technique detailed in section 5.1.1.1 proposed by Pryet et al. (2011). Given that the thickness of the last layer is considered as infinite, in order to obtain a finite 3D model, its thickness was fixed to 2.5 times the thickness of the third layer (Pryet et al., 2012b). At each point, the thickness of each layer varies with respect to the STRM-DEM (30 m resolution). The gridding resulted in a 3D 4-layer resistivity model with variable thickness, in which the range of resistivity allowed the differentiation of different units (seawater intrusion, unsaturated and saturated basalts, unweathered and weathered basalts), showing insights about the internal structure of the island. The surface view of the resistivity model can be seen in figure 5.3. Contrasting the geophysical data against geomorphological observations, perched aquifers ($30-100\ \Omega$m) were identified on the southside of San Cristobal. More specifically, the 4-layers resistivity model around *Cerro Gato* watershed, allows the identification of the low resistivity zones but its thickness and geometry are still challenging to visualize.

In figure 5.4, the surface view of the 4-layer resistivity model in the study zone near *Cerro Gato* watershed can be observed. Two zones of interest can be identified:

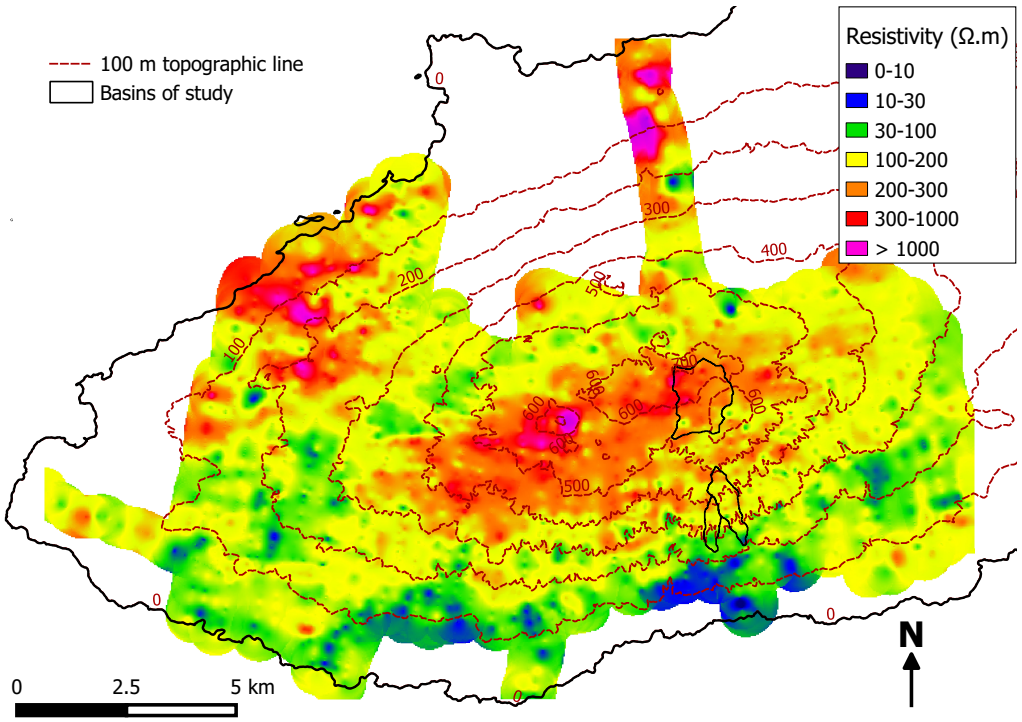

Figure 5.3: Surface view of the 4-layer resisitivity model in San Cristobal (Pryet et al., 2012b). Very low resistivity zone are related to seawater intrusion (< 10 Ωm). Low resistivity zones ($30 - 100$ Ωm) are usually identifed as perched aquifer. Unsaturated weathered basaltic rocks are related with resistivity in the range of $100 - 400$ Ωm. Massive lava flows are related to high resistivy zones (> 400 Ωm). Contour lines are extracted from the IGM-DEM of 10 m horizontal resolution (IGM, 2014).

- The zone at the north of *Cerro Gato*, which shows very high resistivity on the three first layers. This could be interpreted as a thick unsaturated zone, in which, groundwater flow vertically in the downward direction through the permeable and fractured basalt, or the groundwater flow is influenced by an impervious layer (like a thin tile, equivalent to cooked paleosol) that favors sub-horizontal groundwater flow towards other directions. Yet, no spring have been detected near this zone.

- The zone at the north-east, in which low resistivity is found on the third layer over a zone of very high resistivy on the fourth layer. This may suggest that an impervious layer prevent vertical flow to reach the fourth layer, inciting the groundwater storage in the third layer and horizontal flow, which is probably drained by springs. Flow may be directed to the south-west according to the contour of the fourth layer which is in accordance with the alignment of springs on this zone. Yet, there is an incongruence in the altitude respecting to the type of springs. Contact springs have been found on this area at ca. 200 m of elevation, and the resistivity model shows that the assumed impervious layer is at ca. 125 m of elevation, which highlight possibles uncertainties in the model.

The 3D model is subject to uncertainties in their resistivity values. Indeed, a propagation of errors is produced, first from the vertical inversion process, and then, from the kriging in the 2D horizontal matrices. Despite Pryet et al. (2011) reported that these errors are within the acceptable between 250 m-spaced flight lines in a case-study in Santa Cruz (same spacing in San Cristobal), a loss of accuracy is observed in regions far from the flight-lines and also in regions of contrasting resistivity.

Given the rough interpretations from this model and possible uncertainties, a further work on the interpretation of the 1D inversions (4 and 19 layers) is still necessary and will be addressed in the next section.

5.1.2 Interpretation of groundwater occurrence in the study zone from the 3D resistivity models

5.1.2.1 More options for a resistivity model

The 4-layer resistivity model estimated from the SRTM-DEM of 30 m of horizontal resolution (model A) (Pryet et al., 2012b) allows the distinction of geological units at the regional scale. However, for a more detailed interpretation, such as the one needed in *Cerro Gato*, this model might not offer enough details. For this reason two additional models have been contemplated that might address

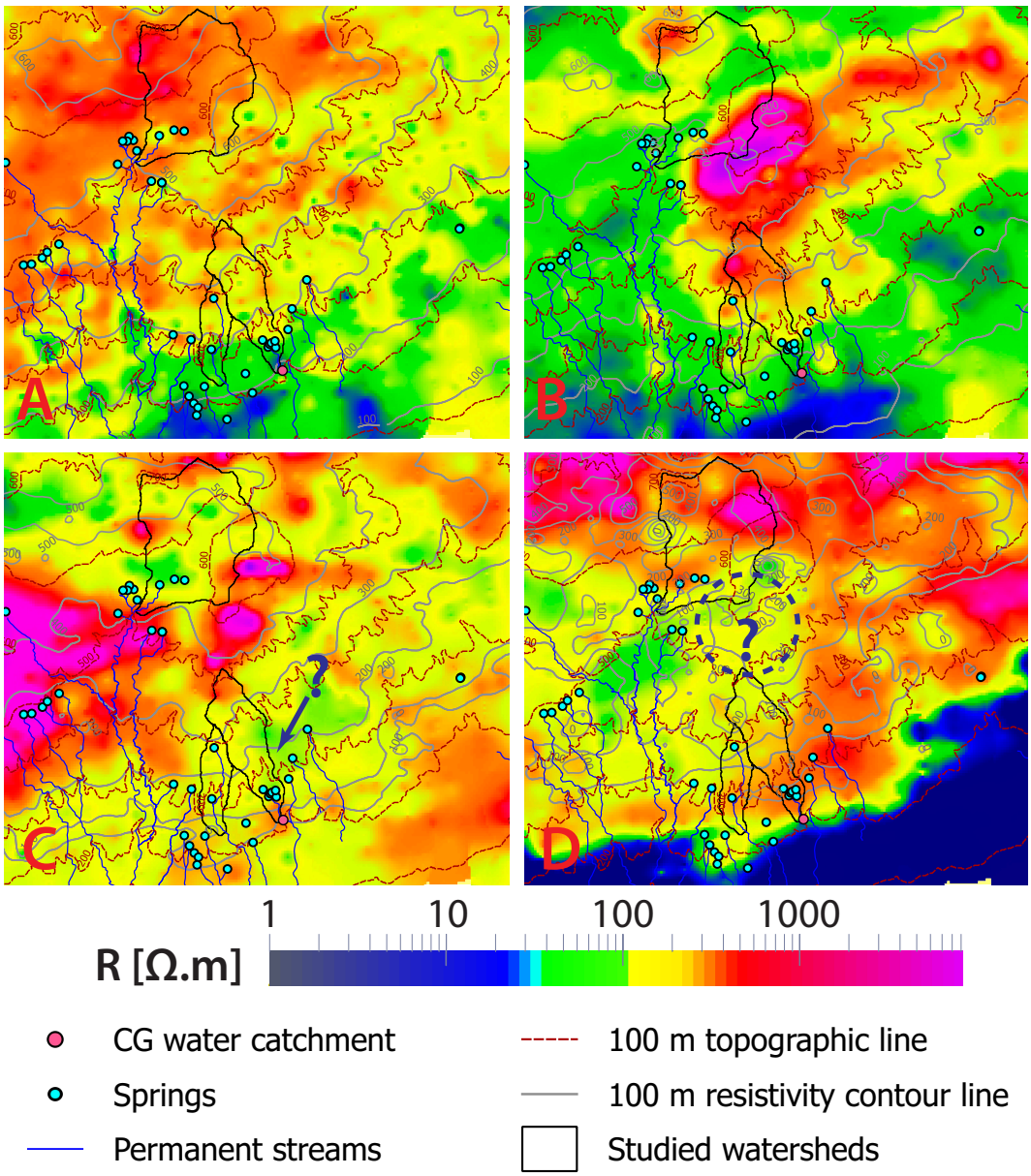

Figure 5.4: Surface view of each layer of the 4-layer resisitivity model (Pryet et al., 2012b). Very low resistivity zones are related to seawater intrusion (< 15 Ωm). Low resistivity zones ($30 - 100$ Ωm) are usually identifed as perched aquifer. Unsaturated weathered basaltic rocks are related with resistivity in the range of $100 - 400$ Ωm. Massive lava flows are related to high resistivy zones (> 400 Ωm). (A), (B), (C) and (D) are the surface resistivity of the first, second, third and fourth layer, respectively. Values of the topographical lines are extracted from the IGM-DEM of 10 m horizontal resolution (IGM, 2014). Contour lines of the resisitivy layers are extracted from the resistivity model based in the SRTM-DEM.

the problem: i) a 4-layer resistivity model estimated from the IGM-DEM of 10 m of horizontal resolution (model B), that may allow a more accurate view of the surface resistivity considering the incised morphology in this part of the island; and, ii) a 19-layer resistivity model estimated from the SRTM-DEM (model C), in which the number of layers might show more detailed geological units. The two models are obtained from the 1D inversions of 4 and 19 layers (Auken et al., 2009), using the same technique proposed by Pryet et al. (2011) for model A.

Figure 5.5 show the three resistivity models obtained for San Cristobal. In a general view, the three models show a similar resistivity distribution. However, the resistivity spatial distribution and magnitude are not the same in the three models. At the surface, model A and B have a similar spatial distribution of resistivity with slightly differences. However, model B is more detailed and allows an easily identification of several features such as the drainage network and location of cones (e.g. *El Junco* Lake). Model C is more contrasted in the surface, but it is expected given that the first layer have a fixed thickness (5 m) contrary to models A and B, where the thickness range is between 4 and 45 m. In the cross section, models A and B are also similar. Both have geological units with several discontinuities. Model B seems to have a more realistic profile of the sea water intrusion. The better resolution at the surface provides an explication of low resistivity spots where the slope is gently that could be related to ponding, something that in model A cannot be explained. Besides the previous aspects, it seems there is not a major improvement when a more detailed DEM is used. On the contrary, model C have geological units which are more continuous, more massive and apparently closer to reality (e.g. the low resistivity layer relative near the surface related to a perched aquifer is more continuous and have a smoother form than the one with the two others). However, sea water intrusion is poorly represented in this model.

In conclusion, the 4-layer resistivity models show more constrasting resistivity. Therefore, it is more suitable in a more regional scale where the intention is to have a better distinction of several geological units with a different range of resistivity and reach higher depths. On the contrary, the 19-layer model shows a more detailed view of the geological units while located in the sub-surface. The fixed thickness of the layer and the smoother transition of resistivity is a limitation at a regional scale, but an advantage in a more local scale because it improves vertical resolution. Given that the objective of this study is to define the geometry of the perched aquifer which should be relatively close to the surface (ca. 80 m), the 19-layer resistivity model would be the more suitable.

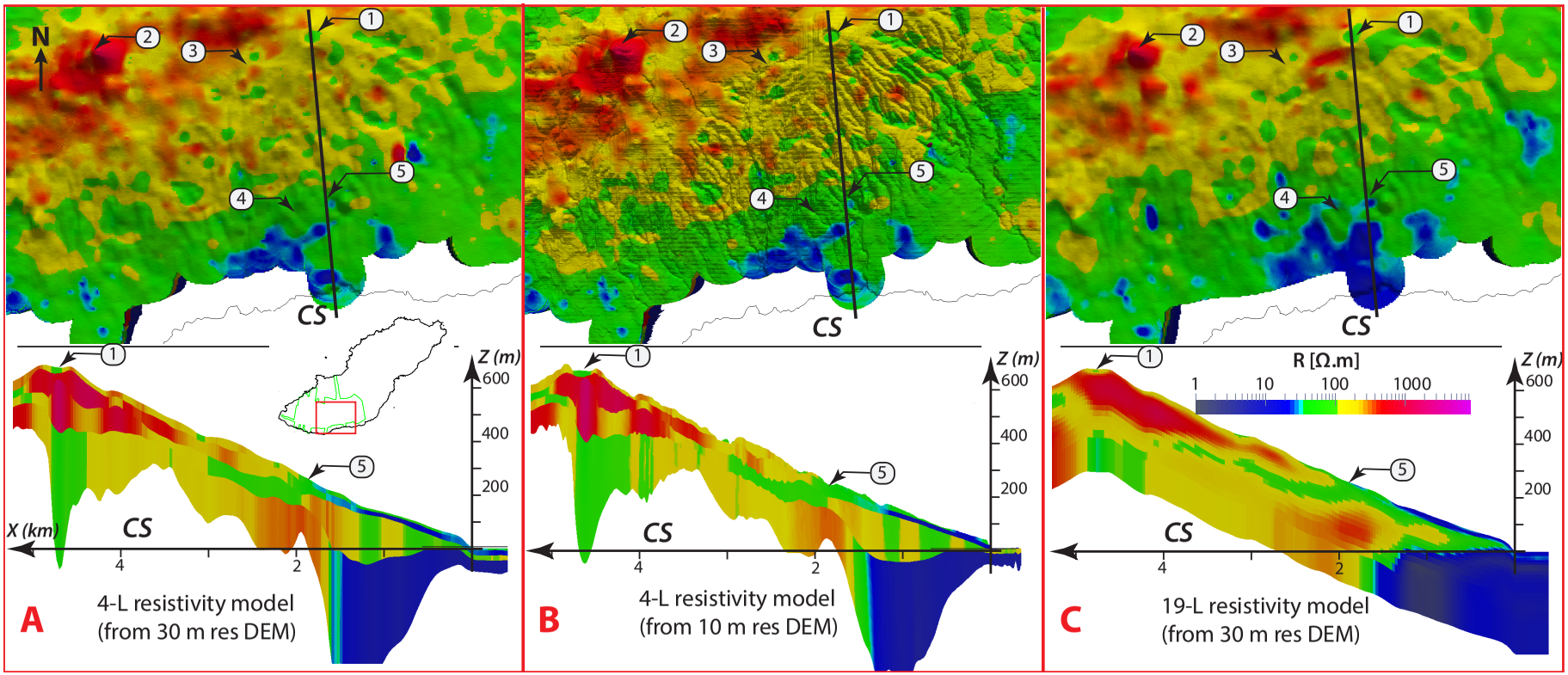

Figure 5.5: Surface view and cross section of three resisitivity models on the southern windward side of San Cristobal: (A) is the 4-layer resistivity model estimated from the SRTM-DEM of 30 m of resolution reported by (Pryet et al., 2012b). (B) is the 4-layer resistivity model estimated from the IGM-DEM of 10 m of resolution (IGM, 2014). (C) is the 19-layer resistivity model estimated from the SRTM-DEM. Very low resistivity zones are related to seawater intrusion (< 15 Ωm). Low resistivity zones ($30 - 100$ Ωm) are usually identified as perched aquifer. Unsaturated weathered basaltic rocks are related with resistivity in the range of $100 - 300$ Ωm. Massive lava flows are related to high resistivy zones (> 300 Ωm). (1) *El Junco* lake. (2) *San Joaquin Cerro*. (3) *El Bayo* control section. (4) *Chuki Marka* control section. (5) *Cerro Gato* springs.

5.1.2.2 Interpretation of the resistivity model in the zone of study

The 19-layer resistivity model cross sections in figure 5.6 allows a view of the internal structure of the sites of interest in this study. Very low resistivity (< 15 Ωm) are observed close to the ocean level which is related to seawater intrusion beneath the basal aquifer (Pryet et al., 2012b). Seawater interface slope is very gently ($< 0.1\%$), so the inland seawater interface is very shallow. This means that the water table of the basal aquifer at this point remains close to the sea level which is related to the high transmissivity of the basal aquifer. Similar conditions in the basal aquifer are also observed in Santa Cruz Island (d'Ozouville et al., 2008a; Pryet, 2011; Violette et al., 2014). Pryet et al. (2012b) estimated that the water table of the basal aquifer on the windward side ranges between 0 and 2.5 m a.s.l. from the sea coast to 1.7 km inland, respectively, using the Ghyben-Herzberg equation and assuming hydrostatic equilibrium and no mixing between fresh and saltwater.

Low to intermediate resistivity ($30 - 200$ Ωm) can be observed in several cross sections (especially near the surface and more specifically in the windward side) and it is related to basaltic rocks subject to several degrees of saturation and weathering (Descloitres et al., 1997; Müller et al., 2002; Pryet et al., 2012b; Vittecoq et al., 2014). Generally, fractured basaltic rocks have high resistivity, however, if enough fractured and saturated with conductive fluids (such as freshwater), their resistivity can be low (Krivochieva and Chouteau, 2003). Chemical weathering of basaltics rocks results in the formation of thick saprolite, which is a rich-clay material that preserves the textural features of the original rock (Palacky, 1987; García-Romero et al., 2005). Because, clay materials have low resistivity, weathered basalts are related to low resistivity units.

Springs located in the windward side are located in outcrops of low resistivity layers ($30 - 100$ Ωm). Because the water table of the basal aquifer seems to remain close to the sea level at the spring locations, it is not possible that the basal aquifer originate those sources. Then, as proposed by Pryet et al. (2012b), the sources are originated from perched aquifers, which can be form above impermeable units such as ash deposits and paleosols. Indeed, impermeable units have been identified in several springs and ravines. In few of them the thickness have been identified (< 1 m) while in the case of the others the identification of their thickness results challenging. However, they are expected to be thin ($<$ 10 m). These units are not detectable with the used AEM technique because its resistivity is not as contrasting to be noticed. Moreover, in the 19-layer model, each layer has a fixed thickness (from 5 to 26 m), so, if these units are thinner, the corresponding layer will not actually represent their thickness. Given that these units are supposed to be saturated, they should be placed within the low

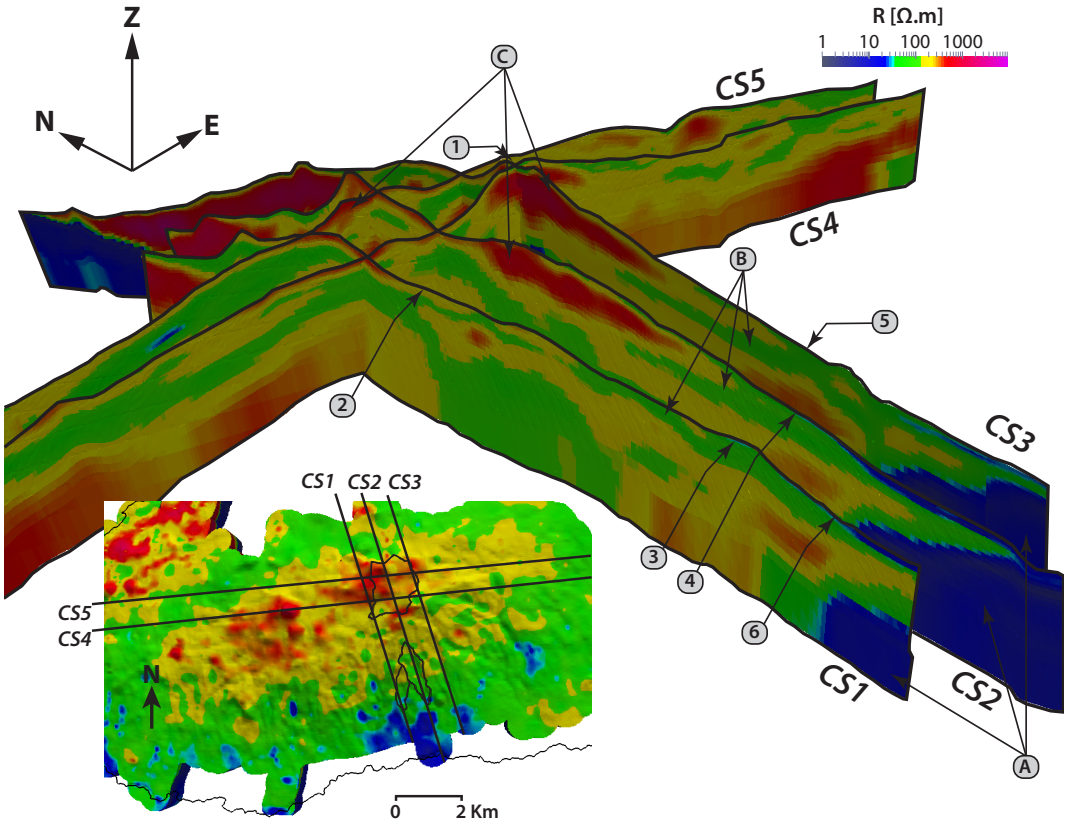

Figure 5.6: Cross sections of the 19-layer resisitivity model on the study zone. (A) Very low resistivity zones (blue) are related to seawater intrusion (< 15 Ωm). (B) Low resistivity zones ($30 - 100$ Ωm) identified as perched aquifer (green). (C) Unsaturated fracture or massive lava flows (red) are related to high resistivy zones (> 300 Ωm). Additionally, unsaturated weathered basaltic rocks are related with resistivity in the range of $100 - 300$ Ωm (yellow). (1) *El Junco* lake (640 m a.s.l). (2) *El Bayo* control section (520 m a.s.l.). (3) *Chuki Marka* spring (275 m a.s.l.). (4) *Cerro Gato* springs (240 m a.s.l.). (5) *Carmela Palmas* spring (300 m a.s.l.). (6) *Aguas* spring (190 m a.s.l.). Location of the springs can be seen in Fig. A.8.

resistivity bodies ($30 - 100\ \Omega$m), at the deeper layer with an unknown thickness.

High resistivity units are related to unweathered and unsaturated fractured or massive basaltic rocks (Descloitres et al., 1997; Krivochieva and Chouteau, 2003; d'Ozouville et al., 2008a; Pryet et al., 2012b). These units can be observed in the subsurface of the leeward side and the highlands but also below low resistivity units. This feature is in accordance to the idea of impermeable layers that retain downward groundwater flow, favors lateral circulation and limits the groundwater percolation below it. Thus, a perched aquifer could exist above this layer and the basalt is unsaturated below this layer.

Sites of interest in figure 5.6 can now be interpreted. *Cerro Gato* (240 m a.s.l.) and *Chuki Marka* (275 m a.s.l.) springs are located just above low resistivity layers that reach the surface. Therefore, these springs are fed by a perched aquifer. In CS1, the perched aquifer of *Chuki Marka* is near the surface and practically continuous until the highlands. This is in accordance with the hydrological model proposed for *Chuki Marka* in section 4.3.4, where the basin gains water from high elevation basins. On the contrary, CS2 shows that the perched aquifer of *Cerro Gato* is deeper than the one of *Chuki Marka*. It also shows that its upper limit does not reaches the highlands. In fact, its length from the spring is lower (ca. km) that the length of the hydrological basin (ca. 1.6 km). Given the different depths of the perched aquifers of *Cerro Gato* and *Chuki Marka*, it does not seem they are connected. However, CS3 shows a perched aquifer with a similar depth to the one of *Cerro Gato* and that reaches higher elevations. It is likely these two units are connected. In such case, the perched aquifer of *Cerro Gato* seems to be orientated towards the north-east. In *El Bayo* watershed, its outlet, is just ca. 100 m downstream of the swamp that fed its stream. In CS1, a saturated layer is not visible at the exit point of *El Bayo*. However, there is a saturated layer just below it. Cross sections show different parts of *El Bayo* watershed. In several locations of the basin, high resistivity layers are observed. These are unsaturated factured or massive lava flows that most likely are highly permeable favoring deep infiltration. Low resistivity units are also observed, but these are located in the subsurface and orientated towards the west and north and at deeper levels towards the south (except in CS1). Therefore, it seems that in most parts of this basin, recharge is whether infiltrated to deeper levels or orientated towards other hydrological basins. In such case, the stream of *El Bayo* is originated by subsuperficial flow in a reduced zone near the stream. This interpretation is in accordance with the relative low streamflow observed in this basin and to the hydrological model proposed in section 4.3.3.2 for *El Bayo*, where a large part of the recharge is lost.

5.1.2.3 Springs of Cerro Gato watershed

From this point, our efforts will be concentrated in *Cerro Gato* watershed because its hydrological model (section 4.3.3.2) shows that its hydrological and hydrogeological watersheds are not compatible. Moreover, the objective of this thesis is to provide a detailed understanding of the hydrodynamic functioning of this watershed, in which water is supplied to most of the inhabitants of the island. In figure 5.7, a cross section along *Cerro Gato* watershed reveals basically three zones of interest: i) the low resistivity layer near the surface which can be associated with an unsaturated or saturated soil layer or weathered basaltic rock, ii) the low resistivity unit at a deeper level which is related to the perched aquifer and, iii) the high resistivity unit related with unsaturated lava flows. The perched aquifer have a form of a spoon. The upper part have a gentle slope (lower than the topographic slope, which is 16%), then it becomes steeper and near the springs it changes sign. Its thickness is low in the upper limit (ca. 15 m) but it increases when approaching the springs.

The relative low resistivity unit ($100-300\ \Omega$m, associated to the yellow color), which is the main core in the cross-section, reveals some degree of weathering in the basaltic rock. It can be seen in most of the section, except above a relative large part of the perched aquifer, where a high resistivity unit is observed (red). The thickness of the unsaturated zone above the aquifer (between 40 and 90 m), could allow a damped response in the recharge signal, which might explain the quasi-constant baseflow observed in this watershed. The first unit near the surface, has an average thickness of 15 m. It presents unsaturated and saturated zones, in which the latter can be observed in gently slope locations and the zone surrounding the spring. This weathered cover could also influence the hydrodynamic behavior of the springs by decreasing infiltration and favoring sub-superficial flow.

The perched aquifer formed above an impermeable unit is the one that originates *Cerro Gato* springs. The impermeable layer, which could be ash deposit or red baked soils, is too thin to be resolved with TEM soundings and therefore it is indistinguishable in the resistivity model. Nevertheless, the geometry of this layer can be interpreted from the model. Figure 5.8 shows possible interpretations of the origin of *Cerro Gato* springs from the 19-layer resistivity model. A first possibility (model A), is that the impermeable layer follows the bottom limit of the low resistivity unit. The springs would be originated because the aquifer water level intersects the surface topography (depression spring). In such case, depending of the groundwater recharge, the water level may vary along time and the groundwater discharge could stop from time to time. However, this is not the case, even during drought period. Moreover, groundwater flow should be

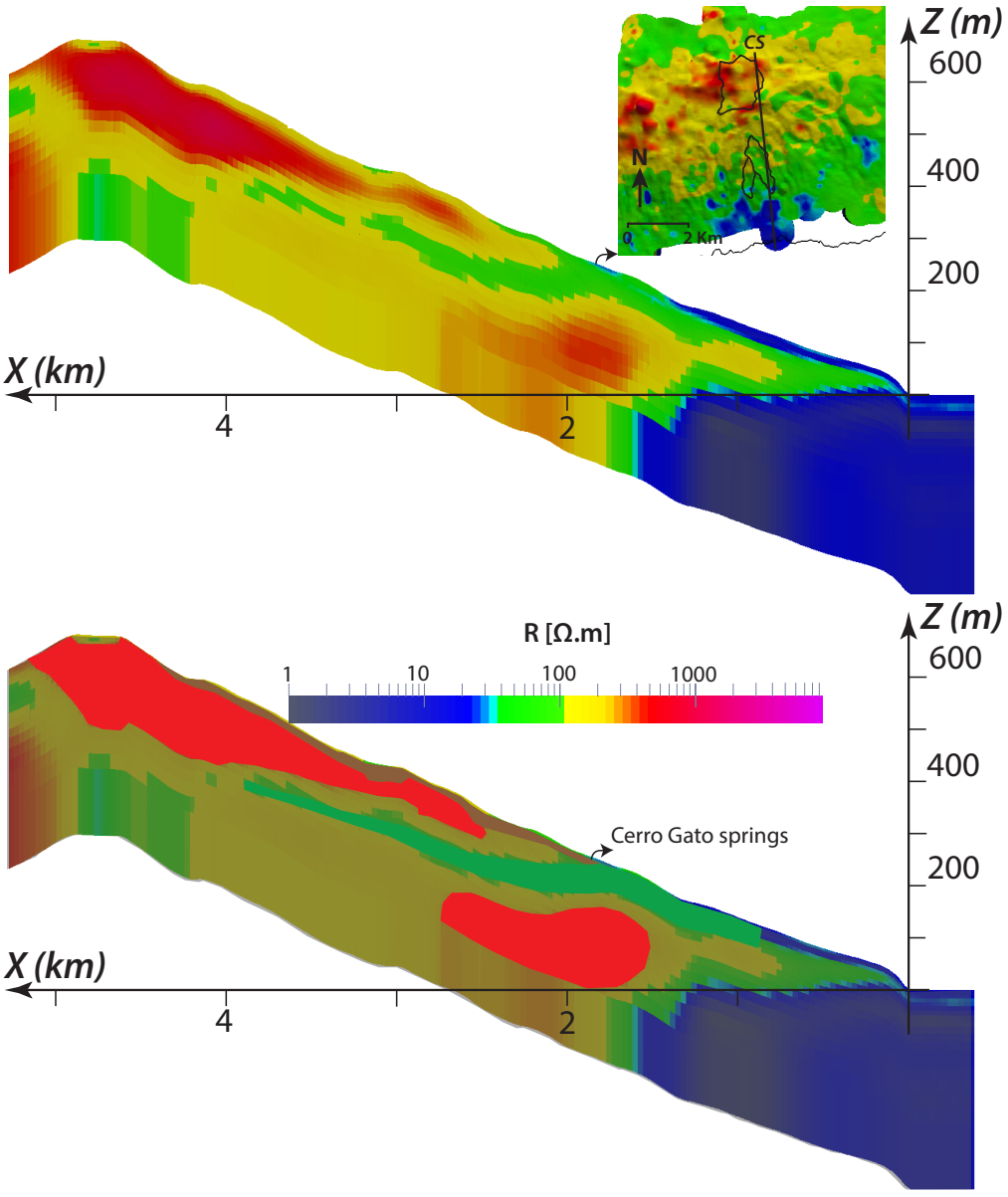

Figure 5.7: Zones of interest in cross section of the 19-layer resisitivity model in *Cerro Gato*. (A) Very low resistivity zones (blue) are related to seawater intrusion (< 15 Ωm). Low resistivity zones ($30 - 100$ Ωm) identified as perched aquifer (green). Unsaturated weathered basaltic rocks are related with resistivity in the range of $100 - 300$ Ωm (yellow). Unsaturated fractured or massive lava flows (red) are related to high resistivy zones (> 300 Ωm). (B) Three zones of interest are identified: i) the low resistivity layer near the surface which can be associated with an unsaturated or saturated soil layer or weathered basaltic rock (brown), ii) the low resistivity unit at a deeper level which is related to the perched aquifer (green) and, iii) the high resistivity unit related with unsaturated lava flows (red).

large enough so the water table level is ca. 30 m above the impermeable layer right after the springs. The second possibility (model B), is that springs are originated because the impermeable layer sustaining the aquifer intersects the surface topography (contact spring). This is in accordance with the observations made in the field, where water outcrops of a lava flow unit just above a very weathered one. Once groundwater pours at the surface after the spring outlet, streamflow is formed and a part of it is re-infiltrated. However, it might require a second impervious unit downstream of the springs that could sustain the thick superficial saturated unit downstream of the spring. Another inconvenient with this possibility is that the saturated unit after the spring should be restricted to the streamflow path, but, the resistivity model show that this unit covers a large area under 200 m of elevation. A third possibility (model C), is a mixed of the former two. An impermeable layer that follows the bottom of the saturated unit and a local impermeable unit, such as a paleo-cone, that redirects the flow of the perched aquifer towards the surface. This is a plausible possibility, given that in this area pyroclastic deposits have been observed near the surface. All three models seem to be subject to a sub-superficial flow upstream of the spring that reaches the perched aquifer just before the spring.

If we use a simple model to represent the perched aquifer, with a constant water flux through the aquifer, no losses through the sustaining layer and no recharge; then using the Darcy's law under steady state conditions the groundwater flow is estimated as:

$$q = K \times A \times i \tag{5.1}$$

where q is the groundwater flow, K is the hydraulic conductivity of the medium, A is the transversal surface and i is the hydraulic gradient. Mean recharge for *Cerro Gato* watershed is ca. 800 mm/year. Using 2200 m as the length of the aquifer and a unit width, then groundwater flow at the spring reaches 2.5×10^{-8} m/s. Slope at this point is 0.08. Thickness is 30 m and given a unit width the surface is 30 m^2. Then, estimated K is ca. 1×10^{-8} m/s, which would be too low for an aquifer with fractured basalt media and similar to a value expected for the impermeable layer. However, this estimation is with an unit width value. Considering the whole recharge in the watershed surface and that the approximated width of the watershed at the springs is 40 m, then q reaches 1.7×10^{-2} m/s, A is 1200 m^2 and estimated K is 1.8×10^{-4} m/s. Given that the watershed surface might be smaller than the hydrogeological one, then using the double surface K reaches 3.6×10^{-4} m/s. This value is more likely for basaltic rocks, but it is still low comparing to 1×10^{-3} reported by Pryet (2011) for the basal aquifer of Santa Cruz. If we use a saturated thickness of 5 m (could be the case of model C), then K reaches 1×10^{-3} m/s. Given the field observations

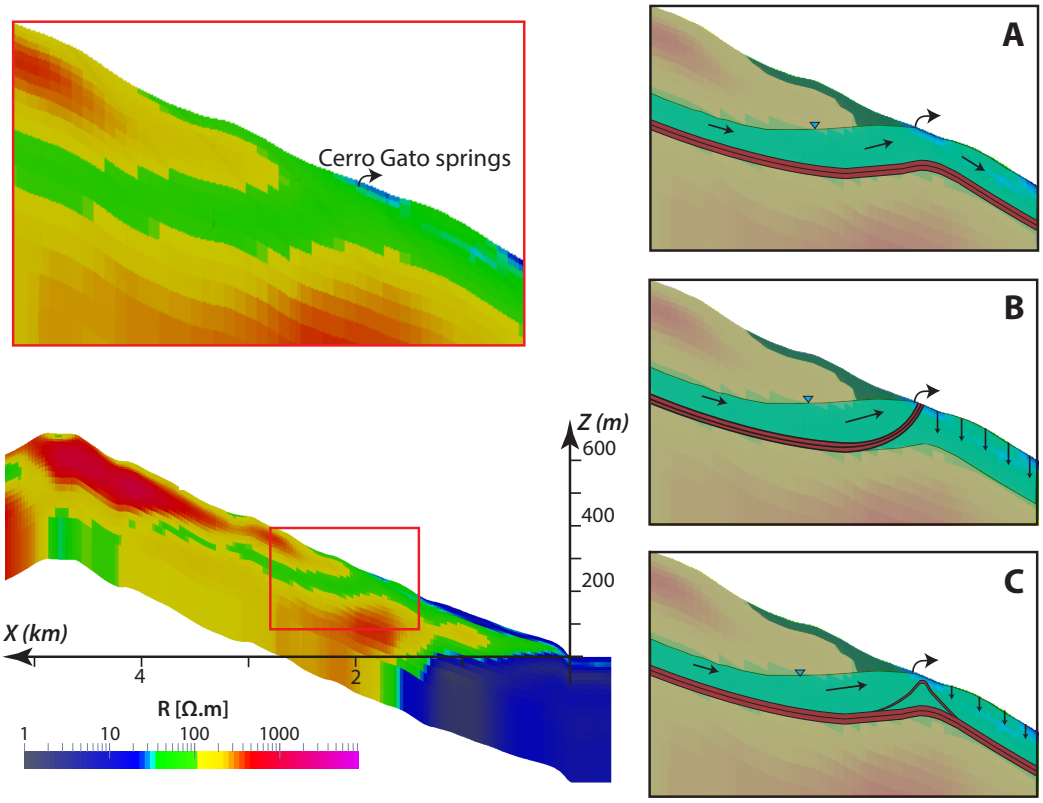

Figure 5.8: Interpretation of the *Cerro Gato* springs from the 19-layer resistivity model. (A) An impermeable layer follows the bottom limit of the low resistivity unit and the springs are originated because the aquifer water level intersects the surface topography (depression spring). (B) Springs are originated because the impermeable layer sustaining the aquifer intersects the surface topography (contact spring). (C) An impermeable layer follows the bottom of the saturated unit and a local impermeable unit, redirects the flow of the perched aquifer towards the surface (contact spring).

and the interpretation from the resistivity model, then model C is more likely to explain the origin of the springs in *Cerro Gato*. It remains to be identified what could be the surface of the sustaining layer of the perched aquifer of *Cerro Gato*.

5.1.3 Geometry of the perched aquifer of *Cerro Gato*

5.1.3.1 Definition of the geometry of the perched aquifer of *Cerro Gato* from the 19-layer resistivity model

The partly buried low-resistivity unit ($30 - 100$ Ωm) associated to freshwater saturated basalts (Pryet et al., 2012b) is easily identified in various cross sections (Fig. 5.6, Fig. 5.7). This unit located in the windward side has been related to a perched aquifer. The interest is to know the spatial extension of the perched aquifer which originates *Cerro Gato* springs. For this, the cells of the 3D grid of the resistivity model must be extracted with a threshold, which is in the range of $10 - 100$ Ωm. The range was extended until 10 Ωm given that in the surface in some locations of the resistivity are lower than 30 Ωm, but most of them correspond to the location of springs or where the stream are located. Vittecoq et al. (2014) found values of resistivity between 7 and 103 Ωm, which correspond to either aquifer formations or alterites. The latter can be an issue because the weathered cover in the surface could be consider within the aquifer threshold. Indeed, at a given length, different layers within the same threshold could form two separated units. For example, in figure 5.7, at $x = 2.3$ km, two low resistivity units ($30-100$ Ωm) can be seen, one at the surface and one buried several meters deeper. Given that the perched aquifer is one continuous entity, then it is necessary to chose the correct one. Therefore, it is necessary to analyze the correct way to do it. The author has not found a general methodology to perform this task, instead an intuitive method is proposed, which is limited to a local region. Analyzing the cross sections of *Cerro Gato*, the following procedure was proposed for all points of the resistivity model. At each horizontal point, vertical resistivity values are checked from the upper layer to the lower layer. If it is found that a layer's value corresponds to the threshold then the following layers are tracked until a layer is not within the threshold. Then, this unit is registered. After the discontinuity, the rest of the layers are also assessed, if there is more layers that belong to the threshold, the same procedure above is used and a new unit is registered. In the case, there is more than one unit then a selection is made based on the following:

- If the highest layer elevation is higher than 200 m, then the second unit is chosen (the second in elevation).

- If the highest layer elevation is below 200 m, then the first unit is chosen (the one with the higher elevation).

Once an unit is chosen or if there is only one unit, the elevation of the bottom layer of the threshold and the thickness (difference of elevation between the first and the last layer that correspond to the threshold) are used for the construction of two rasters (elevation and thickness).

As mention below, the choice between units is proposed after the observation of cross sections in *Cerro Gato*, so the resulted raster is focused in the region of *Cerro Gato* and might not be trustful in other locations. Figure 5.9 shows a thematic map of the threshold extracted from the resistivity model with the above procedure. In the zone of interest (*Cerro Gato* watershed), the mean thickness is 50 m. In the upper part the thickness is lower and increases toward the lower part. Just below the springs, the threshold is thicker reaching 100 m. The contour lines of the bottom of the threshold do not reveal easily the possible limits of the surface that drains towards the springs. However, it seems it is not connected to *Chuki Marka* watershed and it might be larger than the topographic limits on the eastern boundary.

The limits of the hydrogeological basin are obtained using a similar methodology reported in section 2.2.1. First, given the irregularity of the base of the threshold a filter was used to smooth the surface. Then, points where the threshold is nonexistent, were filled up with a linear interpolation because it is necessary to have one continuous surface. Then, the program *HydroSIG* is used. *HydroSIG* estimates the flow direction and slopes from a given DEM. In this case, the DEM is the filled surface of the bottom of the filtered threshold. Then, coordinates of a point in the DEM are given to the program so it estimates the surface that drains into this point. The DEM is usually corrected to avoid sinks or non-flux directions. In this case, the DEM is not corrected because a sink is just what we are trying to find. If figure 5.7 is observed attentive, we can identified that the springs are located just before the bulge of the bottom of the low resistivity unit. If the point of the spring is used, then the drainage surface would be limited to a small area between the top of the bulge and the spring position, given that the flow direction in this point would be north rather than south. for this reason, we used as the drainage point the depression just before the bulge. This point would be fed by the large flow from the north and the small flow from the bulge at the south. The drainage surface towards this point is the hydrogeological watershed of *Cerro Gato*.

Despite the surface might be overestimated because it would include the small area between the springs and the top of the bulge, this area is negligible compared to the rest of the surface. In figure 5.10, the extracted surface can be seen.

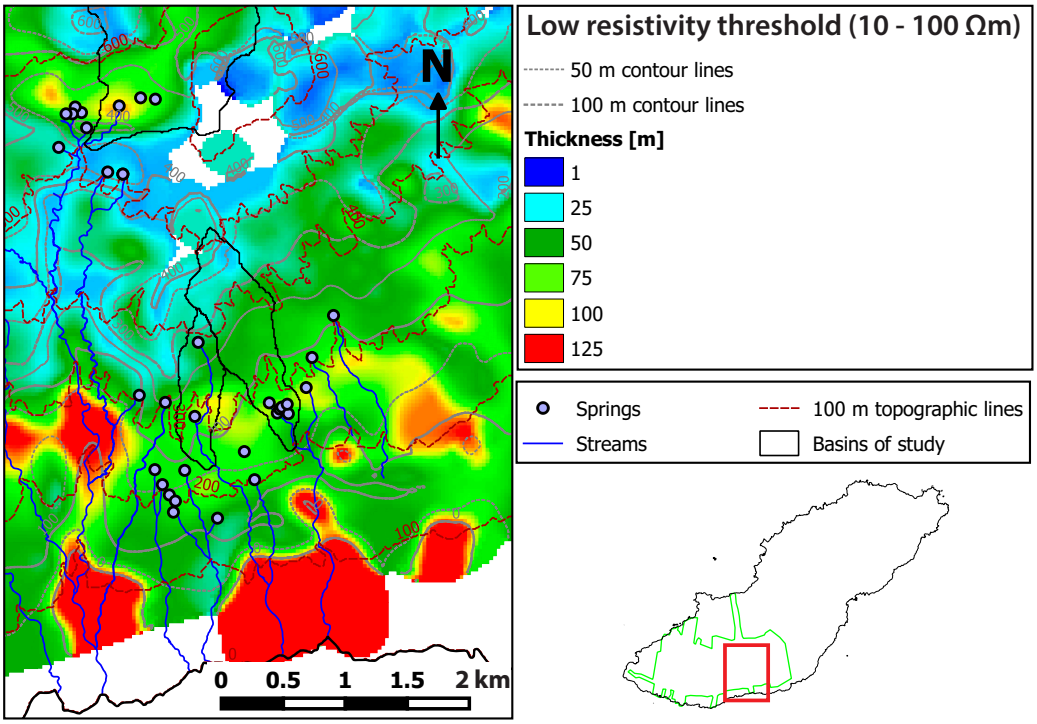

Figure 5.9: Thematic map of the low resistivity threshold ($10 - 100$ Ωm) extracted from the 19-layer resistivity model. The method proposed that the extraction of the threshold is based on observations in the zone surrounding *Cerro Gato*, thus, other zones of the map should not be accounted for any interpretation. Blank spaces correspond to points outside the threshold. Contour lines represent the elevation of the bottom isoline of the threshold.

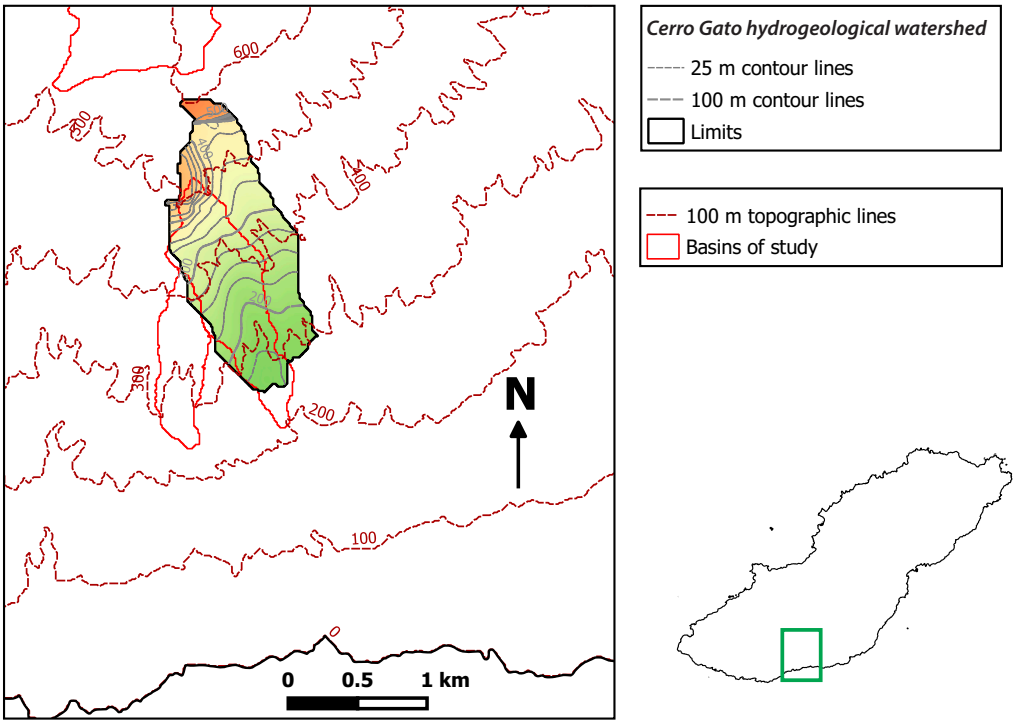

Figure 5.10: First estimation of the hydrogeological watershed of *Cerro Gato*. Contour lines represent the elevation of the bottom isoline of the perched aquifer.

It seems regular except for two zones: at the northern part and the north-western part. These zones seem to be markedly higher than the rest of the surface, which might not be plausible in reality. Probably these two zones were isolated spots of low resistivity near the surface, that could be related to temporarily ponds or just saturated regions with no connection with the perched aquifer. Then, these spots were linked to the perched aquifer surface with the interpolation. These errors show the limitation of the methodology, but to the author's knowledge, it was the only solution. Given that these spots are unlikely to be part of the perched aquifer they were disregarded limiting the perched aquifer surface to a maximum altitude of 400 m. Figure 5.11 shows the corrected hydrogeological watershed corresponding to *Cerro Gato* springs. The hydrogeological watershed have a surface of 1.19 km^2, which is 1.83 times larger than its hydrological watershed. The additional surface of the hydrogeological watershed is located at the eastern boundary of the hydrological watershed and it is also extended towards the highlands. The additional surface is larger than the one estimated with the GR4J model in section 4.3.6 (1.35 - 1.52 times the hydroligical surface). However, the additional surface includes two ungauged springs at the eastern side. Thus, part of the recharge surface should also fed these springs. The additional surface is also in accordance with the conclusions made in section 4.3.6, where the extension of the hydrological surface is more likely to be in the same altitude

rather than at higher elevations.

5.1.3.2 Uncertainties in the perched aquifer definition

The estimation of the geometry of the perched aquifer in *Cerro Gato* can be subject to uncertainties. In the absence of boreholes and outcrops to constraint the resistivity datasets, the distinction of aquifer and non-aquifer might not be accurate. These uncertainties are related to: i) the range of the threshold to define the saturated media and ii) errors in the estimation of 3D resistivity model.

In the literature, the range of resistivity associated to a freshwater saturated media is commonly between 50 and 200 Ωm (Palacky, 1987; Lienert, 1991; Descloitres et al., 1997; Albouy et al., 2001; Müller et al., 2002; Krivochieva and Chouteau, 2003; d'Ozouville et al., 2008a; Pryet et al., 2012b; Vittecoq et al., 2014). However, this range can be larger. Albouy et al. (2001) used vertical and transient electromagnetic soundings (VEM and TEM, respectively) for a coastal groundwater exploration and reported a range between 100 and 800 Ωm for freshwater saturated basalt in La Reunion Island. In the other hand, Krivochieva and Chouteau (2003) reported values between 6 and 30 Ωm for an aquifer in the Chalco Sub-Basin of the Mexico Basin, which consists of pyroclastic material, sand and fractured basalt. In a more comprehensive study, Vittecoq et al. (2014) related the resistivity dataset of a SkyTEM survey with geological database of 55 boreholes to provide a conceptual hydrogeological model of the volcanic island of Mayotte. In 90% of the boreholes intersected by an aquifer formation the range of resistivity was between 5 and 75 Ωm. In the same study, pyroclast (saturated or unsaturated) is associated in a similar range (7 and 103 Ωm). Vittecoq et al. (2014) concluded that the correlation between resistivity data and the nature of volcanic formations is not univocal because this range of resistivity could correspond to aquifer or non-aquifer formations. In the case of San Cristobal, despite the distinction between saturated and unsaturated formation can be somehow constrained with field observations (occurrence of springs, paleosols and weathered cover), the definition of the appropriate range is still under debate. This is critical because the extension and thickness of the perched aquifer depend of this range. Indeed, a smaller range could reduce significantly the dimension of the aquifer (Fig. 5.12), while a larger range could lead to a definition of a regional aquifer all over the island (towards the Canarian hydrogeological model).

Uncertainties in the model are associated to the propagation of errors from the 1D inversion and the kriging in the horizontal matrices. Pryet et al. (2011) estimated this error in the 19-layer 3D resistivity model of Santa Cruz from the total uncertainty variance (inversion variance and kriging variance), reporting

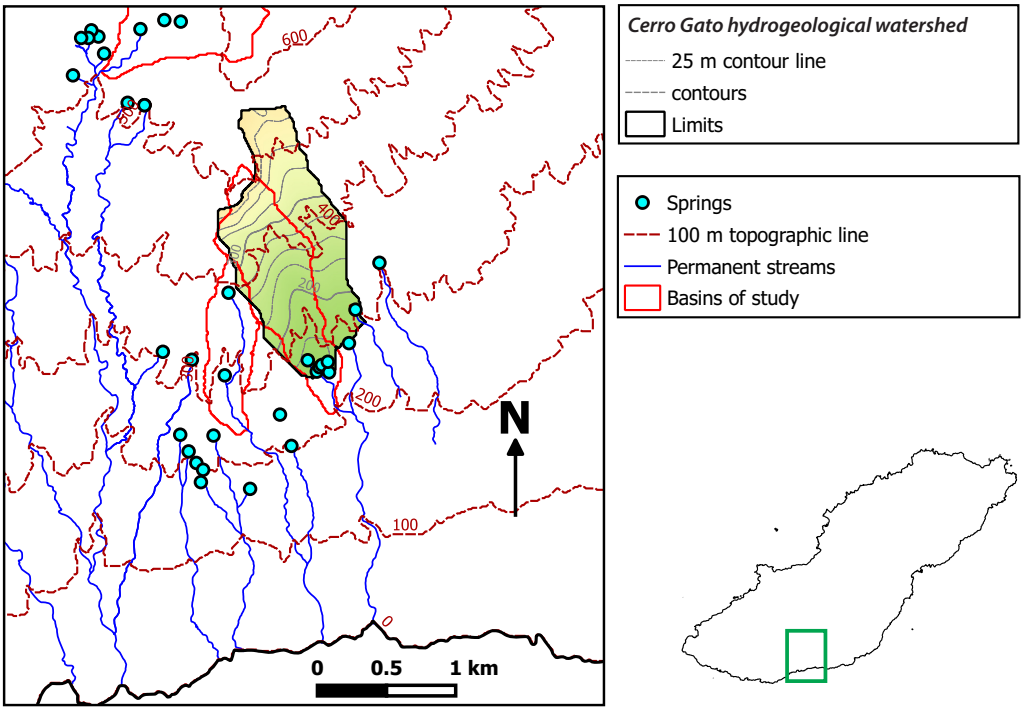

Figure 5.11: Corrected hydrogeological watershed of *Cerro Gato*. The surface has 1.19 km^2, which corresponds to 1.83 times the surface of its hydrological watershed until the springs. Contour lines represent the elevation of the bottom isoline of the perched aquifer.

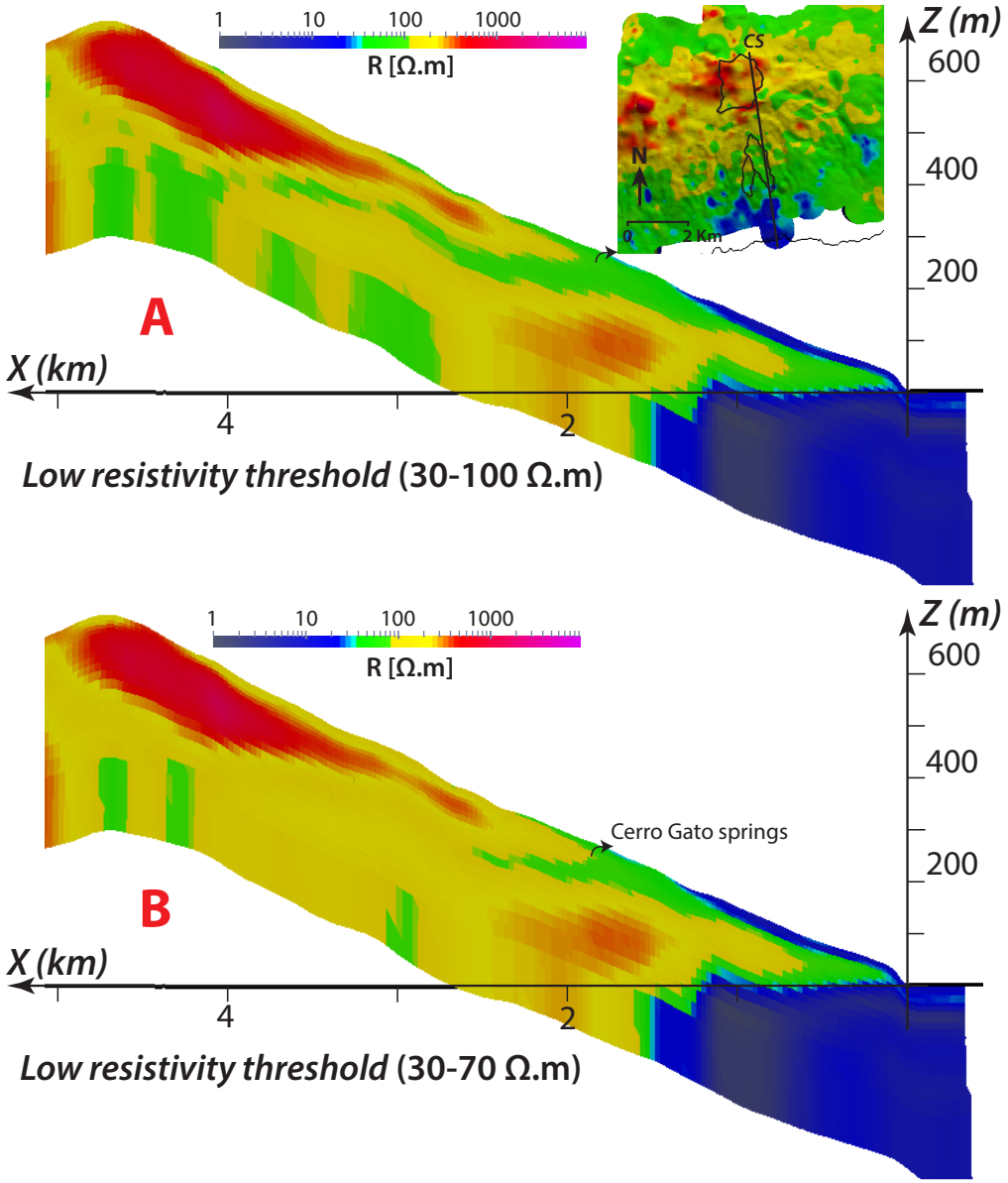

Figure 5.12: Cross section of two different low-resistivity thresholds (green) in the 19-layer resisitivity model, (A) corresponds to a range between $30-100$ Ωm, whereas (B) corresponds to $30-70$ Ωm. Low resistivity is associated to perched aquifers. Very low resistivity zones (blue) are related to seawater intrusion (<15 Ωm). Unsaturated weathered basaltic rocks are related with resistivity in the range between 100 (A) or 70 (B) to 300 Ωm (yellow). Unsaturated fractured or massive lava flows (red) are related to high resistivy zones (>300 Ωm).

a total standard deviation of 0.2 in the log-resistivity of the first layer. Using the same procedure (the description can be seen in Pryet et al. (2011)), the total standard deviation of the log-resistivity for the first layer of the 19-layer resistivity model in San Cristobal is ca. 0.25 (e.g. the confidence interval at 68% of a resistivity value of 100 Ωm is 80 to 125 Ωm). Estimation in the rest of the layers was not performed but it is expected to be similar (Pryet et al., 2011).

Given the uncertainties, to assume only one case of geometry in the perched aquifer would be inappropriate. Therefore, a second case (case B, the former is case A) using a reduced range in the threshold is presented, which is based in the fact that all springs are associated with resistivity values less than 100 Ωm and higher resistivity values might not be suitable given the field observations. In the second option, the geometry is extracted using a threshold of resistivity between 5 and 70 Ωm, which is similar to one reported by Vittecoq et al. (2014). To the author's opinion this range might be the more convenient given that Vittecoq et al. (2014) used the same SkyTEM system and the same inversion process than our study. The confidence interval at 68% of the maximum resistivity value using this threshold (70 Ωm) is 56 to 88 Ωm. The geometry of the perched aquifer is estimated with the same procedure described in the former section.

Figure 5.13 shows the perched aquifers obtained from the two thresholds. The surface of the aquifer B is 0.65 km^2, which corresponds to 55% of the surface of aquifer A. Thickness varies between 19 and 95 m in aquifer A, whereas aquifer B has a thickness that varies between 13 and 77 m. This means that the total volume of aquifer B (2.8×10^7 m^3) reaches 50% of the one of aquifer A (2.8×10^7 m^3), which is a significant difference in terms of storage. Despite the difference in quantitative terms between both aquifers is significant, the location and form is quite similar. Mean slope is similar in both cases (ca. 12%) and the bottom of aquifer B is just ca. 12 m higher than the one of aquifer A in the same surface. Aquifer B has the same shape and dimensions than aquifer A in the lower part, but does not reach the same length. It is like aquifer B is just a section of aquifer A.

Considering discharge and recharge in *Cerro Gato*, the surface of aquifer B, which approximately is the same as the hydrological watershed (0.69 km^2), does not reach the necessary extension to achieve balance (according to GR4J model the surface should be ca. 1.43 times its hydrological watershed). Moreover, this aquifer should also fed the two springs within its limits. From this point of view, aquifer B might not represent the perched aquifer of *Cerro Gato*. However, the weathered cover in the sub-surface might play an important role in the recharge of the aquifer by preventing infiltration in the highlands and favoring sub-superficial flow towards the limits of the aquifer. Whether it is case A, B or both, the

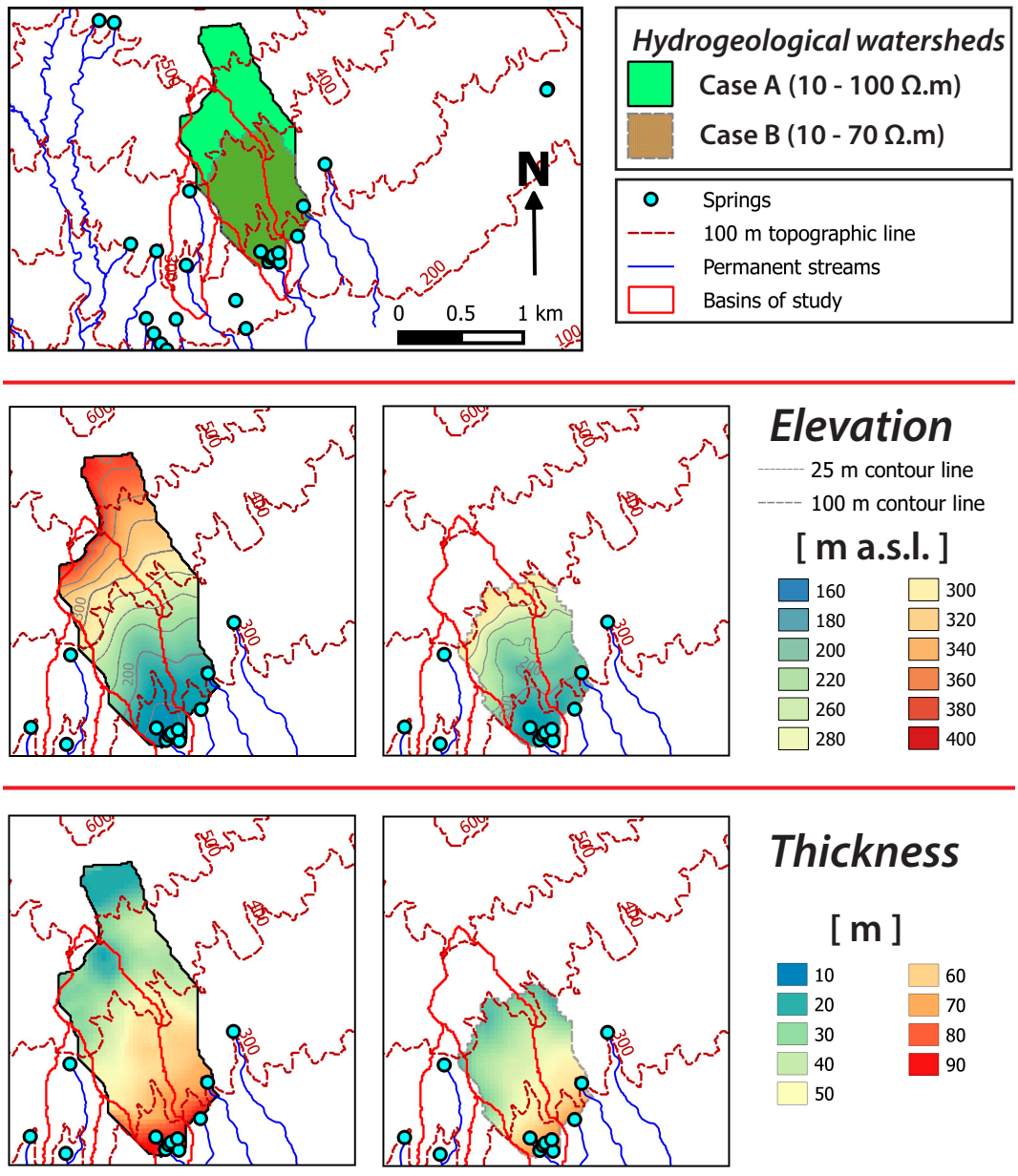

Figure 5.13: Two cases in the definition of the hydrogeological watershed of *Cerro Gato*. Watershed A is extracted from a threshold between $30 - 100$ Ωm, whereas watershed B is obtained with a threshold between $30 - 70$ Ωm. Contour lines represent the elevation of the bottom isoline of the perched aquifer.

plausibility of the proper definition of the perched aquifer could be assessed with a numerical hydrogeological model, which is the next step of this study (chapter 6).

5.2 Seismic tomography

In this section, we describe the results of a seismic refraction survey conducted in San Cristobal. Datasets from this survey not only allow the identification of the thickness of the weathering zones but also the estimation of hydrodynamic properties.

5.2.1 Main concepts and use

Seismic tomography is a reconstruction of the spatial distribution of seismic wave velocities. It is based on the fact that velocity of seismic waves depends of the elastic properties of the media and that these waves are refracted whenever they cross the boundary between two medias with different elastic properties. Wave velocities are obtained from seismic refraction transverse, where geophones, located in an array, register the travel time of an energy source. Two types of waves are commonly registered: i) P-waves (primary waves), which are the compression waves, are the fastest waves, thus it is easier to identify as they are the first to arrive; and ii) S-waves (secondary waves), which are the shear waves, are the second fastest waves and they can only propagate through solid rock (not through a liquid medium as the P-waves).

Seismic tomography has been commonly used to investigate subsurface layering, with applications in several fields (Toksöz et al., 1976; Lankston, 1989; Iyer and Hirahara, 1993; Khalil and Hanafy, 2008; Grelle and Guadagno, 2009). Some of the applications are the estimation of the depth of weathering zone and the determination of the groundwater level. Water table can be attributed to specific velocities of the P-waves (VP) in the same media, or related to the VP/VS ratio if the velocity of the S-wave (VS) is available (Grelle and Guadagno, 2009). Indeed, VP increases in the unsaturated-saturated transition (Grelle and Guadagno, 2009), while S-waves barely change its velocity or even decrease (Toksöz et al., 1976). One of the defaults of this technique is when a media has a lower velocity than the one above, in such case, there is not critical refraction because the refracted ray will be bent towards the normal at the boundary and the signal is loss for the second media. This could happen for example when a sand layer is below a clay layer or a sedimentary rock below an igneous rock. Also, the signal of a thin layer or a layer above a larger with a much faster velocity, cannot be identified. These cases could be identified in an insular volcanic context. For exemple, a paleosol could not be identified or the lower limit of a perched aquifer (unless the media below has a faster velocity than the above saturated media).

Table 5.1: Description of the sites chosen to perform the seismic refraction survey.

Site	Lat	Long	Alt [m]	Sea Dis. [m]	Description
CS1	-89.6069	-0.8969	8	350	Compact soil with rock debris (probably substratum is basaltic rock)
CS2	-89.6145	-0.9225	1	135	Compact soil with scoria debris (probably substratum is basaltic rock)
CS3	-89.6133	-0.9122	10	916	Compact soil with rock debris (probably substratum is scoria deposit)
WS1	-89.4830	-0.9020	590	1294	Clayed soil layer (more than 4 m of thickness)
WS2	-89.4712	-0.9205	230	1790	Silty to clay soil layer
WS3	-89.4760	-0.9243	160	3870	Soil to highly weathered basalt (water table is probably near the surface)

5.2.2 Survey in San Cristobal

5.2.2.1 Sites

In order to have more detailed information about the properties of the basaltic rocks and the overlying weathered layer, a seismic refraction survey was performed in August 2013. 6 sites were picked to perform the survey: three sites in the study area and three on the town of *Puerto Baquerizo Moreno*, near the coast (Fig. 5.14). The three sites on the coast were chosen to have a first estimation of the wave velocities of the basaltic rocks of the island where saturated limit is known (e.g. basalt saturated by salt water and unsaturated basalt). Given the expected layering in these sites the interpretation is much easier and values can be comparable with the ones on the windward side. The first site (CS1) is at the north side of the town, the second site (CS2) is located at the south side, a few meters from *La Loberia* beach and the third site (CS3) is located right next to the airport relatively close to a scoria cone deposit. Sites in the windward side were chosen based on the proximity to the the gauged basins and altitude, but mostly because of the accessibility. The first site (WS1) is located right next to the station SC600, the second (WS2) on the left side of *Cerro Gato* basin and the third (WS3) downstream the control section of *Cerro Gato*. Table 5.1 shows details of each site.

5.2.2.2 Data acquisition

The seismic refraction survey was performed with:

- A seismic source produced by a vertical/horizontal strike of a 8 kg sledge-hammer.

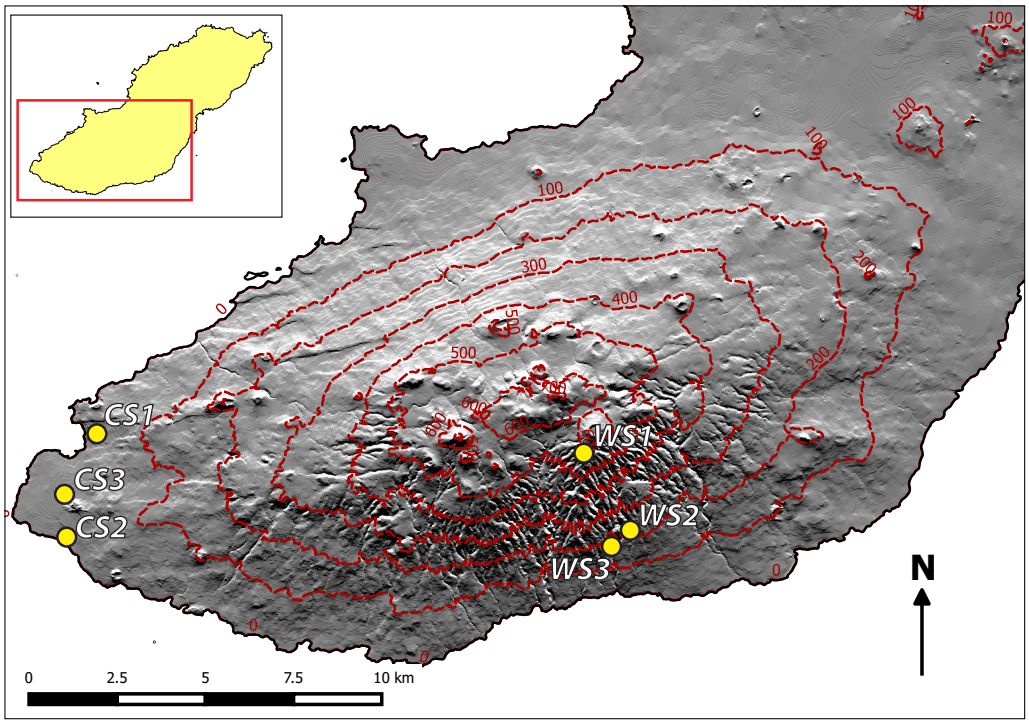

Figure 5.14: Sites chosen for the seismic of refraction survey. CS1, CS2, and CS3 correspond to sites near the coast at Puerto Baquerizo Moreno. WS1, WS2 and WS3 correspond to sites in the windward side near *Cerro Gato* watershed. Topographic lines (brown dashed) and aspect map were extracted from the IGM-DEM of 10 m resolution (IGM, 2014).

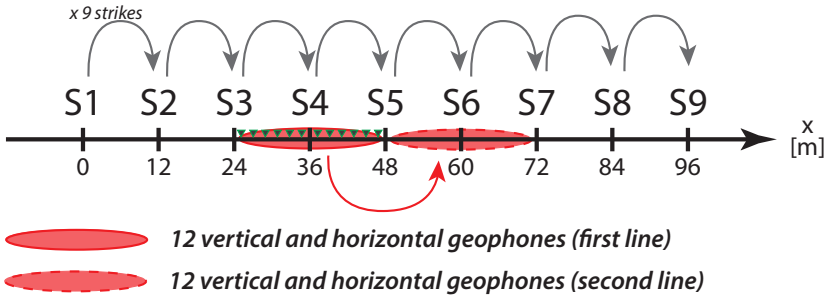

Figure 5.15: Seismic refraction data adquisition scheme. 9 strike bases each 12 m. Geophones were placed each 2 m between S3 and S5 for a first series and between S5 and S7 for the second one. 9 strikes were made at each base and for each series, thus 162 strikes were performed for the P-waves and S+ and S−, respectively.

- 12 vertical and 12 horizontal 1C geophones, which measure the vertical and horizontal soil movements, respectively.
- A station GEODE, for data storage.

The survey is performed within a 96 m array (Fig. 5.15 and Fig. 5.16). 9 strike bases are placed each 12 m within the array. At each base, three types of strikes are produced: strike P (vertical strike of the sledgehammer into a piece of wood), and strike S+ and S− (horizontal strike of the sledgehammer). Geophones are placed next to the transect each 2 m, between base S3 and S5 for the first series and between S5 and S7 for the second series. Each series consists of the three types of strikes at the 9 bases. In this way, the measured transect is duplicated. Horizontal geophones were placed parallel to the transect.

5.2.2.3 Data treatment

After the data acquisition at the field, it was treated in order to estimate the seismic wave velocity along the crossed medias. From the entire dataset, only P-waves are analyzed because only the vertical geophones data have been treated at the moment. Curves of first-arrival travel times are obtained by picking the first arrivals of the P-waves from the collected P-wave records using the *Pickwin* (Pick First Breaks or Dispersion Curves) module from *SeisImager* (Fig. 5.17). First-arrival travel times are used in the module *Plotrefa* to obtain the tomography. Each curve is divided into layers (two or three in this case) according to the corresponding slope. The time-term technique, which is a linear Least-Square approach to determine the best discrete-layer solution from observations; is used

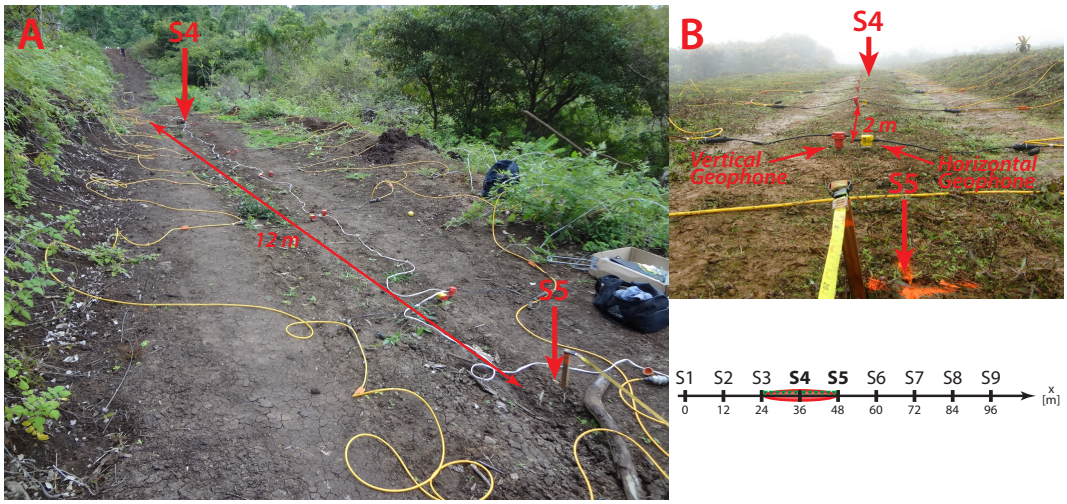

Figure 5.16: Example of data acquisition at the field. (A) corresponds to site WS3 and (B) to site WS1. Vertical and horizontal geophones are placed between S3 and S5 for the first acquisition series. Horizontal and vertical strikes are performed from S1 to S9, then geophones are relocated between S5 and S7 for the second series of strikes.

to obtain the initial velocity model. Finally, the tomography is obtained using the initial velocity model, in which an inversion routine adjusts the initial velocity model until the difference between calculated and measured first-arrival travel times reaches a minimum. The tomography model requires parameters such as numbers of layers and minimum and maximum velocities, which were set to 20, 300 m/s and 5000 m/s, respectively.

5.2.3 Results and interpretation

Figure 5.18 shows the P-waves tomography at the six sites of study. Three layers can be identified from them as follows:

- Low velocity layer ($400 - 500$ m/s), interpreted as the soil layer or highly weathered basalt.
- High velocity layer ($1400 - 1700$ m/s), interpreted as the unsaturated fractured basalt.
- Very high velocity layer ($2400 - 2700$ m/s), interpreted as the saturated fractured basalt.

Sites at the coast (CS1, CS2, CS3) have a thin soil layer at the surface, which is above the fractured basalt. The thickness of the soil layer is less than 1 m at CS1 and CS3 and ca. 2 m at CS2. The thick soil layer observed in CS2 is probably due to the fact that the survey array was placed above a road, which

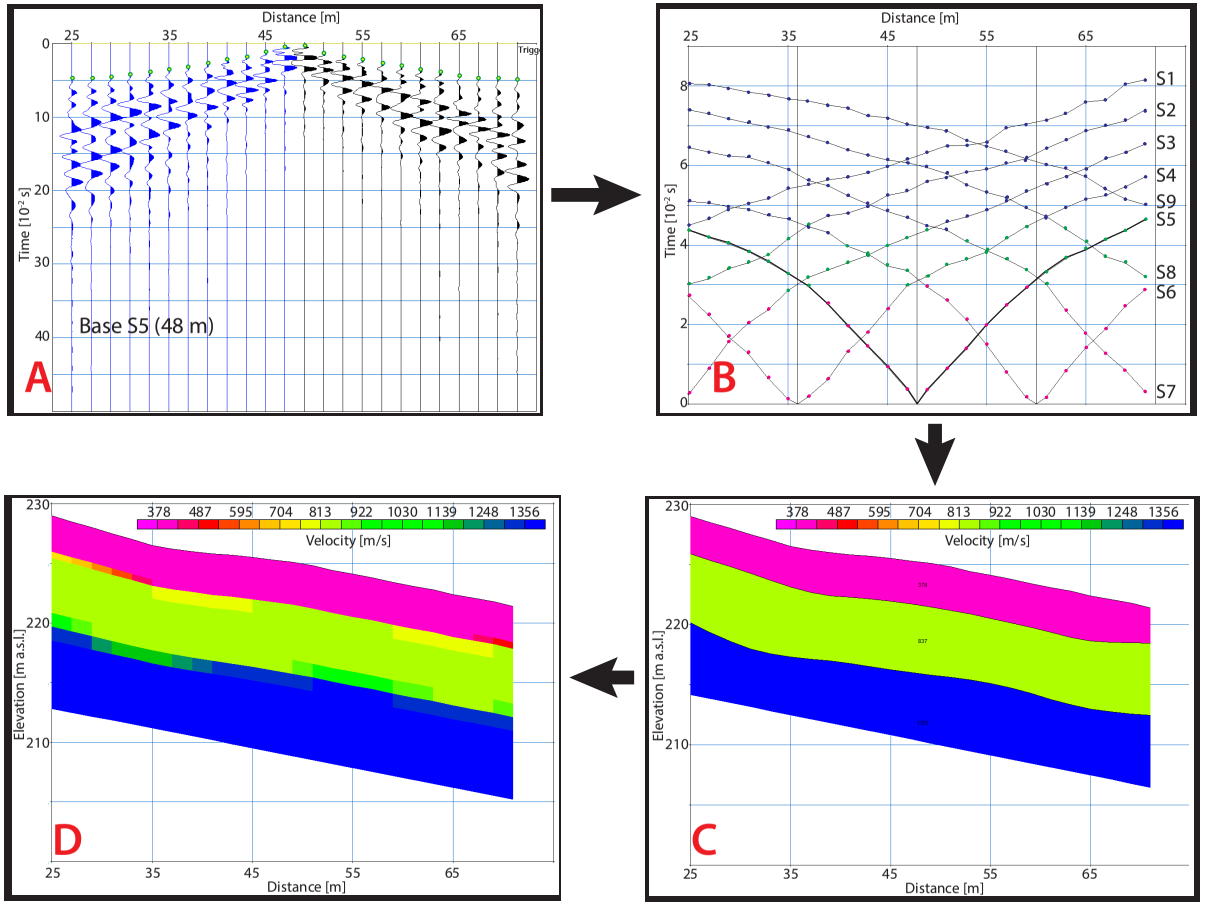

Figure 5.17: Example of the process to obtain the P-wave tomography in site WS2. First, (A) first arrival of the P-waves are selected. Then, (B) layers are assigned at the first-arrival travel times depending of their respective slope. (C) An initial velocity model is obtained. Finally, (D) the tomography is obtained from the initial velocity model. Graphic (A) is the P-waves trace corresponding to the strikes in S5. Green circles correspond to the first arrivals. Graphic (B) is the first arrival travel times separated by layers. Color dots correspond to a respective layer. Graphic (C) and (D) are the initial velocity model and the tomography, respectively.

might had a support base built with scoria and soil. Fractured basalt is observed below the soil. First, the unsaturated part, which have a thickness that depends of the altitude of the surface level, then, the saturated part that can be observed around 0 m of elevation at the three sites, which corresponds to the sea level. Only at site CS2, the unsaturated basalt is barely seen because of the proximity to the sea level. At CS3, the transition between the saturated and unsaturated basalt is smoother than the other two cases at the coast. Moreover, the velocity of the saturated basalt is lower at CS3 (ca. 2400 m/s) compared to CS1 and CS2 (ca. 2700 m/s at both sites). The difference could be related to the proximity of site CS3 to the scoria deposit.

Sites at mid and high elevations at the windward side are contrasting. The highest site (WS1) has a thick soil layer (ca. 8 m) above a probably highly weathered basalt. The soil thickness is in accordance to observations of Geist et al. (1986), which reported that at the end of the formation of the island, it was covered by at least 10 m of pyroclastic deposits. However, in recent surveys, this thickness has not been observed (Izquierdo T., personal communication, 2014). Site WS2 at a lower elevation (230 m a.s.l.), has a thinner soil layer (ca. 3.5 m), which is above a distinguishable fractured basalt layer (the velocity of the basalt corresponds to the values observed in CS1 and CS3). Its thickness cannot be identified though. Site WS3 is the most interesting, as it is located downstream of the *Cerro Gato* spring and near *Cerro Gato* stream (ca. 80 m). Similar to WS2, it has a thin soil layer (ca. 3 m) above apparently fractured basalt. However, there is a third layer that can be associated to the saturated basalt. Indeed, its velocity is similar to the corresponding one in site CS3. Similar to site CS3, WS3 is near *Cerro Gato* cone and pyroclastic deposits have been observed around this zone. However, despite the slope observed in this layer (20%) corresponds to the same direction of the topographic slope (11%) towards the stream of *Cerro Gato* at the left side (ca. 142 m a.s.l.), it might be too steep for a water table. This could be an error related to the measurements or to the assignment of layers, but the existence of the high velocity layer, which is related to a saturated level, is evident.

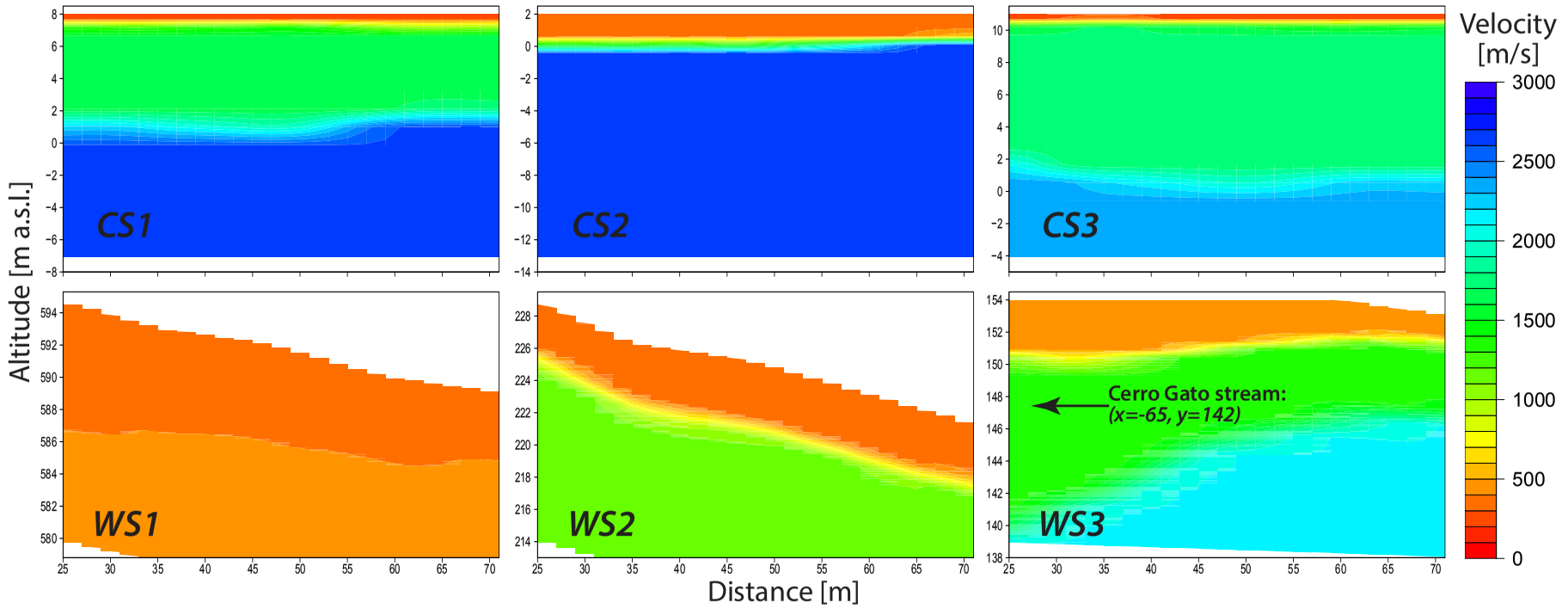

Figure 5.18: P-wave tomographies at the six sites studied. CS1, CS2 and CS3 correspond to sites near the coast. WS1, WS2 and WS3 correspond to sites at the windward side near *Cerro Gato* watershed. Low velocities in orange (400-500 m/s) are related to a soil layer or to a highly weathered basalt. High velocities in green (1400-1700 m/s), are related to unsaturated fractured basalt. Very high velocities in blue (2400-2700 m/s), are related to saturated fractured basalt.

5.3 Estimation of hydrodynamic properties

5.3.1 Introduction

Many physical properties of rocks are related to its pore structure. The relationship between elastic properties of porous solids and pore structure is complex and a whole branch of mechanics is dedicated to the elasticity problem. The seismic wave signal can be used to assess the micro structure and fluid content of rocks. In this section, seismic refraction results are used to estimate the hydrodynamic properties of basaltic rocks. Even though several relations and complex models are used in this section, just a brief description of them is presented. As mentioned before, this is a complicated task and requires advance knowledge of solid mechanics. Given the scoop of this thesis, a detailed explication of the theory behind is not necessary and the basis knowledge of the concepts involved would be enough. However, the author encourages the readers to see the references Gueguen and Palciauskas (1992); David and Zimmerman (2012) in case of interest.

In a porous media, seismic wave velocities (P and S) can be related to the rock elastic properties with:

$$v_P = \sqrt{\frac{K + 4/3 \times G}{\rho}} \tag{5.2}$$

$$v_P = \sqrt{\frac{G}{\rho}} \tag{5.3}$$

where K and G are the bulk and shear rock moduli, respectively, and ρ is the rock density. These equation (Eq. 5.2 and Eq. 5.3) requires continuity in the media, therefore, the media should not have large discontinuities and the wavelength should be larger than the size of any heterogeneity, such as grains, pores and cracks. Given that average wavelength in the seismic refraction survey (ca. 28 m) is expected to be large enough than any fracture within the limits of the survey, then any approach based in these equations can effectively be performed.

5.3.2 Porosity estimation from field measurements

Considering an isotropic solid of a given bulk and shear moduli (K_0, G_0), which has pores with different shapes and randomly orientated, then the overall effective medium can be assumed isotropic (David and Zimmerman, 2012). Total porosity (η) of an effective media can be estimated from the unsaturated-saturated difference of its seismic wave velocity. The unsaturated-saturated relationship

Table 5.2: Parameters used for the estimation of total porosity in sites CS1, CS2, CS3 and WS3

Parameter	Value
ρ_m [kg/m^3]	2700*
ρ_w [kg/m^3]	1000
K_f [GPa]	2.15
K_0 [GPa]	25.6*
G_0 [GPa]	22.7*

* obtained by Loaiza (2012) from samples of Santa Cruz Island

can be assessed with the *Biot-Gassman* equations:

$$K^s = K^d + \frac{b^2 \times K_f}{\eta + (b - \eta) \times K_f / K_0} \tag{5.4}$$

$$G^s = G^d \tag{5.5}$$

where K_0 is the mineral bulk density that can be deduced from measurements at the small scale samples, b is the Biot coefficient, K_f is the bulk modulus of the fluid, and K and G are the bulk and shear of the effective media at saturated (^{s}) and unsaturated conditions (^{d}). Notice that G is the same in saturated and unsaturated conditions. The Biot coefficient can be estimated with:

$$b = 1 - \frac{K^d}{K_0} \tag{5.6}$$

Using Eq. 5.4 and Eq. 5.5, Eq. 5.2 yields:

$$\rho^s \times (v_P^s)^2 = \rho^d \times (v_P^d)^2 + \frac{b^2 \times K_f}{\eta + (b - \eta) \times K_f / K_0} \tag{5.7}$$

Unsaturated and saturated densities are estimated with:

$$\rho^d = (1 - \eta) \times \rho_m \tag{5.8}$$

$$\rho^s = (1 - \eta) \times \rho_m + \eta \times \rho_w \tag{5.9}$$

where ρ_m is the mineral bulk density and ρ_w is the water density.

The four sites where a saturated media is suspected are used to estimate η (the three at the coast and WS3). In these sites, a first rough estimation of the S-wave velocity was performed in order to estimate K^d and to obtain an estimation of the Biot coefficient (b). Then, η is obtained with an iterative process using the saturated and unsaturated P-wave velocities (Eq. 5.8 and Eq. 5.9) and the parameters of Tb. 5.2. The mineral bulk and shear moduli were obtained by

Table 5.3: Seismic velocity and estimated porosity from sites CS1, CS2, CS3 and WS3

	CS1	CS2	CS3	WS3
v_P^d [m/s]	1609	1551	1716	1350
v_P^s [m/s]	2615	2734	2357	2100
v_S* [m/s]	720	685	611	760
η [%]	5.9	3.9	12.4	20.1

* obtained from the slope of S-wave first-arrival travel times.

Loaiza (2012) from measurements in the laboratory of several samples taken from Santa Cruz Island (Galapagos).

A summary of P and S-wave velocities and porosities can be seen in table 5.3 from the resolution of Eq. 5.8 and Eq. 5.9. Results show that total porosity of site CS1 and CS2 are similar (0.06 and 0.04, respectively). This could be expected considering their similar P-wave velocities. However, η in site CS3 is markedly higher (0.12) and close to the value of WS3 (0.2). As mention before, CS3 is close to a pyroclastic deposit. Also, pyroclastic deposits and scoria have been observed near site WS3. Porosity found in CS1, CS2 and CS3 are within the range reported for basaltic formations (1 - 20%) (Custodio, 2004). However, these values are smaller than the ones reported by Loaiza (2012) in Santa Cruz (0.125), except for CS3. Nevertheless, Loaiza (2012) estimated this value assuming $b = 1$ because a S-wave survey was not performed, therefore this value might be overestimated. In the case of WS3, its porosity is above the range for basaltic rocks. The closeness of this site to pyrocalstic deposits may suggest that the media under WS3 is actually pyroclast rather than basaltic rocks. The range of porosity of pyroclastic materials range between 16 and 76% (Mueller et al., 2011). The wide range is due to the fact that their porosity depends of the type of eruption (Mueller et al., 2011). Weathering process could also change the porosity of the material, decreasing its value (Adelinet et al., 2007). Indeed, pore space is filled by clayey alteration products of chemical weathering. However, Adelinet et al. (2007) found that in low-lying areas ($<$ 300 m a.s.l.) the alteration processes in soils are more mechanical rather than chemical. The relative high porosity found in CS3 and WS3 (especially the latter), could then be explained by pyroclastic material subject to a mild effect of weathering.

5.3.3 Permeability and hydraulic conductivity

5.3.3.1 Pore shape model

Effective properties of a given media are related to its elastic moduli, porosity and pore shape (David and Zimmerman, 2012). A pore model is based in the assumption that voids can be represented by spheroids that could have different pore shapes, from infinite thin cracks-like pores to spherical ones. The effective moduli of such a media is described by the differential effective medium scheme described by two coupled differential equations (Le Ravalec and Guéguen, 1996; David and Zimmerman, 2012):

$$(1-\eta) \times \frac{1}{K} \times \frac{dK}{d\eta} = -P(\nu) \tag{5.10}$$

$$(1-\eta) \times \frac{1}{G} \times \frac{dG}{d\eta} = -Q(\nu) \tag{5.11}$$

where P is the pore compressibility, Q is the pore shear compliance and ν is the effective Poisson's ratio, which is a function of K and G:

$$(\nu) = \frac{3K - 2G}{6K + 2G} \tag{5.12}$$

Eq. 5.10 and Eq. 5.11 depend of the porosity, but as reported by Henyey and Pomphrey (1982) and explained by David and Zimmerman (2012), the porosity itself is not the key parameter affecting the effective elastic properties of a cracked solid. Indeed, the porosity can be related to the crank density (Γ) by David and Zimmerman (2012):

$$\eta = \frac{4}{3}\pi\xi\Gamma \tag{5.13}$$

where ξ is the pore aspect ratio, which describes the shape of the pores. In cases where the aperture of pores is very thin compared to its length (crack-like pores), then $\xi \to 0$, whereas $\xi = 1$ for spherical cracks.

The two key paramters that control the effective properties of the media are the crack density and the crack aspect ratio. David and Zimmerman (2012) developed an approach to derive an approximate analytical solution for the effective moduli of a media containing randomly oriented spheroids by using asymptotic approximations (David and Zimmerman, 2011) for the elastic compliance of a spheroidal pore as input in the differential scheme (the author suggests to see David and Zimmerman (2011) for a wider description of the approach), which results in curves that relates Γ against K/K_0 or ν for several values of ξ. The approximate solutions can be applied to a wide range of pore shapes, such as crack-like pores (with $\xi < 0.3$).

This approach is applied in the sites studied in San Cristobal. Table 5.4 shows the elastic properties estimated for all sites. Given that all sites have the

Table 5.4: Elastic properties of the media below sites CS1, CS2, CS3 and WS3 obtained from the seismic refraction survey.

	CS1	CS2	CS3	WS3
K_0[a] [GPa]			25.6	
G_0[a] [GPa]			22.7	
ν_0[d] [-]			0.16	
K[b] [GPa]	4.82	4.62	5.79	2.27
G[c] [GPa]	1.32	1.22	0.88	1.25
ν[d] [-]	0.38	0.38	0.43	0.27

[a] obtained by Loaiza (2012) in two samples of Santa Cruz Island.
[b] obtained with Eq. 5.2.
[c] obtained with Eq. 5.3.
[d] obtained with Eq. 5.12.

same mineral bulk and shear moduli, then one effective media can represent the relation between Γ and K/K_0 or ν for all sites. Figure 5.19 shows this relationship from the solution of the differential effective medium scheme for different options of crack aspect ratio. A simpler way to interpret this graphic is changing its axis. Crack density is related to porosity by Eq. 5.13 and using Eq. 5.2, Eq. 5.3 and Eq. 5.12, K/K_0 and ν can be replaced by the seismic-wave velocity.

The resulting graphics are applied in two ways: i) using P-wave velocity and total porosity to estimate the pore aspect ratio (ξ) (Fig. 5.20) and ii) using P and S-wave velocity to estimate the effective pore aspect ratio (ξ_e) which is related to the fracture porosity (η_f) (Fig. 5.21).

In figure 5.20, identifying a value of ξ for each site is relatively easy. ξ ranges from 8×10^{-3} in CS2 to 4×10^{-2} in WS3 (Tb. 5.5). In the other case (Fig. 5.21), P and S-wave velocities do not fit precisely a single value of η for the same curve of ξ, instead two values are found for each type of wave. The difference is lower when ξ is lower, which suggests that a single value could be found with a curve of ξ lower than 1×10^{-4}. Given that this value is already too low, η from the P-wave is taken. While, the range of values of ξ identified in figure 5.20 is relatively large, in figure 5.21 the same ξ is associated to all sites, which results in similar values of porosity (0.048 to 0.056%). Moreover, values of effective porosity found in these sites with this method are too low. Indeed, Custodio (2004) reported values between 0.1% and 8%. Relating the fracture porosity to the total porosity, it represents less than 0.1% of the total one in all sites. Given that the later method is strongly dependent of S-waves velocity, the low porosity found might be related to an underestimation of the S-waves velocities, which have not been treated extensively yet. Given uncertainties in our S-wave velocities estimation, only the first method is used from this point.

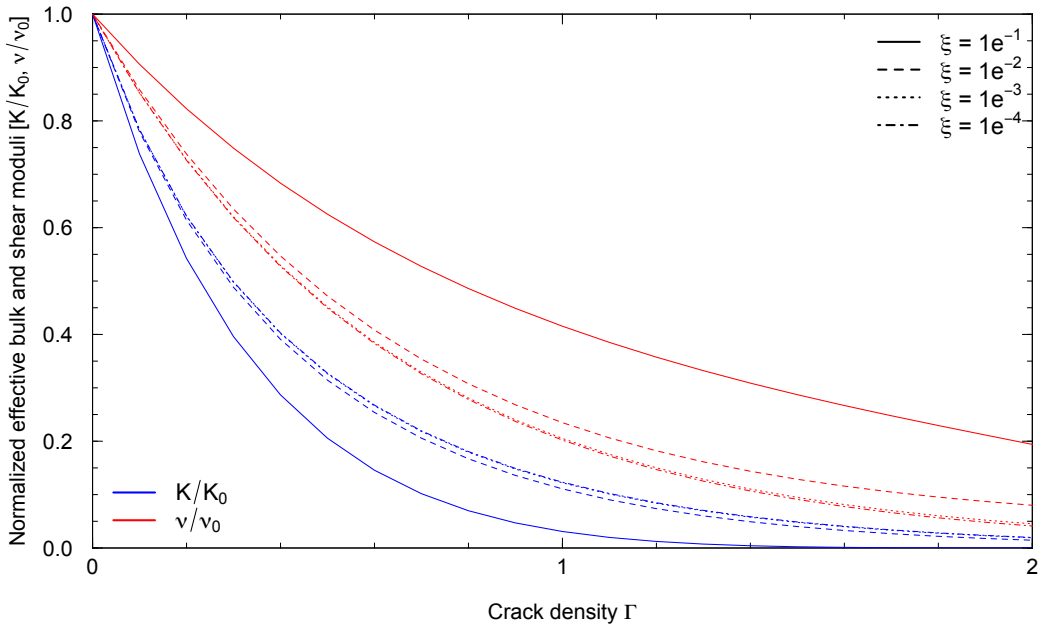

Figure 5.19: Normalized effective bulk moduli and Poisson's ratio of the solid media represented for all sites, which contains spheroidal pores with four values of aspect ratio ($\xi = 0.1$, $\xi = 0.01$, $\xi = 0.001$ and $\xi = 0.0001$).

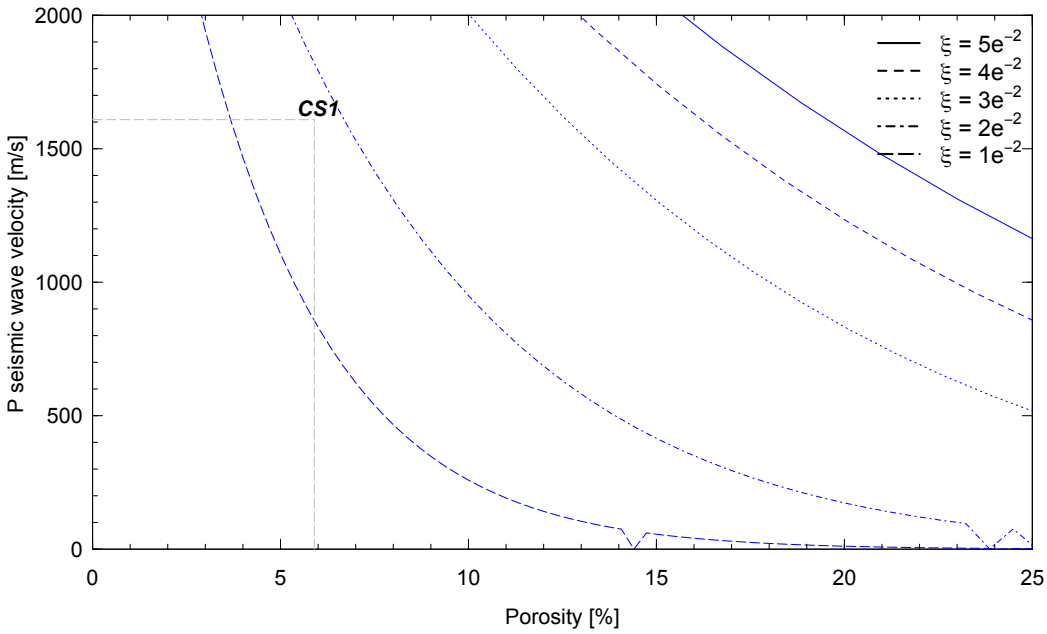

Figure 5.20: Porosity vs P-wave velocity of the solid media represented for all sites, which contains spheroidal pores with five values of aspect ratio ($\xi = 0.05$, $\xi = 0.04$, $\xi = 0.03$, $\xi = 0.02$, and $\xi = 0.01$). Discontinuities observed are consequence of numerical errors in the semi-analytic solution. Dashed lines represent the P-wave velocity and porosity for CS1. The same graphic can be used for the rest of sites.

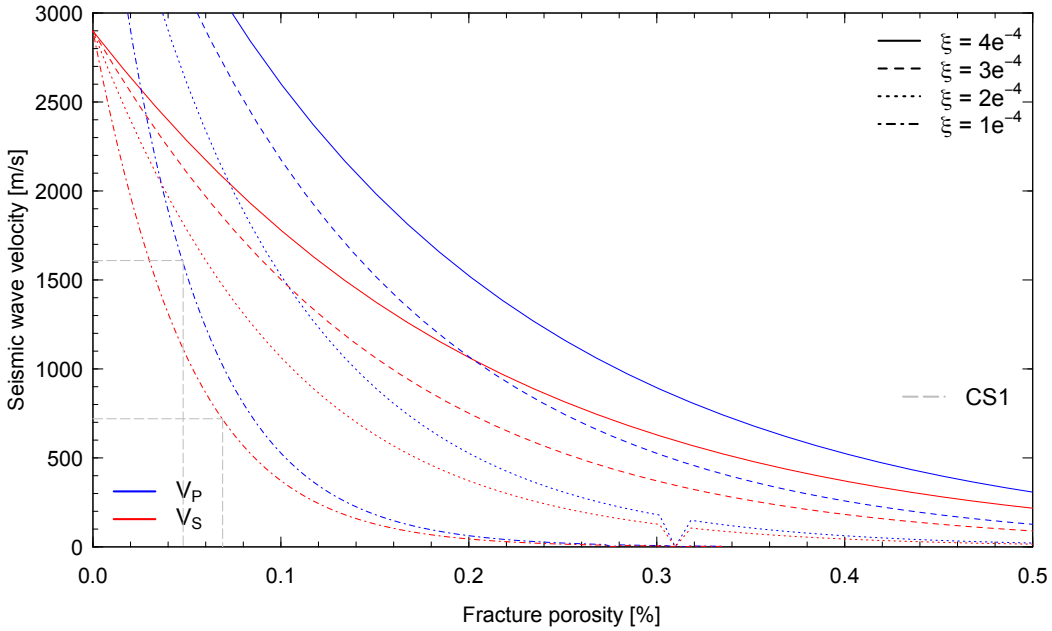

Figure 5.21: Porosity vs P and S-wave velocity of the solid media represented for all sites, which contains spheroidal pores with four values of aspect ratio ($\xi = 0.0004$, $\xi = 0.0003$, $\xi = 0.0002$, and $\xi = 0.0001$). Discontinuities observed are consequence of numerical errors in the semi-analytic solution. Dashed gray lines represent the effective porosity found from the seismic velocities in site CS1. The same graphic can be used for the rest of sites.

5.3.3.2 Estimation of relative permeability

The relation between permeability and porosity is complicated, as it depends of several factors such as: crack density, connectivity and aperture. Two types of permeability models can be found (Gueguen and Palciauskas, 1992), one defining an equivalent porous media and the other which is an approximation that describes a set of tubes or fissures.

In the first case, the permeability is associated to the ratio between the pore volume and surface. A simple approach of this type is the Kozeny-Carman (KC) model, which describes a link between media properties and flow resistances in pores channel. A simple form of the model can be express as (Gueguen and Palciauskas, 1992):

$$k = C_{kc} \times \frac{\eta^3}{(1-\eta^2)} \tag{5.14}$$

where k is the permeability, and C_{kc} is a parameter that expresses the internal pore distribution and geometry. This parameter is extremely challenging to measure. Costa (2006) reported a value of 1×10^{-12} for vesicular basalts.

In the second case, we continue with the effective pore model with a distribution of fractures in which permeability and porosity are described by :

$$k = \frac{4\pi}{15} \times \frac{\omega^3 \times c^2}{L^3} \times f \tag{5.15}$$

$$\eta = 2\pi \times \frac{\omega \times c^2}{L^3} \tag{5.16}$$

where f is the percolation factor (which relates the fracture connectivity) and ω, c and L are the fracture semi-aperture, radius and length, respectively. Combining equations Eq. 5.15 and Eq. 5.16, k can be expresses as a function of ν, ξ and L:

$$k = \frac{1}{30} \times \eta \times \xi \times W^2 \tag{5.17}$$

where W is the fracture aperture.

Eq. 5.14 and Eq. 5.17 are applied to the study sites. However, some data is still missing (e.g. due to the absence of outcrops, fractures have not been analyzed). For this reason, rather than show an absolute estimation of permeability, these equations are used to show the relation of permeability between sites. Therefore, in the case of the KC model, C_{kc} is assumed as constant for all sites, in such way permeability is only affected by porosity. In the fracture model, the value of f is assumed to the unit and W constant in all sites, in such way permeability is related to porosity and the pore aspect ratio.

Table 5.5 shows relative permeabilities estimated by both methods in the four sites respect to the permeability of CS1. Consistency is shown by the two models in the proportion of permeability between sites. Comparing k/k_{CS1}, both

Table 5.5: Estimated relative permeability in sites CS1, CS2, CS3 and WS3 from the Kozeny-Carman and fracture models.

	CS1	CS2	CS3	WS3
Kozeny-Carman				
k/k_{CS1}[a] [-]	1	0.3	9.4	41
Fracture model				
ξ[b] [-]	1.5×10^{-3}	8×10^{-4}	3×10^{-2}	4×10^{-2}
k/k_{CS1}[a] [-]	1	0.2	3.7	10.7

[a] permeability ratio respect to site CS1.
[b] obtained from Fig. 5.20.

methods show a relative similar proportion. However, the proportion from the KC seems to be higher than the fracture model. This is because the second model is directly proportional to the porosity, while the first one follows a more exponential one. Both models show that permeability is comparable in sites CS1 and CS2, whereas it is higher in sites CS3 and WS3. In the fracture model, CS3 could also be compared with the first two sites, which makes sense considering that these sites are located in the same area (site are less than 3 km away). Given that permeability in fractured basalts is affected by the crack aspect ratio, the second model will be used to estimate hydraulic conductivity.

1×10^{-5} to 1×10^{-11} m^2. k is within the range of the values reported by Bear (1972) for highly fractured basalts.

5.3.3.3 Hydraulic conductivity

Hydraulic conductivity is related to permeability by:

$$K = \frac{\rho \times g}{\mu} \times k \tag{5.18}$$

where g is the acceleration due to gravity and μ is the dynamic viscosity of the fluid. In the case of water Eq. 5.18 yields $K = 10^7 \times k$. Table 5.6 shows the range of hydraulic conductivity at each site for a relative large range of fracture apertures. Hydraulic conductivity ranges between ca. 3×10^{-4} and 7×10^{-1} m/s for all sites, which means that depending of the fracture aperture, K in WS3 could reach 2000 times K in CS2. With a similar aperture, the difference in hydraulic conductivity is just ca. 4 times higher, which is the similar to porosity. The range of K found in San Cristobal is in the upper limit reported in the literature for basaltic islands. Depending of the lava flow, hydraulic conductivity usually ranges between 1×10^{-9} and 1×10^{-3} m/s. However, in regional context, this value can be even larger (e.g. Join et al. (2005) reported a value of 1×10^{-2} m/s in young volcano units in La Rèunion). Bear (1972) reported values of

Table 5.6: Estimated hydraulic conductivity (K) and fracture length (L) range in sites CS1, CS2, CS3 and WS3 assuming a fracture aperture (W) range between 0.5 and 10 mm.

	L [m]	K [m/s]
CS1	3.3×10^{-2} - 6.7×10^{-1}	4.9×10^{-4} - 2.0×10^{-1}
CS2	6.3×10^{-2} - 1.3×10^{0}	3.3×10^{-4} - 1.3×10^{-1}
CS3	1.6×10^{-2} - 3.3×10^{0}	1.0×10^{-3} - 4.1×10^{-1}
WS3	1.3×10^{-2} - 2.5×10^{-1}	1.7×10^{-3} - 6.7×10^{-1}

permeability of highly fractured basalt that reaches 1×10^{-6} m^2, which means a hydraulic conductivity of 10 m/s.

It should be noticed that K is estimated from the total porosity and not the fracture porosity. Therefore, the ranges of K might be overestimated. Even though considering the possible high uncertainties in the estimations, results seem to be in a reasonable range.

Conclusions

The AEM SkyTEM survey conducted over San Cristobal Island allowed the 3D visualization of the resistivity model that shows contrasting resistivity units revealing insights about the internal structure of the island. The "smooth" 19-layer resistivity model allows a better description of the geometry of the low resistivity units related to a perched aquifer.

The springs of *Cerro Gato* are originated from a perched aquifer formed above an impermeable unit. A local impermeable layer formed above the impermeable unit that forms the aquifer, redirects the groundwater flow of the perched aquifer towards the surface, and the springs are originated because the local impermeable layer intersects the surface topography and water outcrops from the fractured basaltic rock above it.

The hydrogeological watershed of *Cerro Gato* was defined with two thresholds of resistivity which implies a surface equivalent or larger than its hydrological watershed. The surface of the hydrogeological watershed extends to the east and considering the large surface case, just a small portion extends towards the highlands.

The seismic refraction survey performed in San Cristobal Island reveals insights of the sub-surface structure of several sites of the island. The seismic tomography interpreted from the survey shows three layers with contrasting P-wave velocities that correspond to: i) soil or highly weathered basalt ($400 - 500$ m/s), ii) unsaturated fractured basalt ($1400 - 1700$ m/s) and, iii) saturated fractured basalt ($2400 - 2700$ m/s). The weathered cover in the windward side ranges from 14 m in the highlands to 4 m at mid-elevation.

Hydrodynamic properties ares estimated using an effective elasticity medium model from the wave velocity data. Total porosity ranges between 4 and 12% at the coast sites, whereas it reaches 20% in *Cerro Gato*. Estimated hydraulic conductivity is relatively high comparing with other typical values found in the literature, it ranges between 1×10^{-4} and 1 m/s. However, several assumptions and uncertainties lead to believe that these values are overestimated.

The geometry of the hydrogeological watershed of *Cerro Gato* combined with the surface geometry, some hydrodynamic properties, recharge estimation and the streamflow monitoring, are enough elements to propose and perform a conceptual and numerical hydrogeological model of *Cerro Gato*. Hydrodynamic properties of basalt in the coast sites should be considered in the hydrogeological modeling of *Cerro Gato* rather than the ones found in the site of *Cerro Gato*, which is downstream of the springs and might not represent the media in which the aquifer is formed upstream.

Chapter 6

Hydrogeological modeling

6.1 Introduction

The hydrogeology of basaltic islands is still narrowly known because of the complexity of the configuration of their internal structure and mostly because of the challenging task to obtain enough data to properly characterize its dynamics. Indeed, proposed hydrogeological models are usually poorly constrained for the lack of data and therefore contrasting models have been proposed, such as the case of Piton de la Fournaise (Coudray et al., 1990; Violette et al., 1997). Groundwater simulation of these models is generally restricted to saturated flow without considering the unsaturated media. The advantage of models that include unsaturated flow is that they asses infiltration processes along the unsaturated media. Infiltration rates and its pathway can markedly affect the hydrodynamic response of an aquifer, specially if the overlying unit has a contrasting permeability and a heterogeneous spatial distribution. The unsaturated flow is dependable of the relation between the saturation of the media and its capillary pressure. Thus, the parameters that control this relation also drive the infiltration rates. The Galapagos Archipelago is the perfect scenario to performed a groundwater simulation with saturated and unsaturated flow given that one of its islands, San Cristobal, possess elements to constraint an hydrogeological model at a relative small scale.

San Cristobal Island is located at the eastern end of the Galapagos Archipelago 1000 km west from the Ecuadorian coast. The island was built from alkaline basalt deposits where eruptions were relatively continuous forming permeable layers (fractured basaltic flows) that in some locations they are interbedded with impermeable units (red "baked" soils). The age of the island is ca. 2.35 Ma (Geist et al., 1986). It can be divided into two regions: the southwestern shield culminating at 725 m a.s.l. and a northeastern younger flat region. The southern windward side is characterized by the presence of streams fed by permanent or

perennial springs. A thick soil layer has been formed in the highlands of the windward side and highlands due to weathering of pyroclastic deposits exposed to wet conditions (Pryet et al., 2012b; Violette et al., 2014). The weathered cover forms a morphology which is dissected by a drainage network created by the erosive process of runoff (Violette et al., 2014). Field observations on outcrops reveal that the eastern sector of the windward side is more weathered whereas in the western sector lava flows still show their primary structure (Tatiana Izquierdo et al., 2015). However, the eastern side is more dissected with deep incisions of several tens of meters deep. An airborne transient electromagnetics (SkyTEM) survey was performed over San Cristobal in May 2006 revealing features of the 3D internal structure of the island (d'Ozouville et al., 2008a; Auken et al., 2009; Pryet et al., 2011). Combining the information from the remote sensing and field observations, Pryet et al. (2012b) proposed the first hydrogeological model of the island, which can be related to the Hawaiian model for volcanic islands. The model considers a regional basal aquifer subject to seawater intrusion, several perched aquifers that fed springs in the windward side and a dyke-impounded aquifer in the summit zone that follows the alignment of eruptive cones to form a groundwater channel.

Hydrological data on this area is scarce. Only some punctual measurements of the water discharge on some streams are available. These measurements performed by (Adelinet, 2005) in 2005 reveal that water recharge is less than a few liters per second in most streams. One exception is the stream of *Cerro Gato* watershed located in the central sector of the windward side, with water recharge ranging from 15-25 l/s. This stream is of particular interest because the relative large discharge suggests that the outflow is larger than the input flow from its drainage surface. Besides this hydrological feature, this stream has a municipal water catchment system located at mid-elevation which is used for the 50% of the total water supply to the population of Puerto Baquerizo Moreno. Besides the importance of this watershed in terms of water management, little is known about the stream occurrence.

In the frame of the *GIIWS* project, an hydrological network was set up in *Cerro Gato* and surrounding watersheds to quantify the terms of the water balance. Three weather stations at different altitudes were installed along the windward side to quantify the orographic gradients of rainfall and evapotranspiration. During a representative hydrological year such as the 2013-2014, rainfall at the coast reaches ca. 190 mm and have a gradient of ca. 270 mm/ 100 m of elevation. While the referential evapotranspiration gradient is ca. -50 mm/100 m of altitude, starting with ca. 840 mm at the coast. At the highlands, the semi-permanent presence of fog during six months of the year can have a non-negligible

contribution to the water input. Therefore, fog interception was assessed with a fog net gauge and throughfall measurements. Results show that fog interception reaches 28% of the annual water input during the hydrological year 2013-2014. Weather stations were complemented with soil water suction monitoring to estimate actual evapotranspiration and deep percolation using a joint canopy soil water transfer model. Deep percolation rates along the windward side are heterogeneous in space and time. They are affected by the altitude, land cover and season. At watershed level, *Cerro Gato* has a mean groundwater recharge of ca. 830 mm for the year 2013-2014. Besides climatic and soil measurements, water discharge from several streams was also estimated using measurements from water level sensors. Mean streamflow in *Cerro Gato* during the year 2013-2014 is ca. 25 l/s, ranging from 20 to 65 l/s. 94% of the streamflow corresponds to baseflow. The availability data of water input and output allowed the possibility to perform a lumped rainfall-runoff model (GR4J). The model showed a good performance during the two hydrological years tested. A modified version of GR4J model was used to found an equivalent surface to manage the water budget imbalance in *Cerro Gato*. It was found that the surface necessary to balance the water budget in this watershed is ca. 1.4 times the hydrological surface. This means that the hydrological watershed has a groundwater contribution from surrounding watersheds and thus an hydrogeological approach is necessary.

The AEM SkyTEM survey allowed the visualization of a 3D resistivity model that shows contrasting resistivity units related to different geological units. Low resistivity units are attributed to saturated weathered or unweathered basalt that can be identified near the surface and buried several ten of meters deep as a perched aquifer. A better description of the geometry of low resistivity units attributed to perched aquifers was possible with the 19-layer resistivity model (contrary to the 4-layer resistivity model proposed by Pryet et al. (2012b) that was more suitable in a regional scale). Using a simple algorithm based on a threshold of resistivity, the 19-layer model was used to extract two different geometries for the perched aquifer that fed *Cerro Gato* springs. These springs have been identified as contact springs, in which water outcrops through fractured unweatheared basalt located above a brown clayed substratum. The different geometries correspond to two cases of resistivity thresholds, in this way uncertainties in the definition of the perched aquifer are accounted. Basically, the geometry of the two aquifers differ in the length of the main axis, while the thickness and width remain similar. The two hydrogeological watersheds defined for *Cerro Gato* correspond from 100 to 180% of the extension of the hydrological surface and includes two springs at the southern-eastern limits located ten of meters above *Cerro Gato* spring.

The regional geological, geomorphological and geophysical datasets are combined with detailed information of the hydrology and meteorology and field observations of *Cerro Gato* watershed to define a conceptual hydrogeological model of this watershed. Springs are originated from a local perched aquifer in fractured basalt which is formed above an low permeability unit of an unknown thickness that limits vertical flow. This unit intersects the surface topography, thus water outcrops from the fractured basalt above it. A relative thick highly-weathered basalt layer covers the surface which could influence infiltration towards the aquifer. The geometry defined for the hydrogeological watershed results in two possible cases: A) the extension of the perched aquifer is large enough so the direct accumulated recharge within its limits can satisfy the discharge observed in the stream of *Cerro Gato* and the other two springs; and B) the extension of the perched aquifer is not enough to satisfy the observed discharge, however, the superficial weathered cover allows the possibility that sub-superficial groundwater flow, produced from the surface outside the limits of the aquifer, can recharge the aquifer so the discharge is satisfied.

The objective of this chapter is to test the two conceptual models with a 2D numerical model that simulates unsaturated and saturated flows and considers the width variation of the hydrogeological watershed in steady state conditions. The modeling approach involves determining parameters controlling unsaturated and saturated flow in the fractured basalt. Water input in the model considers the recharge gradient. The plausibility of the model is assessed in a quantitative way with the water discharge measurements of the *Cerro Gato* stream and in a qualitative way with an analysis of its hydrodynamic behavior and comparison with a cross section of the resistivity model. Groundwater age is also estimated. This chapter is organized as follows. First, the different considerations of the numerical model are detailed in section *Methods*. Then, section *Results* shows the outputs of the model. Finally, in section *Discussion* the relevance of the method and results are discussed.

6.2 Methods

6.2.1 Numerical code and flow governing equations

6.2.1.1 METIS

The *METIS* numerical model (modelisation of flow, mass transport and energy in saturated and unsaturated media) developed by Goblet (1981) is used in this study. It is based on the numerical solution in two-dimensional or three-dimensional space of the diffusivity equation in steady or transitory state. The

equation solved for saturated and unsaturated groundwater flow is the fluid mass balance, which is the pressure-based form of the *Richards'* equation:

$$\nabla \cdot (K \times K_r \times h) = (S_s \times S + \eta \times C(h)) \times \frac{\partial h}{\partial t} \tag{6.1}$$

where K [LT^{-1}] is the hydraulic conductivity, K_r [-] is the relative permeability (see Eq. A.2), h [L] is the pressure head, S_s [L^{-1}] is the specific storage coefficient, S [-] is saturation, η [-] is the total porosity, $C(h)$ [L^{-1}] is the specific retention capacity and t [T] is time. The saturation can be related to the water content by:

$$S = \frac{\theta}{\eta} \tag{6.2}$$

where θ is the water content. The relation between fluid saturation, capillary pressure and hydraulic conductivity in the unsaturated media is given by the analytic model proposed by Van Genuchten (1980) in Eq. 2.8 and described in section A 3.

The diffusivity equation can also be expressed for the advection-dispersion mass transport as follows:

$$\nabla \cdot ((\overline{\lambda} \times U + \eta \times d) \times \nabla C - C \times U) = \eta \times \frac{\partial C}{\partial t} + q_m \tag{6.3}$$

where $\overline{\lambda}$ [L] is the dispersivity tensor composed of the longitudinal (λ_L) and transversal (λ_T) dispersivity, U [LT^{-1}] is the specific discharge (darcy velocity), C is the mass concentration [-] and q_m [T^{-1}] is a source term corresponding to the added or withdrawn mass of tracer per unit time.

Eq. 6.1 and Eq. 6.3 are solved by METIS with the Galerkin finite-element method with bi-linear, tri-linear, quadrilateral and hexahedral elements. The discretization of this equation is based on a fully implicit finite-difference scheme for time derivatives and standard finite-element approximations for spatial derivatives. The equation is solved sequentially for each iteration of a time step using the Picard algorithm as a first estimation and then using the Newton-Raphson algorithm which is faster and more robust but requires the initial estimation close to the solution provided by the Picard method. Readers are invited to see section A 3, in which the numerical solution of the soil water transfer 1D model developed for section 2.4 is described. It is not the exact same procedure that METIS follows, however the principles of the resolution are similar.

6.2.1.2 Groundwater age estimation

Groundwater age is estimated by METIS following the methodology proposed by Goode (1996), in which groundwater age is estimated from the advection-dispersion transport equation, using as concentration mean age (A), which corresponds to the weighted average time derived from residence-time distribution

concepts in steady flow and mass-conservation principles applied to the conceptual mass age. The equation is written as follows:

$$\frac{\partial A}{\partial t} = 1 + \nabla \cdot ((\overline{\lambda} \times A + \eta \times d) \times \nabla A - A \times \frac{U}{\eta}) + \frac{F}{\rho_w} \tag{6.4}$$

where ρ_w [ML^{-3}]correspond to the water density and F is the age mass source term [$MTL^{-3} \times T^{-1}$]. Age mass is the product of the water mass and its age, in which age mass is assumed conservative during mixing. With this method, groundwater age can be simulated incorporating the physical effect of diffusion and dispersion, without the necessity of a solute specific modeling.

6.2.2 Configuration of the model

Cerro Gato springs are located between 230 and 240 m of elevation, approximately at the middle of *Cerro Gato* big watershed and ca. 200 m upstream of the outlet of *Cerro Gato* watershed. Catchment surface to the springs is 0.65 km^2, which is 95% of the surface of *Cerro Gato* watershed. Treatment of the 19-layer resistivity model of the internal structure of the island, suggests that the perched aquifer formation extends towards the Est of *Cerro Gato* watershed. The hydrogeological watershed of the springs includes the two small watershed at right side of *Cerro Gato* and also includes its two springs. Two cases of geometry were defined for the sustaining layer of hydrogeological watershed: A) one with a surface of 1.2 km^2, in which a portion extends towards the highlands and B) which is a portion of geometry of case A (0.65 km^2). In both cases, the non-saturated region is extensive because the perched formation is several ten of meters depth. In case A, the sustaining layer reaches 400 m of elevation which corresponds to an elevation of 575 m in the surface. Whereas, case B reaches an elevation of 280 m, which corresponds to 400 m of elevation. Water balance performed in *Cerro Gato* watershed suggests that its discharge is larger than its recharge, and therefore the catchment surface should be larger than the limits of the basin (at least 1.4 times larger). In case A, the surface of the sustaining layer seems to be large enough to satisfy the discharge. However, in the second geometry it is not the case considering the orographic gradient of recharge. Geophysical surveys allow to distinguish a relative thick weathered cover (5-15 m) in the sub-surface which might play an important role in the recharge of the perched aquifer, especially for case B.

The relative complex system which involves the formation of *Cerro Gato* springs is idealized in a 2D vertical cross section along its hydrogeological watershed (Fig. 6.1). The flow circulation model is build based on:

- The identification of the different geological units and properties from geophysical methods and field observations.
- Hydroclimatic observations and water balance performed to define the boundary conditions of the system.

The conceptual model defines two groundwater circulations, i) infiltration through the unsaturated zone along the entire profile and ii) horizontal saturated flow above the sustaining low permeability layer towards the spring. A third type of circulation could also occur, which is horizontal sub-superficial flow in the weathered cover. This is important in case B, because it could recharge the perched aquifer from flow inputs off the limits of its catchment.

The hydrogeological model of *Cerro Gato* was implemented with the *Python* scripting language developing a class module to design, run and post-process *METIS* models. The module also import mesh created in the program *gmsh*.

6.2.2.1 Geometry

The geometry of the model was based in a 2D cross section of the 19-layer resistivity model along *Cerro Gato* hydrogeological watershed. The mesh was designed with *gmsh* and exported to *METIS* with the *Python* class module. It was created in a way to consider the geometry of the low permeable layer (aquitard) that forms the perched aquifer, which has a spoon-like scoop form with a gentler slope than the topographic surface. The structure was designed so the impermeable layer reaches the right boundary 5 m below the surface, which is the location of the springs of *Cerro Gato*. In this way, the depression where the springs are located is represented. The mesh is created with quadrilateral elements from the fixed-structure that accounts the perched aquifer form.

The mesh accounts the two geometries of the sustaining low permeability layer, and it is proposed to represent three different medias: fractured basalt rock, the impermeable layer with a variable thickness and a weathered cover in the surface with a variable thickness. The boundaries of the mesh form a parallelogram with a fixed height of 300 m. The length in the x-axis depends of each case. In case A, the length is 2040 m, which account for the length of the perched aquifer (2000 m) and 40 m extra. In case B, the length is 2140 m, which is the length of the surface catchment of the three springs. The length of the low permeability substratum in the x-axis reaches 1100 m.

Nodes in the x-axis are regularly spaced each 2.5, 5, 10 and 20 m. In the z-axis, nodes are spaced irregularly between 0.3 and 20 m. A total number of ca. 9000 nodes and elements were used in the different mesh designed, in which number varies depending of the thickness and length of the sustaining

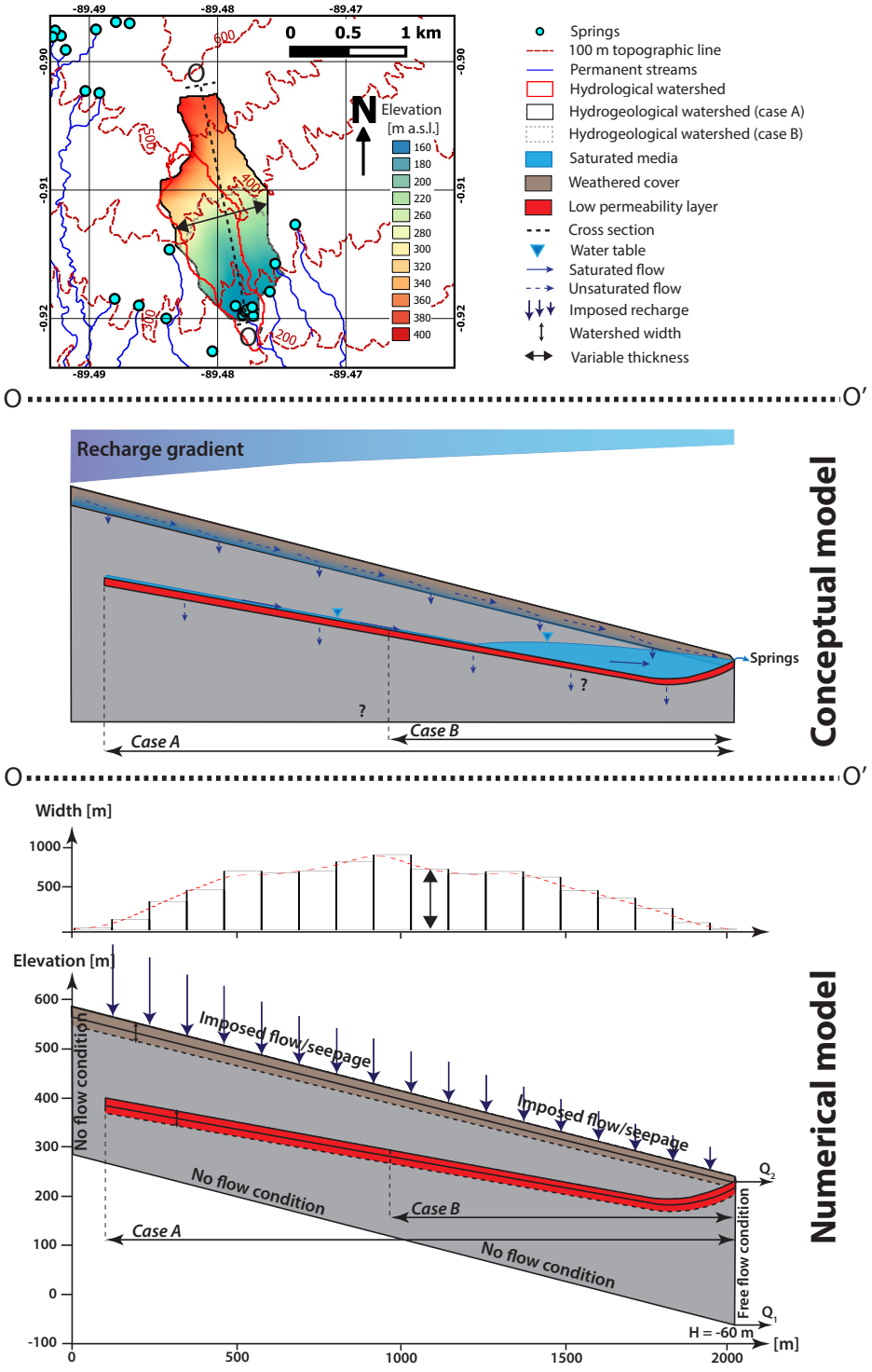

Figure 6.1: Hydrogeological conceptual model and numerical configuration of *Cerro Gato* watershed in the windward side of San Cristobal island. The map shows the hydrological watershed and the extended and reduced surface of the hydrogeological watershed. A conceptual model is proposed in which springs are fed by a perched aquifer formed above a low permeability layer. The 2D numerical configuration of the conceptual model considers an orographic gradient of recharge as well as the variable width of the watershed. Conditions of the bottom boundary do not represent the actual groudwater system, but they are used to simplify the perched aquifer system of the top section.

layer. To account the variable width of the hydrogeological watershed in the 2D representation, each node is attributed with a width that correspond to the y-axis dimension of the watershed at their corresponding z coordinate. In this way the flow will still be parallel, which is strong assumption, but the advantage is that flow is either accelerated in the narrow sections or slowed in the wide ones because the width is used as a scale factor in the fluid mass balance equation at each node.

6.2.2.2 Model parameters

Three primary units are simulated: fractured basalt (FB), the low permeability layer (LPL) and the weathered cover (WC). Each unit has a particular set of parameters which values are either taken from measurements and the literature or calibrated with the model. Parameters includes: porosity (η), hydraulic conductivity (K), residual water content (θ_r), saturated water content (θ_s) and van-Genuchten parameters α and n for non-saturated flow. Saturated water content is assumed equal to the porosity ($\eta = \theta_s$). Additionally, LPL and WC have a variable thickness (TN). Given the quantity of parameters (17), it was necessary to fix various of them. All parameters are calibrated for FB, which is the unit with more calibrated variables because of the uncertainty of their values, especially the non-saturated ones, in which practically there is not references. The only reference found for this type of non-saturated approach in fractured basalt is Unger et al. (2004), which simulated transient water infiltration in a fractured basalt with a perched aquifer condition from an existent dense clay interbeds. For the LPL unit only θ_s and θ_r are fixed parameters, the rest are calibrated. In the case of the WC unit, only its thickness and hydraulic conductivity are calibrated. The rest of parameters were fixed using average values obtained from the soil water transfer simulations (section 3.3.1). Table 6.1 shows how parameters are obtained in the model. It should be noticed that non-saturated parameters (θ_s, θ_r, α and n) are taken from the lower range of values reported in section 3.3.1. This is because volcanic soils, as discussed in section 2.4 and section 3.3.1, have large water holding properties, which implies higher values of α and n and a low storage capacity (θ_s - θ_r). The combination of these parameters implies excessive numerical difficulties and requires more refinement in the mesh. Given that our focus is the perched aquifer, efforts to implement such characteristics in the WC seems to be unnecessary.

6.2.2.3 Boundary and initial conditions

Four types of boundary conditions are used in this model:

Table 6.1: Parameters of each geological unit of the hydrogeological model. Parameters used in the model are taken from the literature (L), measured or estimated (M) or calibrated in the model (L).

	Fractured basalt (FB)	Low permeability layer (LPL)	Weathered cover (WC)
Hydraulic conductivity (K) [m/s]	C	C	C
Saturated water content (θ_s) [-]	C	L	M
Residual water content (θ_r) [-]	C	L	M
Inverse air entry pressure* (α) [1/m]	C	C	M
Pore size distribution* (n) [-]	C	C	M
Unit thickness (TN) [m]	-	C	C

* van Genuchten parameters for non saturated flow (Van Genuchten, 1980).

- No flow condition in the nodes of the left and bottom boundaries.
- Prescribe total head in the node at the bottom right corner which is equal to the elevation at this point (-60 m).
- Free drainage condition in the nodes of the right boundary, in which water could flow without constraint and where the discharge of the aquifer (Q_1) is be calculated.
- Seepage surface condition in the top boundary nodes, which consist of a prescribed flux condition, but in case that the elements below the surface are completely saturated, the model changes the condition to an hydraulic head equivalent to its elevation, so it accounts the atmospheric pressure.

The latter condition is used in the model in order to estimate if all the prescribed recharge is infiltrated, or if a part of it is lost due to saturation conditions. The no flow condition in the bottom and the prescribed head at the bottom right corner, rather than describe real flow conditions in this limit, which at this elevation ($<$ 0 m) the basal aquifer should be accounted, are intended to estimate the flow (Q_2) which is infiltrated through the sustaining layer of the aquifer or which infiltrates directly in the zones off the sustaining layer. In such way, we can have an idea of the proportion of recharge that reaches the springs and the one lost by infiltration.

Recharge is distributed along the profile following its gradient, which is estimated with the same methodology reported in section 3.4. A mean value is used at each node, which represents mean recharge of the width of the hydrogeological watershed at a certain elevation. Initial conditions of saturation are necessary in

all nodes of the mesh, these values have not importance in the model given that they are only used as a starting point for the solution of the model in steady-state conditions. However, this value was fixed to 50% in all nodes.

6.2.3 Modeling strategy

Steady-state regime is used to validate the two conceptual models. Considering that the first hydrological year (2013-2014) is an average year in terms of rainfall, we assume that the recharge rate in this year can be equivalent to the one of previous years, so considering that flow in *Cerro Gato* has not change significantly since 2005 and recharge conditions can be somehow comparable with previous years, it is consistent to simulate a steady flow condition. Indeed, the last El Niño event, which could considerably increase the recharge rate and affect the system conditions, was reported in the hydrological year 1997-1998. Only data from the first year is used to validate the models. In case A, recharge is applied in all nodes within the region of the sustaining low permeability layer (the length of the mesh except for three nodes in the top left corner). In case B, recharge is applied in all nodes of the top boundary. Mean recharge in both models is ca. 2.8×10^{-8} m^3/s per square meter. Using the value of recharge in each node, and multiplying it by its width and by the length of the respective node cross-section, then we obtain the volume of input water at each node. The sum of it is the total volume of water input in the model, dividing it by a year, then we have the total input flow to the model. In case A, it reaches 34 l/s, while in case B it reaches 40 l/s. However, in case B, 19 l/s do not reach the perched aquifer in conditions of only vertical infiltration. Average discharge in *Cerro Gato* stream is 25.1 l/s during the hydrological year 2013-2014. However, this considers the small surface (0.05 km^2) between the springs and the control section. Considering that discharge of the springs is proportional to discharge in the control section by the recharge distribution in the watershed, then discharge in the springs is 24.6 l/s, which is ca. 97%. Measurements in the two other springs that are within the limits of the hydrogeological watersheds have not been performed during this study. However, measurements in 2005 made by (Adelinet, 2005) show that discharge in these streams formed by this springs is very small compared with the one of *Cerro Gato*. Discharge in each stream represents ca. 13% and 3% of the one in *Cerro Gato*. Using these ratios, then the total discharge of the entire aquifer reaches 28.6 l/s. This discharge will be simulated with the respective recharge rate in case A and B. Despite assumption about recharge and discharge might seem rough, they might remain fair considering uncertainties in other parameters.

Parameters of FB and LPL are calibrated with model A, in which the influence of WC is not assessed. Once, that simulation of discharge is satisfied with

Table 6.2: Set of parameters used at each geological unit of the hydrogeological model. Ranges of values are shown in parenthesis. Values from a specific source are mention below, all other parameters are obtained from literature review.

	Fractured basalt (FB)	Low permeability layer (LPL)	Weathered cover (WC)
Hydraulic conductivity (K) [m/s]	(1×10^{-4} - 5×10^{-2})	(1×10^{-9} - 1×10^{-6})	(1×10^{-7} - 1×10^{-4})[a]
Saturated water content (θ_s) [-]	(0.05 - 0.2)[b]	0.53[d]	0.7[a]
Residual water content (θ_r) [-]	(0.03 - 0.18)	0.2[c]	0.35[a]
Inverse air entry pressure (α) [1/m]	(0.1 - 5)	(0.1 - 5)	0.3[a]
Pore size distribution (n) [-]	(1.3 - 2.3)	(1.3 - 2.3)	1.9[c]
Unit thickness (TN) [m]	-	1, 2, 5[e]	5, 10, 15[d]

[a] Obtained from the soil water transfer model in section 3.3.1.
[b] Obtained from seismic wave survey described in section 5.3.
[c] reported by Unger et al. (2004).
[d] Within the range observed in the tomography reported in section 5.2.

a set of parameters in model A, the set is used in model B, where WC parameters can be calibrated. Given that thickness of LPL and WC are complicated to change, just three thicknesses were used in the model: 1, 2 and 5 m for LPL and 5, 7.5 and 10 m for WC. Table 6.2 shows parameters used for simulations.

Groundwater age is estimated in the two models assuming λ_L and λ_T equal to 10 and 1 m, respectively. Water mass age concentration is an input in the top boundary with a value equal to 0, which means that water is entering the system with a mean age of zero.

6.3 Results

6.3.1 Flow calibration

6.3.1.1 Case model A

Simulations of the model were performed with the METIS code in steady-state conditions. First, we used model A for calibration of FB and LPL parameters, using fixed parameters in WC ($K = 1 \times 10^{-4}$ m/s and $TN = 5$ m). We run a first set of simulations (200) to check which parameters are influential. In this first try, it was noticed that saturated and residual water content of basalt do not

have influence in the flow simulations. The only influence they showed was in the calculation time, which was significantly higher when $\theta_s - theta_r$ was high, which is understandable because the model needs more time to fill the aquifer reservoir. In such case, this lead to think that these parameters would have more influence in transient-state. Thus, they were fixed for FB ($\theta_s = 0.1$ and $\theta_r = 0.09$).

Another set of 15000 simulations were performed varying the values of K, α and n of both units, FB ans LPL. Results show that in 1055 of them, it is possible to perched water. In 544 simulations discharge of the aquifer (Q_1) reaches a rate more than 28 l/s and in 458 of them the discharge is between 28 and 30 l/s, which is in the observed range of the springs. Figure 6.2 and figure 6.3 show the sensitivity of the aquifer discharge to the six calibrated parameters. The only parameter which seems to affect discharge is the hydraulic conductivity of the sustaining impermeable layer. Indeed, this value should be the one that controls discharge of the aquifer, as it controls the formation of perched water. When both van Genuchten parameters (α and n) had high values, METIS could not find a solution. This happened for either FB or LPL (especially the later). As mentioned before, large water holding properties which are related to high values of van Genucthen parameters, imply numerical difficulties due to its steep gradient in the saturation-pressure and saturation-specific permeability curve at near saturated conditions, which are expected during the formation of the perched water. Q_1 does not seems to have higher values with a thicker LPL (5 m). Indeed, using 1 m of thickness, Q_1 presents values as high as using 5 m. To see the effect of thickness and hydraulic conductivity, one of the successful simulations was used to test the sensitivity of discharge with respect of the thickness of LPL and the hydraulic conductivity of both geological units. Figure 6.4 shows the variation of discharge with different sets of hydraulic conductivity of FB and LPL with the three different thicknesses of LPL. In all cases, in order to have at least 28 l/s of discharge, the hydraulic conductivity of LPL must be lower than 1×10^{-8} m/s. The hydraulic conductivity of FB also has an effect on discharge, with low values, discharge is small in all cases. Apparently it is necessary to have a stronger contrasting effect between the hydraulic conductivity of both units, so enough perched water can be formed. Indeed, in the region with relative average and high values of K_{FB}, discharge is higher. However, in the case of 1 m of thickness for the LPL, the highest values of K_{FB} seems to reduce discharge. Comparing the LPL thickness, it can observed that, the thickest LPL produces a higher discharge with higher values of hydraulic conductivity, which is logical because infiltration in a thicker layer should take longer time, so it compensates the relative higher permeability.

Only a group of simulations (458) have a discharge within the range observed

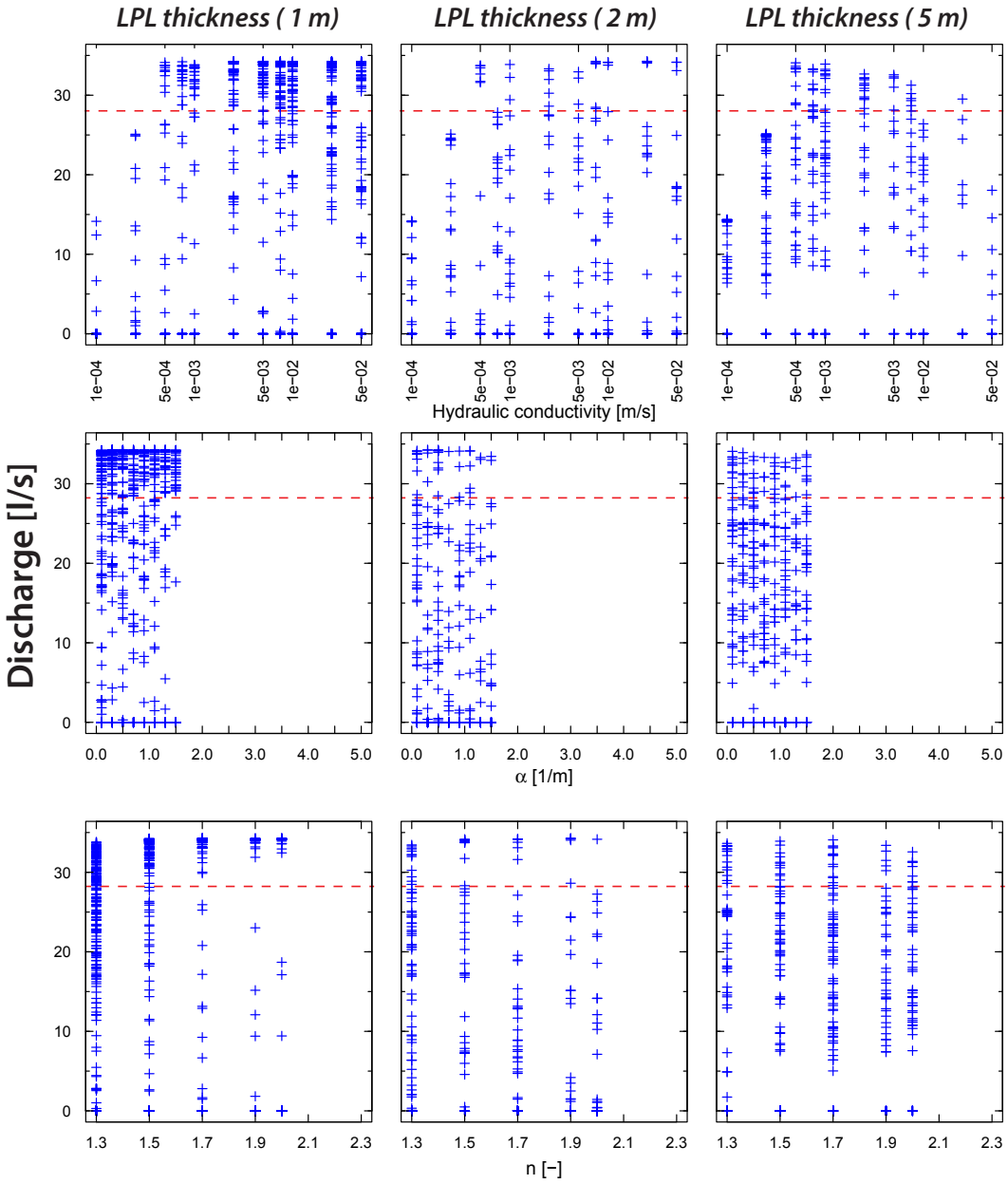

Figure 6.2: Spring discharge sensitibity respect to the fractured basalt parameters using 1, 2 and 5 m of thickness in the low permeability layer (LPL). 5000 simulations were performed for each LPL thickness varying values of K, α and n of both units, FB and LPL. Dashed red lines represents the observed discharge of the perched aquifer (28.6).

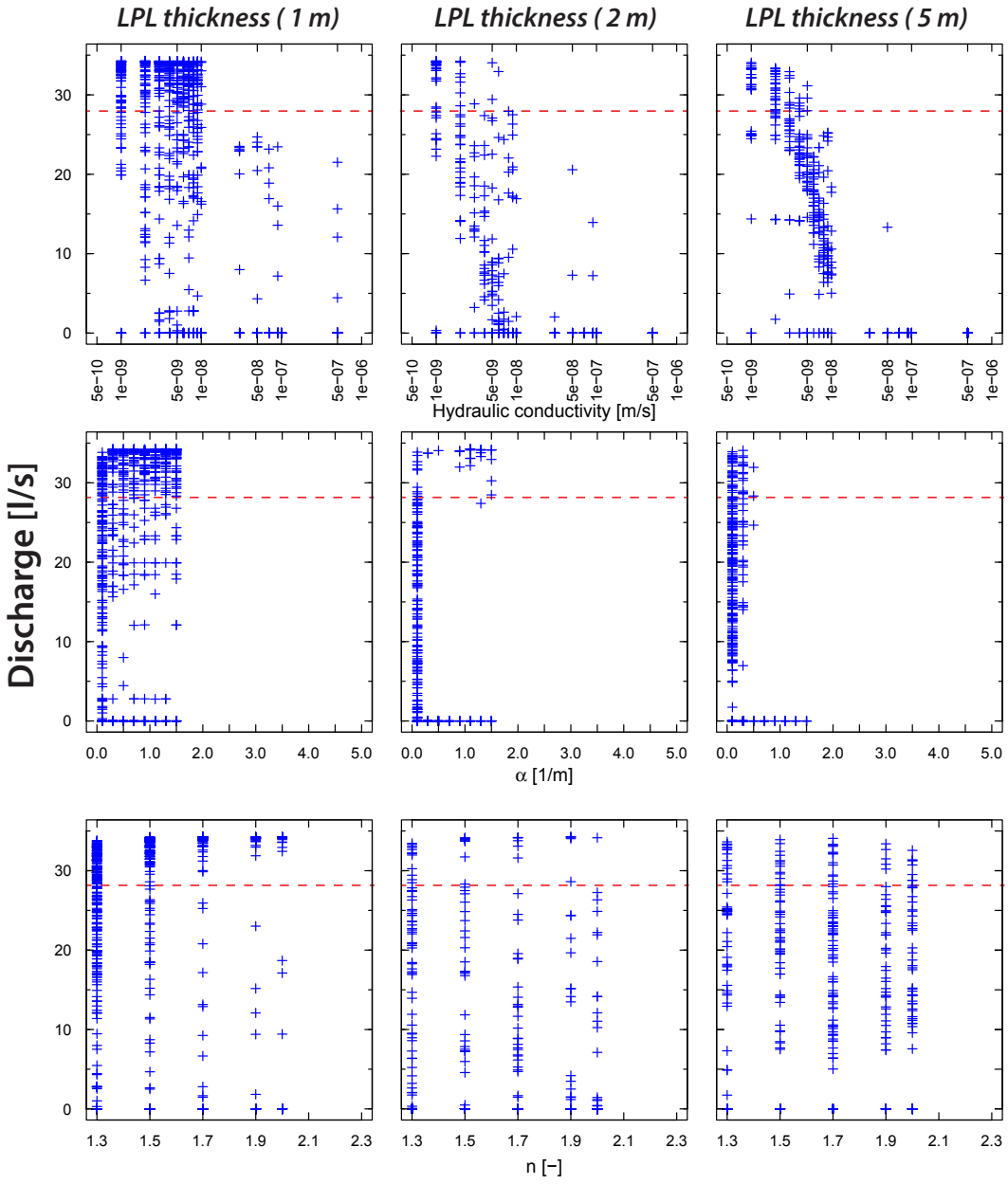

Figure 6.3: Spring discharge sensitibity respect to the low permeability layer (LPL) parameters. 5000 simulations were performed for each LPL thickness varying values of K, α and n of both units, FB and LPL.

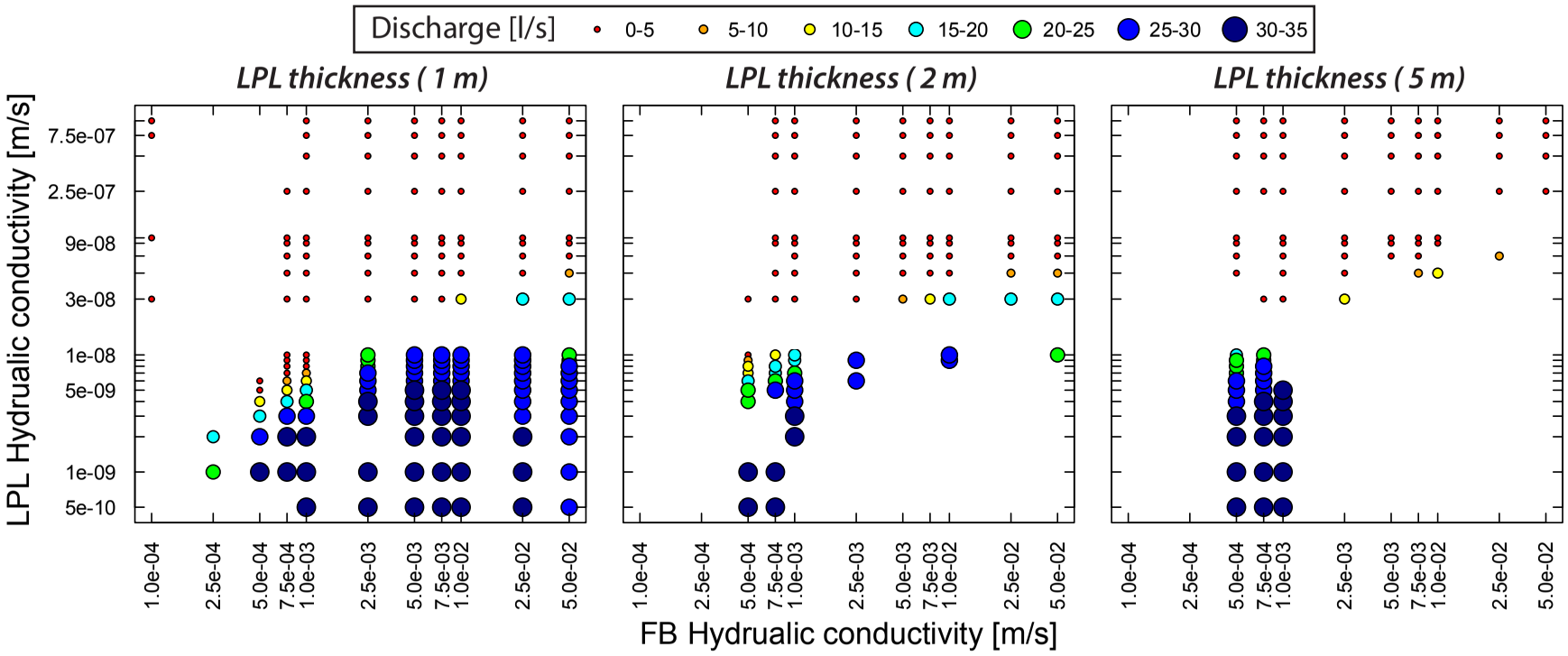

Figure 6.4: Spring discharge sensitibity respect to the hydraulic conductivity of the the fractured basalt (FB) and the low permeability layer (LPL) with three different thickness.

in the springs. A too low hydraulic permeability in LPL produces discharge higher than the observed one whereas too high K_{LPL} could not perched enough water to reach the observed discharge. It implies that, the surface of the hydrogeological watershed of case A is not restricted to the one defined, but it could have a range of values in which the observed discharge could be simulated. However, it should not be too large because even though an increased K_{LPL} could reduce recharge enough to the value observed, there is a limit in which perched water could be formed (clearly seen in Fig. 6.4). On the contrary, the effect of a significant reduction of the surface of LPL, which a priori could not satisfy the observed discharge, is assessed in case B.

6.3.1.2 Case model B

In this case, we use one set of parameters of the simulations of model A, which produces the higher discharges, and we only modified the parameters of the weathered cover. Because there is water inputs along the whole profile, we test if a weathered cover with low permeability and enough thickness could redirect part of the infiltration outside the limits of the LPL towards the aquifer. 100 simulations with a different values of hydraulic conductivity are performed for this objective using a thin WC of 5 m, and two thicker WC (7.5 and 10 m) composed of two layers, the first of 5 meters with a K_{L1} lower than 1×10^{-4} and the second with a K_{L2} lower than K_{L1}. When two layers are simulated, the first layer remains fixed with a thickness of 5 m, while the second layer thickness is either 2.5 or 5 m. A set of different hydraulic conductivity values of both layers is tested. In the case of the single 5 m layer, the maximum discharge simulated reaches 10 l/s. This value is not only lower than the observed discharge but significantly lower than the a priori recharge (21 l/s) expected within the limits of LPL. The simulations with two layers increases discharge of the aquifer. In the case of a thickness of 7.5 m, it is necessary to prescribe K_{L2} lower than 1×10^{-6} m/s and a very contrasting difference of permeability with the upper layer to reach a discharge higher than 20 l/s. With the thicker WC, K_{L2} can have values as high as 5×10^{-6} m/s and not such a contrasting difference of permeability between both layers. In five simulations, discharge reaches more than 28 l/s, which probes the plausibility of model B. In fact, some simulations show discharge values more than 33 l/s, which means that a thinner and less permeable LPL could be used, even similar that the one of model A. In such case, the second layer is preventing infiltration in the upper part and redirecting the flow towards the aquifer. Indeed, ca. 8 l/s are necessary from the zone outside of the limits of LPL to satisfy the observed discharge at the springs.

6.3.2 Hydrodynamic behavior

6.3.2.1 Case model A

In model A, three simulations (S125, S506 and S515) which satisfied discharge and with contrasting parameters were used to analyze their hydrodynamic behavior. Figure 6.5, figure 6.6 and figure Fig. 6.7 show the parameters, total head, pressure head and darcy velocity of each simulation. Even though the three simulations have relatively similar values of discharge of the aquifer, their behavior is contrasting. Model S515 presents a distribution of total head practically uninterrupted following the elevation head, which means that LPL is not influential in total head. In the models S125 and S506, the presence of LPL seems to modify significantly the total head distribution, which basically presents two separate sections (above and below LPL), where total head decreases gradually towards the right boundary. In S125 this effect is more important, and the lower value of total head (-60 m) is practically constant in the lower section. S506 have a more progressive decrease of total head, in which, near the bottom right corner it follows the elevation head. Such a contrasting difference is caused by the suction presented below LPL as seen in the pressure head distribution. Indeed, S515 has not such a large suction below LPL (ca -15 m) whereas in the cases of S506 and S125 it reaches -190 and -320 m, respectively. Suction below LPL is caused by the absence of water in the bottom part of LPL. Water that should infiltrate into this zone is cached by the upper LPL and redirected towards its lower part, in which due to the high hydraulic head in this point, a part of it can finally infiltrate (as seen in S506) or not (such as the case of S125). A more contrasting difference of permeability between BC and LPL reduces the chances of infiltration. However, difference of K_{FB}/K_{LPL} between the three simulations is low (3.3×10^5, 5×10^5 and 2×10^5 for S125, S506 and S515, respectively), barely two times in the worse case. The bottom section of LPL is then very dry. As it is in contact with BC, which is more saturated, water is suctioned by LPL. At dry conditions, depending of the saturation-pressure relationship and the water storage capacity, pressure head could reach extremely low values. van Genuchten parameters α and n are the ones controlling this relation. Models S125 and S506 have a low value of α (0.1 m^{-1}), whereas α is 2 m^{-1} in model S515. Therefore, non saturated parameters of FB combined with non water inputs below LPL produces such a contrasting distribution of total head.

The path and magnitude of Darcy flow show a relative similar behavior of flow in the three simulations. Water infiltrates vertically through WC and FB until it reaches LPL, in which the flow is redirected horizontally above LPL. Flow follows the surface of LPL increasing its magnitude while moving to the

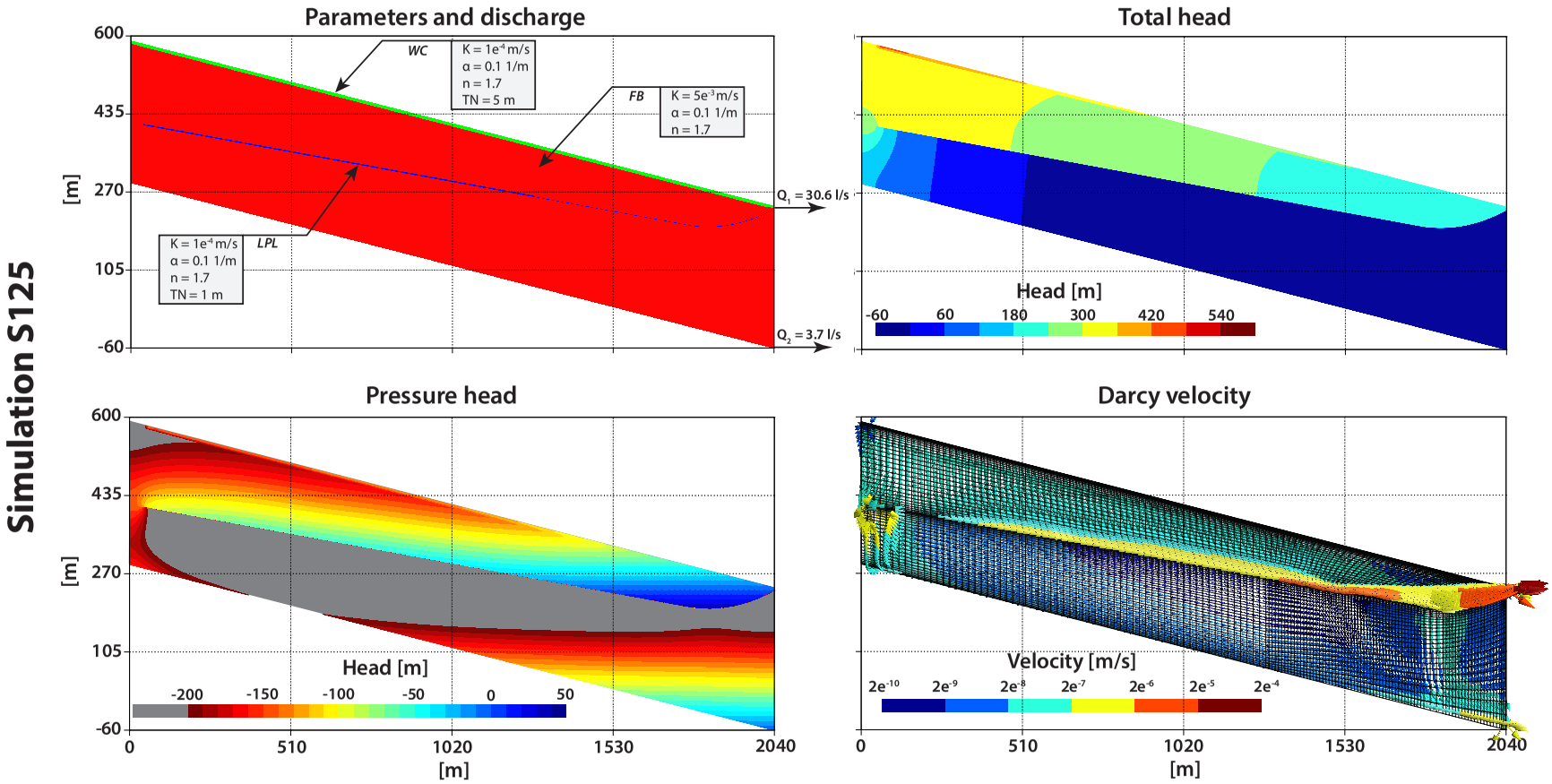

Figure 6.5: Flow simulation S125: Set of parameters and estimated discharge, total head distribution, pressure head distribution and darcy velocity distribution.

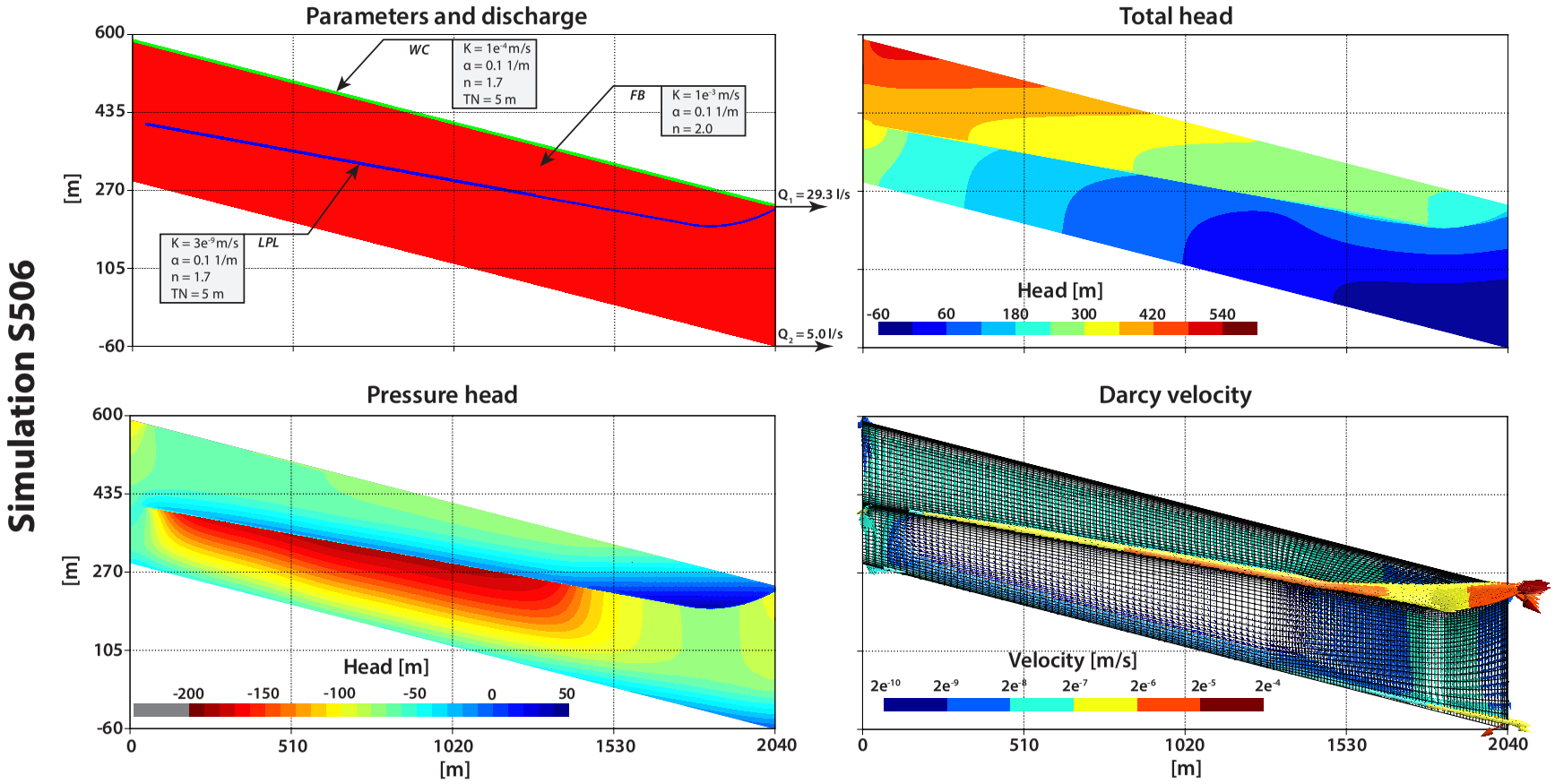

Figure 6.6: Flow simulation S506: Set of parameters and estimated discharge, total head distribution, pressure head distribution and darcy velocity distribution.

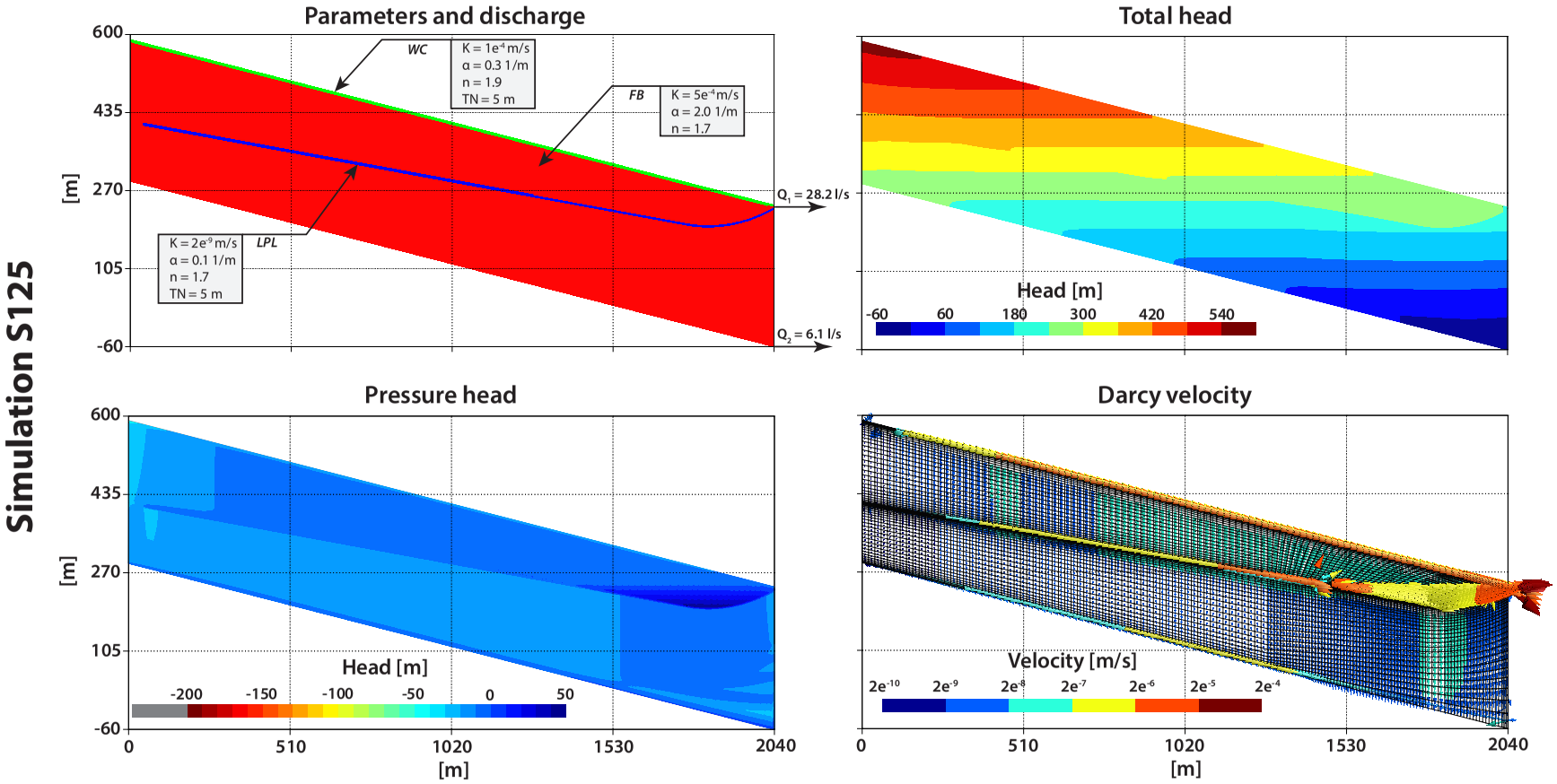

Figure 6.7: Flow simulation S515: Set of parameters and estimated discharge, total head distribution, pressure head distribution and darcy velocity distribution.

right boundary as a consequence of the new flow from the vertical infiltration. In the lowest part of LPL, flow continues towards the right edge, even though the LPL slope changes of sense, until the accumulated flow exit the system for the narrow section in the right top corner. Simulation S515 presents a particular feature in the weathered cover, in which part of the water flows sub-horizontally through the weathered cover. It seems that the low contrasting difference in K between WC and FB can also produce sub-superficial flow. However, it is small comparing with the infiltrated part. In simulations S125 and S206, near the edge of LPL, flow seems to go to the left (contrary to the direction of the rest) towards the edge and then passes through the small free section into the part below LPL. This strange behavior against gravity is produced by the strong suction above LPL that seems to affect the region located near the edge of LPL. It appears that simulation S515 is the one with a behavior that could be closer to reality.

6.3.2.2 Case model B

We use simulation S721 to assess the hydrodynamic behavior of a model with a thick relative low permeability weathered cover (Fig. 6.8). Indeed, the weathered cover has implications in the distribution of total head. Total head decreases following a strange path, first in the WC decreases normally then it passes to the top FB zone (above LPL) where it starts to climb until it reaches the length of LPL. At the left zone, total head is practically constant, it starts to decrease again below LPL. Looking at the pressure head distribution, it can be observed that there is a zone of high suction just below the WC in the top section. Such a suction is provoked for the same reason as it happens below LPL. It appears that suction is larger in the case of the interaction between WC and FB. It would be necessary to prescribe another set of non saturated parameters for FB to reduce this effect. However, we found several numerical difficulties when we tried to increase the value of α and n in FB. So we do not have a simulation with such a set of parameters to see if it is possible to reduce such suction and maintain the value of discharge. Suction of this zone also affects the flow, redirecting part of the flow, that normally should infiltrate vertically towards LPL, outside of it. This is probably the cause why discharge of the aquifer could not reach the a priori vertical recharge within the limits of LPL with a low value of K (1×10^{-9} m/s) when one single WC layer was used. As expected, there is a sub-superficial flow in WC which seems to be significant. However, it is also observed that most of the flow is infiltrated towards the aquifer. In such case, the component of discharge from the aquifer remains significantly higher than the one from the sub-superficial flow of WC.

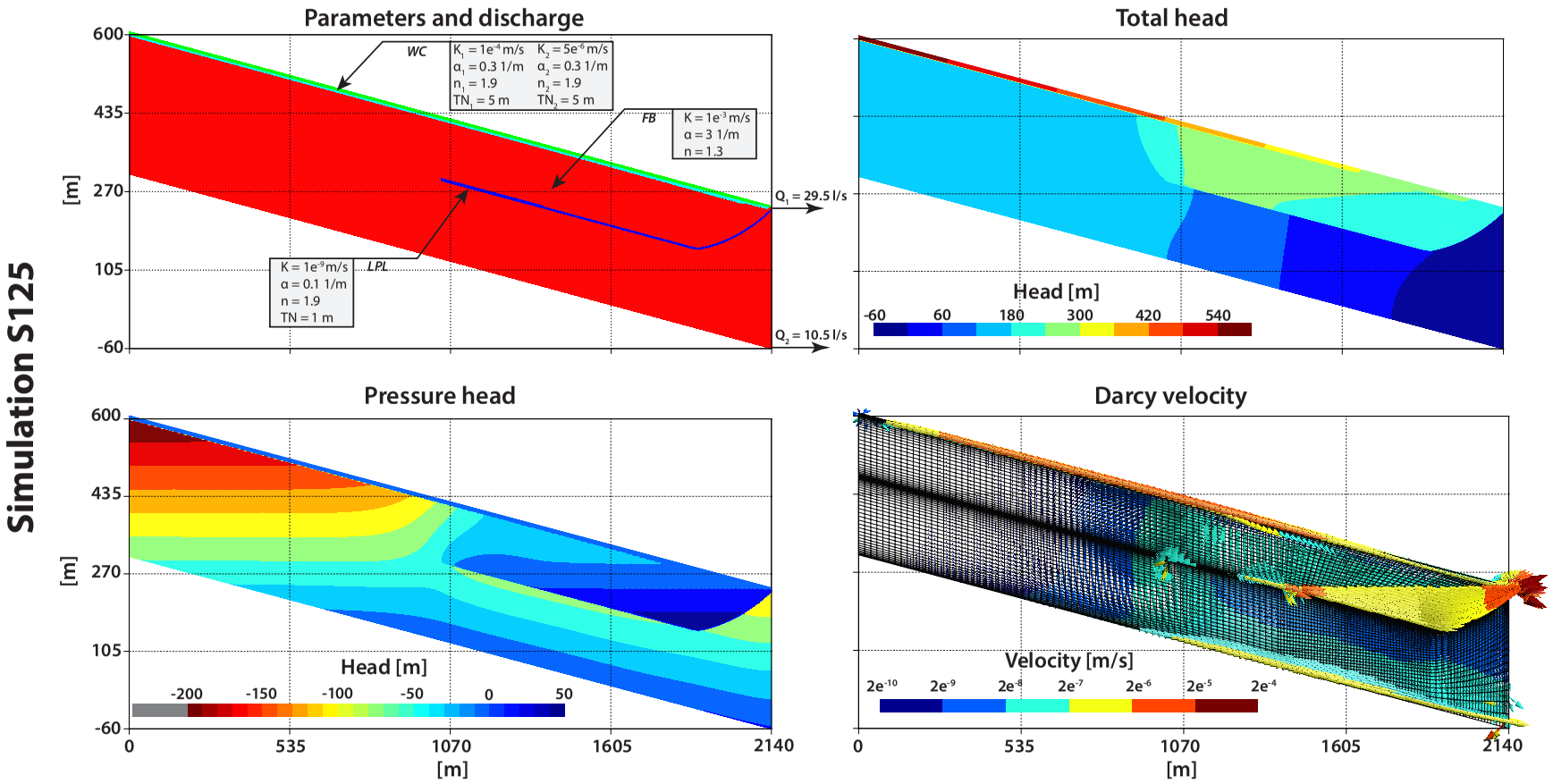

Figure 6.8: Flow simulation S721: Set of parameters and estimated discharge, total head distribution, pressure head distribution and darcy velocity distribution.

6.3.3 Saturation comparison

Spatial distribution of saturation in S125, S506, S515 and S721 is relatively similar (Fig. 6.9 and Fig. 6.10). Most of FB is unsaturated with zones more or less saturated than others. In all simulations, it is easily identified the saturated zone of the perched aquifer. In models S125, S506 and S721 there is a progressive transition between the saturated and non-saturated zone, whereas this transition is very thin in S515. This simulation also shows that LPL is saturated or almost saturated along all the profile, while the rest of the simulations show that LPL is mostly unsaturated. S506 even shows a less saturated zone below LPL. All simulations show a saturated or near saturated WC zone near the aquifer. In simulations S515 and S721, practically all WC is at saturated or near saturated conditions.

The saturation simulations are compared with the cross section of the 19-layer resistivity model. Given that there is not an exact relation between saturation degree and resistivity, comparisons are qualitative rather than quantitative. First, the green zones of the resistivity model ($30 - 100$ Ωm and $30 - 70$ Ωm) are associated with saturated fractured basalt or weathered basalt. Yellow zones with resistivity in the range of $100 - 300$ Ωm are associated to unsaturated basaltic rock and zones with resistivity higher than > 400 Ωm (red zones) are associated with unsaturated massive lava flows. Comparing the saturation degree with the 19-layer resistivity model, it can be seen that simulations can produce a relatively similar distribution as the resistivity model in the main zone. The lower part of the perched aquifer in all simulations is quite similar to the resistivity cross section, showing the top part of the aquifer plane and a saturated zone in the WC near the aquifer. In the case of the $30 - 100$ Ωm threshold, the saturated zone has a relative large extension in which the thickness remains thick. Simulation S506 can produce a similar thickness with a relative high saturation. Simulation S515 also shows saturation or near saturation conditions in such an extension, however it is in LPL which is very thin. In the case of S125, the saturated zone might be too thick. All models fail to produce the high resistivity zone in the top left part of the section and below the perched aquifer in the bottom right boundary. The first is probably because it might correspond to another geological unit which is not simulated in our models, whereas the second shows that these models fail to avoid infiltration in the the thickest part of the aquifer, where the resistivity section shows drier conditions. Infiltration could be a consequence of the designed geometry of LPL, that could be less steep to reduce such a high hydraulic head in its lower level.

It should also be noticed that, the resistivity section corresponds to a snapshot taken in May 2006 during a dry period. As simulations show steady-state

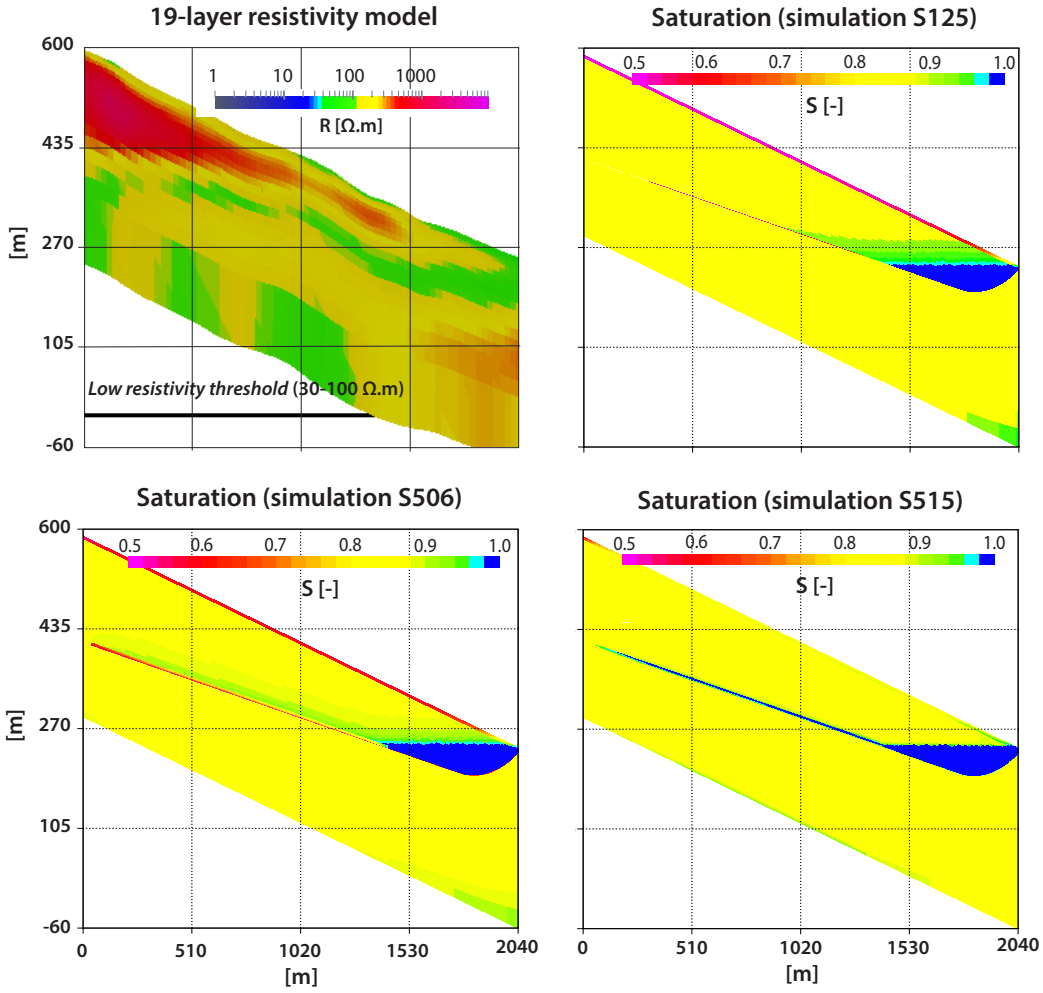

Figure 6.9: Comparison between resistivity and saturation of simulations S125, S506 and S515. Cross section taken from the 19-layer resistivity model, in which low resistivity zones ($30 - 100$ Ωm) are associated to perched aquifer, unsaturated weathered basaltic rocks are related with resistivities in the range of $100 - 300$ Ωm and massive unsaturated lava flows are related to high resistivy zones (> 300 Ωm).

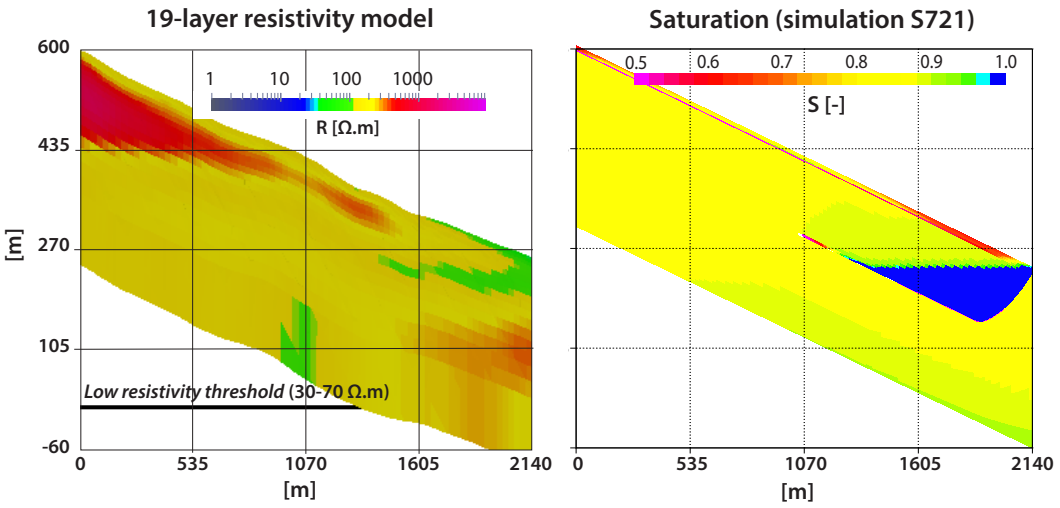

Figure 6.10: Comparison between resistivity and saturation of simulation S721. Cross section taken from the 19-layer resistivity model, in which low resistivity zones ($30-100$ Ωm) are associated to perched aquifer, unsaturated weathered basaltic rocks are related with resistivities in the range of $100-300$ Ωm and massive unsaturated lava flows are related to high resistivy zones (>300 Ωm).

conditions in equilibrium with yearly mean recharge, such comparison losses some credibility. In any case, to the author's opinion, the zones of interest are the saturated ones, especially the thickest part of the perched water. While the degree of saturation in others zones could be affected by variations of the recharge rates; the perched water zone, which saturation is constant, would be less sensitive to this variations, and thus, its geometry is more likely to remain constant either in dry or wet conditions. Therefore, such type of comparison remains valid for this zone regardless of the temporal variability of the recharge conditions. However, it would be interesting to see a comparison under different recharge conditions, which at the moment have not been tested.

6.3.4 Groundwater age

Groundwater age distribution for simulations S125, S506, S515 and S721 is shown in figure 6.11. First it should be noticed that distribution of groundwater age in the left boundary of models S125, S506 and S525, is affected by the non flux condition of the first nodes of the top boundary near the left corner, so it might not be representative of what should happen in a complete section. Models S125 and S506 present a similar age distribution, in which groundwater age increases progressively towards LPL. Once infiltration reaches LPL, groundwater takes a long period of time to pass through LPL (ca. 130 years), except in the position where perched water is formed where it infiltrates faster (15 to 30 years). In

model S515, similar to the total head distribution, groundwater age decreases gradually to the bottom. LPL barely affects the age distribution in the left part of LPL, taking ca. 8 years to pass it through, whereas in the part of the perched water formation, infiltration is accelerated. Model S721, presents the most contrasting distribution in which the section can be divided into two parts, the left side with an old groundwater age even near the surface, as water takes ca. 70 years to pass through the 10 m of WC and then even longer in the FB, and the right side with younger waters in which despite WC has the same thickness, groundwater infiltrates a lot faster (ca. 1 year, which is probably caused by the accumulated sub-superficial flow), then, through FB, infiltration continues relatively fast until it reaches LPL in ca. 11 years, where finally similar to the first two models (S125 and S506), it takes a long time to pass through LPL (ca. 190 years).

All simulations show a relative young groundwater age at the location of the spring, which is result of the mix between the young recharge near the outlet section and an older recharge which is coming from far upward and passing through the perched aquifer before reaching the outlet. Model S125 shows that groundwater age at the spring is ca. 24 years and it is clearly observed from the distribution that it corresponds to water from the aquifer rather than water from the WC. Model S506 has a similar distribution but the groundwater age at the spring is ca. 11 years. The model with the younger spring water age is S515, where it is observed that recharge near the spring has a more influential component in its discharge. Even though, model S721 has a thick low permeable WC that could promote sub-superficial flow near the spring directly towards it and therefore the spring could have a younger age, this is not the case. It is probably because we used a thinner WC near the spring to avoid numerical problems, so the accumulated sub-superficial flow infiltrates in the thinner WC before reaching the spring as it is observed in the groundwater age distribution. The groundwater age is ca. 14 years, however it could be significantly reduced if WC is thicker near the spring as the rest of the section.

6.4 Discussion

6.4.1 Parameters and plausibility of the conceptual models

Results of the groundwater flow model show that with a different set of parameters, enough perched water can be produced to simulate the observed discharge of the springs of *Cerro Gato*. However, a more reduced number (10) can sim-

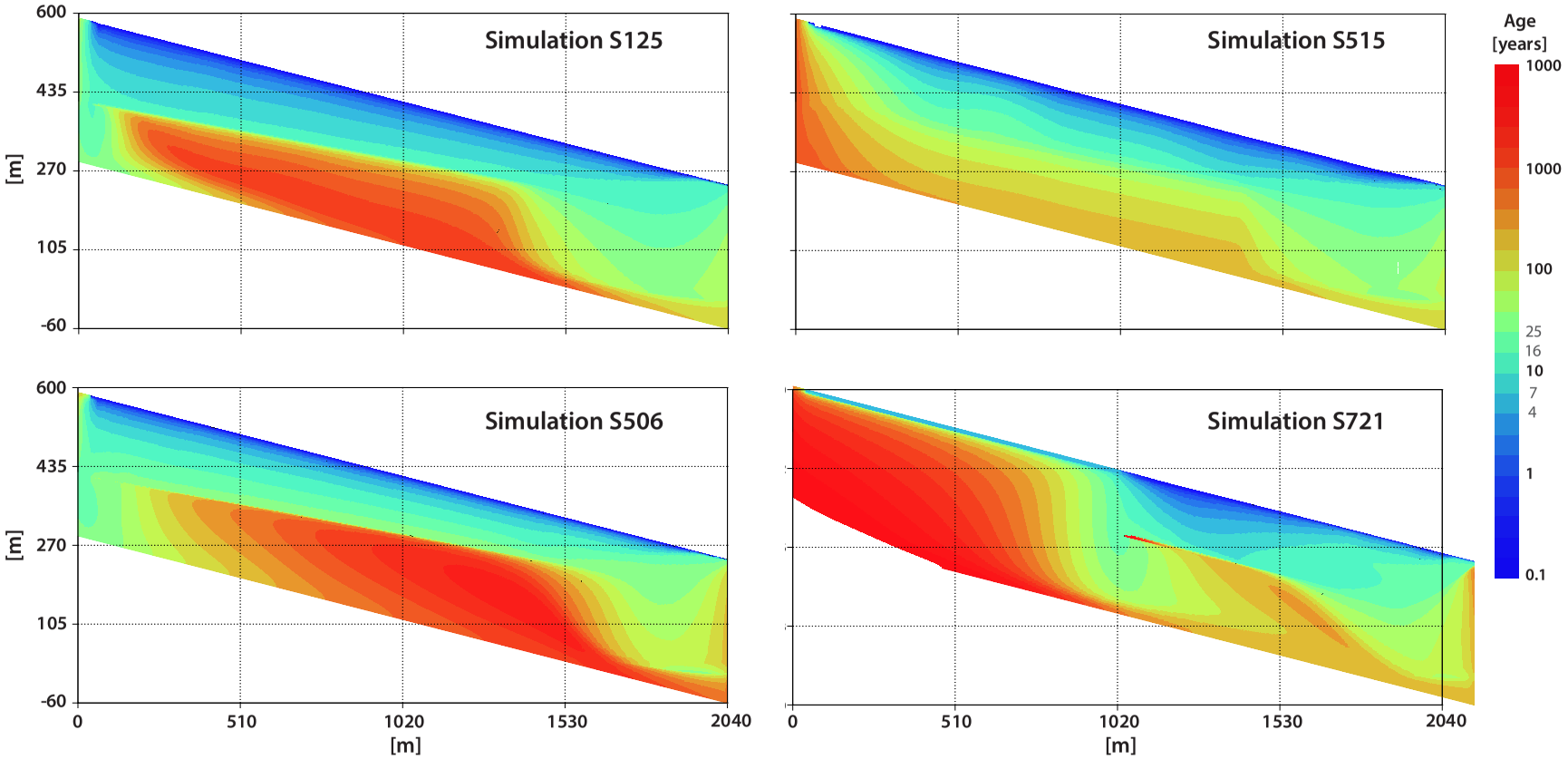

Figure 6.11: Groundwater age distribution of simulations S125, S506, S515 and S721. Groundwater age of the springs ranges between 8 and 24 years.

ulate similar values of discharge. In all cases, the parameter controlling the spring's discharge is the hydraulic conductivity of LPL, in which regardless of its thickness and any parameter used in FB, the value of K_{LPL} should be less than 1×10^{-8} m/s in order to reach the observed discharge (ca. 28 l/s). Given that LPL seems to be paleosol, which basically is cooked clay, then a very low permeability is expected. To the author's knowledge, there is no reference about the hydraulic conductivity of paleosols except for Unger et al. (2004), which in a similar context, they simulated discharge from a perched aquifer in fractured basalt and found a hydraulic conductivity of 2.5×10^{-9} m/s for a dense clay interbed. This value corresponds well to the range found in this study (1×10^{-9} to 1×10^{-8} m/s). Hydraulic conductivity of FB did not show much influence in the discharge alone, however K_{FB} combined with a more contrasting K_{LPL} shows an increase of the discharge. A distinctive range of K_{FB} which produces better simulations of the discharge could not be found. With the proper combination of values from the whole range used, discharge could be satisfied even with hydraulic permeability values as high as the ones found in the seismic wave survey (ca. 1×10^{-2} m/s). In the case of the reduced length of LPL (case of model B), it is necessary a WC thickness of at least 7.5 m and values of K_{WC} ranging between 1×10^{-6} and 3×10^{-5} m/s to reach the observed discharge. Such hydraulic conductivity values correspond the ones found by the soil water transfer model in section 3.3.1. Simulated discharge at the spring shows no sensitivity to the van Genuchten parameters (α and n) of FB and LPL. Indeed, given that the perched formation in the FB and LPL is expected to be saturated, non-saturated parameters should not be influential. Unger et al. (2004) also found that α and n of the clayed interbed are not sensitive to the perched aquifer discharge. Despite these parameters does not seem to affect discharge, non saturated parameters of FB showed a contrasting hydrodynamic behavior, in which simulations with a low α_{FB}, have a relative large zone with intense suction below LPL, which might be out of the expected functioning of the model.

Simulations performed in the two case models, one in a extensive LPL and one with a reduced one, show that both could simulate the the observed discharge of *Cerro Gato* springs. As mentioned before, even though several simulations can satisfy the observed discharge, some of them present an unexpected hydrodynamic behavior that could be far from reality. The simulation with relative high van Genuchten parameters of FB, is the one which shows the more logical hydrodynamic functioning. This simulation also has a saturation distribution relatively similar to the resistivity model. Moreover, estimated groundwater age (ca. 8 years) at the spring location, is in accordance to the values found by Warrier et al. (2012) in springs near to *Cerro Gato* (5 to 8 years) and springs

in the windward zone (7 to 15 years), using a combining noble gas and stable isotope study. Such low values in the simulation are the consequence of the mixing between young recharge flow from the zone near the spring and an older groundwater flow from the perched formation, which is the more important component. Such behavior corresponds well to the hydrograph observed in *Cerro Gato* stream, where discharge shows a large groundwater semi-constant component along time, but after wet months, it can be seen an increase in the observed baseflow signal. Simulations of the second case (model B), show that it is possible to reach the observed discharge of the spring with a smaller LPL with the observed thickness by the seismic refraction survey and using hydrodynamic parameters similar to measurements or estimated from a different approach. Even though estimated residence groundwater time (ca. 14 years) is also in accordance to values found by Warrier et al. (2012), the hydrodynamic behavior shows a significantly large water suction zone below the WC at high altitude, which might not correspond to values expected in reality. It remains to be seen if it is possible to assess a better hydrodynamic functioning with a set of non saturated parameters close to the best simulation for model A, which could be realistic as it is observed sub-superficial flow in the thin WC of this simulation.

With the quantity of uncertainties in the boundary conditions (recharge and discharge), the geometry (extension of LPL) and the parameters (very few measured or obtained from another approach) and the reduced number of constraints (unknown piezometry, another method to validate estimations), it was impossible to validate such conceptual model with only one groundwater model. However, we show the likelihood that such models can explain groundwater flow of *Cerro Gato* watershed.

6.4.2 Improvement of the methodology and perspectives

Even though we proved the plausibility of the proposed conceptual model, questions remain about: which model is the most pertinent to represent *Cerro Gato* watershed? Which hydrodynamic parameters such model should have? And, what would be its hydrodynamic functioning? More constraints would be definitively needed, but using the current available data, it is still possible to improve our knowledge of the system. Indeed, a detail dataset of two contrasting hydrological years is available, therefore a transient-state modeling of the system is contemplated in the near future. Hydrograph of the stream of *Cerro Gato* reveals fluctuations in the baseflow signal, even though they are small (ca. 2 l/s), their proper simulation could provide insights about the properties of the system. Hydrodynamic parameters of the fractured basalts, such as hydraulic conductivity and the non saturated ones, that at the moment are not influential

in the discharge simulation, would definitively play a more important role in transient state. Considering the large unsaturated zone, such parameters would control the infiltration rate and K_{FB} would control the perched aquifer transmissivity, that both would have an impact in the discharge signal. The difficulty of the trasient state approach is the initial saturation conditions. Estimations show that groundwater age at springs could be at least 8 years old, which means that the initial recharge conditions are unavailable. This inconvenient could be overcome with several testing using mean recharge conditions in previous years. A point to be improved is the possibility to use a larger set of non saturated parameters. As seen in the results, it seems that the best simulation is provided with the combination of high values of these parameters, which at the moment is very limited. This could imply restructuring completely the current mesh design, which could include a refinement of it. Another solution to improve the calculation difficulties with these parameters is the use of a more simple law for the saturation-pressure and saturation-specific permeability relations than the ones of van Genuchten, that considers a steep gradient in this curve in near saturation conditions which implies numerical complications for the model. Indeed, Unger et al. (2004) used the Brooks-Corey specific permeability relation (Brooks and Corey, 1964) to reduce the calculation difficulties during the formation of a perched aquifer. However, such relation should be handle with care, because they usually reduce the water holding capacity of the porous media, which might lead to difficult the formation of enough perched water to produce discharge at the spring. A proper parameter equivalence between both relations should be consider and tested, such as the one proposed by Morel-Seytoux et al. (1996).

6.4.3 Water management implication

Cerro Gato springs produce the stream, in which water is taken to supply the population of Puerto Baquerizo Moreno. Therefore, the conservation and sustainable management of this ecosystem is extremely important. This study shows that springs are fed by a perched aquifer that is recharged from a catchment surface larger than its hydrological watershed, which reaches the highlands. Such catchment surface is defined as the big *Cerro Gato* watershed until the location of the water catchment system. A significant part of the catchment surface is located in the highlands, in which the semi-permanent presence of fog is an additional water input to the system. Water age of the spring is ca. 8-14 years, which means that probably any intervention within the hydrogeological watershed in recent or next years would not have immediate effect in the springs. Given the baseline knowledge of this groundwater system, some considerations should be prioritized to preserve it, which are basically focused in two main points:

- *protective measurements*, in which local authorities should define an environmental protection zone within the perimeter of the hydrogeological watershed (Fig. 6.12), so this zone is safe from all types of pollution such as fertilizers, solid wastes and animal dropping, and also it could be preserved from farming and harvesting, prioritizing the conservation of endemic vegetation which have shown to improve the groundwater recharge.

- *maintenance measurements*, a system of hydrological monitoring by the local authorities should be implemented, including measurements of climatic variables, streamflow and water quality, in this way the effect of climate and human disturbance can be assessed. Also, this system would help to quantify the efficiency of the water management policies applied.

6.5 Conclusions

Dataset interpretation from a multi-disciplinary study at watershed level leads to build a hydrogeological conceptual model of the groundwater occurrence of the springs of *Cerro Gato* watershed, in which the groundwater flow of springs is originated from a local perched aquifer in fractured basalt formed above a thin low permeability layer (LPL). With a simple 2D saturated unsatured flow modeling approach, the conceptual model is tested using an extended and reduced length of the sustaining unit, in which the influence of the weathered cover is assessed. The geometry of the model is designed from a cross section of the main axis of the hydrogeological watershed defined from the resistivity model of the island. Boundary conditions are set based from the knowledge of the system and measurements. Hydrodynamic parameters are either measured, taken from the literature or calibrated. The plausibility of a perched formation is assessed comparing the simulated discharge of the water body with the observed discharge at the springs.

Several simulations with a different set of parameters show to perched enough water, so that discharge is close to observed one in the springs, even with the reduced length of the sustaining layer. Simulated discharge has not sensitivity to most of the parameters, except to the hydraulic conductivity of the sustaining layer, which must be lower than 1×10^{-8} m/s to reach the observed discharge. Using the reduced length of the sustaining layer, the weathered cover must have at least 7.5 m of thickness and an hydraulic conductivity lower than 1×10^{-8} m/s with an hydraulic conductivity lower than 3×10^{-5} m/s, to form enough subsuperficial flow that can reach the sustaining layer limits. Such properties of the weathered cover, corresponds to measurements, observations or values estimated

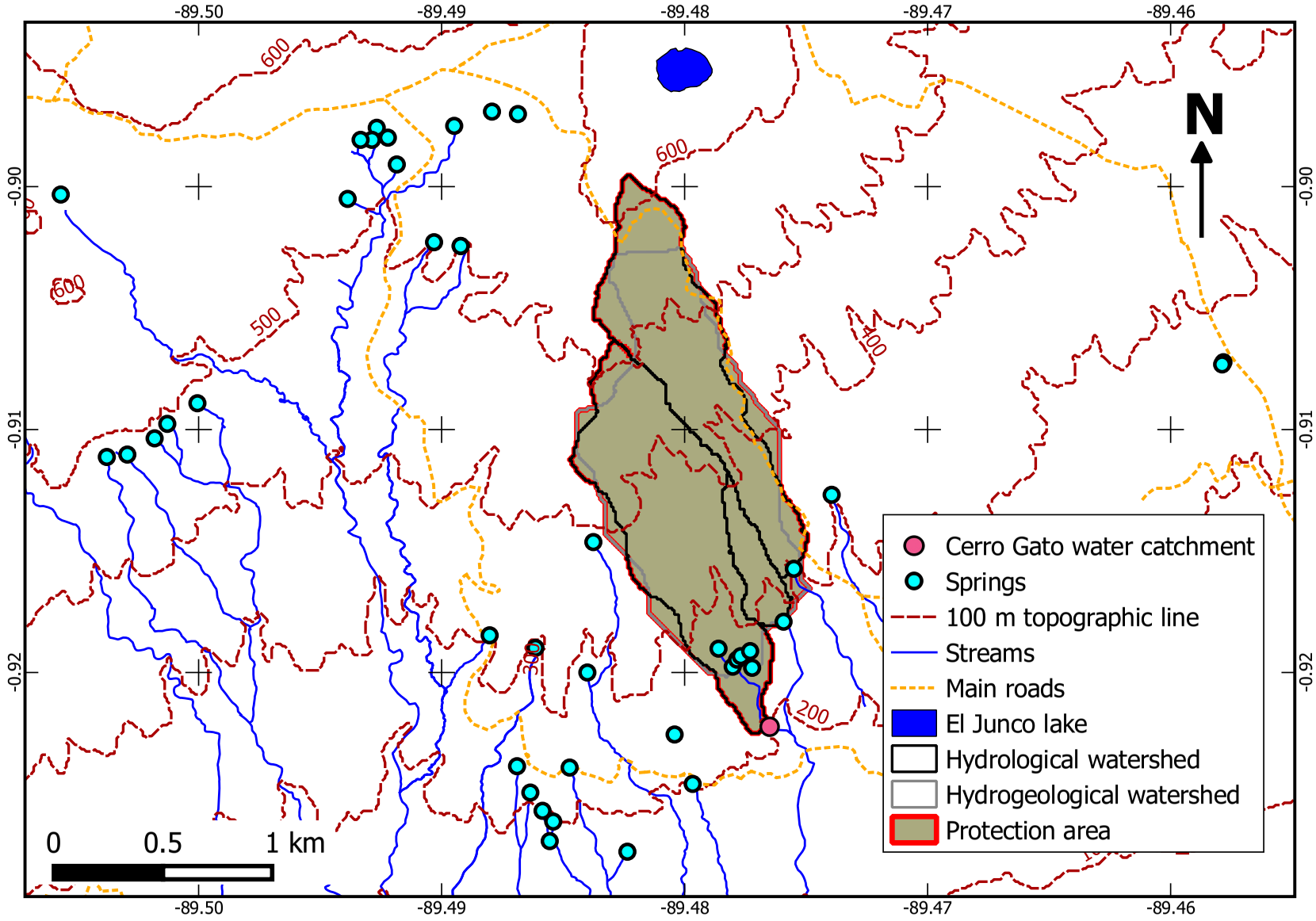

Figure 6.12: Protection area of the *Cerro Gato* water catchment. The protection area is composed of the three hydrological watersheds that corresponds to the hydrogeological watershed of *Cerro Gato* obtained from the large resistivity threshold ($30 - 100$ Ωm).

with a different approach. The best simulation, the one that fits the observed discharge, that its hydrodynamic functioning is closer to the one expected and that its saturation distribution is relatively similar to the resistivity distribution of the same cross section; has a groundwater residence time of ca. 8 years, where the groundwater age at the spring location is a mix between sub-superficial flow of young recharge from a relative near zone and the groundwater flow from the perched formation, which is the most influential.

These results arise from a simplification of the hydrogeological system, in which a simple geometry has been tested with average values of recharge and discharge. To improve the current knowledge of the system, a most elaborated modeling that considers a more complex configuration would require more data to constraint the model. Nevertheless, with the available data at the moment, modeling in transitory state could help to this objective, and it is expected as a perspective of this work.

Chapter 7

Conclusions and perspectives

7.1 Conclusions

This thesis propose the first study of the hydrogeological functioning of watersheds on the southern windward side of San Cristobal Island. A multidisciplinary approach, based on the set up of an experimental site, field observations and modeling, have been used to: i) characterize the internal structure of the watersheds from field and indirect methods, ii) quantify inputs and outputs of the water balance from plot to watershed scale and iii) understand the surface and groundwater dynamics from hydrological and hydrogeological modeling.

The experimental site is located in *Cerro Gato* and surrounding watersheds, in which an hydrological network was installed. The network includes three weather stations along the windward side, where monitoring in the station of the highlands includes throughfall and stemflow measurements. Soil monitoring is performed at mid and high elevations. The network is completed with streamflow monitoring in three watersheds: one at the highlands (*El Bayo* at 607 m a.s.l.) and two at mid elevation (*Chuki Marka* and *Cerro Gato* at 320 and 373 m a.s.l., respectively).

Results of this thesis are summarized in five main aspects.

Climatic characteristics

Monitoring of stations allows the first climatic characterization in the windward side of the island. Long-term records reveal that, the first hydrological year (2013-2014) is an average year in terms of rainfall and temperature, while the second one (2014-2015) could be consider as a hot and relative wet year (near the top quantile in terms of rainfall). Records from stations installed in the study site, show a median annual rainfall of ca. 1000 mm (300 m a.s.l.) with an orographic rainfall gradient of 270 mm/100 m of elevation and a median refer-

ential potential evapotranspiration of 680 mm (300 m a.s.l.) with its respective orographic gradient of -50 mm/100 m of elevation.

Recharge estimation

Cloud water interception (CWI) by the endemic vegetation is estimated using a Rutter-type canopy model with inputs from rainfall and fog measurements and it is validated with net precipitation measurements. The model shows that CWI at the windward highlands (600 m a.s.l.) is not negligible. It represents ca. 28% of the water input during the cool seasons, and it reaches 23% of the total water input for the representative year.

Deep percolation (DP) is estimated using the joint modeling of a physically-based canopy and soil water transfer model. Results from modeling show that DP rates are markedly different depending of the altitude, land cover and seasonality. At a watershed scale, recharge is more affected by altitude in mid-elevation watersheds, whereas land cover is the main controlling factor at high-elevation watersheds, in which fog interception has a marked influence depending of the surface of land cover that can intercept fog and their exposure to the prevailing winds. Mean recharge estimated for the three gauged watersheds reaches ca. 1530, 690 and 830 mm at *El Bayo*, *Chuki Marka* and *Cerro Gato*, respectively.

Hydrological analysis

Hydrographs from the three watersheds studied reveal that their streamflow is markedly different. Median daily streamflow is ca. 8 l/s in the high-elevation basin (*El Bayo*), while it reaches 17 and 29 l/s in *Chuki Marka* and *Cerro Gato* (low-elevation basins), respectively. Baseflow represents 53%, 80% and 87% of total streamflow at *El Bayo*, *Chuki Marka* and *Cerro Gato*, respectively.

Streamflow is simulated using a lumped hydrological model, in which the hydrodynamic behavior of these watersheds is assessed from the streamflow simulation and calibrated parameters. Results show a striking difference in the behavior of the three watersheds. In *El Bayo*, most of the water input (ca. 60%) is lost by the inter-exchange with watersheds at lower elevations. In *Chuki Marka*, groundwater inter-exchange results in groundwater gains that corresponds to the ca. 40% of the total input. In *Cerro Gato*, groundwater income is from other watersheds and corresponds to ca. 18% of the total input. *Cerro Gato* hydrogeological watershed, which corresponds to 140% of its topographic catchment surface, is extended in the same elevation of its hydrological one according to the analysis of the equivalent surface of the model.

Internal structure

Results from the hydrological monitoring lead to investigate the potential extension of the hydrogeological watershed of *Cerro Gato*. The AEM SkyTEM survey conducted over San Cristobal Island (May 2006) is used to define its extension. The geometry is extracted from the"smooth" 19-layer resistivity model, in which two thresholds of resistivity are used that imply a surface equivalent or larger than its hydrological watershed where both surfaces are extended to the east.

A seismic of refraction survey was performed in San Cristobal revealing insights of the sub-surface weathered cover of the watersheds, where its thickness ranges from 14 m in the highlands to 4 m at mid elevation. From wave velocity estimations of this survey and an effective elastic porous media model, total porosity and hydraulic conductivity is estimated, ranging from 4 to 20% and 1×10^{-4} and 1 m/s, respectively.

Hydrogeological approach

Elements from the interpretation of the different studies allowed the possibility to propose a hydrogeological conceptual model for *Cerro Gato* watershed, in which springs are fed from a local perched aquifer in fractured basalt formed above a thin low permeability layer that intersects the topography. The conceptual model is evaluated using 2D saturated/unsaturated groundwater flow modeling in steady state conditions, where the geometry is designed from a cross section of the hydrogeological watershed and the topography, the average gradient of recharge is used as boundary condition and parameters are taken from measurements, literature or calibrated. The model is tested with the average discharge observed in the springs and a comparison of saturation with the corresponding resistivity cross section.

Results show that several simulations with contrasting parameters can form a perched aquifer which discharge can reach the observations. The only parameter that influences perched groundwater formations is the hydraulic conductivity of the low permeability sustaining layer. Simulations with a reduced length of the perched aquifer sustaining layer can also reach the observed discharge when the proper combination of thickness and hydraulic conductivity of the weathered cover produce sub-superficial flow that recharge the aquifer. The best simulation show that the groundwater age at the spring is ca. 8 years, in which discharge is a combination of the sub-superficial flow from the weathered cover and groundwater flow from the perched aquifer, being the latter the most influential.

This approach considers a simplification of the complex hydrogeological sys-

tem and could be improved with more constraints data. Nevertheless, it provides for a first time an integrated understanding of the watershed system of *Cerro Gato*, in which the methodological build up of each part leads to important results than can be used in different disciplines and that highlight the pertinence of a multi-disciplinary study. Moreover, it helps to improve the general knowledge of the hydrogeology of basaltic islands, especially of high-level perched aquifers.

7.2 Perspectives

Several aspects of the hydrology of Galapagos were treated during this work, in which results lead to a further examination of some of them or to a whole new set of questions than remain unanswered. The participation of local authorities and national institutions were fundamental to complete this work. In this spirit, perspectives are focus in two main aspects.

Scientific perspectives

- Fog interception by the vegetation is an additional input to the water balance in the highlands of San Cristobal, but in the case of mid-elevation watersheds its influence is reduced. This is because we assumed an orographic gradient of fog interception in which its intensity is heavily reduced at the elevation in which fog is formed. A spatial monitoring of fog interception along the windward slope could help to assess the spatial distribution of fog interception and identify the influence of elevation, terrain slope and orientation.

- The joint canopy and soil water transfer modeling allows the estimation of real evapotranspiration, but it is based in the assumption that evapotranspiration is reduced proportionally to the canopy saturation. It would be interesting to prove this hypothesis by eddy covariance or sapflow methods. Such estimations could also help to understand the role of fog in the physiological functioning of the endemic vegetation.

- Records from the hydro-climatic network installed in San Cristobal could be used to assess the impact of El Niño or La Niña events in the dynamic behavior of the surface and groundwater flows. With long-term records, it could be observed if in fact the groundwater system is massively recharged during El Niño events followed by a long recession over several years or not.

- As mentioned before, the hydrogeological approach used in this thesis is a first step towards a more comprehensive understanding of the local and regional hydrogeology. Modeling in transient state would definitively improve knowledge of the local system. However, this is a short time perspective. A more ambitious approach would be the 3D modeling of the entire zone surrounding *Cerro Gato*, which includes several watershed such as *Chuki Marka* and that could integrate features as inter-exchange groundwater between hydrogeological watersheds. The difficulty is that it would require an entire monitoring of springs and streams of this zone, which is very challenging in terms of logistic and equipment resources. It could also be complemented with hydrochemical and geochemical monitoring to have additional constraints and determine best candidates as tracers of the groundwater pathways.

- At the moment, any comparison between recharge conditions in the windward side of Santa Cruz and San Cristobal islands has only be in qualitative terms. The *GIIWS* team currently have and hydrological monitoring network in both islands, which provide the unique opportunity to make a quantitative comparison of recharge that could help to improve the understanding of such contrasting islands in hydrogeological terms.

- In the frame of this thesis, only San Cristobal and slightly Santa Cruz have been investigated. The approach used in this thesis could be replicated in the two other inhabitant islands (Floreana and Isabela).

Collaboration perspectives

- Any study expected in the future related to the hydrology of the Galapagos Islands would imperative need the continuity of the hydrological monitoring done in Santa Cruz and installed in the frame of this thesis at San Cristobal. At the moment, the *GIIWS* team is responsible but the more logical step is that local authorities should take in charge of this responsibility, defining politics to assure the long-term monitoring, which is crucial for the proper water management of the islands against climate change and El Niño events.

- This thesis is a proof of the results that could be obtained through the collaboration between local and international institutions. In the frame of the *GIIWS* project, the transfer of technology to local authorities and Ecuadorian institutions have resulted in a process to form national students through internships, thesis and inter-exchanges. Such type of collaboration

should continue, so that national professionals formed through these experiences can take the lead, and manage projects of this magnitude, including itself.

Bibliography

Abbott, M. and Refsgaard, J. (2012). *Distributed Hydrological Modelling*. Water Science and Technology Library. Springer Netherlands. 4.3.1.1

Aboal, J., Jiménez, M., Morales, D., and Gil, P. (2000). Effects of thinning on throughfall in canary islands pine forest — the role of fog. *Journal of Hydrology*, 238(3–4):218 – 230. 3.2.1, 3.2.5.2

Adams, R., Black, T., and Fleming, R. (1991). Evapotranspiration and surface conductance in a high elevation, grass-covered forest clearcut. *Agricultural and Forest Meteorology*, 56(3-4):173–193. 2.4.4.2

Adar, E. M., Neuman, S. P., and Woolhiser, D. A. (1988). Estimation of spatial recharge distribution using environmental isotopes and hydrochemical data, i. mathematical model and application to synthetic data. *Journal of hydrology*, 97(3):251–277. 3.4.1

Adelinet, M. (2005). *Etude du fonctionnement hydrologique des bassins versant de San Cristobal (Galapagos - Equateur*. Master, Université Pierre et Marie Curie - Paris VI, Paris. 1.2.6.1, 1.3, 2.1.1.2, 2.2.2, 2.2.2, 2.3.2.4, 4.1.1.1, 4.2.2, 4.5, 6.1, 6.2.3, A.8

Adelinet, M., Fortin, J., d'Ozouville, N., and Violette, S. (2007). The relationship between hydrodynamic properties and weathering of soils derived from volcanic rocks, galapagos islands (ecuador). *Environmental Geology*, 56(1):45–58. 1.2.6.1, 2.1.1, 2.3.2.3, 2.4.4.2, 3.3.1.2, 4.1.1.1, 5.3.2

Aksoy, H., Kurt, I., and Eris, E. (2009). Filtered smoothed minima baseflow separation method. *Journal of Hydrology*, 372(1-4):94–101. 4.2.1, 4.4

Albouy, Y., Andrieux, P., Rakotondrasoa, G., Ritz, M., Descloitres, M., Join, J.-L., and Rasolomanana, E. (2001). Mapping coastal aquifers by joint inversion of dc and tem soundings-three case histories. *Ground Water*, 39(1):87–97. 5.1.3.2

Alegre, J. C. and Cassel, D. (1996). Dynamics of soil physical properties under alternative systems to slash-and-burn. *Agriculture, Ecosystems & Environment*, 58(1):39–48. 2.4.1

Allen, R., Pereira, L.S., Raes, D., and Smith, M. (1998). Crop evapotranspiration: Guidelines for computing crop water requirements. *FAO*, 56. 2.4.1, 2.4, 3.1.2.3, 3.1.2.3, 3.1.2.3

Armas-Espinel, S., Hernández-Moreno, J., Muñoz-Carpena, R., and Regalado, C. (2003). Physical properties of "sorriba"-cultivated volcanic soils from tenerife in relation to andic diagnostic parameters. *Geoderma*, 117(3-4):297–311. 2.4.3.2, 2.4.4.2, 3.3.1.1, 3.3.1.2

Arnold, J. G., Muttiah, R. S., Srinivasan, R., and Allen, P. M. (2000). Regional estimation of base flow and groundwater recharge in the upper mississippi river basin. *Journal of Hydrology*, 227(1):21–40. 1.1.2

Aster, R., Borchers, B., and Thurber, C. (2013). Parameter estimation and inverse problems second edition elsevier inc. 2.4.2.4

Aston, A. (1979). Rainfall interception by eight small trees. *Journal of Hydrology*, 42(3-4):383–396. 3.2.5.1

ATV-DVWK (2002). Verdunstung in Bezug zur Landnutzung, Bewuchs und Boden - Merkblatt M 504. ATV-DVWK-Regelwerk, Band M 504. Technical Report 144 S, ATV-DVWK Deutsche Vereinigung für Wasserwirtschaft, Abwasser und Abfall. Gesellschft zur Förderung der Abwassertechnik, Hennef. 2.4.1

Auken, E., Violette, S., d'Ozouville, N., Deffontaines, B., Sørensen, K. I., Viezzoli, A., and de Marsily, G. (2009). An integrated study of the hydrogeology of volcanic islands using helicopter borne transient electromagnetic: Application in the Galápagos Archipelago. *Comptes Rendus Geoscience*, 341(10–11):899–907. 1.2.6.1, 1.2.6.2, 5.1.1.2, 5.1.2.1, 6.1

Bear, J. (1972). Dynamics of fluids in porous media. *American Else-vier, New York*. 5.3.3.2, 5.3.3.3

Beven, K. (1989). Changing ideas in hydrology—the case of physically-based models. *Journal of hydrology*, 105(1):157–172. 4.3.1.1

Bormann, H., Breuer, L., Gräff, T., and Huisman, J. A. (2007). Analysing the effects of soil properties changes associated with land use changes on the simulated water balance: A comparison of three hydrological catchment models for scenario analysis. *Ecological Modelling*, 209(1):29–40. 2.4.1

Bosch, J. and Hewlett, J. (1982). A review of catchment experiments to determine the effect of vegetation changes on water yield and evapotranspiration. *Journal of Hydrology*, 55(1-4):3–23. 2.4.1, 3.1.2.3

Bosveld, F. and Bouten, W. (2003). Evaluating a model of evaporation and transpiration with observations in a partially wet douglas-fir forest. *Boundary-Layer Meteorology*, 108(3):365–396. 2.4.1

Brauman, K. A., Freyberg, D. L., and Daily, G. C. (2010). Forest structure influences on rainfall partitioning and cloud interception: A comparison of native forest sites in kona, hawai'i. *Agricultural and Forest Meteorology*, 150(2):265–275. 3.2.1

Brauman, K. A., Freyberg, D. L., and Daily, G. C. (2012). Potential evapotranspiration from forest and pasture in the tropics: A case study in kona, hawai'i. *Journal of Hydrology*, 440-441:52–61. 1.1.2, 2.4.1, 2.4.4.2, 2.4.4.3, 3.3.1.1, 3.3.1.2

Brooks, R. H. and Corey, A. T. (1964). Hydraulic properties of porous media and their relation to drainage design. *Transactions of the ASAE*, 7(1):26–0028. 6.4.2

Bruijnzeel, L. (2001). Hydrology of tropical montane cloud forests: a reassessment. *Land use and water resources research*, 1(1):1. 3.2.1

Bruijnzeel, L., Eugster, W., and Burkard, R. (2006). Fog as a Hydrologic Input. In Anderson, M. G. and McDonnell, J. J., editors, *Encyclopedia of Hydrological Sciences*. John Wiley & Sons, Ltd, Chichester, UK. 3.2.3.2

Bruijnzeel, L. A., Mulligan, M., and Scatena, F. N. (2011). Hydrometeorology of tropical montane cloud forests: emerging patterns: HYDROMETEOROLOGY OF TROPICAL MONTANE CLOUD FORESTS. *Hydrological Processes*, 25(3):465–498. 3.1.2.1, 3.2.5.2

Brunner, P., Bauer, P., Eugster, M., and Kinzelbach, W. (2004). Using remote sensing to regionalize local precipitation recharge rates obtained from the chloride method. *Journal of Hydrology*, 294(4):241–250. 1.1.2

Caine, J. S., Evans, J. P., and Forster, C. B. (1996). Fault zone architecture and permeability structure. *Geology*, 24(11):1025–1028. 1.1.1

Calder, I. and Kidd, C. (1978). A note on the dynamic calibration of tipping-bucket gauges. *Journal of Hydrology*, 39:383–386. 3.2.3.1

Campbell, D. (1989). Energy balance and transpiration from tussock grassland in new zealand. *Boundary-Layer Meteorology*, 46(1-2):133–152. 2.4.4.2, 3.3.1.2

Carpenter, T. M. and Georgakakos, K. P. (2006). Intercomparison of lumped versus distributed hydrologic model ensemble simulations on operational forecast scales. *Journal of Hydrology*, 329(1–2):174 – 185. 4.3.1.1

Carvajal, L. F. and Roldan, E. (2007). Calibration of gr4j lumped rainfall-runoff model application: Rio aburra cachtment. *DYNA*, 74(152):73–87. 4.3.1.2

Cavelier, J. and Goldstein, G. (1989). Mist and fog interception in elfin cloud forests in colombia and venezuela. *Journal of Tropical Ecology*, 5:309–322. 3.2.1, 3.2.5.2

Celia, M. A., Bouloutas, E. T., and Zarba, R. L. (1990). A general mass-conservative numerical solution for the unsaturated flow equation. *Water resources research*, 26(7):1483–1496. 2.4.2.2, A 3.2, A 3.2

Chang, S.-C., Lai, I.-L., and Wu, J.-T. (2002). Estimation of fog deposition on epiphytic bryophytes in a subtropical montane forest ecosystem in northeastern taiwan. *Atmospheric Research*, 64(1):159–167. 3.2.1

Clement, T., Wise, W. R., and Molz, F. J. (1994). A physically based, two-dimensional, finite-difference algorithm for modeling variably saturated flow. *Journal of Hydrology*, 161(1):71–90. 2.4.2.2, A 3.2, A 3.2

Cook, P. and Solomon, D. K. (1995). Transport of atmospheric trace gases to the water table: Implications for groundwater dating with chlorofluorocarbons and krypton 85. *Water Resources Research*, 31(2):263–270. 1.1.2

Costa, A. (2006). Permeability-porosity relationship: A reexamination of the kozeny-carman equation based on a fractal pore-space geometry assumption. *Geophysical research letters*, 33(2). 5.3.3.2

Coudray, J., Mairine, P., Nicolini, E., and Clerc, J. (1990). Approche hydrogéologique. *Le volcanisme de la Réunion, Monographie*, pages 307–356. 6.1

Courteaud, M., Ritz, M., Robineau, B., Join, J., and Coudray, J. (1997). New geological and hydrogeological implications of the resistivity distribution inferred from audiomagnetotellurics over la fournaise young shield volcano (reunion island). *Journal of hydrology*, 203(1):93–100. 1.1.3.3

Crosbie, R. S., Binning, P., and Kalma, J. D. (2005). A time series approach to inferring groundwater recharge using the water table fluctuation method. *Water Resources Research*, 41(1). 1.1.2

Cruz, J. V. (2003). Groundwater and volcanoes: examples from the Azores archipelago. *Environmental Geology*, 44(3):343–355. 1.1.3.2, 1.1.3.3

Cruz, J. V. and França, Z. (2006). Hydrogeochemistry of thermal and mineral water springs of the azores archipelago (portugal). *Journal of Volcanology and Geothermal Research*, 151(4):382–398. 1.1.3.3, 2.1.1.2

Custodio, E. (2004). Hydrogeology of volcanic rocks. *Groundwater studies: an international guide for hydrogeological investigations. IHP-VI Series on Groundwater*, 3:395–425. 5.3.2, 5.3.3.1

Custodio, E., Guerra, J., Jimenez, J., Medina, J., and Soler, C. (1983). The effects of agriculture on the volcanic aquifers of the canary islands. *Environmental Geology*, 5(4):225–231. 1, 1.1.3.2

Custodio, E., Lopez Garcia, L., and Amigo, E. (1988). Simulation in the volcanic island of teneriffe (canary island) by mathematical model. *Hydrogeologie (France)*. 1, 1.1.3.2

David, E. and Zimmerman, R. (2011). Compressibility and shear compliance of spheroidal pores: Exact derivation via the eshelby tensor, and asymptotic expressions in limiting cases. *International Journal of Solids and Structures*, 48(5):680 – 686. 5.3.3.1

David, E. C. and Zimmerman, R. W. (2012). Pore structure model for elastic wave velocities in fluid-saturated sandstones. *Journal of Geophysical Research: Solid Earth*, 117(B7):n/a–n/a. B07210. 5.3.1, 5.3.2, 5.3.3.1, 5.3.3.1, 5.3.3.1

De Groot, R. (1983). Tourism and conservation in the galapagos islands. *Biological Conservation*, 26(4):291–300. 1.2.4

Dean, J. F., Webb, J. A., Jacobsen, G. E., Chisari, R., and Dresel, P. E. (2014). Where to locate a tree plantation within a low rainfall catchment to minimise impacts on groundwater resources. *Hydrology and Earth System Sciences Discussions*, 11(8):10001–10041. 2.4.1

Descloitres, M., Ritz, M., Robineau, B., and Courteaud, M. (1997). Electrical structure beneath the eastern collapsed flank of Piton de la Fournaise volcano, Reunion Island: Implications for the quest for groundwater. *Water Resources Research*, 33(1):13–19. 1.1.3.3, 5.1.2.2, 5.1.3.2

DGNP (2013). Informe anual de visitantes que ingresaron a las islas galápagos. Technical report, Galápagos National Park. 1.2.1, 1.2.4

Doherty, J. (2010). PEST, Model-Independent Parameter Estimation User Manual: 5th Edition. Technical report. 2.4.2.4, 3.2.3.3.2, 4.3.2, 4.9

Doherty, J. (2013). Addendum to the PEST Manual. Technical report, Watermark Numerical Computing. 2.4.2.4

Domingo, F., Sánchez, G., Moro, M., Brenner, A., and Puigdefábregas, J. (1998). Measurement and modelling of rainfall interception by three semiarid canopies. *Agricultural and Forest Meteorology*, 91(3-4):275–292. 2.4.4.2

Domínguez Gonzalez, C. (2011). *Análisis de la variabilidad espacial y temporal de la trascolación en la isla Santa Cruz*. Master, Escuela Politécnica Nacional, Facultad de Ingeniería Civil y Ambiental, Ecuador. 2.4.3.2, 3.2.3.1

Dörner, J., Dec, D., Peng, X., and Horn, R. (2009). Change of shrinkage behavior of an andisol in southern chile: Effects of land use and wetting/drying cycles. *Soil and Tillage Research*, 106(1):45–53. 3.3.1.2

Dörner, J., Dec, D., Peng, X., and Horn, R. (2010). Effect of land use change on the dynamic behaviour of structural properties of an andisol in southern chile under saturated and unsaturated hydraulic conditions. *Geoderma*, 159(1-2):189–197. 2.4.1

d'Ozouville, N. (2007). *Etude du Fonctionnement Hydrologique Dans les Iles Galápagos : caractérisation d'un milieu volcanique insulaire et préalable à la gestion de la ressource*. Ph.d., Université Pierre et Marie Curie - Paris VI, Paris. 1.2.1, 1.2.2, 1.2.5, 1.2.6.1, 1.2.6.2, 1.3, 2.1.1.2, 3.2.2.1, A.8

d'Ozouville, N., Auken, E., Sorensen, K., Violette, S., de Marsily, G., Deffontaines, B., and Merlen, G. (2008a). Extensive perched aquifer and structural implications revealed by 3d resistivity mapping in a galapagos volcano. *Earth and Planetary Science Letters*, 269(3-4):518–522. 1.2.6.1, 1.2.6.2, 5, 5.1.1.2, 5.1.2.2, 5.1.2.2, 5.1.3.2, 6.1

d'Ozouville, N., Deffontaines, B., Benveniste, J., Wegmüller, U., Violette, S., and de Marsily, G. (2008b). DEM generation using ASAR (ENVISAT) for addressing the lack of freshwater ecosystems management, santa cruz island, galapagos. *Remote Sensing of Environment*, 112(11):4131–4147. 1.2.6.1, 2.2.1

Dunbar, R. B., Wellington, G. M., Colgan, M. W., and Glynn, P. W. (1994). Eastern pacific sea surface temperature since 1600 a.d.: The δ^{18} o record of

climate variability in galápagos corals. *Paleoceanography*, 9(2):291–315. 1.2.2, 1.2.6.1, 2.4.3.1, 3.2.2.1

Dunkerley, D. L. (2009). Evaporation of impact water droplets in interception processes: Historical precedence of the hypothesis and a brief literature overview. *Journal of Hydrology*, 376(3-4):599–604. 2.4.4.1, 3.2.5.3

Edmunds, W., Fellman, E., Goni, I., and Prudhomme, C. (2002). Spatial and temporal distribution of groundwater recharge in northern nigeria. *Hydrogeology Journal*, 10(1):205–215. 1.1.2

Eilers, V., Carter, R., and Rushton, K. (2007). A single layer soil water balance model for estimating deep drainage (potential recharge): An application to cropped land in semi-arid North-east Nigeria. *Geoderma*, 140(1-2):119–131. 1.1.2

El-Swaify, S. (1980). Physical and mechanical characteristics of andisols in theng, new zealand. *Society of Soil Science*, pages 303–323. 2.4.4.2, 3.3.1.2

Engott, J. and Vana, T. (2007). Effects of agricultural land-use changes and rainfall on ground-water recharge in central and west maui. Technical report, Hawaii, 1926–2004. 3.4.1

Eugster, W., Burkard, R., Holwerda, F., Scatena, F. N., and Bruijnzeel, L. S. (2006). Characteristics of fog and fogwater fluxes in a puerto rican elfin cloud forest. *Agricultural and Forest Meteorology*, 139(3):288–306. 3.2.1

Fayer, M., Gee, G., Rockhold, M., Freshley, M., and Walters, T. (1996). Estimating recharge rates for a groundwater model using a gis. *Journal of Environmental Quality*, 25(3):510–518. 1.1.2

Feddes, R. A., Kowalik, P. J., and Zaradny, H. (1978). *Simulation of field water use and crop yield*. Centre for Agricultural Pub. and Documentation, Wageningen. 2.4.2.2, 2.4.2.2

Fernandopullé, D. (1976). Climatic characteristics of the canary islands. In Kunkel, G., editor, *Biogeography and Ecology in the Canary Islands*, volume 30 of *Monographiae Biologicae*, pages 185–206. Springer Netherlands. 1.1.2

Finch, J. (1998). Estimating direct groundwater recharge using a simple water balance model - sensitivity to land surface parameters. *Journal of Hydrology*, 211:112–125. 2.4.1

Fontes, J., Gonçalves, M., and Pereira, L. (2004). Andosols of Terceira, Azores: measurement and significance of soil hydraulic properties. *CATENA*, 56(1-3):145–154. 2.4.4.2

Forrer, I., Kasteel, R., Flury, M., and Flühler, H. (1999). Longitudinal and lateral dispersion in an unsaturated field soil. *Water resources research*, 35(10):3049–3060. 1.1.2

Fowler, C. M. R. (1990). *The solid earth: an introduction to global geophysics*. Cambridge University Press. 1.1.1

Frumau, K., Bruijnzeel, L., Tobón, C., et al. (2006). Hydrological measurement protocol for montane cloud forests. annex 2, final technical report on dfid-frp project no. r7991. 2.4.4.1, 3.2.5.3

Gabriel, G. and Jauze, L. (2008). Fog water interception by sophora denudata trees in a reunion upper-montane forest, indian ocean. *Atmospheric Research*, 87(3):338–351. 3.2.1

Gandolfi, C., Facchi, A., and Maggi, D. (2006). Comparison of 1D models of water flow in unsaturated soils. *Environmental Modelling & Software*, 21(12):1759–1764. 1.1.2, 2.4.1, 2.4.2.2

García-Romero, E., Vegas, J., Baldonedo, J., and Marfil, R. (2005). Clay minerals as alteration products in basaltic volcaniclastic deposits of la palma (canary islands, spain). *Sedimentary Geology*, 174(3–4):237 – 253. 5.1.2.2

García-Santos, G., Bruijnzeel, L., and Dolman, A. (2009). Modelling canopy conductance under wet and dry conditions in a subtropical cloud forest. *Agricultural and Forest Meteorology*, 149(10):1565–1572. 3.1.2.3

García-Santos, G. and Bruijnzeel, L. A. (2011). Rainfall, fog and throughfall dynamics in a subtropical ridge top cloud forest, National Park of Garajonay (La Gomera, Canary Islands, Spain): HYDROMETEOROLOGY OF TROPICAL MONTANE CLOUD FORESTS. *Hydrological Processes*, 25(3):411–417. 1.1.2

Gash, J. (1979). An analytical model of rainfall interception by forests. *Quarterly Journal of the Royal Meteorological Society*, 105(443):43–55. 2.4.1, 3.2.1

Gash, J. and Morton, A. (1978). An application of the rutter model to the estimation of the interception loss from thetford forest. *Journal of Hydrology*, 38(1):49–58. 2.4.2.1, 2.4.2.1, 3.2.3.2

Gavin, H. and Agnew, C. (2000). Estimating evaporation and surface resistance from a wet grassland. *Physics and Chemistry of the Earth, Part B: Hydrology, Oceans and Atmosphere*, 25(7-8):599–603. 2.4.4.2

Geist, D., Naumann, T., and Larson, P. (1998). Evolution of galápagos magmas: Mantle and crustal fractionation without assimilation. *Journal of Petrology*, 39(5):953–971. 1.2.1

Geist, D. J., McBIRNEY, A. R., and Duncan, R. A. (1986). Geology and petrogenesis of lavas from san cristobal island, galapagos archipelago. *Geological Society of America Bulletin*, 97(5):555. 1, 1.2.1, 2.1.1, 5.2.3, 6.1

Giambelluca, T. (1986). Land-use effects on the water balance of a tropical island. *National Geographic Research (USA)*. 3.4.1

Giambelluca, T. and Nullet, D. (1991). Influence of the trade-wind inversion on the climate of a leeward mountain slope in Hawaii. *Climate Research*, 1(3):207–216. 1.1.2

Giambelluca, T. W., DeLay, J. K., Nullet, M. A., Scholl, M. A., and Gingerich, S. B. (2011). Canopy water balance of windward and leeward Hawaiian cloud forests on Haleakalā, Maui, Hawai'i: CANOPY WATER BALANCE OF HAWAIIAN CLOUD FORESTS ON HALEAKALĀ. *Hydrological Processes*, 25(3):438–447. 1.1.2, 3.1.2.1, 3.2.5.2

Gingerich, S. B. and Voss, C. I. (2005). Three-dimensional variable-density flow simulation of a coastal aquifer in southern oahu, hawaii, usa. *Hydrogeology Journal*, 13(2):436–450. 1.1.3.1, 1.1.3.2, 1.1.3.3

Gislason, S. R., Veblen, D. R., and Livi, K. J. (1993). Experimental meteoric water-basalt interactions: Characterization and interpretation of alteration products. *Geochimica et Cosmochimica Acta*, 57(7):1459–1471. 4.1.1.1

Goblet, P. (1981). *Modélisation des transferts de masse et d'énergie en aquifère*. Ecole nationale superieure des mines de Paris. 6.2.1.1

Gómez-Ortiz, D., Martín-Velázquez, S., Martín-Crespo, T., Márquez, A., Lillo, J., López, I., Carreño, F., Martín-González, F., Herrera, R., and De Pablo, M. (2007). Joint application of ground penetrating radar and electrical resistivity imaging to investigate volcanic materials and structures in tenerife (canary islands, spain). *Journal of applied geophysics*, 62(3):287–300. 1.1.3.3

Gomez-Peralta, D., Oberbauer, S. F., McClain, M. E., and Philippi, T. E. (2008). Rainfall and cloud-water interception in tropical montane forests in the eastern

andes of central peru. *Forest Ecology and Management*, 255(3–4):1315 – 1325. 3.2.1

González, A. (2013). *Cálculo del balance hídrico a nivel del suelo en la zona agrícola de la cuenca Pelikanbay en la Isla Santa Cruz-Galápagos, Ecuador*. Master, Escuela Politécnica Nacional, Facultad de Ingeniería Civil y Ambiental, Quito, Ecuador. 1.3

Goode, D. J. (1996). Direct simulation of groundwater age. *Water Resources Research*, 32(2):289–296. 6.2.1.2

Grant, P. R. and Boag, P. T. (1980). Rainfall on the galápagos and the demography of darwin's finches. *The Auk*, 97(2):pp. 227–244. 1.2.2, 1.2.6.1, 2.4.3.1, 3.2.2.1

Gray, D. M. (1961). Interrelationships of watershed characteristics. *Journal of Geophysical Research*, 66(4):1215–1223. 4.2.3

Grelle, G. and Guadagno, F. M. (2009). Seismic refraction methodology for groundwater level determination: "Water seismic index". *Journal of Applied Geophysics*, 68(3):301–320. 5.2.1

Gueguen, Y. and Palciauskas, V. (1992). *Introduction à la physique des roches*. Hermann. 5.3.1, 5.3.3.2

Guevara-Escobar, A., Gonzalez-Sosa, E., Ramos-Salinas, M., and Hernandez-Delgado, G. D. (2007). Experimental analysis of drainage and water storage of litter layers. *Hydrology and Earth System Sciences*, 11(5):1703–1716. 2.4.4.2

Gunn, R. and Kinzer, G. D. (1949). THE TERMINAL VELOCITY OF FALL FOR WATER DROPLETS IN STAGNANT AIR. *Journal of Meteorology*, 6(4):243–248. 3.2.3.3.1

Hamamoto, S., Tokida, T., Miyazaki, T., and Mizoguchi, M. (2008). Dense gas flow in volcanic ash soil: Effect of pore structure on density-driven flow. *Soil Science Society of America Journal*, 72(2):480. 2.4.4.2

Hamann, O. (1984). Changes and threats to the vegetation. *KEY ENVIRON. SER.*, pages 115–131. 1.2.3, 1.2.6.1, 2.4.3.1

Hamilton, L. S., Juvik, J. O., and Scatena, F. N. (1995). The puerto rico tropical cloud forest symposium: introduction and workshop synthesis. In *Tropical montane cloud forests*, pages 1–18. Springer. 3.2.1

Harlan, D., Wangsadipura, M., and Munajat, C. M. (2010). Rainfall–runoff modeling of citarum hulu river basin by using gr4j. In *Proc. World Congress on Engineering 2010*, pages 1607–1611. 4.3.1.2

Healy, R. W. and Cook, P. G. (2002). Using groundwater levels to estimate recharge. *Hydrogeology journal*, 10(1):91–109. 1.1.2

Heilweil, V. M., Solomon, D. K., Gingerich, S. B., and Verstraeten, I. M. (2009). Oxygen, hydrogen, and helium isotopes for investigating groundwater systems of the cape verde islands, west africa. *Hydrogeology journal*, 17(5):1157–1174. 1.1.3.2, 1.1.3.3, 2.1.1.2

Hendriks, M. (2010). *Introduction to Physical Hydrology*. OUP Oxford. 2.4.2.2

Henyey, F. S. and Pomphrey, N. (1982). Self-consistent elastic moduli of a cracked solid. *Geophys. Res. Lett*, 9(8):903–906. 5.3.3.1

Herrada, M. A., Gutiérrez, A., and Montanero, J. M. (2014). Modeling infiltration rates in a saturated/unsaturated soil under the free draining condition. *Journal of Hydrology*. 1.1.2, 2.4.1, 2.4.2.2, 2.4.2.2, A 3.5, A 3.5

Herrera, C. and Custodio, E. (2008). Conceptual hydrogeological model of volcanic Easter Island (Chile) after chemical and isotopic surveys. *Hydrogeology Journal*, 16(7):1329–1348. 1.1.3.2, 1.1.3.3

Herwitz, S. R. (1985). Interception storage capacities of tropical rainforest canopy trees. *Journal of Hydrology*, 77(1-4):237–252. 3.2.5.1

Herwitz, S. R. and Slye, R. E. (1995). Three-dimensional modeling of canopy tree interception of wind-driven rainfall. *Journal of Hydrology*, 168(1-4):205–226. 3.2.3.3.1

Hey, R., Johnson, G. L., and Lowrie, A. (1977). Recent plate motions in the galapagos area. *Geological Society of America Bulletin*, 88(10):1385. 1.2.1

Hibbert, A. R. (1969). Water yield changes after converting a forested catchment to grass. *Water Resources Research*, 5(3):634–640. 2.4.1

Holder, C. D. (2004). Rainfall interception and fog precipitation in a tropical montane cloud forest of guatemala. *Forest Ecology and Management*, 190(2):373–384. 3.2.1

Holwerda, F., Bruijnzeel, L., Muñoz-Villers, L., Equihua, M., and Asbjornsen, H. (2010). Rainfall and cloud water interception in mature and secondary

lower montane cloud forests of central Veracruz, Mexico. *Journal of Hydrology*, 384(1-2):84–96. 2.4.4.1, 3.1.2.1, 3.2.1, 3.2.3.1, 3.2.3.2, 3.2.5.1, 3.2.5.2, 3.2.5.3

Holwerda, F., Bruijnzeel, L., Oord, A., and Scatena, F. (2011). 29 fog interception in a puerto rican elfin cloud forest: a wet-canopy water budget approach a 5—. *Tropical Montane Cloud Forests: Science for Conservation and Management*, page 282. 3.2.1, 3.2.5.3

Holwerda, F., Bruijnzeel, L., Scatena, F., Vugts, H., and Meesters, A. (2012). Wet canopy evaporation from a Puerto Rican lower montane rain forest: The importance of realistically estimated aerodynamic conductance. *Journal of Hydrology*, 414-415:1–15. 2.4.4.1

Holwerda, F., Burkard, R., Eugster, W., Scatena, F. N., Meesters, A. G. C. A., and Bruijnzeel, L. A. (2006). Estimating fog deposition at a puerto rican elfin cloud forest site: comparison of the water budget and eddy covariance methods. *Hydrological Processes*, 20(13):2669–2692. 2.3.2.2, 3.1.2.1, 3.2.1, 3.2.3.3.1, 3.2.3.3.1, 3.2.3.3.1, 3.2.5.2

Hudson, R. and Fraser, J. (2005). Introduction to salt dilution gauging for streamflow measurement part IV: The mass balance (or dry injection) method. *Streamline Watershed Management Bulletin*, 9(1):6–12. 2.3.2.4, 4.1.1

Hutley, L. B., Doley, D., Yates, D. J., and Boonsaner, A. (1997). Water Balance of an Australian Subtropical Rainforest at Altitude: the Ecological and Physiological Significance of Intercepted Cloud and Fog. *Australian Journal of Botany*, 45(2):311. 3.1.2.1, 3.2.5.2

IGM (2014). DEMs and ortophotos from the galápagos islands. Technical report, MAGAP. (document), 2, 2.2.1, 2.3, 2.4, 2.5, 2.6, 2.7, 2.9, 2.11, 2.15, 2.19, 3.7, 3.4.1, 5.2, 5.3, 5.4, 5.5, 5.14

INEC (2010). Resultados del censo 2010 de población y vivienda en el ecuador. Technical report, Instituto Nacional de Estadísticas y Censos, Quito, Ecuador. 1.2.1

Ingala, Pronareg, a. O. (1989). Ingala, Pronareg, and Orstom, Inventario cartografico de los resurcos naturales, geomorfología, vegetación, ecológicos, y biofísicos de las islas Galápagos, Ecuador. Technical report. 1.2.6.1

Ingraham, N. L. and Matthews, R. A. (1988). Fog drip as a source of groundwater recharge in northern kenya. *Water Resources Research*, 24(8):1406–1410. 3.2.1

Itow, S. (2003). Zonation pattern, succession process and invasion by aliens in species-poor insular vegetation of the galapagos islands. *Global Environmental Research*, 7(1):39–58. 1.2.3

Iyer, H. and Hirahara, K. (1993). *Seismic Tomography: Theory and practice*. Springer Netherlands. 5.2.1

Izquierdo, T. (2014). Conceptual hydrogeological model and aquifer system classification of a small volcanic island (la gomera; canary islands). *Catena*, 114:119–128. 1.1.1, 1.1.3.3

Izquierdo, T., Márquez, A., and Herrera, R. (2010). El cálculo de la recarga como primer paso para una gestión sostenible de los recursos hídricos subterráneos de un sistema acuífero volcánico. El caso de La Gomera. Technical report, CONAMA10, Madrid. 3.4.1

Izuka, S. K. and Gingerich, S. B. (2003). A thick lens of fresh groundwater in the southern lihue basin, kauai, hawaii, usa. *Hydrogeology Journal*, 11(2):240–248. 1.1.3.2

Izuka, S. K., Oki, D. S., and Engott, J. A. (2010). Simple method for estimating groundwater recharge on tropical islands. *Journal of Hydrology*, 387(1-2):81–89. 1.1.2, 3.4.1

Jackson, M. H. (1993). *Galápagos, a natural history*. University of Calgary press. 1.2.4

Jackson, T. J. (2002). Remote sensing of soil moisture: implications for groundwater recharge. *Hydrogeology journal*, 10(1):40–51. 1.1.2

Jäger, H., Kowarik, I., and Tye, A. (2009). Destruction without extinction: long-term impacts of an invasive tree species on galápagos highland vegetation. *Journal of Ecology*, 97(6):1252–1263. 1.2.3

Johnson, A. G. (2012). A water-budget model and estimates of groundwater recharge for guam. *US Geol Surv Sci Invest Rep*, 5028. 2.4.1, 3.1.2.3

Join, J.-L., Coudray, J., and Longworth, K. (1997). Using principal components analysis and na/cl ratios to trace groundwater circulation in a volcanic island: the example of reunion. *Journal of Hydrology*, 190(1):1–18. 1.1.3.2, 1.1.3.3

Join, J.-L., Folio, J.-L., and Robineau, B. (2005). Aquifers and groundwater within active shield volcanoes. Evolution of conceptual models in the Piton de la Fournaise volcano. *Journal of Volcanology and Geothermal Research*, 147(1-2):187–201. 1.1, 5.3.3.3

Keim, R., Skaugset, A., and Weiler, M. (2005). Temporal persistence of spatial patterns in throughfall. *Journal of Hydrology*, 314(1-4):263–274. 3.2.3.1

Kelliher, F., Leuning, R., Raupach, M., and Schulze, E.-D. (1995). Maximum conductances for evaporation from global vegetation types. *Agricultural and Forest Meteorology*, 73(1-2):1–16. 2.4.4.2, 2.4.4.3

Kelliher, F. M., Leuning, R., and Schulze, E. D. (1993). Evaporation and canopy characteristics of coniferous forests and grasslands. *Oecologia*, 95(2):153–163. 2.4.1, 2.4.2.1, 2.4.4.3, 3.2.3.2

Khalil, M. H. and Hanafy, S. M. (2008). Engineering applications of seismic refraction method: A field example at Wadi Wardan, Northeast Gulf of Suez, Sinai, Egypt. *Journal of Applied Geophysics*, 65(3-4):132–141. 5.2.1

Kitching, R., Shearer, T., and Shedlock, S. (1977). Recharge to bunter sandstone determined from lysimeters. *Journal of Hydrology*, 33(3):217–232. 1.1.2

Klemeš, V. (1986). Operational testing of hydrological simulation models. *Hydrological Sciences Journal*, 31(1):13–24. 4.3.2

Klinge, R., Schmidt, J., and Fölster, H. (2001). Simulation of water drainage of a rain forest and forest conversion plots using a soil water model. *Journal of Hydrology*, 246(1-4):82–95. 2.4.1

Körner, C. (1995). Leaf diffusive conductances in the major vegetation types of the globe. In Schulze, E.-D. and Caldwell, M., editors, *Ecophysiology of Photosynthesis*, volume 100 of *Springer Study Edition*, pages 463–490. Springer Berlin Heidelberg. 2.4.4.2

Kozak, J. A., Ahuja, L. R., Green, T. R., and Ma, L. (2007). Modelling crop canopy and residue rainfall interception effects on soil hydrological components for semi-arid agriculture. *Hydrological Processes*, 21(2):229–241. 2.4.1

Kozlowski, T. T. (1983). *Additional Woody Crop Plants V7*. Elsevier Science, New York. 2.4.1

Krivochieva, S. and Chouteau, M. (2003). Integrating {TDEM} and {MT} methods for characterization and delineation of the santa catarina aquifer (chalco sub-basin, mexico). *Journal of Applied Geophysics*, 52(1):23 – 43. 5.1.2.2, 5.1.3.2

Langensiepen, M., Fuchs, M., Bergamaschi, H., Moreshet, S., Cohen, Y., Wolff, P., Jutzi, S. C., Cohen, S., Rosa, L. M. G., Li, Y., and Fricke, T. (2009).

Quantifying the uncertainties of transpiration calculations with the penman–monteith equation under different climate and optimum water supply conditions. *Agricultural and Forest Meteorology*, 149(6-7):1063–1072. 3.1.2.3

Lankston, R. W. (1989). The seismic refraction method: A viable tool for mapping shallow targets into the 1990s. *Geophysics*, 54(12):1535–1542. 5.2.1

Larsson, S. (1981). Influence of intercepted water on transpiration and evaporation of salix. *Agricultural Meteorology*, 23:331–338. 2.4.1

Laruelle, J. (1967). Galápagos. *Natuurwet Tijdschr*, page 236. 2.1.1

Laws, J. O. and Parsons, D. A. (1943). The relation of raindrop-size to intensity. *Transactions, American Geophysical Union*, 24(2):452. 3.2.3.3.1

Le Moine, N. (2008). *Le bassin versant de surface vu par le souterrain : une voie d'amélioration des performances et du réalisme des modèles pluie-débit ?* PhD thesis, Université Pierre et Marie Curie - Paris VI. 4.3.1.3

Le Moine, N., Andréassian, V., and Mathevet, T. (2008). Confronting surface- and groundwater balances on the La Rochefoucauld-Touvre karstic system (Charente, France): CLOSING THE CATCHMENT-SCALE WATER BALANCE-A CASE STUDY. *Water Resources Research*, 44(3):n/a–n/a. 4.3.1.2

Le Moine, N., Andréassian, V., Perrin, C., and Michel, C. (2007). How can rainfall-runoff models handle intercatchment groundwater flows? Theoretical study based on 1040 French catchments: DEALING WITH IGF IN RAINFALL-RUNOFF MODE. *Water Resources Research*, 43(6):n/a–n/a. 4.3.1.2, 4.3.1.2, 4.3.1.2, 4.3.1.3, 4.3.2, 4.3.5

Le Ravalec, M. and Guéguen, Y. (1996). High-and low-frequency elastic moduli for a saturated porous/cracked rock-differential self-consistent and poroelastic theories. *Geophysics*, 61(4):1080–1094. 5.3.3.1

Lee, C.-H., Chen, W.-P., and Lee, R.-H. (2006). Estimation of groundwater recharge using water balance coupled with base-flow-record estimation and stable-base-flow analysis. *Environmental Geology*, 51(1):73–82. 3.4.1

Lénat, J.-F., Fitterman, D., Jackson, D. B., and Labazuy, P. (2000). Geoelectrical structure of the central zone of piton de la fournaise volcano (réunion). *Bulletin of volcanology*, 62(2):75–89. 1.1.3.3

Levine, J. and Salvucci, G. (1999). Equilibrium analysis of groundwater–vadose zone interactions and the resulting spatial distribution of hydrologic fluxes across a canadian prairie. *Water Resources Research*, 35(5):1369–1383. 3.4.1

Lienert, B. R. (1991). An electromagnetic study of maui's last active volcano. *Geophysics*, 56(7):972–982. 1.1.3.3, 5.1.3.2

Limousin, J.-M., Rambal, S., Ourcival, J.-M., and Joffre, R. (2008). Modelling rainfall interception in a mediterranean Quercus ilex ecosystem: Lesson from a throughfall exclusion experiment. *Journal of Hydrology*, 357(1-2):57–66. 2.4.4.1

Link, T. E., Unsworth, M., and Marks, D. (2004). The dynamics of rainfall interception by a seasonal temperate rainforest. *Agricultural and Forest Meteorology*, 124(3-4):171–191. 3.2.3.3.2

Liu, J. (2011). Investigación de la calidad bacteorológica del agua y de las enfermedades relacionadas al agua en la isla Santa Cruz-Galápagos. Technical, Fundación Charles Darwin and Fullbright, Ecuador. 1.2.5

Liu, S. (1997). A new model for the prediction of rainfall interception in forest canopies. *Ecological Modelling*, 99(2):151–159. 2.4.1, 3.2.1

Liu, S. (2001). Evaluation of the liu model for predicting rainfall interception in forests world-wide. *Hydrological Processes*, 15(12):2341–2360. 2.4.2.1

Liu, Y., Pereira, L., and Fernando, R. (2006). Fluxes through the bottom boundary of the root zone in silty soils: parametric approaches to estimate groundwater contribution and percolation. *Agricultural Water Management*, 84(1):27–40. 1.1.2

Lloyd, C., Gash, J., Shuttleworth, W., and de O. Marques F, A. (1988). The measurement and modelling of rainfall interception by Amazonian rain forest. *Agricultural and Forest Meteorology*, 43(3-4):277–294. 3.2.5.1

Loaiza, S. (2012). *Étude des proprietés physiques et du comportement mécanique des basalts*. PhD thesis, Université Paris-Est, Paris. 5.2, 5.3.2, 5.3.2, 5.4

Loescher, H., Gholz, H., Jacobs, J., and Oberbauer, S. (2005). Energy dynamics and modeled evapotranspiration from a wet tropical forest in costa rica. *Journal of Hydrology*, 315(1-4):274–294. 3.1.2.3

Ludescher, J., Gozolchiani, A., Bogachev, M. I., Bunde, A., Havlin, S., and Schellnhuber, H. J. (2014). Very early warning of next el niño. *Proceedings of the National Academy of Sciences*, 111(6):2064–2066. 3.1.1

Lyne, V. and Hollick, M. (1979). Stochastic time-variable rainfall-runoff modelling. In *Institute of Engineers Australia National Conference*, volume 79, pages 89–93. 4.2.1

Macdonald, G. A., Abbott, A. T., and Peterson, F. L. (1983). *Volcanoes in the sea: the geology of Hawaii*. University of Hawaii Press. 1, 1.1.1, 1.1.3.2, 1.2.6.2, 2.1.1.2

Malik, H. U. (1990). *Characterization and mineralogical interpretation of shrink-swell behavior of Hawaiian kaolinitic Vertisols*. PhD thesis. 3.3.1.2

Manda, A. K., Mabee, S. B., Boutt, D. F., and Cooke, M. L. (2013). A method of estimating bulk potential permeability in fractured-rock aquifers using field-derived fracture data and type curves. *Hydrogeology Journal*, 21(2):357–369. 1.1.1

Mannaerts, C. and Gabriels, D. (2000). Rainfall erosivity in cape verde. *Soil and Tillage Research*, 55(3–4):207 – 212. 1.1.2

Marshak, S. and Repcheck, J. (2004). *Essentials of geology*. WW Norton. 1.1.1

McJannet, D., Wallace, J., and Reddell, P. (2007). Precipitation interception in Australian tropical rainforests: II. Altitudinal gradients of cloud interception, stemflow, throughfall and interception. *Hydrological Processes*, 21(13):1703–1718. 3.1.2.1, 3.2.1, 3.2.5.2

Min, Q., Su, J., Zhang, R., and Rong, X. (2015). What hindered the el niño pattern in 2014? *Geophysical Research Letters*, 42(16):6762–6770. 2015GL064899. 3.1.1

Monteith, J.L. (1965). Evaporation and the enviroment. symposium of the society for experimental biology, the state and movement of water in living organisms. *Acedemic Press, Inc., NY*, 19:205–234. 2.4.2.1, 3.2.3.2

Moon, S.-K., Woo, N. C., and Lee, K. S. (2004). Statistical analysis of hydrographs and water-table fluctuation to estimate groundwater recharge. *Journal of Hydrology*, 292(1):198–209. 1.1.2

Moore, R. (2005). Introduction to salt dilution gauging for streamflow measurement part III: Slug injection using salt in solution. *Streamline Watershed Management Bulletin*, 8(2):1–6. 2.3.2.4, 4.1.1

Morel-Seytoux, H. J., Meyer, P. D., Nachabe, M., Tourna, J., Genuchten, M. v., and Lenhard, R. J. (1996). Parameter equivalence for the brooks-corey and van

genuchten soil characteristics: Preserving the effective capillary drive. *Water Resources Research*, 32(5):1251–1258. 6.4.2

Moukandi-N, D., Nganga, D., Mabiala, B., Thaty, C., and Deleport, P. (2011). Parameterization of the hydric transfer models in three eucalyptus plantations in congo. *Journal of Environmental Science and Technology*, 4(3):340–353. 2.4.1

Mueller, S., Scheu, B., Kueppers, U., Spieler, O., Richard, D., and Dingwell, D. B. (2011). The porosity of pyroclasts as an indicator of volcanic explosivity. *Journal of Volcanology and Geothermal Research*, 203(3–4):168 – 174. 5.3.2

Murakami, S. (2007). Application of three canopy interception models to a young stand of Japanese cypress and interpretation in terms of interception mechanism. *Journal of Hydrology*, 342(3-4):305–319. 2.4.4.1, 3.2.5.3

Muzylo, A., Llorens, P., Valente, F., Keizer, J., Domingo, F., and Gash, J. (2009). A review of rainfall interception modelling. *Journal of Hydrology*, 370(1-4):191–206. 2.4.1, 2.4.2.1, 3.2.3.2

Müller, M., Hördt, A., and Neubauer, F. M. (2002). Internal structure of mount merapi, indonesia, derived from long-offset transient electromagnetic data. *Journal of Geophysical Research: Solid Earth*, 107(B9):ECV 2–1–ECV 2–14. 2187. 5.1.2.2, 5.1.3.2

Neris, J., Jiménez, C., Fuentes, J., Morillas, G., and Tejedor, M. (2012). Vegetation and land-use effects on soil properties and water infiltration of Andisols in Tenerife (Canary Islands, Spain). *CATENA*, 98:55–62. 2.4.4.3

Nullet, D., Juvik, J., and Wall, A. (1995). A hawaiian mountain climate cross-section. *Clim. Res*, 5(2):131–137. 1.1.2

Oudin, L., Michel, C., and Anctil, F. (2005). Which potential evapotranspiration input for a lumped rainfall-runoff model? *Journal of Hydrology*, 303(1-4):275–289. 4.3.1.2, 4.3.2, 4.3.5

Palacky, G. (1987). Clay mapping using electromagnetic methods. *First Break*, 5(8). 5.1.2.2, 5.1.3.2

Palmer, C. E. and Pyle, R. L. (1966). The climatological setting of the galápagos. *University of California Press, Berkeley and Los Angeles*, pages 93–99. 1.2.2, 1.2.6.1, 3.2.2.1

Panigrahi, B. and Panda, S. N. (2003). Field test of a soil water balance simulation model. *Agricultural Water Management*, 58(3):223–240. 1.1.2, 2.4.1

Parton, W., Lauenroth, W., and Smith, F. (1981). Water loss from a shortgrass steppe. *Agricultural Meteorology*, 24:97–109. 2.4.4.2, 3.3.1.2

Perrin, C. (2000). *Vers une amélioration d'un modèle global pluie-débit au travers d'une approche comparative*. PhD thesis, INPG. 4.3.3.1

Perrin, C., Michel, C., and Andréassian, V. (2003). Improvement of a parsimonious model for streamflow simulation. *Journal of Hydrology*, 279(1-4):275–289. 4.3.1.2, 4.3.1.2, 4.3.1.3, 4.3.2

Peterson, F. L. (1972). Water development on tropic volcanic islands—type example: Hawaiia. *Ground Water*, 10(5):18–23. 1, 1.1.3.2, 1.2.6.2, 2.1.1.2

Prada, S. (2000). *Geologia e Recursos Hídricos Subterrâneos da Ilha da Madeira. Ph.D.* Ph.D., Universidade da Madeira. 1.1.2

Prada, S., Menezes de Sequeira, M., Figueira, C., and da Silva, M. O. (2009). Fog precipitation and rainfall interception in the natural forests of Madeira Island (Portugal). *Agricultural and Forest Meteorology*, 149(6-7):1179–1187. 1.1.2, 3.2.1

Prada, S. N., Da Silva, M. O., and Cruz, J. V. (2005). Groundwater behaviour in madeira, volcanic island (portugal). *Hydrogeology Journal*, 13(5-6):800–812. 1.1.3.2, 1.1.3.3, 2.1.1.2

Pryet, A. (2011). *Hydrogéologie des milieux volcaniques insulaires: apports d'une étude intégrée aux îles Galapagos*. PhD thesis, Université Pierre et Marie Curie - Paris VI. 1.1.1, 1.1.3.1, 1.1.3.2, 1.2, 1.2.1, 1.2.5, 1.2.6.1, 1.2.6.2, 1.3, 2.1.1, 2.1.1.1, 2.2, 3.4.1, 5.1.2.2, 5.1.2.3

Pryet, A., Domínguez, C., Tomai, P. F., Chaumont, C., d'Ozouville, N., Villacís, M., and Violette, S. (2012a). Quantification of cloud water interception along the windward slope of santa cruz island, galapagos (ecuador). *Agricultural and Forest Meteorology*, 161:94–106. 1, 1.1.2, 1.2.2, 1.2.6.1, 1.3, 2.3.2.1, 2.3.2.2, 2.4.2.1, 2.4.2.3, 2.4.3.1, 2.4, 2.4.3.2, 2.4.3.3.2, 2.4.4.1, 2.4.4.2, 3.1.2.1, 3.2.1, 3.2.2.1, 3.2.2.2, 3.2, 3.2.3.1, 3.2.3.1, 3.2.3.2, 3.2.3.2, 3.2.3.2, 3.2.3.2, 3.2.3.3.2, 3.2.4.2, 3.2.5.1, 3.2.5.2, 3.2.5.3

Pryet, A., d'Ozouville, N., Violette, S., Deffontaines, B., and Auken, E. (2012b). Hydrogeological settings of a volcanic island (san cristóbal, galapagos) from joint interpretation of airborne electromagnetics and geomorphological observations. *Hydrology and Earth System Sciences*, 16(12):4571–4579. 1.1.1, 1.2.2, 1.2.6.1, 1.2.6.2, 1.3, 2.1.1.2, 3.2.2.1, 5, 5.1.1.2, 5.1.1.2, 5.1.1.3, 5.3, 5.1.2.1, 5.4, 5.5, 5.1.2.2, 5.1.2.2, 5.1.3.1, 5.1.3.2, 6.1

Pryet, A., Ramm, J., Chilès, J.-P., Auken, E., Deffontaines, B., and Violette, S. (2011). 3d resistivity gridding of large AEM datasets: A step toward enhanced geological interpretation. *Journal of Applied Geophysics*, 75(2):277–283. 1.2.6.1, 1.3, 5.1.1.1, 5.1, 5.1.1.3, 5.1.1.3, 5.1.2.1, 5.1.3.2, 6.1

Rabus, B., Eineder, M., Roth, A., and Bamler, R. (2003). The shuttle radar topography mission—a new class of digital elevation models acquired by spaceborne radar. *ISPRS Journal of Photogrammetry and Remote Sensing*, 57(4):241–262. 1.2.6.1, 2.2.1, 2.3

Ramdani, W. and Fauchet, D. (2010). Etude structurale et caracterisation du reseau de drainage sur l'ile de san cristobal. Technical report, Université Pierre et Marie Curie - Paris VI, Paris. 2.2.2

Refsgaard, J. C. (1997). Parameterisation, calibration and validation of distributed hydrological models. *Journal of Hydrology*, 198(1-4):69–97. 4.3.1.1

Reyes, M. F., Trifunović, N., Sharma, S., and Kennedy, M. (2015). Data assessment for water demand and supply balance on the island of Santa Cruz (Galápagos Islands). *Desalination and Water Treatment*, pages 1–15. 1.2.5, 1.2.6.1

Richards, L. A. (1931). Capillary conduction of liquids through porous mediums. *Physics*, 1(5):318. 2.4.1

Richardson, B. A., Richardson, M. J., Scatena, F. N., and Mcdowell, W. H. (2000). Effects of nutrient availability and other elevational changes on bromeliad populations and their invertebrate communities in a humid tropical forest in puerto rico. *Journal of Tropical Ecology*, 16:167–188. 3.2.5.1

Ritter, A., Muñoz-Carpena, R., Regalado, C., Vanclooster, M., and Lambot, S. (2004). Analysis of alternative measurement strategies for the inverse optimization of the hydraulic properties of a volcanic soil. *Journal of Hydrology*, 295(1-4):124–139. 2.4.4.4

Ritter, A., Regalado, C. M., and Aschan, G. (2008). Fog Water Collection in a Subtropical Elfin Laurel Forest of the Garajonay National Park (Canary Islands): A Combined Approach Using Artificial Fog Catchers and a Physically Based Impaction Model. *Journal of Hydrometeorology*, 9(5):920–935. 1.1.2, 3.2.1, 3.2.5.2

Rushton, K., Eilers, V., and Carter, R. (2006). Improved soil moisture balance methodology for recharge estimation. *Journal of Hydrology*, 318(1-4):379–399. 1.1.2, 2.4.1, 2.4.2.2

Rutter, A., Kershaw, K., Robins, P., and Morton, A. (1971). A predictive model of rainfall interception in forests, 1. derivation of the model from observations in a plantation of corsican pine. *Agricultural Meteorology*, 9:367–384. 2.4.2.1, 2.4.2.1, 3.2.3.2

Rutter, A. J., Morton, A. J., and Robins, P. C. (1975). A predictive model of rainfall interception in forests. II. generalization of the model and comparison with observations in some coniferous and hardwood stands. *The Journal of Applied Ecology*, 12(1):367. 2.4.1, 2.4.2.1, 2.4.2.1, 2.4.2.1, 3.2.1, 3.2.3.2, 3.2.3.2

Saito, T., Matsuda, H., Komatsu, M., Xiang, Y., Takahashi, A., Shinohara, Y., and Otsuki, K. (2013). Forest canopy interception loss exceeds wet canopy evaporation in Japanese cypress (Hinoki) and Japanese cedar (Sugi) plantations. *Journal of Hydrology*, 507:287–299. 2.4.4.1

Santamarta, J. C., Lario-Bascones, R. J., Rodríguez-Martín, J., Hernández-Gutiérrez, L. E., and Poncela, R. (2014). Introduction to hydrology of volcanic islands. *IERI Procedia*, 9:135–140. 1.1.3.1

Saraf, A. and Choudhury, P. (1998). Integrated remote sensing and gis for groundwater exploration and identification of artificial recharge sites. *International journal of Remote sensing*, 19(10):1825–1841. 1.1.2

Scanlon, B. R. and Cook, P. G. (2002). Theme issue on groundwater recharge. *Hydrogeology Journal*, 10(1):3–4. 1.1.2

Scanlon, B. R., Healy, R. W., and Cook, P. G. (2002). Choosing appropriate techniques for quantifying groundwater recharge. *Hydrogeology Journal*, 10(1):18–39. 1.1.2

Scatena, F. (1990). Watershed scale rainfall interception on two forested watersheds in the Luquillo Mountains of Puerto Rico. *Journal of Hydrology*, 113(1-4):89–102. 2.4.4.1, 3.2.5.3

Schellekens, J., Scatena, F., Bruijnzeel, L., and Wickel, A. (1999). Modelling rainfall interception by a lowland tropical rain forest in northeastern Puerto Rico. *Journal of Hydrology*, 225(3-4):168–184. 2.4.2.1, 2.4.2.1, 2.4.2.1, 2.4.4.1, 3.2.5.3

Sharon, D. (1980). The distribution of hydrologically effective rainfall incident on sloping ground. *Journal of Hydrology*, 46(1-2):165–188. 3.2.3.3.2, 3.4, 3.8

Shuttleworth, W. J. (1988). Evaporation from amazonian rainforest. *Proceedings of the Royal Society B: Biological Sciences*, 233(1272):321–346. 2.4.4.2

Simunek, J., Sejna, M., Saito, H., Sakai, M., and Van Genuchten, M. T. (2013). *The HYDRUS-1D software package for simulating the one-dimensional movement of water, heat, and multiple solutes in variably-saturated media*. Version 4.16. University of California Riverside, Riverside, California, department of environmental sciences edition. 2.4.1, A 3.4

Snell, H. and Rea, S. (1999). The 1997-1998 el niño in galapagos: can 34 years of data estimate 120 years of pattern? *Noticias de Galápagos*, 60:11–20. 1.2.2, 1.2.6.1

Song, Z., Shu, Q., Bao, Y., Yin, X., and Qiao, F. (2015). The prediction on the 2015/16 el niño event from the perspective of fio-esm. *Acta Oceanologica Sinica*, 34(12):67–71. 3.1.1

Sørensen, K. I. and Auken, E. (2004). Skytem–a new high-resolution helicopter transient electromagnetic system. *Exploration Geophysics*, 35(3):194–202. 5.1.1.2

Staelens, J., De Schrijver, A., Verheyen, K., and Verhoest, N. E. (2006). Spatial variability and temporal stability of throughfall water under a dominant beech (fagus sylvatica l.) tree in relationship to canopy cover. *Journal of Hydrology*, 330(3-4):651–662. 1.1.2, 2.4.4.1, 3.2.3.1

Stoops, G. (2014). Soils and paleosoils of the galápagos islands: What we know and what we don't know, a meta-analysis. *Pacific Science*, 68(1):1–17. 1.2.6.1

Taboada, T., Rodríguez-Lado, L., Ferro-Vázquez, C., Stoops, G., and Martínez Cortizas, A. (2016). Chemical weathering in the volcanic soils of Isla Santa Cruz (Galápagos Islands, Ecuador). *Geoderma*, 261:160–168. 1.2.6.1, 3.3.1.2

Takahashi, M., Giambelluca, T. W., Mudd, R. G., DeLay, J. K., Nullet, M. A., and Asner, G. P. (2011). Rainfall partitioning and cloud water interception in native forest and invaded forest in Hawai'i Volcanoes National Park: CANOPY WATER PROCESSES IN NATIVE AND INVADED CLOUD FOREST IN HAWAI'I. *Hydrological Processes*, 25(3):448–464. 3.2.5.1

Taniguchi, M. and Sharma, M. (1993). Determination of groundwater recharge using the change in soil temperature. *Journal of Hydrology*, 148(1-4):219–229. 2.4.1, 3.1.2.3

Tatiana Izquierdo, Christian Dominguez, Sophie Violette, and Marcos Villacís (2015). Volcanic island evolution and their implications for the groundwater conceptual model development in San Cristóbal (Galápagos). 6.1

Thimonier, A. (1998). Measurement of atmospheric deposition under forest canopies: Some recommendations for equipment and sampling design. *Environmental Monitoring and Assessment*, 52(3):353–387. 2.3.2.2

Thomas, D. M. and Benson, M. A. (1970). *Generalization of streamflow characteristics from drainage-basin characteristics*. US Government Printing Office Washington, DC, USA. 4.2.3

Thompson, A. (2007). Simulating the adiabatic ascent of atmospheric air parcels using the cloud chamber. *Department of Meteorology, Penn State*. 3.2.5.2

Thorburn, P. J., Cowie, B. A., and Lawrence, P. A. (1991). Effect of land development on groundwater recharge determined from non-steady chloride profiles. *Journal of Hydrology*, 124(1-2):43–58. 2.4.1

Tian, Y., Xu, Y.-P., and Zhang, X.-J. (2013). Assessment of climate change impacts on river high flows through comparative use of gr4j, hbv and xinanjiang models. *Water Resources Management*, 27(8):2871–2888. 4.3.1.2

Toksöz, M. N., Cheng, C. H., and Timur, A. (1976). Velocities of seismic waves in porous rocks. *Geophysics*, 41(4):621–645. 5.2.1

Tournebize, J., Gregoire, C., Coupe, R., and Ackerer, P. (2012). Modelling nitrate transport under row intercropping system: Vines and grass cover. *Journal of Hydrology*, 440–441:14 – 25. 3.3.2.2

Traore, V. B. (2014). Calibrating the Rainfall-Runoff Model GR4j and GR2m on the Koulountou River Basin, a Tributary of the Gambia River. *American Journal of Environmental Protection*, 3(1):36. 4.3.1.2

Trueman, M. and d'Ozouville, N. (2010). Characterizing the galapagos terrestrial climate in the face of global climate change. *Galapagos Research*, 67:26–37. 1.2.2, 1.2.6.1, 2.4.3.1, 3.2.2.1

Trueman, M., Hobbs, R. J., and Van Niel, K. (2013). Interdisciplinary historical vegetation mapping for ecological restoration in galapagos. *Landscape Ecology*, 28(3):519–532. 1.2.3, 2.4.3.1

Trueman, M., Standish, R. J., and Hobbs, R. J. (2014). Identifying management options for modified vegetation: Application of the novel ecosystems framework to a case study in the galapagos islands. *Biological Conservation*, 172:37–48. 2.4.3.1

Uehara, Y. and Kume, A. (2012). Canopy Rainfall Interception and Fog Capture by Pinus pumila Regal at Mt. Tateyama in the Northern Japan Alps, Japan. *Arctic, Antarctic, and Alpine Research*, 44(1):143–150. 3.1.2.1, 3.2.1, 3.2.5.2

UKIH, U. I. o. H. (1980). Low Flow Studies. Research Report. Research, Wallingford, Oxon. 4.2.1

Unger, A. J., Bodvarsson, G. S., and Simmons, A. M. (2004). Simulating infiltration in unsaturated basalt for the large-scale aquifer pumping and infiltration test at ineel. *Journal of Hydraulic Research*, 42(S1):105–113. 6.2.2.2, 6.2, 6.4.1, 6.4.2

Valente, F., David, J., and Gash, J. (1997). Modelling interception loss for two sparse eucalypt and pine forests in central portugal using reformulated rutter and gash analytical models. *Journal of Hydrology*, 190(1):141–162. 2.4.2.1, 2.4.2.1, 2.4.2.1, 2.4.2.1, 3.2.3.2, 3.2.3.2, 3.2.3.2

van Dijk, A. and Bruijnzeel, L. (2001). Modelling rainfall interception by vegetation of variable density using an adapted analytical model. Part 2. Model validation for a tropical upland mixed cropping system. *Journal of Hydrology*, 247(3-4):239–262. 2.4.4.1

van Dijk, A. I., Gash, J. H., van Gorsel, E., Blanken, P. D., Cescatti, A., Emmel, C., Gielen, B., Harman, I. N., Kiely, G., Merbold, L., Montagnani, L., Moors, E., Sottocornola, M., Varlagin, A., Williams, C. A., and Wohlfahrt, G. (2015). Rainfall interception and the coupled surface water and energy balance. *Agricultural and Forest Meteorology*, 214-215:402–415. 3.2.1, 3.2.5.3

Van Genuchten, M. T. (1980). A closed-form equation for predicting the hydraulic conductivity of unsaturated soils. *Soil Science Society of America Journal*, 44(5):892–898. 2.4.2.2, 2.4.3.2, 3.3.1.1, 6.2.1.1, 6.1, A 3.1, A 3.1

Villegas, J. C., Tobón, C., and Breshears, D. D. (2008). Fog interception by nonvascular epiphytes in tropical montane cloud forests: dependencies on gauge type and meteorological conditions. *Hydrological Processes*, 22(14):2484–2492. 3.2.1, 3.2.3.2, 3.2.5.1, 3.2.5.2, 3.2.5.3

Violette, S., d'Ozouville, N., Pryet, A., Deffontaines, B., Fortin, J., and Adelinet, M. (2014). Hydrogeology of the galápagos archipelago: An integrated and comparative approach between islands. In Harpp, K. S., Mittelstaedt, E., d'Ozouville, N., and Graham, D. W., editors, *Geophysical Monograph Series*, pages 167–183. John Wiley & Sons, Inc, Hoboken, New Jersey. 1.1.3.1, 1.1.3.2,

1.2.2, 1.2.6.1, 1.2.6.2, 1.3, 2.1.1, 2.1.1.1, 2.2, 2.1.1.2, 2.4.3.1, 3.2.2.1, 4.5, 5.1.2.2, 6.1

Violette, S., Ledoux, E., Goblet, P., and Carbonnel, J.-P. (1997). Hydrologic and thermal modeling of an active volcano: the piton de la fournaise, reunion. *Journal of Hydrology*, 191(1):37–63. 1.1.3.2, 1.1.3.3, 2.1.1.2, 6.1

Vittecoq, B., Deparis, J., Violette, S., Jaouën, T., and Lacquement, F. (2014). Influence of successive phases of volcanic construction and erosion on Mayotte Island's hydrogeological functioning as determined from a helicopter-borne resistivity survey correlated with borehole geological and permeability data. *Journal of Hydrology*, 509:519–538. 1.1.3.2, 1.1.3.3, 5.1.2.2, 5.1.3.1, 5.1.3.2, 5.1.3.2

Wallace, J. and McJannet, D. (2006). On interception modelling of a lowland coastal rainforest in northern Queensland, Australia. *Journal of Hydrology*, 329(3-4):477–488. 3.2.5.1

Warkentin, B. and Maeda, T. (1980). Physical and mechanical characteristics of andisols. *Soils with variable charge. New Zealand Society of Soil Science*, pages 281–302. 2.4.4.2

Warrier, R. B., Castro, M. C., and Hall, C. M. (2012). Recharge and source-water insights from the galapagos islands using noble gases and stable isotopes: RECHARGE AND SOURCE-WATER INSIGHTS FROM THE GALAPAGOS ISLANDS. *Water Resources Research*, 48(3):n/a–n/a. 1.2.6.1, 1.3, 2.1.1.2, 6.4.1

Watson, J., Trueman, M., Tufet, M., Henderson, S., and Atkinson, R. (2010). Mapping terrestrial anthropogenic degradation on the inhabited islands of the galápagos archipelago. *Oryx*, 44(01):79–82. 1.2.4

White, W. M., McBirney, A. R., and Duncan, R. A. (1993). Petrology and geochemistry of the galápagos islands: Portrait of a pathological mantle plume. *Journal of Geophysical Research*, 98(B11):19533. 1, 1.2.1

Whitehead, D. and Kelliher, F. (1991). A canopy water balance model for a pinus radiata stand before and after thinning. *Agricultural and Forest Meteorology*, 55(1-2):109–126. 2.4.2.1, 2.4.2.1, 3.2.3.2

Wilkinson, M. T., Richards, P. J., and Humphreys, G. S. (2009). Breaking ground: Pedological, geological, and ecological implications of soil bioturbation. *Earth-Science Reviews*, 97(1-4):257–272. 2.4.4.3

Williams, J. R., Nicks, A., and Arnold, J. G. (1985). Simulator for water resources in rural basins. *Journal of Hydraulic Engineering*, 111(6):970–986. 2.4.1

Xu, C.-Y. and Chen, D. (2005). Comparison of seven models for estimation of evapotranspiration and groundwater recharge using lysimeter measurement data in germany. *Hydrological processes*, 19(18):3717–3734. 1.1.2

Young, M., Wierenga, P., and Mancino, C. (1996). Large weighing lysimeters for water use and deep percolation studies. *Soil Science*, 161(8):491–501. 1.1.2

Zeng, N., Shuttleworth, J. W., and Gash, J. H. (2000). Influence of temporal variability of rainfall on interception loss. part i. point analysis. *Journal of Hydrology*, 228(3):228–241. 2.4.1, 3.2.1

Ziegler, A., Giambelluca, T., Nullet, M., Sutherland, R., Tantasarin, C., Vogler, J., and Negishi, J. (2009). Throughfall in an evergreen-dominated forest stand in northern thailand: Comparison of mobile and stationary methods. *Agricultural and Forest Meteorology*, 149(2):373–384. 1.1.2, 2.3.2.2, 2.4.4.1, 3.2.3.1

Ziegler, A. D., Negishi, J. N., Sidle, R. C., Noguchi, S., and Nik, A. R. (2006). Impacts of logging disturbance on hillslope saturated hydraulic conductivity in a tropical forest in peninsular malaysia. *CATENA*, 67(2):89–104. 2.4.1

Zimmermann, A. and Zimmermann, B. (2014). Requirements for throughfall monitoring: The roles of temporal scale and canopy complexity. *Agricultural and Forest Meteorology*, 189-190:125–139. 2.4.4.1, 3.2.3.1

Zimmermann, A., Zimmermann, B., and Elsenbeer, H. (2009). Rainfall redistribution in a tropical forest: Spatial and temporal patterns: RAINFALL REDISTRIBUTION. *Water Resources Research*, 45(11):n/a–n/a. 1.1.2, 2.4.2.3, 2.4.4.1, 3.2.3.1

Zimmermann, B., Elsenbeer, H., and De Moraes, J. M. (2006). The influence of land-use changes on soil hydraulic properties: Implications for runoff generation. *Forest Ecology and Management*, 222(1-3):29–38. 2.4.1

Zimmermann, B., Papritz, A., and Elsenbeer, H. (2010). Asymmetric response to disturbance and recovery: Changes of soil permeability under forest–pasture–forest transitions. *Geoderma*, 159(1-2):209–215. 2.4.1, 2.4.4.3, 3.1.2.3

Appendices

Appendix

A 1 Cerro Gato localization

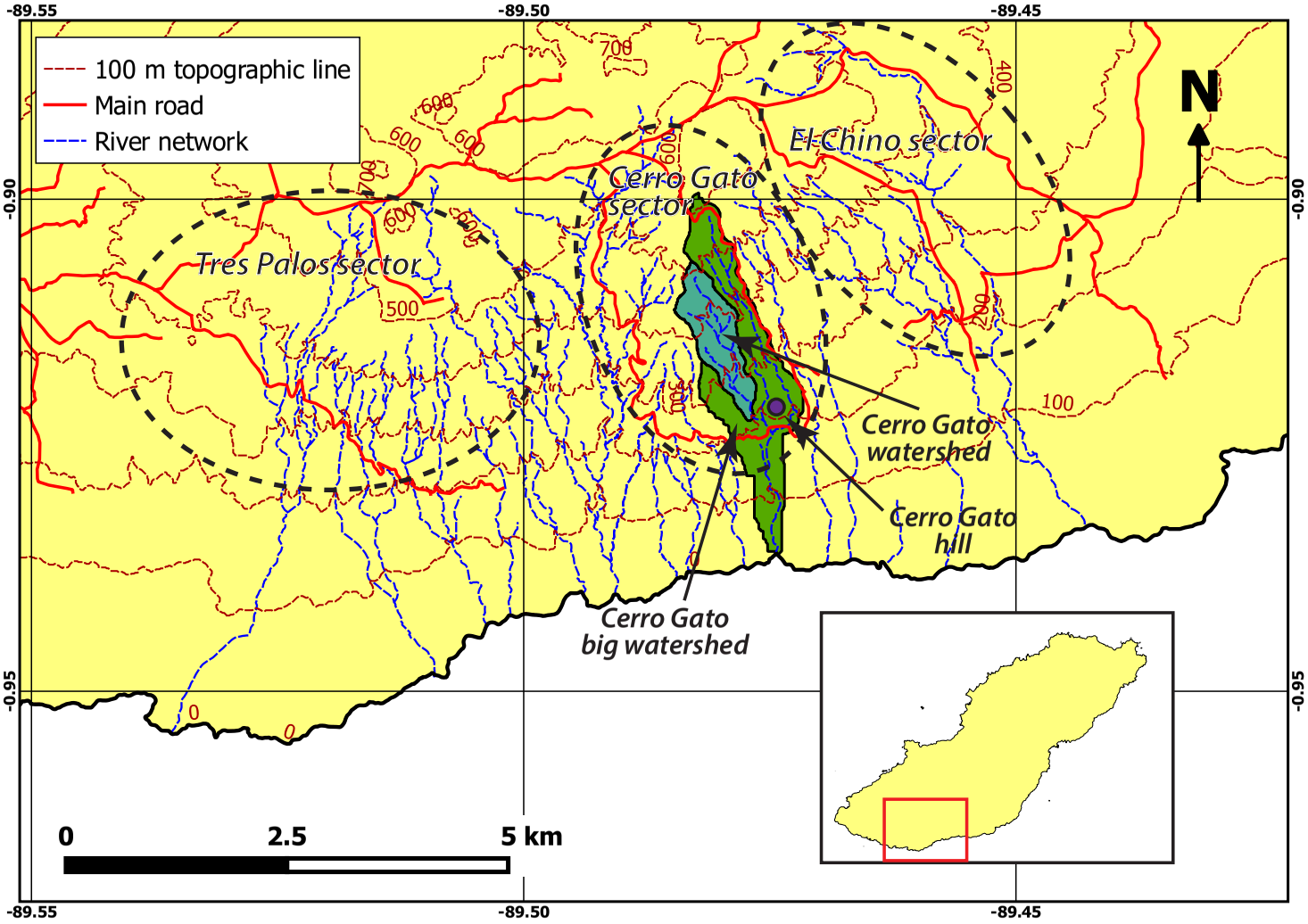

Figure A.1: Map of the localization of the different terms of *Cerro Gato*. In this thesis *Cerro Gato* is reffered to the sector, the big watershed that reaches the sea and the watershed. It is also reffered to the hill within the watershed.

A 2 Data availability

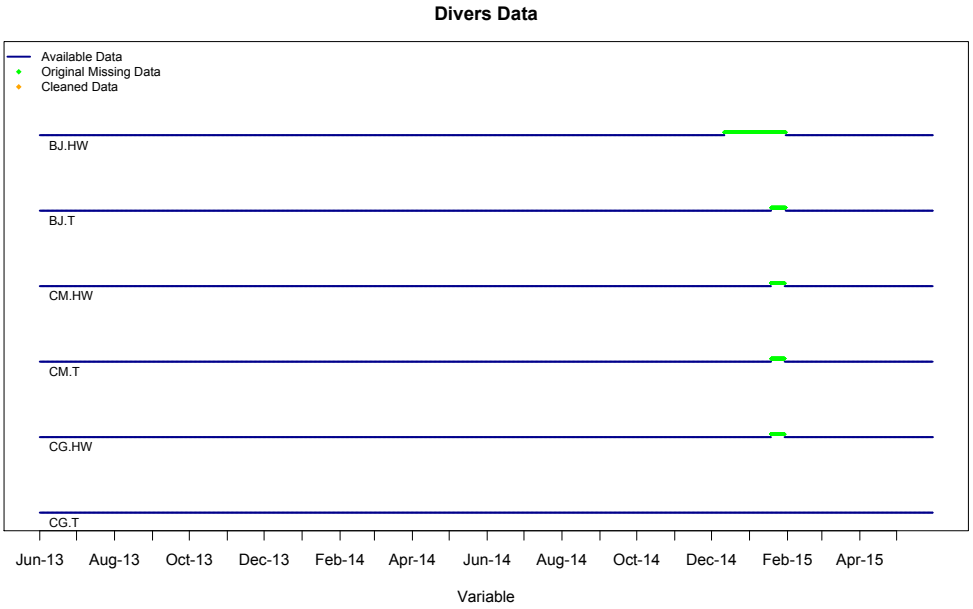

Figure A.2: Divers data availabity in the three sections of control during the period June 2013 - May 2015. *BJ* is *El Bayo*, *CM* is *Chuki Marka* and *CG* is *Cerro Gato*. *T* correspond to temperature and *HW* corespond to height of water.

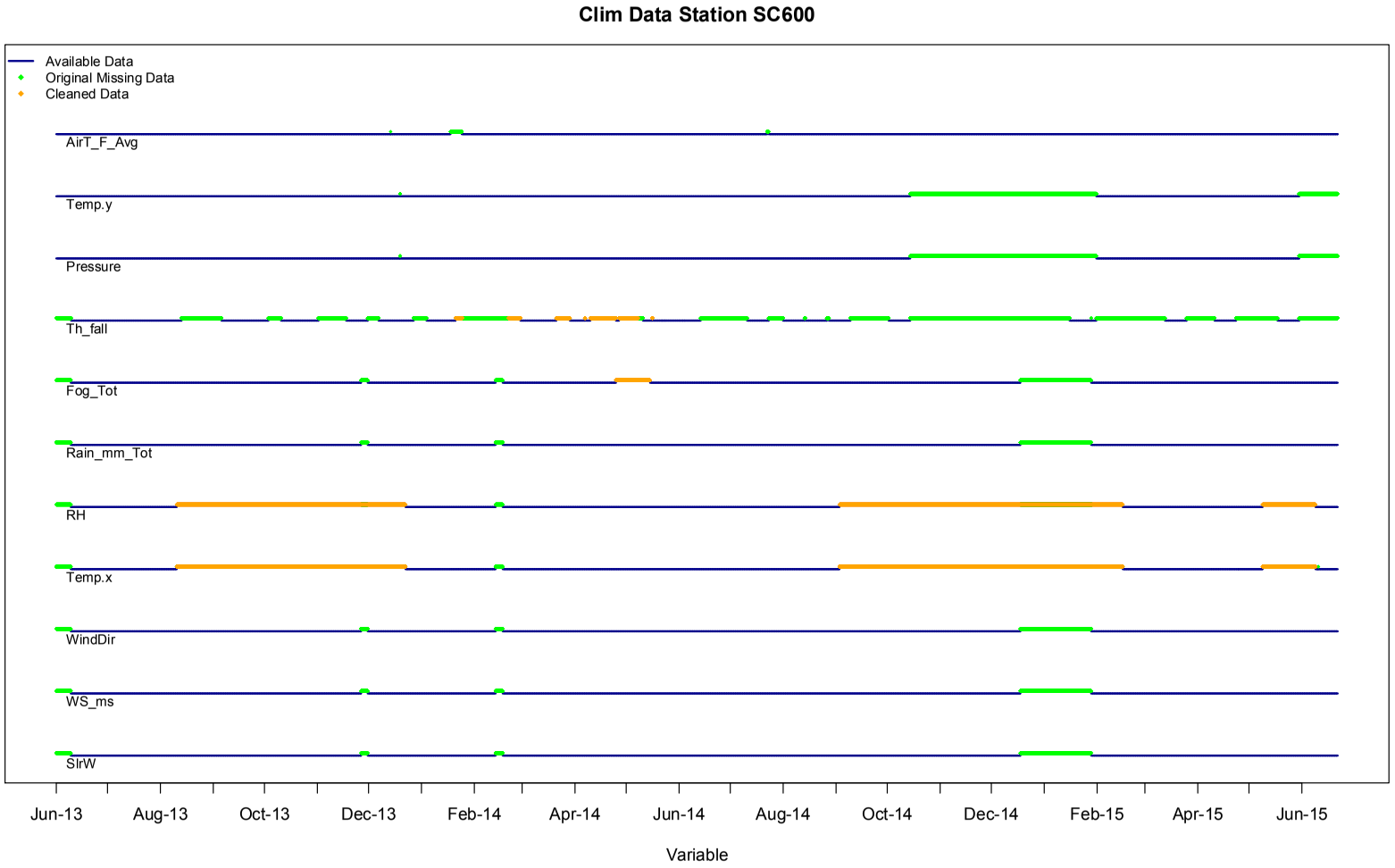

Figure A.3: Climatic data availabity in station SC600 during the period June 2013 - May 2015. *SlrW* is solar radiation. *WS ms* is wind speed. *WindDir* is wind direction. *Temp.x* is air temperature from the CS215. *RH* is relative humidity. *Rain mm Tot* is rainfall. *Fog Tot* is fog interception by the fog net. *Th fall* is throughfall. *Pressure* is air pressure from barodiver. *Temp.y* is temperature from barodiver. *AirT F Avg* is air temperature from a secondary sensor.

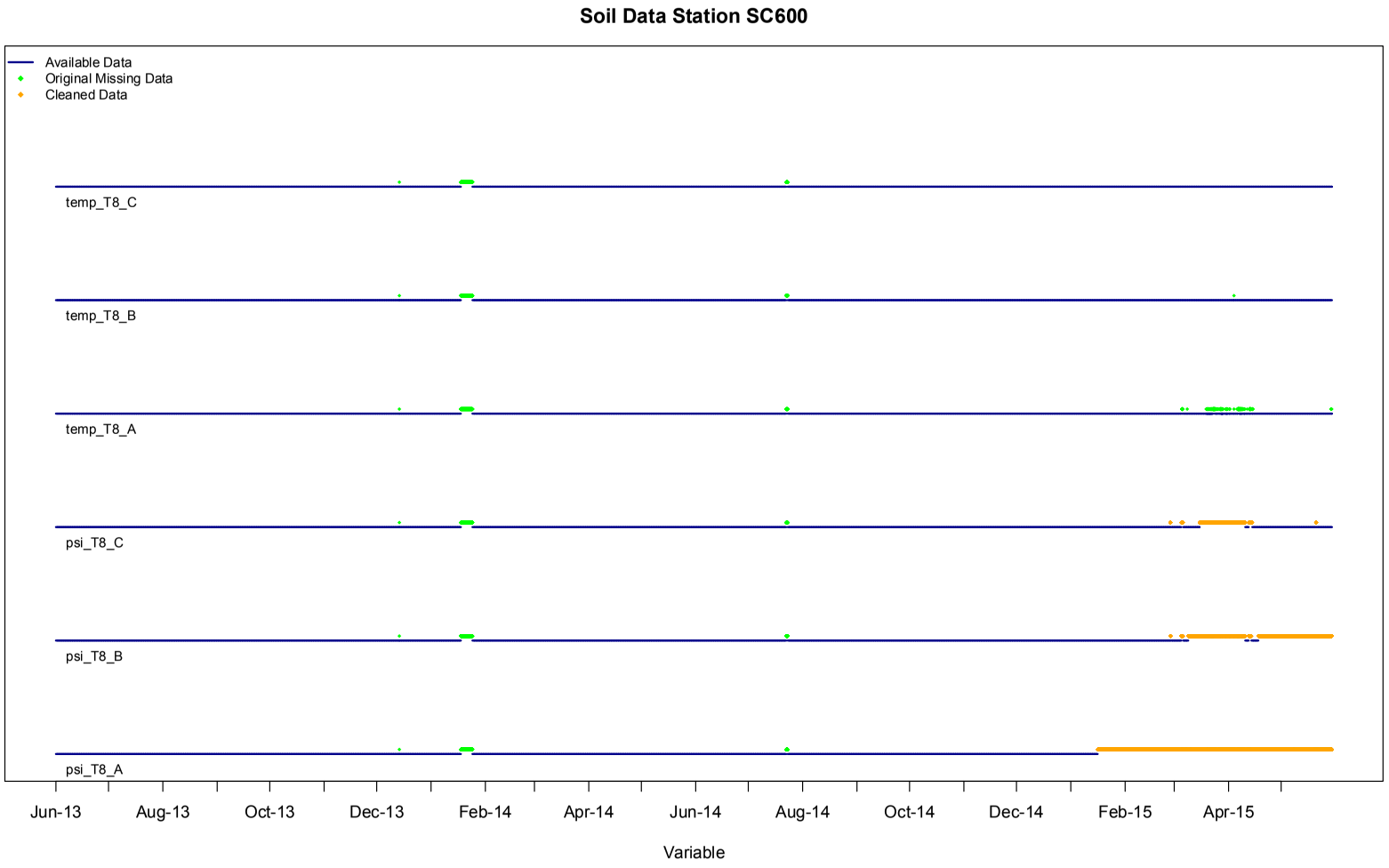

Figure A.4: Soil data availabity in station SC600 during the period June 2013 - May 2015. *psi T8 A*, *psi T8 B* and *psi T8 C* are the soil water pressure at depth: 25 cm (A), 40 cm (B) and 55 cm (C). *temp T8 A*, *temp T8 B* and *temp T8 C* are the soil temperature at depth: 25 cm (A), 40 cm (B) and 55 cm (C).

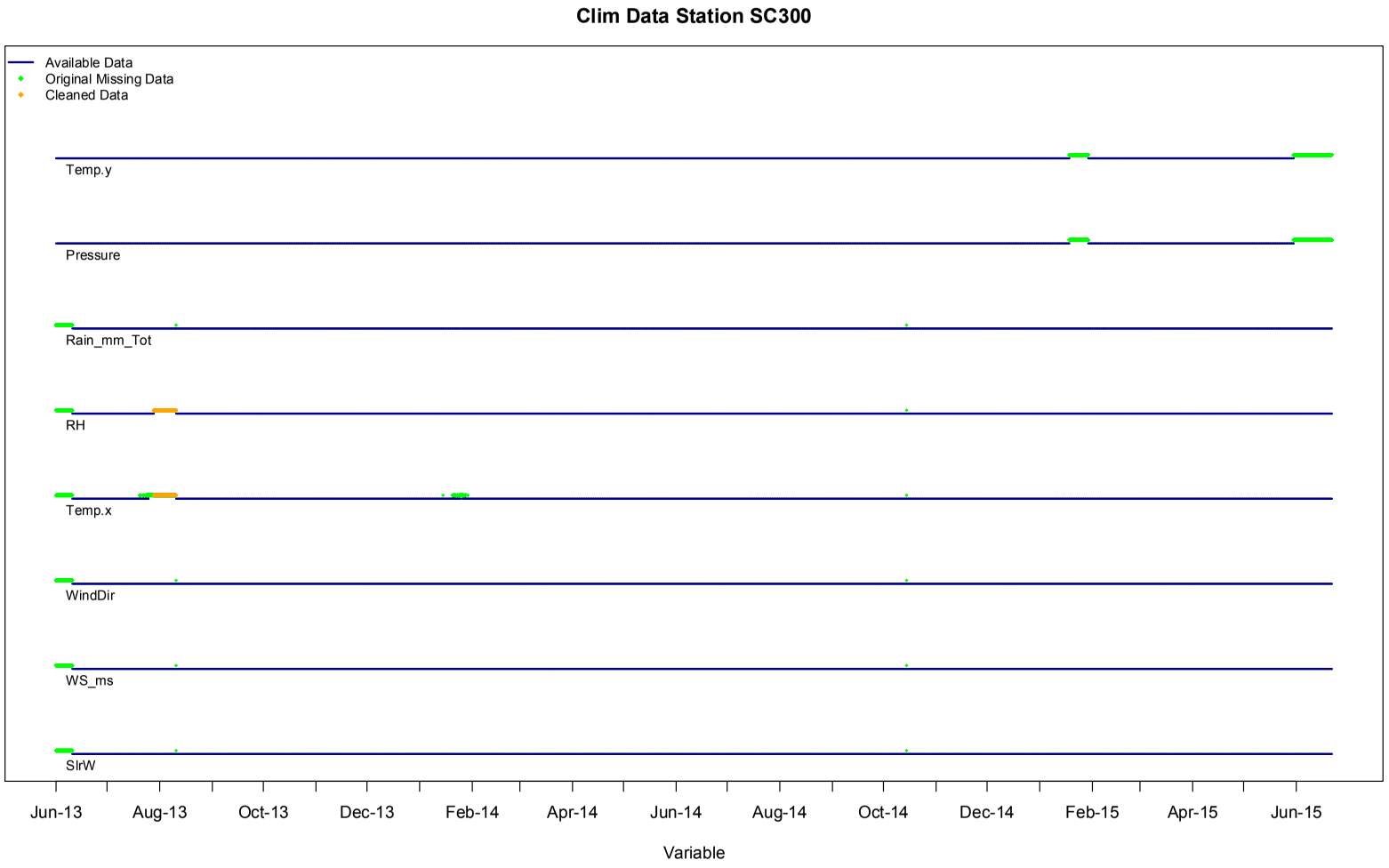

Figure A.5: Climatic data availabity in station SC300 during the period June 2013 - May 2015. *SlrW* is solar radiation. *WS ms* is wind speed. *WindDir* is wind direction. *Temp.x* is air temperature from the CS215. *RH* is relative humidity. *Rain mm Tot* is rainfall. *Pressure* is air pressure from barodiver. *Temp.y* is temperature from barodiver.

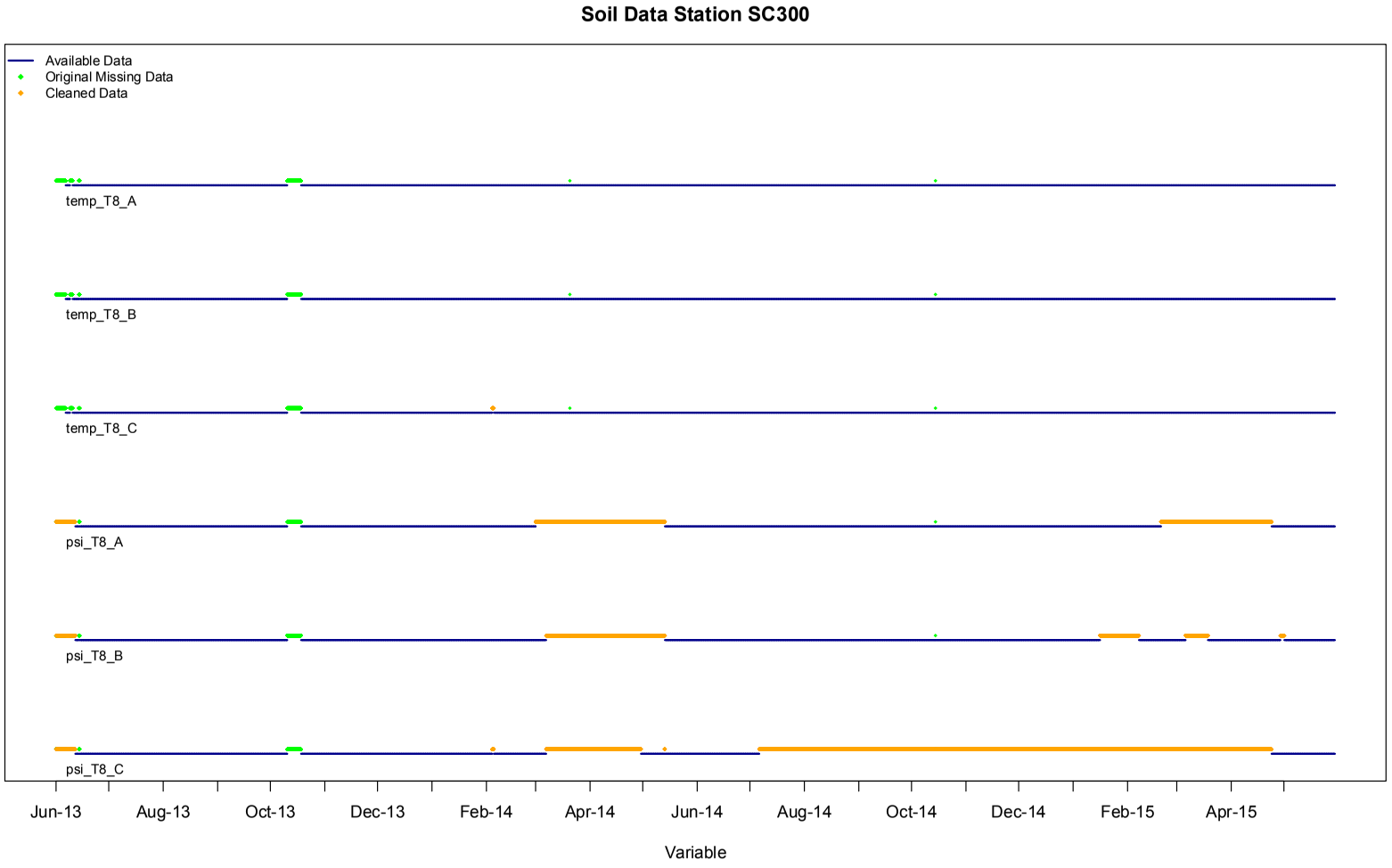

Figure A.6: Soil data availabity in station SC300 during the period June 2013 - May 2015. *psi T8 A*, *psi T8 B* and *psi T8 C* are the soil water pressure at depth: 25 cm (A), 40 cm (B) and 55 cm (C). *temp T8 A*, *temp T8 B* and *temp T8 C* are the soil temperature at depth: 25 cm (A), 40 cm (B) and 55 cm (C).

A 3 Fully implicit, finite-differences resolution of variably saturated flow in 1D

A 3.1 Soil hydraulic properties

In unsaturated conditions, water content θ can be expressed with the closed-form equation provided by Van Genuchten (1980) (Eq. 2.8). For any $h > 0$, $\theta(h) = \theta_s$. The derivative of Eq. 2.8 with respect to h reads:

$$\frac{d\theta}{dh}(h) = mn\alpha^n h^{n-1}(\theta_s - \theta_r)\left(1 + |\alpha h|^n\right)^{-m-1} \tag{A.1}$$

This expression is equivalent to *Eq.23* in Van Genuchten (1980). The derivative was obtained with the condition $h < 0$.

The relative permeability $K(h)$ is given in Eq. 2.8.

$$K_r(h) = \frac{\left(1 - |\alpha h|^{n-1}(1 + |\alpha h|^n)^{-m}\right)^2}{(1 + |\alpha h|^{m/2})} \tag{A.2}$$

A 3.2 Model implementation

We consider the mixed-form equation for variably saturated flow proposed by Celia et al. (1990) and modified by Clement et al. (1994):

$$S_s\frac{\theta}{\eta}\frac{\partial h}{\partial t} + \frac{\partial \theta}{\partial t} = \frac{\partial}{\partial z}\left(-K(\theta)\frac{\partial H}{\partial z}\right) + Q \tag{A.3}$$

where S_s [L^{-1}] is the specific storage, H [L] is the hydraulic head, θ [-] is the water content, η [-] is the porosity, K [LT^{-1}] is the hydraulic conductivity and Q [T^{-1}] the source term. Contrary to the original Richards' equation accounts for the effect of specific storage, which makes it valid for transient saturated flow.

The hydraulic head is defined by $H = h + z$, where h is the pressure head and z the coordinate along the (Oz) vertical upward axis Eq. A.3 yields:

$$S_s\frac{\theta}{\eta}\frac{\partial h}{\partial t} + \frac{\partial \theta}{\partial t} = \frac{\partial}{\partial z}\left(K\frac{\partial h}{\partial z}\right) + \frac{\partial K}{\partial z} \tag{A.4}$$

Notice that Eq. A.3 yields Eq. 2.7 if S_s is zero. Spatial derivation is obtained with a central differences scheme as follows :

$$\frac{\partial}{\partial z}\left(K\frac{\partial h}{\partial z}\right)+\frac{\partial K}{\partial z}\approx\frac{1}{dz}\left\{\left(\frac{K_i^{n+1,m}+K_{i+1}^{n+1,m}}{2}\right)\left(\frac{h_{i+1}^{n+1,m+1}-h_i^{n+1,m+1}}{dz}\right)-\left(\frac{K_i^{n+1,m}+K_{i-1}^{n+1,m}}{2}\right)\left(\frac{h_i^{n+1,m+1}-h_{i-1}^{n+1,m+1}}{dz}\right)\right\}+\frac{1}{dz}\left(\left(\frac{K_i^{n+1,m}-K_{i+1}^{n+1,m}}{2}\right)-\left(\frac{K_i^{n+1,m}+K_{i-1}^{n+1,m}}{2}\right)\right) \tag{A.5}$$

where n denotes the nth time step, when the solution is known, dt is the time step, K_i is the value of hydraulic conductivity at the ith node and h_i the value of pressure head at the ith node. The current and previous Picard iteration are denoted as $m+1$ and m, respectively.

A backward finite-difference expression is used for temporal derivative :

$$S_s\frac{\theta}{\eta}\frac{\partial h}{\partial t}\approx\frac{S_s}{\eta}\theta_i^{n+1,m}\left(\frac{h_i^{n+1,m+1}-h_i^n}{dt}\right) \tag{A.6}$$

After Celia et al. (1990) and Clement et al. (1994), time derivative of water content is approximated as follows:

$$\frac{\partial\theta}{\partial t}\approx\left(\frac{\theta_i^{n+1,m}-\theta_i^n}{dt}\right)+C_i^{n+1,m}\left(\frac{h_i^{n+1,m+1}-h_i^{n+1,m}}{dt}\right) \tag{A.7}$$

where C is the derivative of the water content with respect to the pressure head (Eq. A.1)

Eq. A.5, Eq. A.6 and Eq. A.7 can be re-arranged to form a system of linear algebraic equations :

$$m_1h_{i-1}^{n+1,m+1}+m_2h_i^{n+1,m+1}+m_3h_{i+1}^{n+1,m+1}=-b_1h_i^{n+1,m}-b_2h_i^n+b_3+b_4 \tag{A.8}$$

with:

$$m_1 = \left(\frac{K_i^{n+1,m} + K_{i-1}^{n+1,m}}{2dz^2} \right) \tag{A.9}$$

$$m_3 = \left(\frac{K_i^{n+1,m} + K_{i+1}^{n+1,m}}{2dz^2} \right) \tag{A.10}$$

$$b_1 = \frac{C_i^{n+1,m}}{dt} \tag{A.11}$$

$$b_2 = \frac{S_s \theta_i^{n+1,m}}{\eta dt} \tag{A.12}$$

$$b_3 = -\left(\frac{K_{i-1}^{n+1,m} - K_{i+1}^{n+1,m}}{2dz} \right) \tag{A.13}$$

$$b_4 = \left(\frac{\theta_i^{n+1,m} - \theta^n}{dt} \right) \tag{A.14}$$

$$m_2 = -(m_1 + m_3 + b_1 + b_2) \tag{A.15}$$

The following system should then be solved iteratively :

$$\mathbf{M}^{n+1,m} \mathbf{h}^{n+1,m+1} = \mathbf{B}^{n+1,m} \tag{A.16}$$

where $\mathbf{M}$ is a sparse matrix containing in its central diagonals the coefficients m_1, m_2, m_3 and vector $\mathbf{B}$ gather the second member of Eq. A.8.

The resolution of the system is obtained with the Python `scipy.sparse.cgs` function.

A 3.3 Boundary conditions

We consider a soil column subject to infiltration at the top. The boundary condition at the bottom is free drainage.

A 3.3.1 Fixed flow at top

With a flux q_z [LT^{-1}] imposed to one of the boundaries of the soil column, Darcy law yields:

$$q_z = -K \frac{\partial H}{\partial z} \iff q_z = -K \left(\frac{\partial h}{\partial z} + 1 \right) \tag{A.17}$$

If the flux q_{top} is imposed to the bottom of the column, the discretization of Eq. A.17 yields:

$$q_{top} = K_{I-1/2} \left(\frac{h_I - h_{I-1}}{dz} + 1 \right) \tag{A.18}$$

A mass conservancy solution can be assessed with the mass balance equation:

$$\frac{\partial \theta}{\partial t} = -\frac{\partial q}{\partial z} - Q \tag{A.19}$$

The discretization of Eq. A.19 on the top node yields:

$$\left(\frac{\theta_i^{n+1,m} - \theta^n}{dt}\right) = -2\frac{q_I^{n+1} - q_{I-1/2}^{n+1,m}}{dz} - Q_I^n \tag{A.20}$$

Inserting Eq. A.18 and Eq. A.20 into Eq. A.8 yields:

$$m_1 h_{I-1}^{n+1,m+1} - (\frac{b_1}{2} + b_2 + m_1) h_I^{n+1,m+1} = -\frac{b_1}{2} h_I^{n+1,m} - b_2 h_I^n + \frac{b_4}{2} + \frac{K_{I-1/2}^n}{dz} + \frac{q_{top}}{dz} + Q_I^n \tag{A.21}$$

Where q_{top} is the flux imposed at the top of the soil profile. Note that infiltration into the soil column is simulated with a negative q_{top}.

A 3.3.2 Free drainage at the bottom of the column

Fixed flow at the bottom can be obtained similar to section A 3.3.1. Eq. A.8 yields:

$$-(\frac{b_1}{2} + b_2 + m_3) h_0^{n+1,m+1} + m_3 h_1^{n+1,m+1} = -\frac{b_1}{2} h_0^{n+1,m} - b_2 h_1^n + \frac{b_4}{2} - \frac{K_{1/2}^n}{dz} - \frac{q_{bot}}{dz} + Q_0^n \tag{A.22}$$

Where q_{bot} is the drainage flux.

Free drainage is expressed with a unit vertical hydraulic head gradient:

$$\begin{aligned} \frac{\partial H}{\partial z} = 1 &\iff \frac{\partial}{\partial z}(z + h) = 1 \\ &\iff \frac{\partial h}{\partial z} = 0 \\ &\iff \frac{(h_1 - h_0)}{dz} = 0 \\ &\iff h_0 = h_1 \end{aligned} \tag{A.23}$$

In this case, using the Darcy law, the flux is equal to K, so for free drainage conditions Eq. A.22 yields:

$$-(\frac{b_1}{2} + b_2 + m_3) h_0^{n+1,m+1} + m_3 h_1^{n+1,m+1} = -\frac{b_1}{2} h_0^{n+1,m} - b_2 h_1^n + \frac{b_4}{2} - \frac{K_{1/2}^n}{dz} - \frac{K_0^n}{dz} + Q_0^n \tag{A.24}$$

A 3.4 Flux calculation

The flux for each node is calculated when the flow equation is solved at each time. We used the discretized form of the Darcy's Law (Eq. A.17) for all nodes

except for the node at the top of the soil profile. At the top node, we solved q_{top} for the mass balance equation and Darcy's Law equation incorporated in Eq. A.21, as it seems a more stable and mass-conservative solution (Simunek et al., 2013). Then the node flux is calculated as follows:

$$\begin{aligned} q_0 &= -K_{1/2}\left(\frac{h_1 - h_0}{dz} + 1\right) \\ q_i &= \frac{-K_{i+1/2}\left(\frac{h_{i+1}-h_i}{dz} + 1\right) - K_{i-1/2}\left(\frac{h_i - h_{i-1}}{dz} + 1\right)}{2} \\ q_I &= -K_{I-1/2}\left(\frac{h_I - h_{I-1}}{dz} + 1\right) - \frac{dz}{2}\left(\frac{\theta_I^{n+1} - \theta_I^n}{dt} + S_p\right) \end{aligned} \tag{A.25}$$

Notice that q_I is the infiltration rate, and q_0 is the drainage rate, that in our study is the deep percolation rate.

A 3.5 Runoff estimation

When the rainfall rate exceeds the soil infiltration capacity, a pounding condition occurs at the top of a plane terrain. In time, the pounded water will infiltrate to the soil. Contrary, on sloping terrains the pounding condition is negligible while water is loss as runoff. Following Herrada et al. (2014), the pounding condition is reached when the upper soil surface saturates. A transient *fixed flow* is prescribed at the upper boundary (Herrada et al., 2014):

$$In = q(I, n) = q_{rainfall} = q_{top} \tag{A.26}$$

where In is the infiltration rate. According to Herrada et al. (2014), this condition applies when $\theta(I, n) < \theta_s$, if $\theta(I, n)$ reaches saturation, $\theta(I, n) = \theta_s$. In our case, as we use the mixed form of the Richard's equation, our boundary conditions are different and the system resolution complex. Following the approach of Herrada et al. (2014), we use the saturation condition from the pressure head h to modify the upper boundary condition. When $h_I^{n+1} < 0$, the upper boundary condition is the Eq. A.21. In the case where $h_I^{n+1} \geq 0$, the fixed flux upper boundary condition switches to a fixed head condition, where $h_{top}^{n+1} = 0$. On this scenario, the linear system is resolved again with the new conditions to obtain h^{n+1}. The infiltration rate is solved using Eq. A.25 for the top node, and surface runoff is calculated as (Herrada et al., 2014):

$$q_{runoff} = q_{rainfall} - In \tag{A.27}$$

A 4 Rating curve equations

A 4.1 El Bayo

The equation is obtain from the calibration of two power functions:

$$Q = \begin{cases} 8 \times 10^{-7} \times WH^{5.45} & \text{if} \quad WH < 22.8 \\ \\ 3 \times 10^{-4} \times WH^{3.55} & \text{if} \quad WH \geq 22.8 \end{cases} \tag{A.28}$$

where Q [l/s] is discharge and WH [cm] is the water height.

A 4.2 Chuki Marka

The equation is obtain from the calibration of a power function:

$$Q = 9 \times 10^{-1} \times WH^{1.61} \tag{A.29}$$

where Q [l/s] is discharge and WH [cm] is the water height.

A 4.3 Cerro Gato

Discharge equation is deduced using the general form of the weir equation from the geometry of *Cerro Gato*'s control section (Fig. A.7):

$$Q = \begin{cases} 8/15 \times (2g)^{0.5} \times D_c \times tan(A/2) \times WH^{2.5} & \text{if} \quad WH \leq WH_t \\ \\ (2g)^{0.5} \times D_c \times [-2/15 \times tan(A/2) \times \\ (10 \times WH \times WH_r^{1.5} - 6 \times WH_r^{2.5} - 4 \times WH^{2.5}) + \\ 2/3 \times L_t \times WH_r^{1.5}] + \\ 2/3 \times (2g)^{0.5} \times D_c \times (L_r - L_t) \times WH_r^{1.5} & \text{if} \quad WH > WH_t \end{cases} \tag{A.30}$$

where Q [m^3/s] is discharge, g [m/s^2] is the gravity acceleration (9.8), D_c [-] is the discharge coefficient (0.58), A is the triangular section angle, WH [m] is total water height, WH_t [m] is the water height at triangular section, WH_r [m] is the water height at rectangular section, L_t [m] is the length of the triangular section and L_r [m] is the length of the rectangular section.

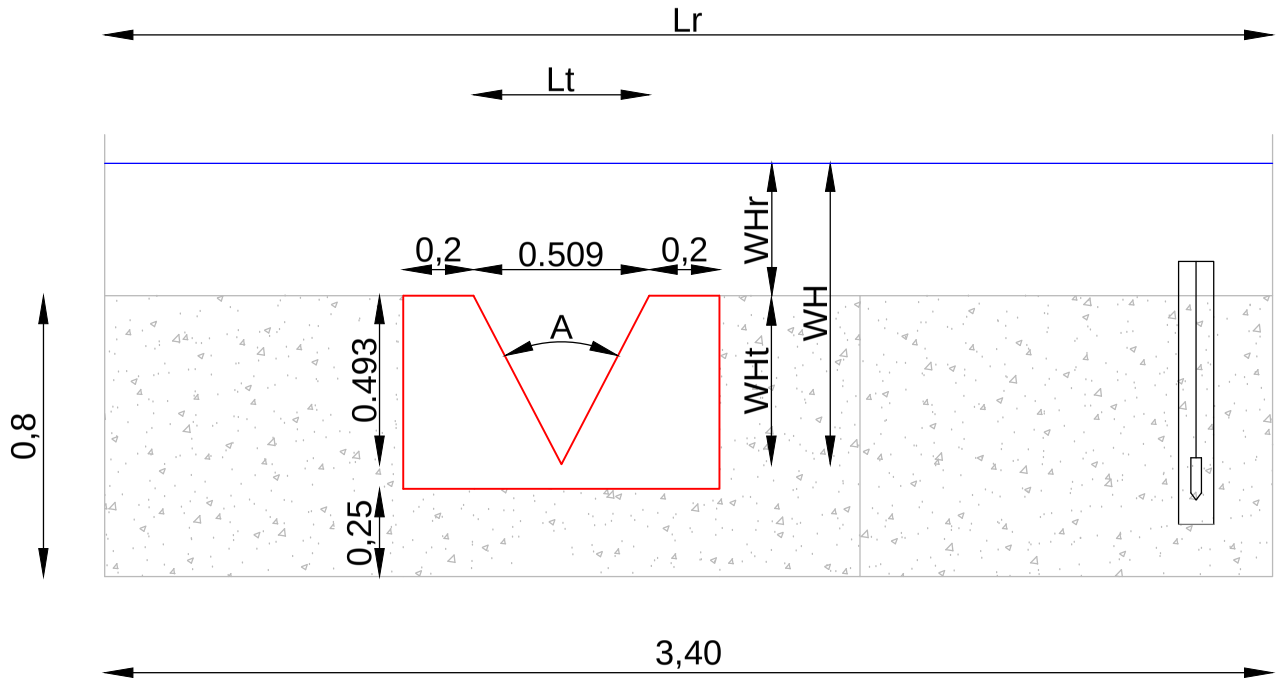

Figure A.7: Weir dimensions of Cerro Gato. Discharge equation is deduced from the general form of the weir equation.

A 5 Localization of previous hydrological monitoring

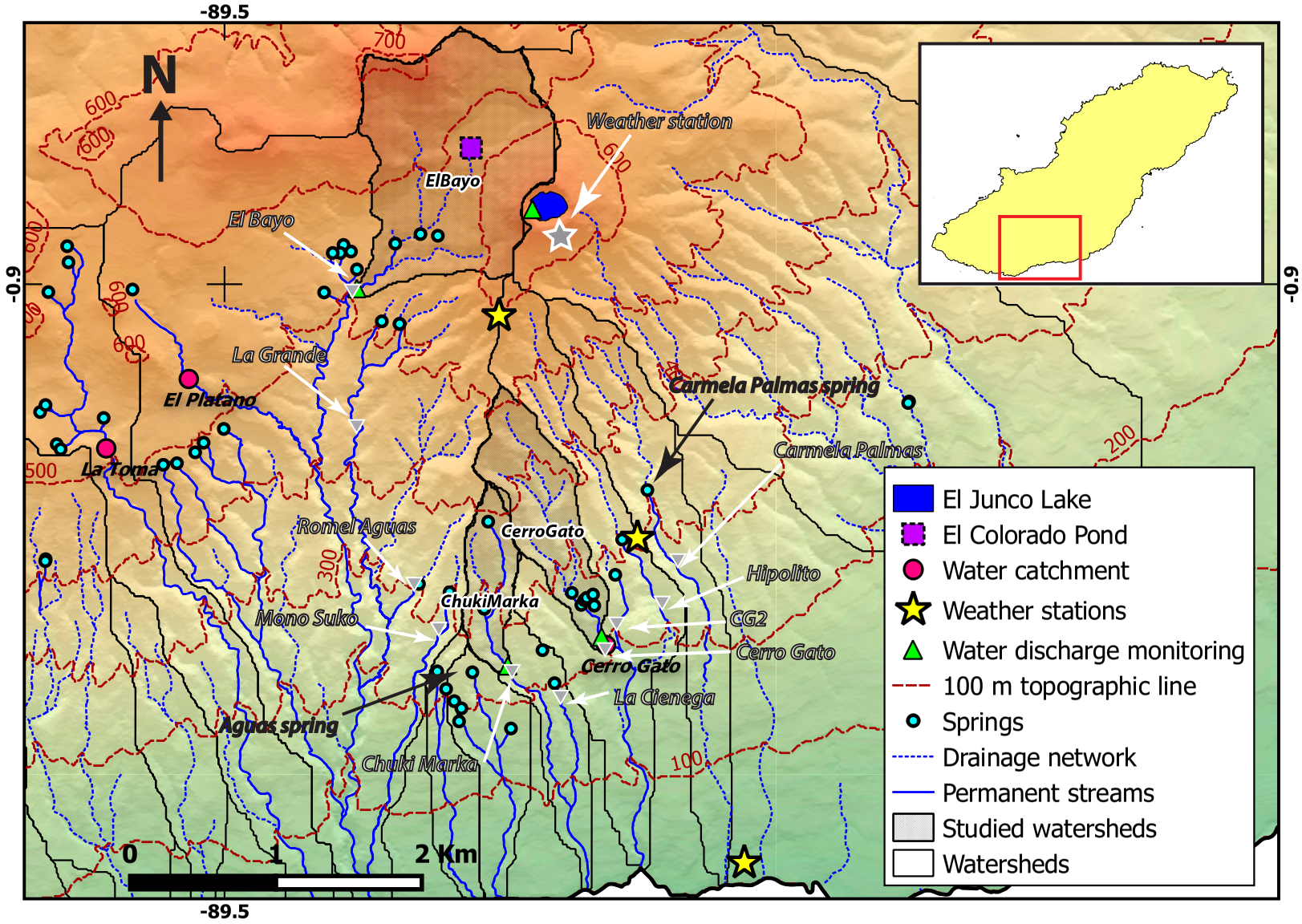

Figure A.8: Map of the localization of previous hydrological monitoring (Adelinet, 2005; d'Ozouville, 2007) in the current monitoring network. Previous monitoring is represented in gray figures surrounded by white lines. Triangules correspond to weekly punctual measurements of discharge measurements with the time/volume technique from May 2005 to September 2006. The start represent a weather station installed at the summit of *El Junco* lake from November 2004 to November 2006.